공학박사 학위논문

The velocity-construction algorithm using the Laplace-Fourier-domain inversion for a land dataset

- 라플라스-푸리에 영역 역산기법을 이용한 육상탐사자료에 대한 속도 모델 구축 알고리즘-

2014년 2월

서울대학교 대학원

계산과학 협동과정

유 제 우

Abstract

Currently, brilliant advances in the acquisition offer the possibility of solving the problem of the absence of low-frequency components that hinders the full-waveform inversion, yet, most real datasets do not contain these components. Thus, the long-wavelength velocity model that can be obtained using the Laplace- or Laplace-Fourier-domain inversion should be conducive to delineating the subsurface structure via migration or Fourier-domain inversion starting from this algorithm.

In this thesis, the 2D elastic Laplace-Fourier inversion algorithm was developed for the application to a land dataset could recover the long-wavelength velocity models. This velocity-estimation algorithm adopts the finite element method on an unstructured grid with expectation of mitigating the high nonlinearity observed in datasets that originate from topography via accurate depiction of an irregular surface.

For the inversion methodology, the novel pseudo-Hessian matrix is suggested in this thesis. This modified pseudo-Hessian matrix allows for a deeper penetration depth of the inverted result and promises a more convergent result regardless of damping factor that generally required for pseudo-Hessian matrix. Also, the normalized stopping criterion was introduced using multi-objective assumption based on the property of the logarithmic objective function, the natural separation of the phase and amplitude error, to ensure that the phase and amplitude information contribute to the inversion result with parity. This method could help to prevent the result of an acquiring of an over- or under-inverted result caused by over-fitting or an unsuitable determination of

the number of inversion iterations.

The developed inverse algorithm was tested using a time domain synthetic dataset generated with a realistic foothill model. The results of the test demonstrate that this algorithm can recover an adequate velocity model without requiring low-frequency information and with the dataset containing an expected noise.

Keywords: 2D elastic domain, Full-waveform inversion, Unstructured grid, Stopping criterion, Pseudo-Hessian matrix, Laplace-Fourier domain

Student Number: 2009-22977

Contents

List of Tables

List of Figures

Chapter 1. Introduction

Full-waveform inversion (FWI) has been used as a reasonable tool for recovering subsurface parameters using pre-stack seismic data since Laily and Tarantola introduced the back-propagation algorithm (Laily, 1983; Tarantola, 1984). In the past 30 years, seismic inversion has dramatically developed with the advancement of inversion theories and computational environments (Tarantola, 1984; Tarantola, 1986; Mora, 1987; Bunks et al., 1995; Pratt, 1998, Operto et al., 2004; Shin and Min, 2006; Shin et al., 2007; Shin and Cha, 2008, 2009). Also, the advance of the FWI strategy could be possible to apply the FWI to the real dataset has been suffered from the lack of low-frequency information via inversion starting from a long wavelength velocity model computed using reflection tomography (Brenders and Pratt, 2007; Virieux and Operto, 2009) or the Laplace inversion algorithm (Shin and Cha, 2008; Shin and Cha, 2009; Ha et al., 2012). In recent years, the brilliant developments in the acquisition field have demonstrated success in obtaining good land datasets that contain sufficient low-frequency information and wide-aperture long-offset data (Plessix, 2012; Baeten, 2013), and these developments are promising for the use of FWI for velocity-model building in production lines in the future. However, most of the FWI research has been performed using an acoustic environment, and the application of FWI using the elastic wave equation remains a topic of future work.

FWI using the elastic wave equation must be a more appropriate algorithm than the acoustic assumption for land datasets because the earth supports both P- and S- waves; however, the successful case studies using elastic FWI with

real datasets are not easy to find.

Elastic full-waveform inversions have been studied by many geo-physicists. They have presented partially successful results and have explained why elastic FWI encounters more difficulties than acoustic FWI (Mora, 1987, 1988; Tarantola, 1987; Shipp and Singh, 2002; Gelis et al., 2007). For instance, multiple parameters of elastic FWI are interdependent on one another. This interdependency causes the inversion to converge more easily to a local minimum than in the acoustic case (Brossier et al., 2009, 2010; Bae et al., 2010; Lee et al., 2010). The complex topography of an acquisition region produces extremely complex seismic signals, especially for surface waves of large amplitude energy, and this complexity disturbs the convergence of the inverse problem by increasing the nonlinearity (Anouar et al., 2011). Moreover, the difference in surface-wave propagation between the 2D and 3D elastic wave equations is one of the most critical hindrances to attempt to perform a land inversion using the elastic approach. In addition, the problem of the lack of low-frequency components is still extant for most real land datasets. Because the novel acquisition method that is capable of obtaining low-frequency information suffers from limitations concerning applicable sites and for sources, it is not possible to apply this method for every land acquisition site.

This research was started with the purpose of recovering a proper velocity model from a real land dataset using the Laplace-Fourier inverse algorithm suggested by Shin and Cha, 2009.

The Laplace-Fourier algorithm offers some advantages for elastic inversion. Most importantly, this method does not suffer from the absence of the low-frequency components, as has been verified in many studies (Shin et al., 2008, 2009; Cha et al., 2010; Ha et al., 2010; Chung et al., 2010; Bae et al., 2010;

Kim et al., 2013). Additionally, especially for the elastic case, this method allows the use of the 2D elastic wave equation for the inversion of a 3D land dataset. The most critical difference between the 2D and 3D elastic equations is the damped (3D) or un-damped (2D) surface waves. This difference means that the discrepancy increases with increasing offset distance between the modeled data and the observed data when the 2D modeling scheme is used. However, the existence of time damping constant in the Laplace or Laplace-Fourier approach could effectively reduce this discrepancy. Ha et al. (2010) have inverted synthetic elastic data using the acoustic wave equation without removing the Rayleigh waves in the Laplace domain by exploiting this characteristic. They were able to suppress the Rayleigh wave via the damping applied in the Laplace transformation. Therefore, we believe that the 2D Laplace-Fourier-domain inversion could mitigate this difference in surface-wave propagation.

Elastic inversion using a Laplace-transformed dataset has already been performed by Chung et al., in 2010. They successfully demonstrated that the Laplace inversion method has the ability to recover long-wavelength velocity for the elastic parameters. However, this study was performed using the assumption of an upper flat surface; thus, their algorithm does not have the ability to handle with real data that of complex topography. For realistic elastic wave propagation, the presence of the complex topography is one of the most predominant factors that affect successful inversion (Gelis et al., 2007; Romdhane et al., 2011). Several studied have indicated that complex topography drastically influences the amplitudes and phases of the seismic signal (Bleibinhaus and Rondenay, 2009; Shiann-Jong et al., 2009; Romdhane et al, 2011).

Thus, this FWI algorithm adopts unstructured grids to describe the complex topography of a land acquisition site. The modeling algorithm, gradient calculation, and updating are performed on unstructured grids, and only the output result is mapped to a structured grid to apply a seismic inversion method such as reverse time migration after the inversion is completed.

Also in this paper, a novel gradient-scaling method for elastic Laplace-Fourier inversion is introduced which is obtained by modifying the pseudo-Hessian matrix derived by Shin et al., 2001. The newly introduced pseudo-Hessian matrix could increases the penetration depth of the inverted result, and it also could give proper preconditioning to the steepest descent gradient direction without a damping factor defined in the original pseudo-Hessian with the purpose of stabilization. In addition, the stopping criterion using normalized amplitude and phase error is suggested. The amplitude and phase error can be extracted from the error of logarithmic objective function and the new stopping criterion could prevent a biased inversion to the amplitude or phase.

To address the problem of the interdependency among elastic parameters, the density was assumed as a constant value; thus it was not included in the updating process, following the approach taken in other studies (Brossier et al., 2009, 2010; Bae et al., 2010; Lee et al., 2010, Romdhane, 2011; Jeong et al, 2012), and this conventional density assumption did not disturb the recovery of the velocity model in numerical tests using a synthetic dataset.

This work begins with the definition of the Laplace and Laplace-Fourier-transformed datasets. And then, the simulation algorithm of the 2D elastic wave propagation was reviewed. The finite element method was used on unstructured grid for complex topography. The perfectly matched layer (PML)

boundary condition is applied for this modeling algorithm (Cohen, 2002).

In chapter 2.4, some theories of full-waveform inversion was described, such as the computation of the steepest-gradient direction, how to estimate source wavelets, some details concerning the novel pseudo-Hessian matrix, and the normalized stopping criterion.

In chapter 3, the developed elastic Laplace-Fourier-domain FWI is applied to a synthetic dataset. The first test was performed using the same modeling algorithm in the forward and inverse problems to confirm the performance of the developed inversion algorithm. The second test was performed with 3 different purposes; the observation of the dependency on low-frequency information in the dataset, the robustness against noisy data, and the performance with respect to the results of the acoustic approach. The synthetic dataset used in this study was generated using the time-domain 2D elastic interior penalty discontinuous Galerkin method on an unstructured grid (Appendix A). This time-domain dataset was computed using realistic foothill velocity models with complex topography.

Chapter 2. Theory

2.1 The elastic wavefield in the Laplace and Laplace-Fourier domains

The Laplace-Fourier transform of a time domain wavefield is given by (Shin and Cha, 2009)

$$\tilde{u}(s) = \int_0^\infty u(t)e^{-st}dt, \qquad (2\text{-}1)$$
$$s = i\omega + \sigma,$$

where s is a complex number, σ is the real Laplace damping constant, ω is the real angular frequency (given by $2\pi f$, where f is the frequency), t is the time, $u(t)$ is the time-domain wavefield, and $\tilde{u}(t)$ is the Laplace-Fourier transform of $u(t)$.

In equation (2-1), we can observe that the Laplace-Fourier-transformed wavefield is the same as the Laplace-transformed wavefield when ω is zero. The Laplace-transformed wavefield is the integral of the damped time-domain wavefield with respect to time and the damping constant σ, and it can take on only real values. The Laplace transform for large σ turns the time-domain signal into a delta-like signal that shows the first arrival event, and the transform for small σ contains a larger contribution from late-arrival signals and is expected to include the reflections from deeper regions.

In contrast, the Laplace-Fourier-transformed wavefield contains both an amplitude term and a phase term, and it contributes to the acquisition of high-resolution parameter models when it is used for inversion.

For the observation of the properties of the Laplace-Fourier-transformed wavefield with respect to the damping constant and angular frequency, *the* amplitude of the Green's function of the elastic wave equation in the Laplace-Fourier domain is presented in Figure 2 and 3, calculated with 3 damping constants ($\sigma = 1, 5, \text{and } 10$), 3 angular frequencies ($\omega = 0, 10\pi, \text{and } 20\pi$), and the modeling parameters shown in Figure 1.

From Figure 2 and Figure 3, an estimation of some characteristics of the Laplace-Fourier-domain inversion is possible. First, we can see that the amplitude of the Laplace-Fourier wavefield becomes concentrated at the source point as the damping constant is increased, and this property is related to the penetration depth of the inversion.

Figure 4 and 5 show the phase component of the Laplace-Fourier-domain Green's function. In these figures, it is possible to confirm that the Laplace transform does not contain the phase information; thus, the Laplace-domain inversion can be considered to be a purely dynamic algorithm (Pyun et al., 2007). Therefore, the Laplace-domain inversion might be sensitive to impedance variations in the subsurface. On the other hand, the Laplace-Fourier wavefield contains both amplitude and phase information. It is interesting to note that the amplitude spectrum varies drastically with respect to the Laplace damping constant, but the phase spectrum seems to be influenced little or not at all by Laplace damping.

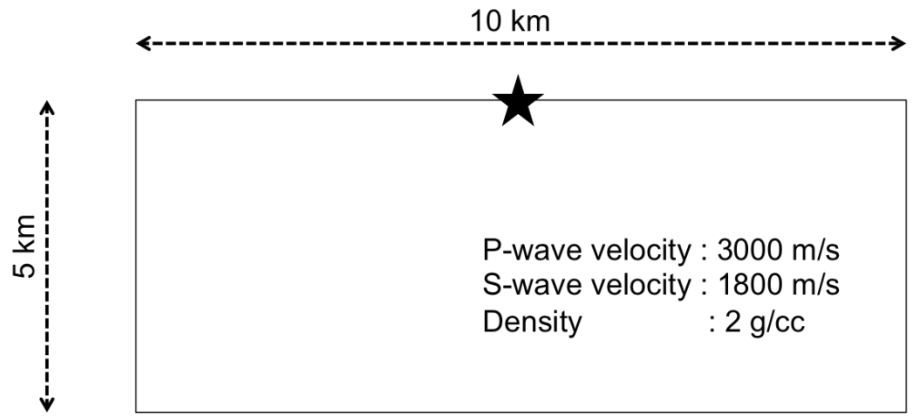

Figure 1. The geometry and homogeneous elastic parameters for computing the Green's function in the Laplace-Fourier domain.

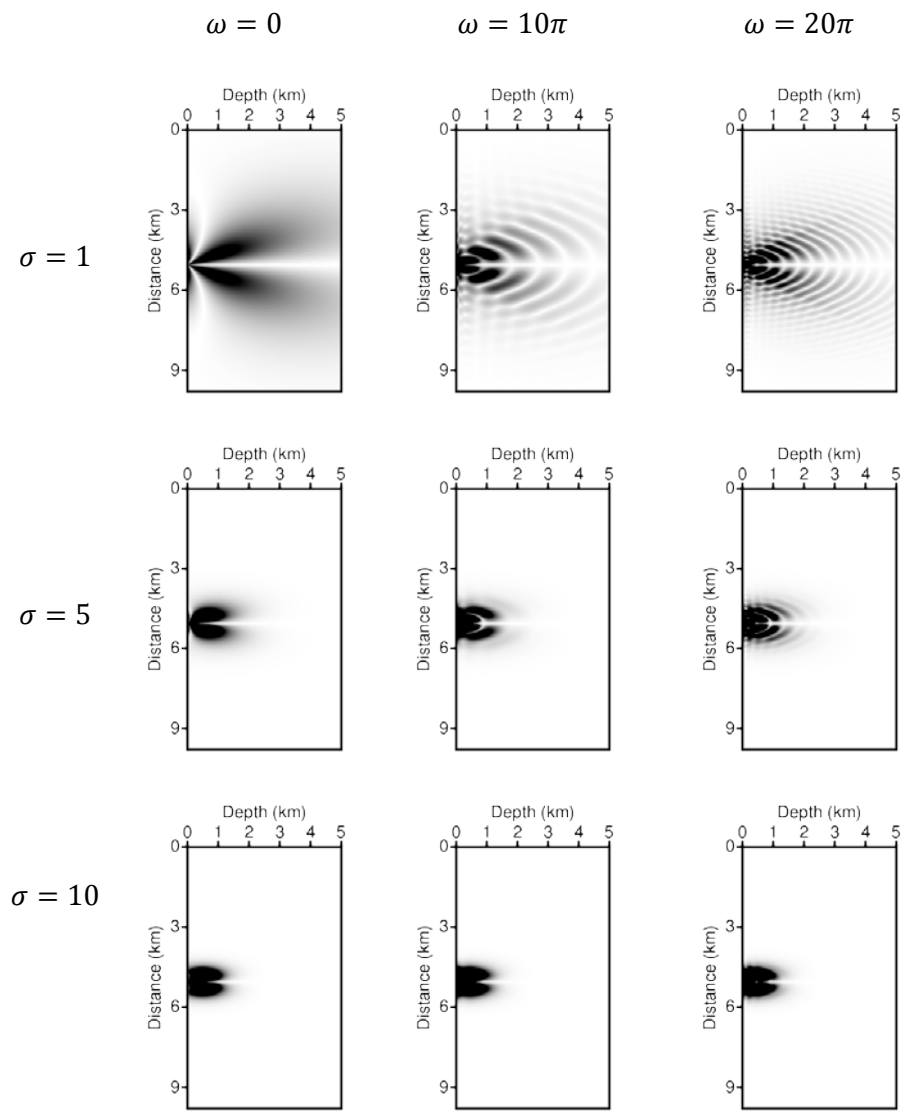

Figure 2. The amplitude spectrum of the horizontal Green's function in the Laplace-Fourier domain with respect to the 3 Laplace damping constants and 3 angular-frequency components.

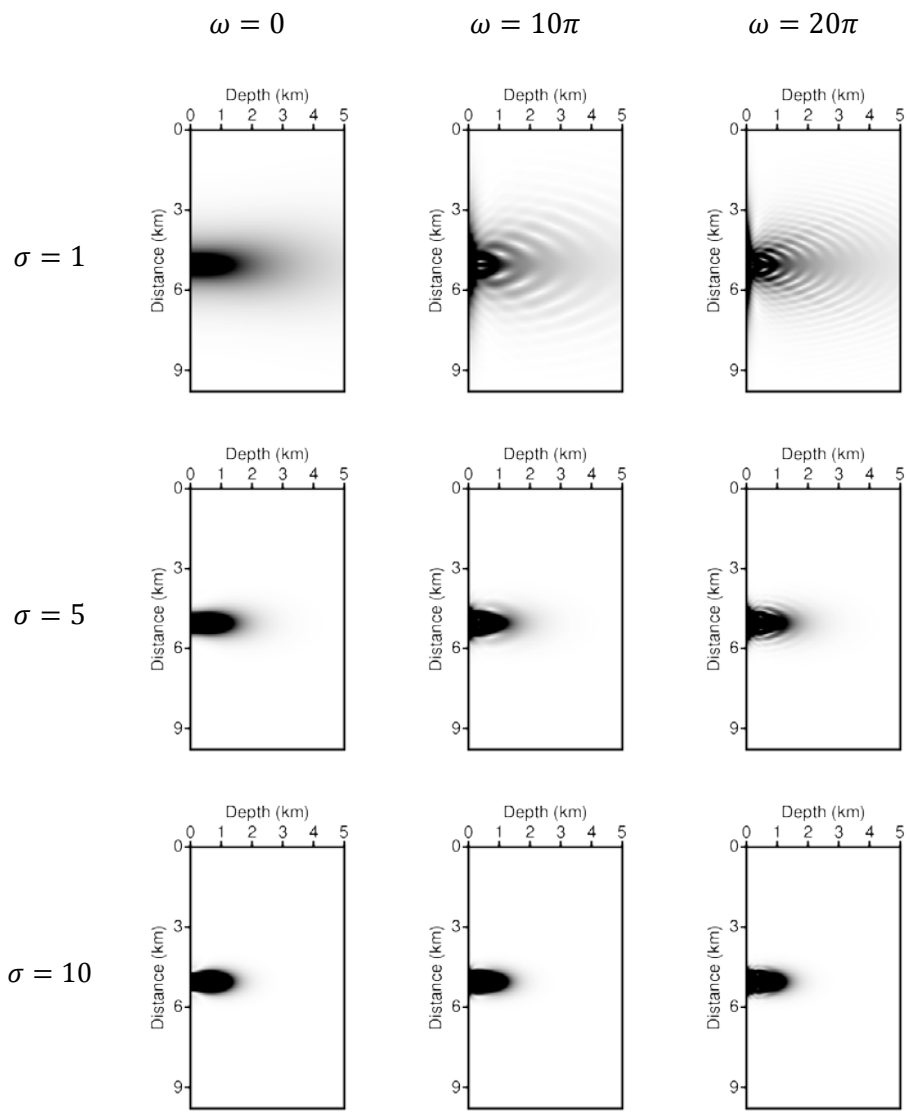

Figure 3. The amplitude spectrum of the vertical Green's function in the Laplace-Fourier domain with respect to the 3 Laplace damping constants and 3 angular-frequency components.

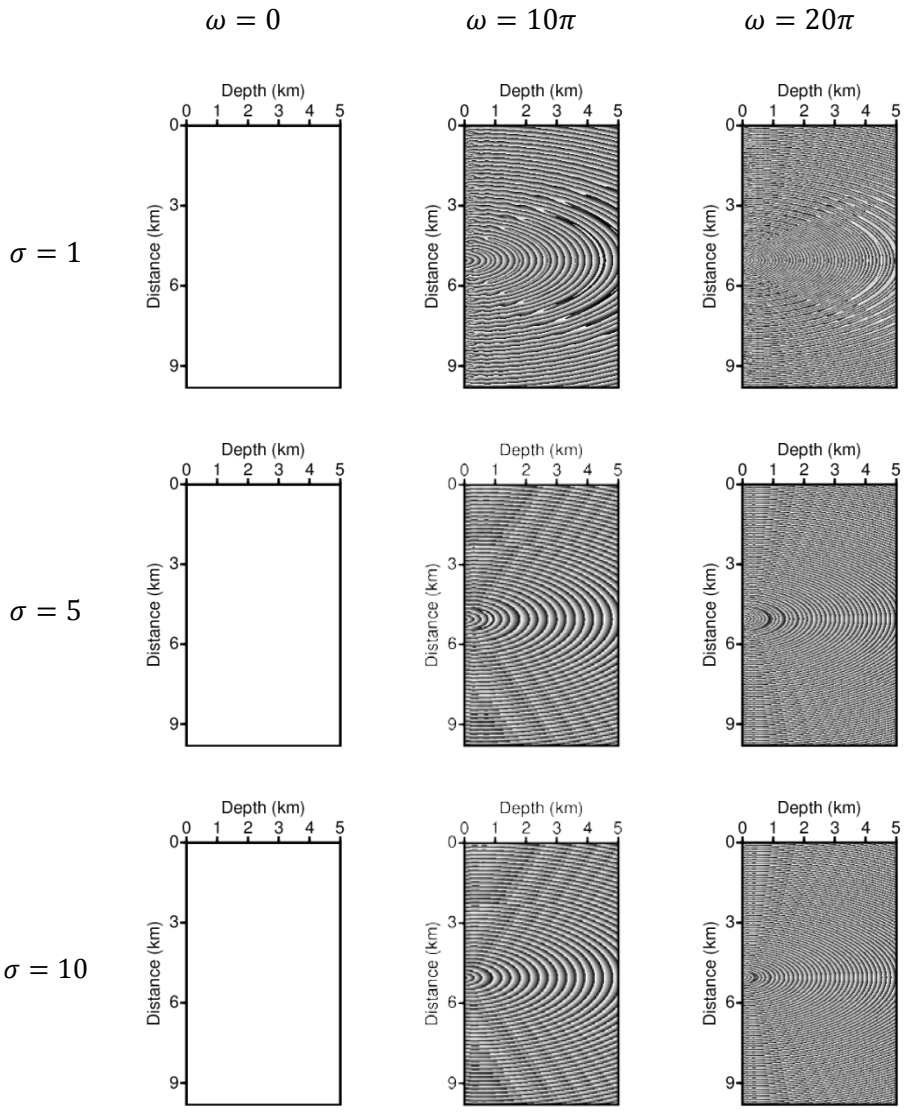

Figure 4. The phase spectrum of the vertical Green's function in the Laplace-Fourier domain with respect to the 3 Laplace damping constants and 3 angular-frequency components.

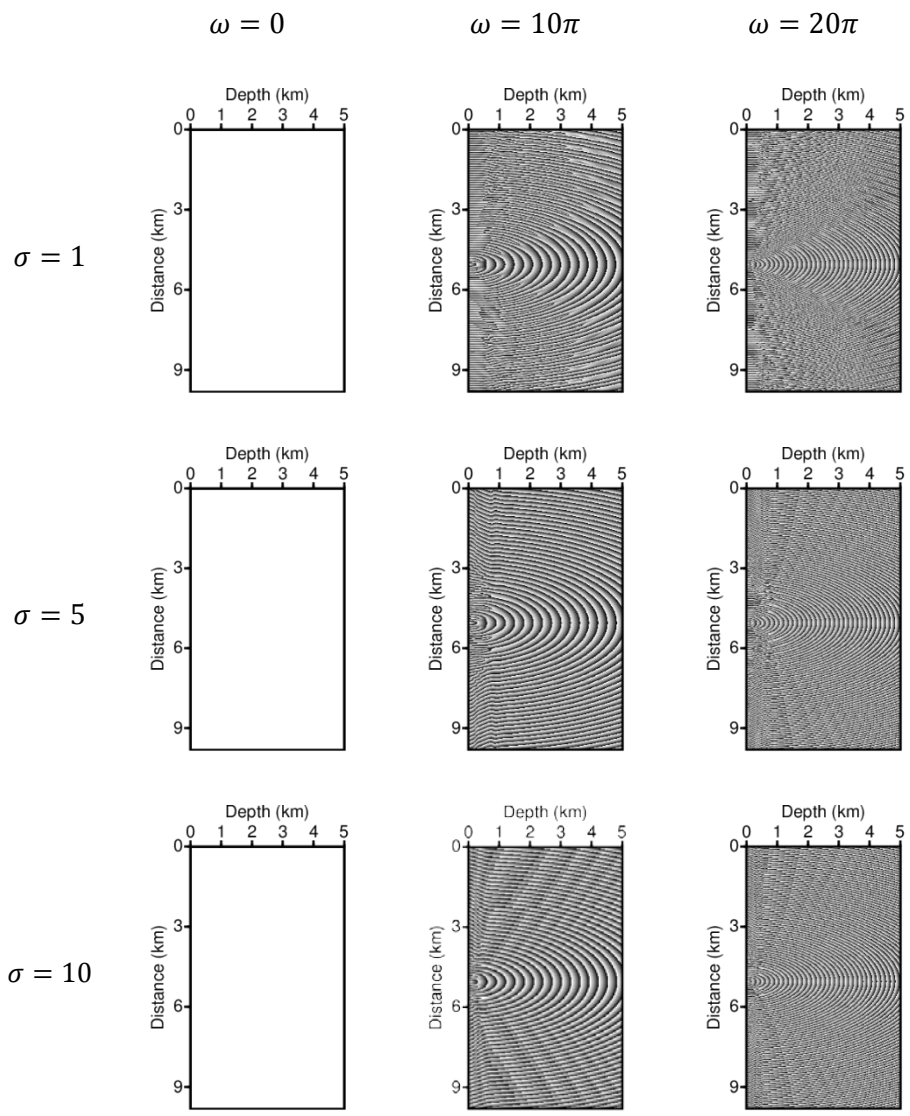

Figure 5. The phase spectrum of the vertical Green's function in the Laplace-Fourier domain with respect to the 3 Laplace damping constants and 3 angular-frequency components.

2.2 The elastic wave equation in the Laplace-Fourier domain

The elastic wave equation in the time domain for an isotropic and heterogeneous medium is defined as (Officer, 1958)

$$\rho \frac{d^2}{dt^2} u_x(\boldsymbol{x}, t) = \frac{\partial}{\partial x} \sigma_{xx}(\boldsymbol{x}, t) + \frac{\partial}{\partial z} \sigma_{xz}(\boldsymbol{x}, t), \tag{2-2}$$

$$\rho \frac{d^2}{dt^2} u_z(\boldsymbol{x}, t) = \frac{\partial}{\partial x} \sigma_{zx}(\boldsymbol{x}, t) + \frac{\partial}{\partial z} \sigma_{zz}(\boldsymbol{x}, t), \tag{2-3}$$

with

$$\sigma_{xx} = (\lambda + 2\mu) \frac{\partial u_x}{\partial x} + \lambda \frac{\partial u_z}{\partial z}, \tag{2-4}$$

$$\sigma_{xz} = \sigma_{zx} = \mu \left(\frac{\partial u_z}{\partial x} + \frac{\partial u_x}{\partial z} \right), \tag{2-5}$$

$$\sigma_{zz} = \lambda \frac{\partial u_x}{\partial x} + (\lambda + 2\mu) \frac{\partial u_z}{\partial z}, \tag{2-6}$$

where $\boldsymbol{x}$ denotes position vector (x, z), $u_x(\boldsymbol{x}, t)$ is the horizontal displacement, and $u_z(\boldsymbol{x}, t)$ is the vertical displacement in the time domain. σ_{xx}, σ_{xz}, and σ_{zz} are stresses. λ, μ, and ρ are the Lamé parameters, which have a particular relation to the P-wave and S-wave velocities.

$$\alpha = \sqrt{\frac{(\lambda + 2\mu)}{\rho}}, \tag{2-7}$$

$$\beta = \sqrt{\frac{\mu}{\rho}}, \tag{2-8}$$

where α is the P-wave velocity, and β is the S-wave velocity.

The elastic wave equation in the Laplace-Fourier domain can be obtained by taking the Laplace-Fourier transforms of equations (2-2) - (2-3), yielding

$$\rho s^2 \tilde{u}_x(\boldsymbol{x}, s) = \frac{\partial}{\partial x}\left(\lambda\Delta + 2\mu\frac{\partial \tilde{u}_x(\boldsymbol{x}, s)}{\partial x}\right) + \frac{\partial}{\partial z}\left(\mu\frac{\partial \tilde{u}_z(\boldsymbol{x}, s)}{\partial x} + \mu\frac{\partial \tilde{u}_x(\boldsymbol{x}, s)}{\partial z}\right), \tag{2-9}$$

$$\rho s^2 \tilde{u}_z(\boldsymbol{x}, s) = \frac{\partial}{\partial x}\left(\mu\frac{\partial \tilde{u}_z(\boldsymbol{x}, s)}{\partial x} + \mu\frac{\partial \tilde{u}_x(\boldsymbol{x}, s)}{\partial z}\right) + \frac{\partial}{\partial z}\left(\lambda\Delta + 2\mu\frac{\partial \tilde{u}_z(\boldsymbol{x}, s)}{\partial z}\right), \tag{2-10}$$

$$\Delta = \frac{\partial \tilde{u}_x(\boldsymbol{x}, s)}{\partial x} + \frac{\partial \tilde{u}_z(\boldsymbol{x}, s)}{\partial z}, \tag{2-11}$$

where,

$$\tilde{u}_x(\boldsymbol{x}, s) = \int_0^\infty u_x(\boldsymbol{x}, t)e^{-st}dt, \tag{2-12}$$

$$\tilde{u}_z(\boldsymbol{x}, s) = \int_0^\infty u_z(\boldsymbol{x}, t)e^{-st}dt. \tag{2-13}$$

2.3 Simulation of the elastic wave propagation using the FEM

The accurate simulation of wave propagation is the one of the most important factors that could make successful full-waveform inversion possible. For the elastic case, the exact simulation of elastic wave propagation for a land dataset depends on a description of complex topography of the acquisition site.

Many prior studies have been conducted regarding elastic inversion; however, most of them have used Cartesian grids for simulation, the flat-surface assumption and the 2D elastic wave equation. They have produced well-inverted results and promising algorithms. However, the flat-surface assumption makes that their studies are not suitable for the application to land datasets.

The flat-surface assumption imposes the different seismic responses with the acquired data. The most energetic signal of the elastic wave equation is the ground roll, which propagates along the surface, and an irregular surface generates much more complexity in this phenomenon. Thus, in this study, we tried to describe the complex topography by using the finite element method (FEM), which can easily handle complex boundaries and unstructured grids meshes, even when higher-order discretization is applied.

2.3.1 The finite element method for the 2D elastic wave equation

The simulation of the elastic wave propagation was computed in the domain shown in Figure 6. The symbol Ω represents the domain of elastic modeling. The symbol Ω_{pml} denotes the absorbing zone for the application of the perfectly matched boundary condition, and it is included in Ω. The Neumann boundary condition is applied to all outer boundaries, $\partial\Omega$.

For the given domain Ω, we consider shape-irregular meshes Γ_h that partitions the domain Ω into a triangular elements K, such that $\Omega = \sum K$. The 2D elastic wave equation in the Laplace-Fourier domain, equations (2-9) and (2-10), can then be express in the FEM formulation.

$$\rho s^2 \int_\Omega {u_x}^h v^h \mathrm{d}\Omega = \int_\Omega \frac{\partial}{\partial x}\left(\lambda \frac{\partial {u_x}^h}{\partial x} + \lambda \frac{\partial {u_z}^h}{\partial z} + 2\mu \frac{\partial {u_x}^h}{\partial x}\right) v^h d\Omega + \int_\Omega \frac{\partial}{\partial z}\left(\mu \frac{\partial {u_z}^h}{\partial x} + \mu \frac{\partial {u_x}^h}{\partial z}\right) v^h d\Omega, \tag{2-14}$$

$$\rho s^2 \int_\Omega {u_z}^h v^h \mathrm{d}\Omega = \int_\Omega \frac{\partial}{\partial x}\left(\mu \frac{\partial {u_z}^h}{\partial x} + \mu \frac{\partial {u_x}^h}{\partial z}\right) v^h d\Omega + \int_\Omega \frac{\partial}{\partial z}\left(\lambda \frac{\partial {u_x}^h}{\partial x} + \lambda \frac{\partial {u_z}^h}{\partial z} + 2\mu \frac{\partial {u_z}^h}{\partial x}\right) v^h d\Omega, \tag{2-15}$$

where, ${u_x}^h = \sum_i^{n_{dof}} \hat{u}_i \phi_i$, ${u_z}^h = \sum_i^{n_{dof}} \hat{v}_i \phi_i$, $v^h = \sum_j^{n_{dof}} \phi_j$, ϕ is the shape function, and i and j are nodal points, n_{dof} denotes total degree of freedom.

The equation (2-14) and (2-15) can be rewritten in a matrix form as follows (Marfurt, 1984),

$$\mathbf{Su} = (\mathbf{M} + \mathbf{K})\mathbf{u} = \mathbf{f}, \tag{2-16}$$

where, $\mathbf{S}$ is the complex impedence matrix composed of $\mathbf{M}$, the mass matrix, and $\mathbf{K}$, the stiffness matrix. $\mathbf{f}$ denotes the source vector.

$$\mathbf{u} = \begin{pmatrix} \hat{u} \\ \hat{v} \end{pmatrix}, \tag{2-17}$$

$$\mathbf{M} = \begin{pmatrix} m_{11} & 0 \\ 0 & m_{22} \end{pmatrix}, \tag{2-18}$$

$$\mathbf{K} = \begin{pmatrix} k_{11} & k_{12} \\ k_{21} & k_{22} \end{pmatrix}, \tag{2-19}$$

$$\mathbf{f} = \begin{pmatrix} f_x \\ f_z \end{pmatrix}, \tag{2-20}$$

where f_x and f_z are the horizontal and vertical source vector, respectively. The components of the mass matrix and the stiffness matrix are expressed as follows,

$$m_{11} = m_{22} = \sum_K \int_k \rho_k \, s^2 \, {a_k}^x {a_k}^z \phi_i \phi_j dk, \tag{2-21}$$

$$k_{11} = \sum_K \int_k \left\{ (\lambda_k + 2\mu_k) \frac{{a_k}^z}{{a_k}^x} \frac{\partial \phi_i}{\partial x} \frac{\partial \phi_j}{\partial x} + \mu_k \frac{{a_k}^x}{{a_k}^z} \frac{\partial \phi_i}{\partial z} \frac{\partial \phi_j}{\partial z} \right\} dk, \tag{2-22}$$

$$k_{12} = \sum_K \int_k \left\{ \lambda_k \frac{\partial \phi_i}{\partial z} \frac{\partial \phi_j}{\partial x} + \mu_k \frac{\partial \phi_i}{\partial x} \frac{\partial \phi_j}{\partial z} dk \right\}, \tag{2-23}$$

$$k_{21} = \sum_K \int_k \left\{ \lambda_k \frac{\partial \phi_i}{\partial x} \frac{\partial \phi_j}{\partial z} + \mu_k \frac{\partial \phi_i}{\partial z} \frac{\partial \phi_j}{\partial x} dk \right\}, \tag{2-24}$$

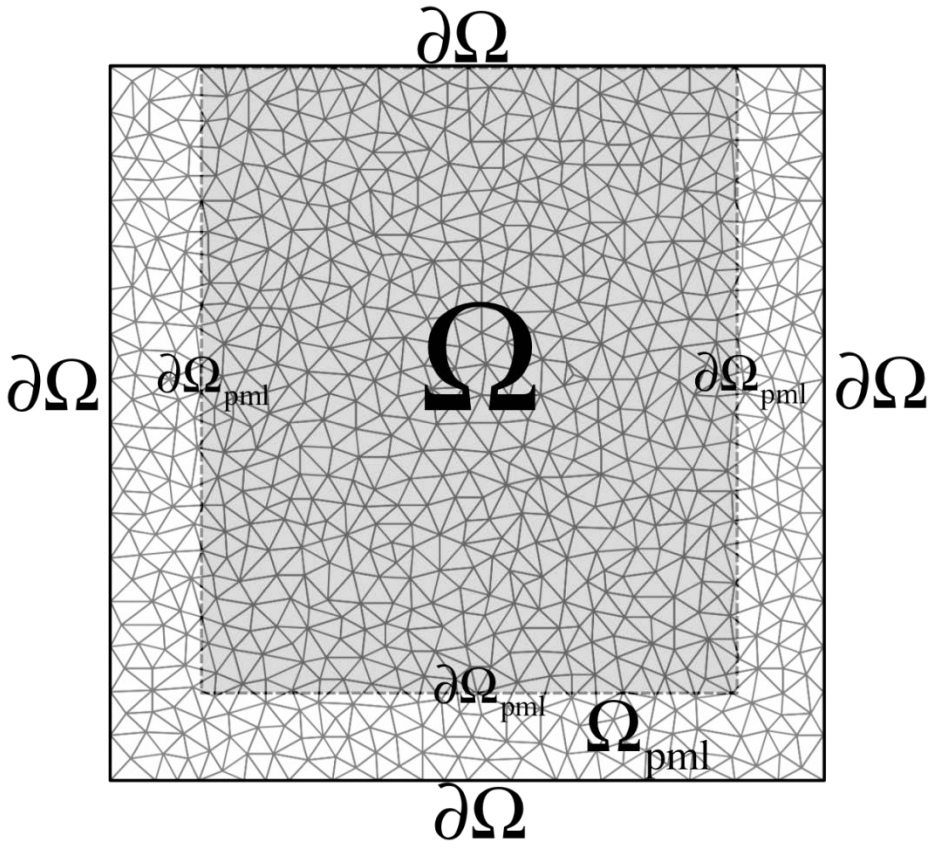

Figure 6. An elastic modeling domain for wave propagation. Ω is the entire domain, and ∂Ω is the Neumann boundary condition. Ω_{pml} denotes the domain for absorbing boundary condition, and $\partial\Omega_{pml}$ represents the boundaries of PML zone.

$$k_{22} = \sum_{K} \int_{k} \left\{ \mu_k \frac{{a_k}^z}{{a_k}^x} \frac{\partial \phi_i}{\partial x} \frac{\partial \phi_j}{\partial x} + (\lambda_k + 2\mu_k) \frac{{a_k}^x}{{a_k}^z} \frac{\partial \phi_i}{\partial z} \frac{\partial \phi_j}{\partial z} dk \right\}. \tag{2-25}$$

Where, k is an element and K is a finite set of element. The number of the local node point for an arbitrary element k is defined with respect to the shape function order (l_k) of each element.

$${n_{dof}}^k = (l_k + 1)(l_k + 2)/2 \tag{2-26}$$

${a_k}^x$ and ${a_k}^z$ is equation (2-21) are the PML constants that are defined for each element. For the unstructured-grids model, the PML constants is computed using the center coordinate of the element and the distance from the PML boundary $\partial\Omega_{pml}$. The practical definitions of the PML constants can be written in the forms

$${a_k}^x = \begin{cases} 1 & (k \notin \Omega_{pml}) \\ 1 + i\varsigma_x/s & (k \in \Omega_{pml}) \end{cases}, \tag{2-27}$$

$$\varsigma_x = \frac{3c_0}{2a} \log R \left(\frac{x'}{a} \right)^2, \tag{2-28}$$

$${a_k}^z = \begin{cases} 1 & (k \notin \Omega_{pml}) \\ 1 + i\varsigma_z/s & (k \in \Omega_{pml}) \end{cases} \tag{2-29}$$

$$\varsigma_z = \frac{3c_0}{2a} \log R \left(\frac{z'}{a} \right)^2, \tag{2-30}$$

where a is the thickness of the boundary layer, c_0 is the velocity of the PML zone, R=1000, x′ is the x-axis distance from the $\partial\Omega_{pml}$, and z´ is the z-axis distance from the $\partial\Omega_{pml}$ (Cohen, 2002).

The components of the mass matrix in equation (2-21) can be computed using the shape function $\hat{\phi}$ of the master element $\hat{K}$; F_k, which is the mapping

function of the k element; and the relationship $\phi_i = \hat{\phi}_I \circ {F_k}^{-1}$ between ϕ and $\hat{\phi}$.

$$
\begin{aligned}
m_{11} &= \sum_K \int_k \rho_k s^2 {a_k}^x {a_k}^z \phi_i \phi_j dk \\
&= s^2 \sum_K \rho_k {a_k}^x {a_k}^z \int_k \hat{\phi}_I \circ {F_k}^{-1} \hat{\phi}_J \circ {F_k}^{-1} dk \\
&= s^2 \sum_K \rho_k {a_k}^x {a_k}^z \int_k \left(\hat{\phi}_I \hat{\phi}_J\right) \circ {F_k}^{-1} dk \\
&= s^2 \sum_K \rho_k {a_k}^x {a_k}^z |det J_k| \int_{\hat{K}} \left(\hat{\phi}_I \hat{\phi}_J\right) d\hat{K} \\
&= m_{22}.
\end{aligned}
\tag{2-31}
$$

The mapping function is shown in Figure 7, and it is defined for a triangular element as follows:

$$
\begin{aligned}
F_k(\hat{x}, \hat{y}) &= \begin{pmatrix} x_1 \\ y_1 \end{pmatrix} + \begin{pmatrix} x_2 - x_1 & x_3 - x_1 \\ y_2 - y_1 & y_3 - x_1 \end{pmatrix} \begin{pmatrix} \hat{x} \\ \hat{y} \end{pmatrix}, \\
&= b_k + J_k \begin{pmatrix} \hat{x} \\ \hat{y} \end{pmatrix},
\end{aligned}
\tag{2-32}
$$

where, (x_1, y_1), (x_2, y_2), and (x_3, y_3) are the global coordinates of the vertex of the triangular element k. $(\hat{x}, \hat{y})$ represents its corresponding coordinates on the master triangular element $\hat{K}$.

For the stiffness matrix, all components of it can be computed the components using the quantities above and the relationship $\nabla\phi_i = {J_k}^{-\mathrm{T}} \nabla\hat{\phi}_I \circ {F_k}^{-1}$ between ϕ and $\hat{\phi}$.

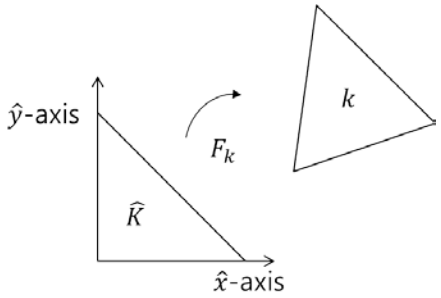

Figure 7. Illustration of the mapping from the master to the global element via F_k.

$$k_{11} = \sum_K \int_k \left\{ (\lambda_k + 2\mu_k) \frac{{a_k}^z}{{a_k}^x} \frac{\partial \phi_i}{\partial x} \frac{\partial \phi_j}{\partial x} + \mu_k \frac{{a_k}^x}{{a_k}^z} \frac{\partial \phi_i}{\partial z} \frac{\partial \phi_j}{\partial z} \right\} dk \tag{2-33}$$

$$= \sum_K (\lambda_k + 2\mu_k) \frac{{a_k}^z}{{a_k}^x} |detJ_k| \int_{\widehat{K}} \nabla \hat{\phi}_I {J_k}^{-1} \begin{pmatrix} 1 & 0 \\ 0 & 0 \end{pmatrix} {J_k}^{-\mathrm{T}} \nabla \hat{\phi}_J d\widehat{K}$$

$$+ \sum_K \mu_k \frac{{a_k}^x}{{a_k}^z} |detJ_k| \int_{\widehat{K}} \nabla \hat{\phi}_I {J_k}^{-1} \begin{pmatrix} 0 & 0 \\ 0 & 1 \end{pmatrix} {J_k}^{-\mathrm{T}} \nabla \hat{\phi}_J d\widehat{K},$$

$$k_{12} = \sum_K \int_k \left\{ \lambda_k \frac{\partial \phi_i}{\partial z} \frac{\partial \phi_j}{\partial x} + \mu_k \frac{\partial \phi_i}{\partial x} \frac{\partial \phi_j}{\partial z} \right\} dk \tag{2-34}$$

$$= \sum_K \lambda_k |detJ_k| \int_{\widehat{K}} \nabla \hat{\phi}_I {J_k}^{-1} \begin{pmatrix} 0 & 0 \\ 1 & 0 \end{pmatrix} {J_k}^{-\mathrm{T}} \nabla \hat{\phi}_J d\widehat{K}$$

$$+ \sum_K \mu_k |detJ_k| \int_{\widehat{K}} \nabla \hat{\phi}_I {J_k}^{-1} \begin{pmatrix} 0 & 1 \\ 0 & 0 \end{pmatrix} {J_k}^{-\mathrm{T}} \nabla \hat{\phi}_J d\widehat{K},$$

$$k_{21} = \sum_K \int_k \left\{ \lambda_k \frac{\partial \phi_i}{\partial x} \frac{\partial \phi_j}{\partial z} + \mu_k \frac{\partial \phi_i}{\partial z} \frac{\partial \phi_j}{\partial x} \right\} dk \tag{2-35}$$

$$= \sum_K \lambda_k |detJ_k| \int_{\widehat{K}} \nabla \hat{\phi}_I {J_k}^{-1} \begin{pmatrix} 0 & 1 \\ 0 & 0 \end{pmatrix} {J_k}^{-\mathrm{T}} \nabla \hat{\phi}_J d\widehat{K}$$

$$+ \sum_K \mu_k |detJ_k| \int_{\widehat{K}} \nabla \hat{\phi}_I {J_k}^{-1} \begin{pmatrix} 0 & 0 \\ 1 & 0 \end{pmatrix} {J_k}^{-\mathrm{T}} \nabla \hat{\phi}_J d\widehat{K},$$

$$k_{22} = \sum_K \int_k \left\{ \mu_k \frac{{a_k}^z}{{a_k}^x} \frac{\partial \phi_i}{\partial x} \frac{\partial \phi_j}{\partial x} + (\lambda_k + 2\mu_k) \frac{{a_k}^x}{{a_k}^z} \frac{\partial \phi_i}{\partial z} \frac{\partial \phi_j}{\partial z} \right\} dk \tag{2-36}$$

$$= \sum_K \mu_k \frac{{a_k}^z}{{a_k}^x} |detJ_k| \int_{\widehat{K}} \nabla \hat{\phi}_I {J_k}^{-1} \begin{pmatrix} 1 & 0 \\ 0 & 0 \end{pmatrix} {J_k}^{-\mathrm{T}} \nabla \hat{\phi}_J d\widehat{K}$$

$$+ \sum_K (\lambda_k + 2\mu_k) \frac{{a_k}^x}{{a_k}^z} |detJ_k| \int_{\widehat{K}} \nabla \hat{\phi}_I {J_k}^{-1} \begin{pmatrix} 0 & 0 \\ 0 & 1 \end{pmatrix} {J_k}^{-\mathrm{T}} \nabla \hat{\phi}_J d\widehat{K},$$

where ∇ is the gradient operator.

The forward modeling was performed using the derived FEM algorithm with the heterogeneous velocity model that has the complex surface shown in Figure 8. Figure 8, 9a, and 9b show the P-wave and S-wave velocity models and the density model, respectively. The size of the domain is 20,000 m $\times$ 3,700 m. The unstructured grid was showed in the P-wave velocity model. Figure 10 shows the horizontal and vertical displacements obtained via the forward-problem algorithm with the given models, a Laplace-damping value of 1.0, and a frequency value of 20π. In this modeling example, the complication of the elastic wave propagation caused by the topography was able to observe. And it can be an example why the inversion approach using the flat-surface assumption and the corrected dataset, which considers only the time delay that originates from differences in elevation, is highly susceptible to failure when applied to a land dataset that was acquired in a region with complex topography.

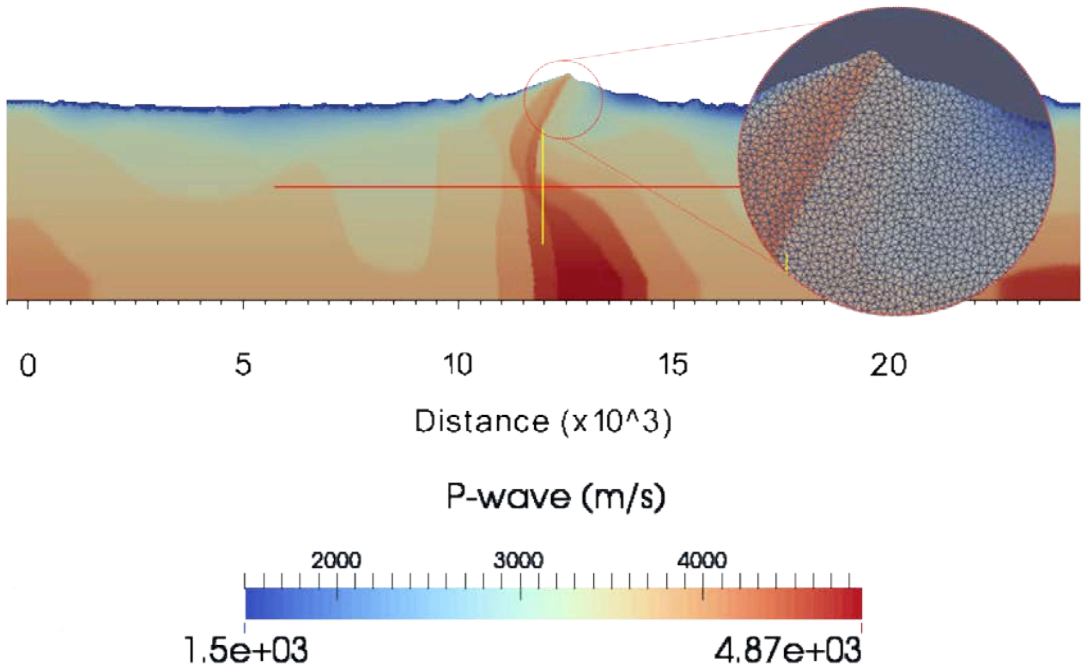

Figure 8. P-wave velocity model defined on the unstructured grids for a modeling test.

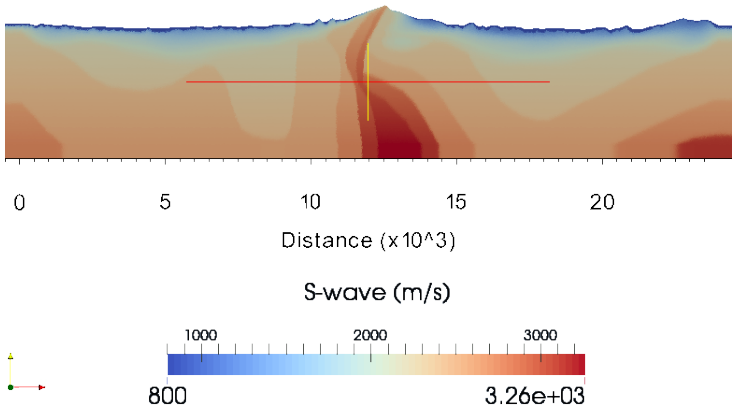

(a)

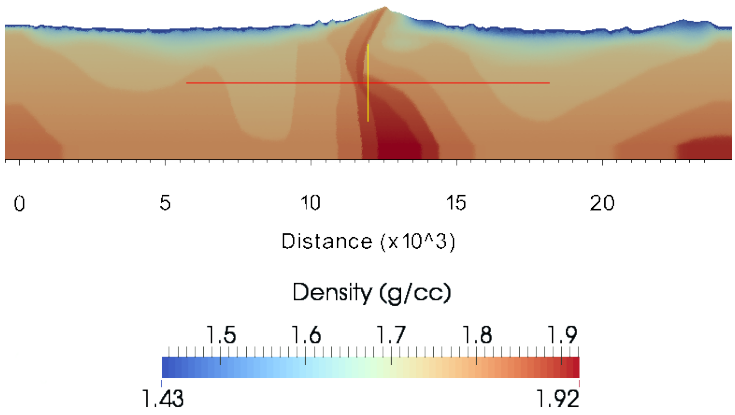

(b)

Figure 9. Parameters defined on unstructured grids for a modeling test: (a) S-wave velocity and (b) density.

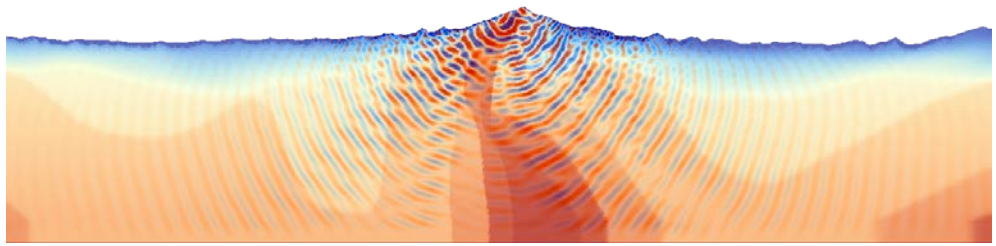

(a)

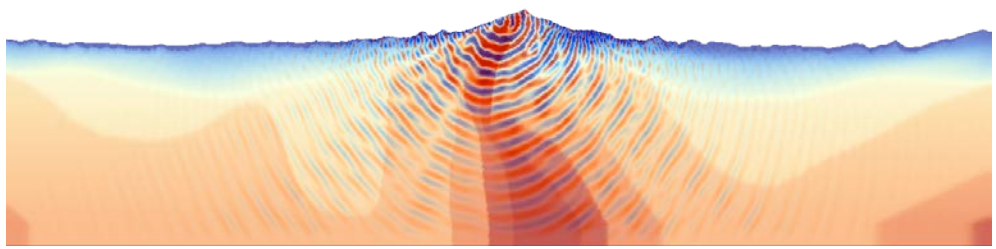

(b)

Figure 10. The (a) horizontal and (b) vertical displacement computed in the Laplace-Fourier domain using the parameters given in Figure 8 and 9, $\sigma = 1$ for and $\omega = 20\pi$.

2.3.2 Source and receiver distributions

A simulation of the wave equation using FEM in the Laplace and Laplace-Fourier domains can compute a stable numerical solution using a grid size ten times coarser grid size than that required for similar simulations using time- or frequency-domain FEM (Shin and Cha, 2008). However, this advantage cannot be exploited when the exact nodal positions of the sources and receivers are applied during the meshing procedure. Thus, the original coordinates of the sources and receivers changed to the distributed coordinates with weighting at the corresponding locations, as shown in Figure 11.

This approach allows for the control of the mesh size and shape without any consideration for the coordinates of the original sources and receivers, based on the definitions of the integral of the delta function, the mapping function F_k and its determinant. A point source located at $\boldsymbol{x}_s$ in the inner region of element k_{src}, an element that contains a source, can be expressed in terms of the distributed sources that are located at the coordinates of the nodal points of the master element. The source vector in equation (2-20) can be written as follows,

$$\begin{aligned} \mathbf{f} &= \sum_{K} \int_{k} \delta(\boldsymbol{x} - \boldsymbol{x}_s) A\phi_j dk \\ &= \int_{k_s} \delta(\boldsymbol{x} - \boldsymbol{x}_s) A\phi_j dk \\ &= \sum_{j}^{{n_{dof}}^{k_s}} A\phi_j(\boldsymbol{x} - \boldsymbol{x}_s) \end{aligned} \tag{2-37}$$

$$= \left|detJ_{k_s}\right| A \sum_{J}^{n_{dof}^{\hat{K}}} \hat{\phi}_J(\boldsymbol{x}_s)$$

where A is the amplitude of the source vector in the Laplace-Fourier domain, j represents the local nodal points on the source element k_s, and J represents the local nodal points on the master element $\hat{K}$. Examples of simulation of the vertical and horizontal wavefields using distributed coordinate are presented in Figure 12 to verify the feasibility of using distributed sources and receivers. The 1st test was performed using the exact source and receiver positions, and the 2nd was performed using distributed sources and receivers. The Figure 12b and Figure 12c show that the calculated wavefields are perfectly consistent.

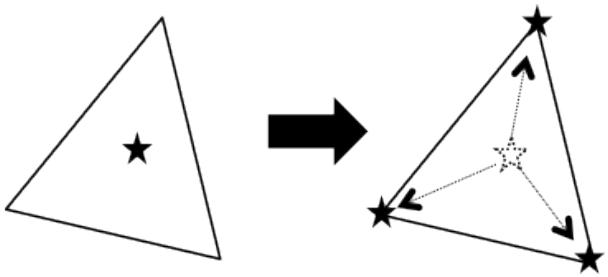

Figure 11. Illustration of the mapping of an arbitrary position to a nodal position.

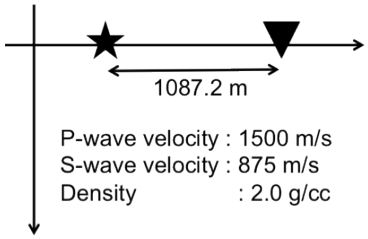

(a)

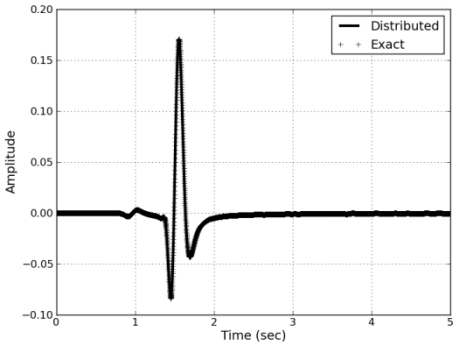

(b)

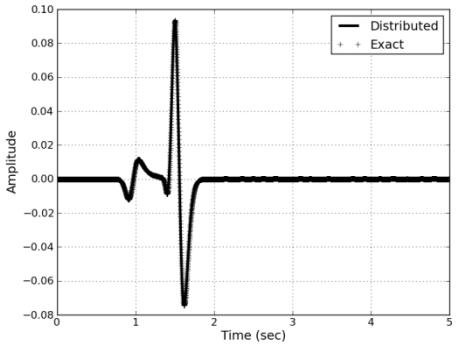

(c)

Figure 12. (a) Domain for testing the elastic wave propagation using the exact and distributed positions of the sources and receivers. (b) Vertical displacement and (c) horizontal displacement.

2.4 Full waveform inversion in the Laplace-Fourier domain

In this section, the Laplace-Fourier-domain inversion algorithm is presented using the steepest descent method introduced by Shin and Cha in 2009 with the logarithmic objective function suggested by Shin and Min (2006). The logarithm objective function must be used for Laplace and Laplace-Fourier-domain inversion because the amplitude of a Laplace-Fourier-transformed wavefield has such a large amplitude range with respect to the offset; thus, no other widely used objective function, such as the l_1 or l_2 norm, is suitable (Shin and Ha, 2008).

The source-estimation algorithm of logarithmic wavefield is also reviewed in this chapter. The full Newton method suggested by Shin et al. (2007) is applied for an estimating of the source wavelet and it is performed for each source, independently.

Next, it is showed that how to distribute the source and receiver position from their original coordinate to node point of mesh. The mixed type mesh is applied to minimize the error originated from mapping the result obtained on unstructured grid to the structured grid.

The novel pseudo-Hessian matrix and stopping criterion using normalized amplitude and phase error were proposed in this chapter. The suggested pseudo-Hessian matrix could promise proper regularized gradient direction than the original one for elastic inversion. Also, the stopping criterion could prevent to be partial inversion toward the amplitude or phase. These methods were introduced with numerical examples.

2.4.1 Determination of gradient direction in the Laplace-Fourier domain using the steepest descent

The Laplace and Laplace-Fourier domain wavefields can be obtained via frequency-domain modeling using a Laplace damping constant and an angular-frequency constants; thus, the inversion algorithm can be implemented in the same manner as in the frequency-domain method using a logarithmic wavefield.

The residual is defined in terms of the ratio of the logarithmic modeled wavefield and the observed wavefields based on the l_2 norm, as follows:

$$\tilde{r}_{i,j} = \ln\tilde{u}_{i,j} - \ln\tilde{d}_{i,j} = \ln\frac{\tilde{u}_{i,j}}{\tilde{d}_{i,j}}, \tag{2-38}$$

where $\tilde{u}_{i,j}$ and $\tilde{d}_{i,j}$ are the modeled and observed wavefields in the Laplace-Fourier domain at the location of the j_{th} receiver of the i_{th} source. In particular, the observed dataset was assumed that it contains only a vertical component, as this assumption is consistent with many real land datasets. Thus, the modeled data $\tilde{u}_{i,j}$ also contains a vertical component. The objective function E can be defined as

$$E = \sum_{i}^{n_s}\sum_{j}^{n_r}\frac{1}{2}\tilde{r}_{i,j}\left(\tilde{r}_{i,j}\right)^{*}, \tag{2-39}$$

where n_s and n_r are the numbers of sources and receivers, respectively. The notation * indicates a complex conjugated value.

The steepest-decent method is an iterative method of minimizing the objective function using the gradient directions for the various unknown parameters.

$$\mathbf{m}^{(l+1)} = \mathbf{m}^{(l)} - \alpha^{(l)}\nabla_{\boldsymbol{m}}E, \tag{2-40}$$

where $\mathbf{m}^{(l)}$ is the model parameter vector at the l_{th} iteration, and $\nabla_{\boldsymbol{m}} E$ is the steepest-decent gradient direction. α is the step length for updating.

The steepest-descent gradient direction for the k element can be computed from the partial derivative of the logarithmic objective function with respect to the model parameter m_k.

$$\nabla_{m_k} E = \frac{\partial E}{\partial m_k} = \sum_{i}^{n_s} \sum_{j}^{n_r} \frac{1}{\tilde{u}_{i,j}} \frac{\partial \tilde{u}_{i,j}}{\partial m_k} \left(\tilde{r}_{i,j}\right)^* \tag{2-41}$$

The partial derivative of the modeled wavefield can be computed by taking the partial derivative of equation (2-16) with respect to the model parameter m_k, and then the following equation can be obtained:

$$\frac{\partial \mathbf{S}}{\partial m_k}\mathbf{u} + \mathbf{S}\frac{\partial \mathbf{u}}{\partial m_k} = 0 \tag{2-42}$$

$$\frac{\partial \mathbf{u}}{\partial m_k} = \mathbf{S}^{-1}\left(-\frac{\partial \mathbf{S}}{\partial m_k}\mathbf{u}\right) \text{ or } \frac{\partial \mathbf{u}}{\partial m_k} = \mathbf{S}^{-1}(\mathbf{v}_k) \tag{2-43}$$

where $\mathbf{v}_k$ is the virtual source vector with respect to the parameter m_k (Pratt et al., 1998), expressed as

$$\mathbf{v}_k = -\frac{\partial \mathbf{S}}{\partial m_k}\mathbf{u} \tag{2-44}$$

Now, the steepest-descent gradient direction of a model parameter for the k element can be calculated using back propagation algorithm (Shin and Min, 2006), and it can be expressed as

$$\nabla_{m_k} E = \sum_{i}^{n_s} \mathbf{v}_k{}^{\mathrm{T}} \mathbf{S}^{-\mathrm{T}} \mathbf{r}_i \tag{2-45}$$

where $\mathbf{S}^{-\mathrm{T}}$ is the inverse of the transposed impedance matrix, and it can be replaced by $\mathbf{S}^{-1}$ because of its symmetry. The residual vector $\mathbf{r}_i$ can be expressed as

$$\mathbf{r}_i = \begin{pmatrix} 0 \\ \vdots \\ 0 \\ \frac{1}{\tilde{u}_{i,1}} \frac{\partial \tilde{u}_{i,1}}{\partial m_k} \left(\tilde{r}_{i,1}\right)^* \\ \vdots \\ \frac{1}{\tilde{u}_{i,n_r}} \frac{\partial \tilde{u}_{i,n_r}}{\partial m_k} \left(\tilde{r}_{i,n_r}\right)^* \\ 0 \\ \vdots \\ 0 \end{pmatrix}. \tag{2-46}$$

2.4.2 Preconditioning of the gradient direction using pseudo-Hessian matrix

The gradient direction computed using the steepest-descent method of equation (2-45) requires preconditioning because it is computed without consideration of the geometrical spreading effect. Pratt et al. suggested the Gauss-Newton method and the full-Newton method for regularizing the gradient direction in 1998, and Shin et al. introduced the pseudo-Hessian matrix, which uses only the diagonal component of the approximated Hessian in Gauss-Newton method, to reduce the computational cost of this task in 2001.

Researches on Laplace- or Laplace-Fourier-domain inversion usually used the diagonal element of the pseudo-Hessian matrix using the virtual source vector, defined in equation (2-47), for preconditioning of the steepest descent gradient.

$$\mathbf{H}^{p} = \mathrm{Re}\left(\sum_{i}^{n_s} \mathbf{v}^{\mathrm{T}}(\mathbf{v})^{*}\right). \tag{2-47}$$

The preconditioned gradient direction for updating is obtained using steepest decent direction normalized by the diagonal element of the pseudo-Hessian matrix, as follows,

$$\delta m_k = \frac{\sum_i^{n_s} \mathbf{v}_k{}^{\mathrm{T}} \mathbf{S}^{-\mathrm{T}} \mathbf{r}_i}{\mathrm{Re}\left(\sum_i^{n_s} \mathbf{v}_k{}^{\mathrm{T}} (\mathbf{v}_k)^{*}\right) + \eta} \tag{2-48}$$

where δm_k is the preconditioned gradient direction for the model parameter of the k element and η is the damping factor to stabilize the normalization. Now, the updating method in equation (2-40) is need to be changed with the preconditioned gradient direction, as follows

$$\mathbf{m}^{(l+1)} = \mathbf{m}^{(l)} + \alpha^{(l)}\delta m, \tag{2-49}$$

In some numerical tests, the pseudo-Hessian matrix presented in equation (2-47) could not be reasonably preconditioned because of the damping factor. The damping factor η is applied to stabilize the gradient direction. In this context, the damping factor must solely stabilize the gradient, and it must not affect to the global trend of the gradient direction. However, it was contributed to the inverted result.

A simple test was performed to investigate the effect of the damping factor on the pseudo-Hessian matrix. Figure 13 shows the 3 types of true model sets that were used for this test. The P-wave velocity models were constructed using a 1500 m/s background velocity and a 3000 m/s box-shaped structure at depths of 1000 m to 2000 m, 1500 m to 2500 m, and 2000 m to 3000 m. The S-wave velocity models were constructed using a 866 m/s background velocity and a 1732 m/s box-shaped structure at depths of 1000 m to 2000 m, 1500 m to 2500 m, and 2000 m to 3000 m, relatively. The density model was a 2 g/cc homogeneous model. Figure 14 shows the initial velocity models; the initial P-wave model was a 2000 m/s constant model, and the initial S-wave model was a 1200 m/s constant model. The density was assumed to be 2 g/cc.

The inversion was performed using 6 Laplace damping constants (2, 4, 6, 8, 10, and 12) and 3 different damping factors. The damping factor was determined as a proportion of the maximum of the pseudo-Hessian matrix as follows:

$$\eta = d \times \max(\mathbf{H}^{p}) \tag{2-50}$$

In Figure 15, the inverted P-wave results was presented using the 3 types of datasets with 3 different damping factors after 30 iterations. The results

demonstrate that the damping factor affects the determination of the inverted depth. The inverted result for $d = 10^{-1}$ is biased in the upwind direction, and the result for $d = 10^{-5}$ is biased in the downward direction. These results indicate that elastic Laplace-Fourier-domain inversion cannot always yield a reasonable result because of the effect of the damping factor.

For a more detailed analysis, the 1D steepest-descent direction and the pseudo-Hessian was extracted at 10,000 m from the left origin for the 1st test, with a high-velocity structure located at a depth of 1000 m to 2000m and for a Laplace damping constant of 2. First, in Figure 16, the steepest gradient, pseudo-Hessian without the damping factor, and the gradient direction were presented and the gradient direction was preconditioned using a pseudo-Hessian without a damping factor.

The preconditioned gradient using a pseudo-Hessian without a damping factor cannot compensate for the geometrical-spreading effect in this analysis. Second, Figure 17 shows the pseudo-Hessian matrixes are computed using the 5 damping factors $d = 10^{-1}, 10^{-2}, 10^{-3}, 10^{-4}, \text{and } 10^{-5}$ to illustrate how the matrix changes with respect to the damping factor. In this plot, it is apparent that the value of the applied damping factor plays a role in the minimum tolerance limit for the Hessian, and it causes unexpected changes in the preconditioned gradient, as shown in Figure 18. The preconditioned gradient direction is tend to emphasize a deeper region following as the damping factor goes to small. From results of this analysis, it seems to that the pseudo-Hessian matrix derived using the conventional l_2 norm is not appropriate for applying to this algorithm.

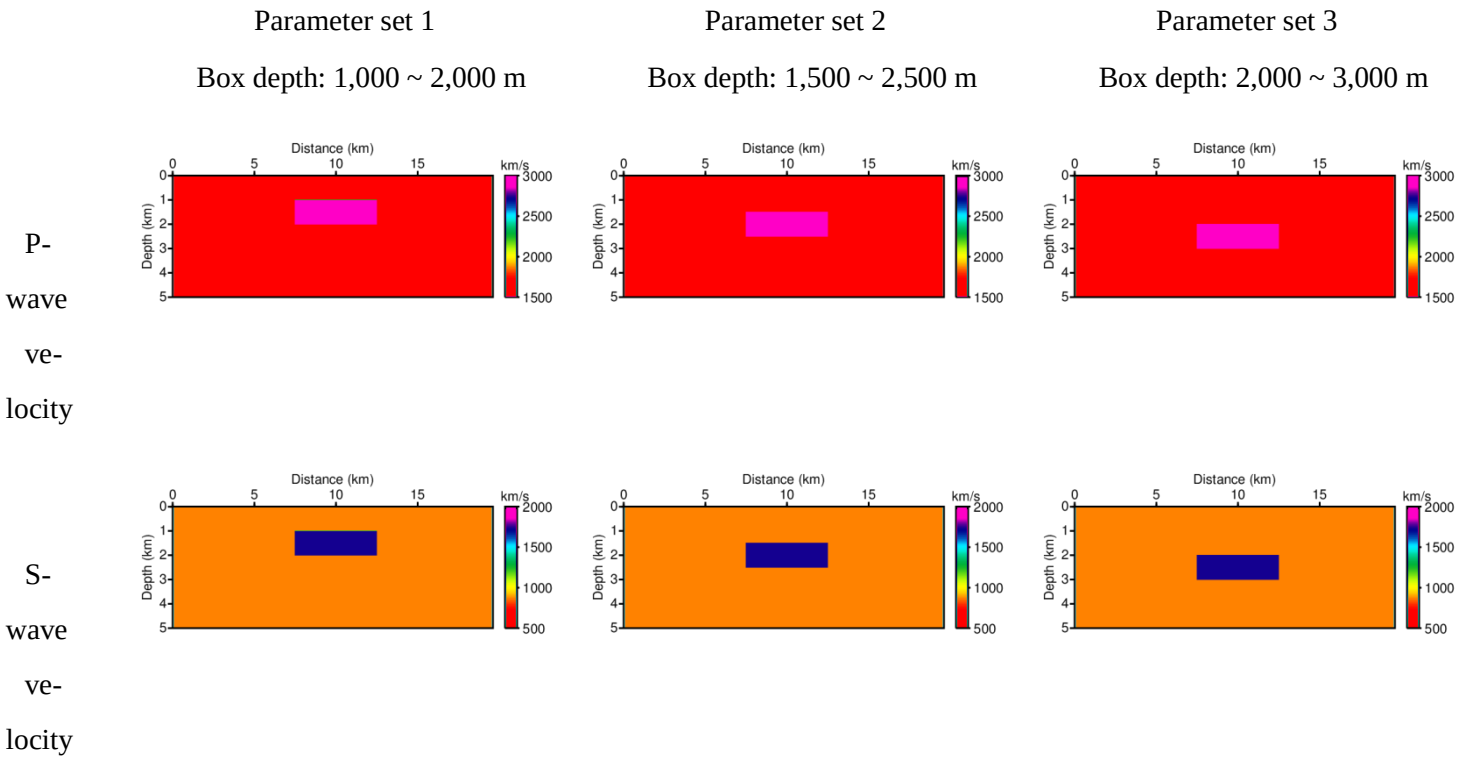

Figure 13. Parameter sets containing the box-shaped structures at different depths for testing the pseudo-Hessian matrix.

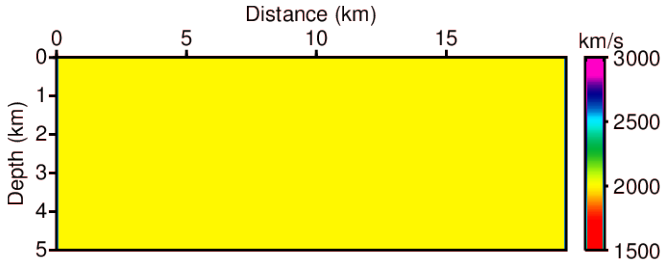

(a)

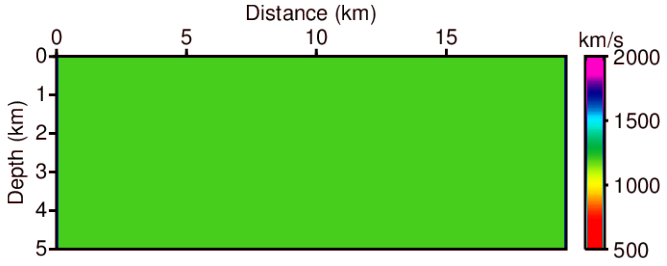

(b)

Figure 14. The initial models for the tests of the pseudo-Hessian matrix: (a) 2000 m/s homogeneous P-wave velocity model and (b) 1200 m/s homogeneous S-wave velocity model.

In 2012, Ha et al. introduced a modified pseudo-Hessian matrix that was derived for the logarithmic objective function. Presented below is the modified pseudo-Hessian matrix for the logarithmic objective function.

$$\mathbf{H}^p = \mathrm{Re}\left(\sum_i^{n_s}\left(-\frac{\partial \mathbf{S}}{\partial m}\mathbf{c}\right)^{\mathrm{T}}\left(-\frac{\partial \mathbf{S}}{\partial m}\mathbf{c}\right)^{*}\right), \tag{2-51}$$

where $\mathbf{c}^{\mathrm{T}} = (1, 1, \cdots, 1)$. This pseudo-Hessian matrix does not contain the information about the modeled wavefield. They have demonstrated that their pseudo-Hessian matrix properly preconditions the steepest-descent gradient direction in the acoustic inversion problem. From here, to prevent confusing names, the pseudo-Hessian matrix derived from the conventional l_2 norm is indicated with $\mathbf{H}_{l_2}{}^p$, while the other is expressed as $\mathbf{H}_{log}{}^p$.

$\mathbf{H}_{log}{}^p$ is applied to the elastic equation. First, the partial-derivative of the impedance matrix for arbitrary element *k* with respect to the model parameters of the elastic wave equation ($\lambda, \mu,$ and ρ) can be expressed using the following equations:

$$-\frac{\partial \mathbf{S}}{\partial \lambda_k}\mathbf{c} = |detJ_k|\begin{pmatrix} a^{k,1} & a^{k,2} \\ a^{k,3} & a^{k,4} \end{pmatrix}\mathbf{c}, \tag{2-52}$$

$$-\frac{\partial \mathbf{S}}{\partial \mu_k}\mathbf{c} = |detJ_k|\begin{pmatrix} 2a^{k,1} + a^{k,4} & a^{k,3} \\ a^{k,2} & a^{k,1} + 2a^{k,4} \end{pmatrix}\mathbf{c}, \tag{2-53}$$

$$-\frac{\partial \mathbf{S}}{\partial \rho_k}\mathbf{c} = |detJ_k|\begin{pmatrix} \int_{\widehat{K}} (\hat{\phi}_I\hat{\phi}_J)d\widehat{K} & 0 \\ 0 & \int_{\widehat{K}} (\hat{\phi}_I\hat{\phi}_J)d\widehat{K} \end{pmatrix}\mathbf{c}, \tag{2-54}$$

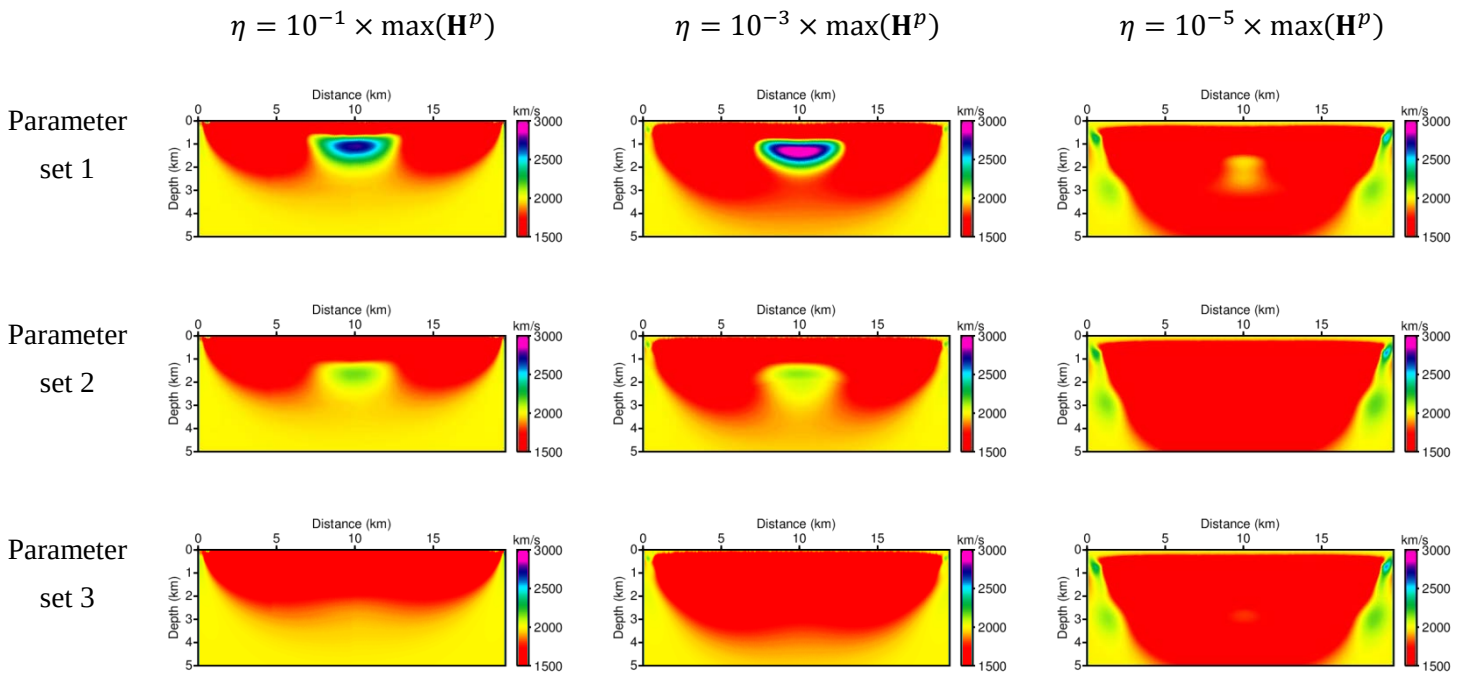

Figure 15. Inverted P-wave velocity using 3 types of damping factors for 3 datasets.

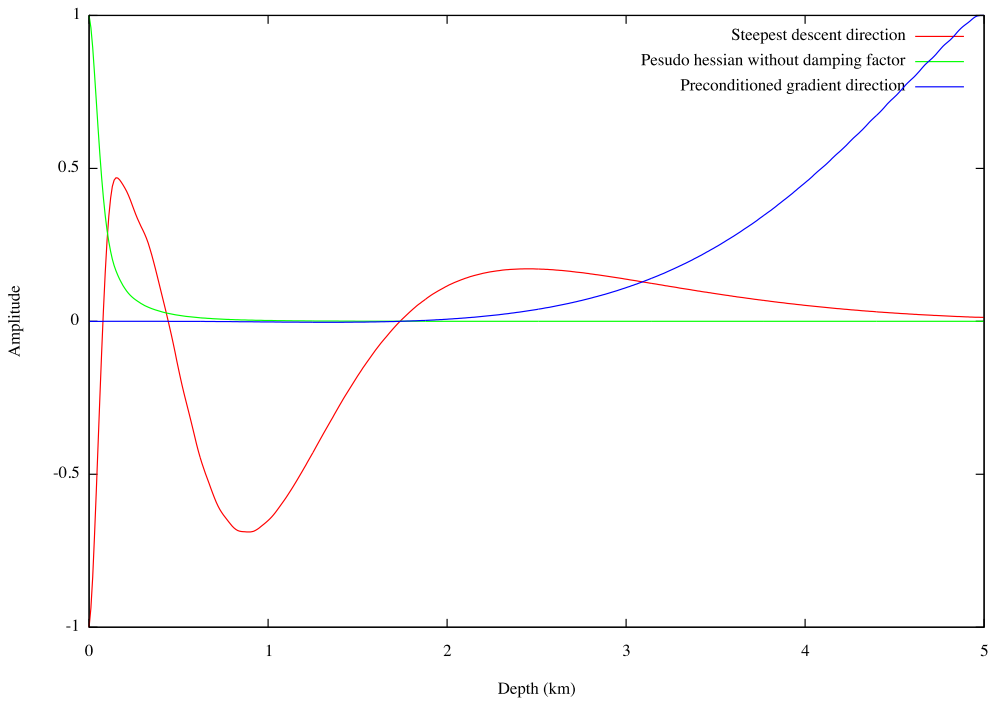

Figure 16. The plots of the 1D steepest-descent direction, the pseudo-Hessian without the damping factor, and the gradient direction obtained when preconditioned using the pseudo-Hessian without damping. These 1D plots were extracted for the location 10,000 m from the left origin for the Hessian test using 1st dataset.

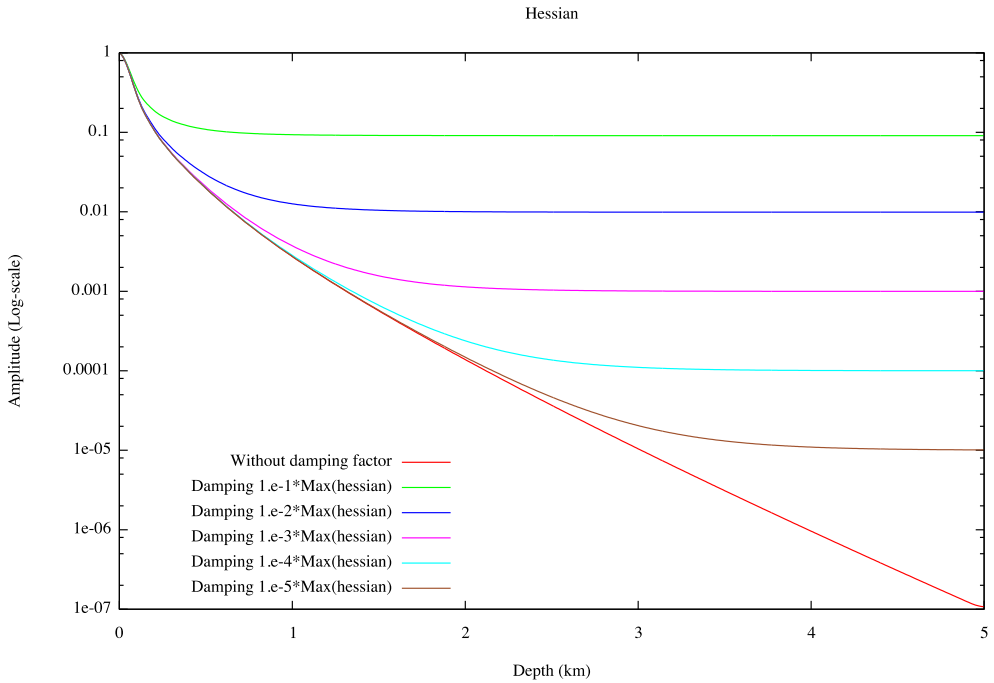

Figure 17. The 1D Hessian matrix without a damping factor and with the various damping factors The 1D pseudo-Hessian matrix without a damping factor and with the various damping factors $d = 10^{-1}, 10^{-2}, 10^{-3}, 10^{-4},$ and 10^{-5}.

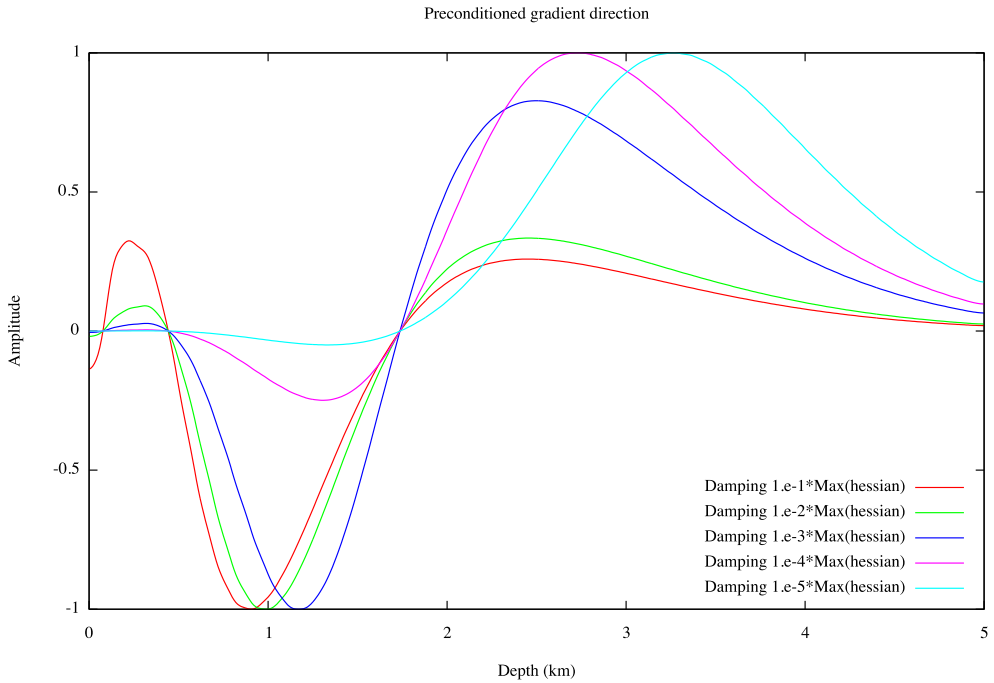

Figure 18. The 1D preconditioned gradient directions obtained using pseudo-Hessians with various damping factors: $\boldsymbol{d = 10^{-1}, 10^{-2}, 10^{-3}, 10^{-4},}$ **and** $\boldsymbol{10^{-5}}$.

Where a^k matrix is consist of ${a_{I,J}}^k$ with size of ${n_{dof}}^k \times {n_{dof}}^k$. The matrix size of partial derivatives is $2{n_{dof}}^k \times 2{n_{dof}}^k$ and the size of vector $\mathbf{c}$ is $2{n_{dof}}^k$.

$$ {a_{I,J}}^{k,1} = \int_{\widehat{K}} \nabla\phi_I {J_k}^{-1} \begin{pmatrix} 1 & 0 \\ 0 & 0 \end{pmatrix} {J_k}^{-\mathrm{T}} \nabla\phi_J d\widehat{K}, \tag{2-55} $$

$$ {a_{I,J}}^{k,2} = \int_{\widehat{K}} \nabla\phi_I {J_k}^{-1} \begin{pmatrix} 0 & 0 \\ 1 & 0 \end{pmatrix} {J_k}^{-\mathrm{T}} \nabla\phi_J d\widehat{K}, \tag{2-56} $$

$$ {a_{I,J}}^{k,3} = \int_{\widehat{K}} \nabla\phi_I {J_k}^{-1} \begin{pmatrix} 0 & 1 \\ 0 & 0 \end{pmatrix} {J_k}^{-\mathrm{T}} \nabla\phi_J d\widehat{K}, \tag{2-57} $$

$$ {a_{I,J}}^{k,4} = \int_{\widehat{K}} \nabla\phi_I {J_k}^{-1} \begin{pmatrix} 0 & 0 \\ 0 & 1 \end{pmatrix} {J_k}^{-\mathrm{T}} \nabla\phi_J d\widehat{K}, \tag{2-58} $$

From these derivatives demonstrate that ${\mathbf{H}_{log}}^p$ are computed using the values of $|detJ_k|$ and J_k for each element k. It means that it contains only information of the element; thus, it cannot compensate for the geometrical-spreading effect for the elastic case. For example, ${\mathbf{H}_{log}}^p$ gives a constant value when the mesh is a structured grid.

Now, we propose that another pseudo-Hessian matrix for the logarithmic objective function can be used for the elastic inversion. This novel Hessian matrix is derived from the difference between ${\mathbf{H}_{l_2}}^p$ and ${\mathbf{H}_{log}}^p$. The difference is whether the modeled wavefield $\boldsymbol{u}$ is contained in the matrix. The virtual source of the ${\mathbf{H}_{l_2}}^p$ with respect to the model parameters, for the each element, can be expressed as follows:

$$ -\frac{\partial \mathbf{S}}{\partial \lambda_k}\boldsymbol{u}_k = |detJ_k| \begin{pmatrix} a^{k,1} & a^{k,2} \\ a^{k,3} & a^{k,4} \end{pmatrix} \boldsymbol{u}_k, \tag{2-59} $$

$$-\frac{\partial \mathbf{S}}{\partial \mu_k}\boldsymbol{u}_k = |detJ_k|\begin{pmatrix} 2a^{k,1}+a^{k,4} & a^{k,3} \\ a^{k,2} & a^{k,1}+2a^{k,4} \end{pmatrix}\boldsymbol{u}_k, \tag{2-60}$$

$$-\frac{\partial \mathbf{S}}{\partial \rho_k}\boldsymbol{u}_k = |detJ_k|\begin{pmatrix} \int_{\widehat{K}} (\hat{\phi}_I\hat{\phi}_J)d\widehat{K} & 0 \\ 0 & \int_{\widehat{K}} (\hat{\phi}_I\hat{\phi}_J)d\widehat{K} \end{pmatrix}\boldsymbol{u}_k, \tag{2-61}$$

where the modeled wavefield $\boldsymbol{u}_k$ contains the horizontal and vertical wavefield on the nodes of element k and the size of this vector is $2{n_{dof}}^k$. And then, the ${\mathbf{H}_{l_2}}^p$ can be expressed by substitute these virtual sources to the equation (2-47).

To derive it, we assume that the energy level for the geometrical spreading of the modeled wavefield is similar for each nodal point on the same element; thus, it can be replaced by certain representable value g_k as follows:

$$\begin{aligned} {\mathbf{H}_{l_2}}^p &= \mathrm{Re}\left(\sum_i^{n_s}\left(-\frac{\partial \mathbf{S}}{\partial m}\boldsymbol{u}\right)^{\mathrm{T}}\left(-\frac{\partial \mathbf{S}}{\partial m}\boldsymbol{u}\right)^*\right) \\ &= \mathrm{Re}\left(\sum_i^{n_s}\left(-\frac{\partial \mathbf{S}}{\partial m}\mathbf{c}g_k\right)^{\mathrm{T}}\left(-\frac{\partial \mathbf{S}}{\partial m}\mathbf{c}g_k\right)^*\right) \\ &= \mathrm{Re}\left(\sum_i^{n_s}\left(-\frac{\partial \mathbf{S}}{\partial m}\mathbf{c}g_k\right)^{\mathrm{T}}\left(-\frac{\partial \mathbf{S}}{\partial m}\mathbf{c}g_k\right)^*\right) \\ &= g_k(g_k)^*\mathrm{Re}\left(\sum_i^{n_s}\left(-\frac{\partial \mathbf{S}}{\partial m}\mathbf{c}\right)^{\mathrm{T}}\left(-\frac{\partial \mathbf{S}}{\partial m}\mathbf{c}\right)^*\right) \\ &= g_k(g_k)^*{\mathbf{H}_{log}}^p. \end{aligned} \tag{2-62}$$

Here, the geometrical energy term $g_k(g_k)^*$ for an element k is defined as the following equation:

$$g_k(g_k)^* = \sum_{i}^{{n_{dof}}^k} \left({u_{x,i}}^k \left({u_{x,i}}^k\right)^* + {u_{z,i}}^k \left({u_{z,i}}^k\right)^*\right) / 2{n_{dof}}^k \tag{2-63}$$

From the relationship in equations (2-62), the new pseudo-Hessian matrix for the logarithmic objective function can be obtained as follows,

$$\mathbf{H}_{log}{}^p = \mathbf{H}_{l_2}{}^p / \, g_k(g_k)^* \tag{2-64}$$

The Figure 19 shows the newly derived Hessian matrix, and Figure 20 shows the preconditioned gradient directions. These figures demonstrate that the derived Hessian can compensate the geometrical-spreading effect without damping factor, reasonably.

The same inversion tests were performed using 3 types of datasets and the derived pseudo-Hessian matrix. Figure 21 shows the inverted P-wave results for each dataset after 30 iterations. The inverted results seem to recover successfully the high-velocity structures at the exact positions at which they were located.

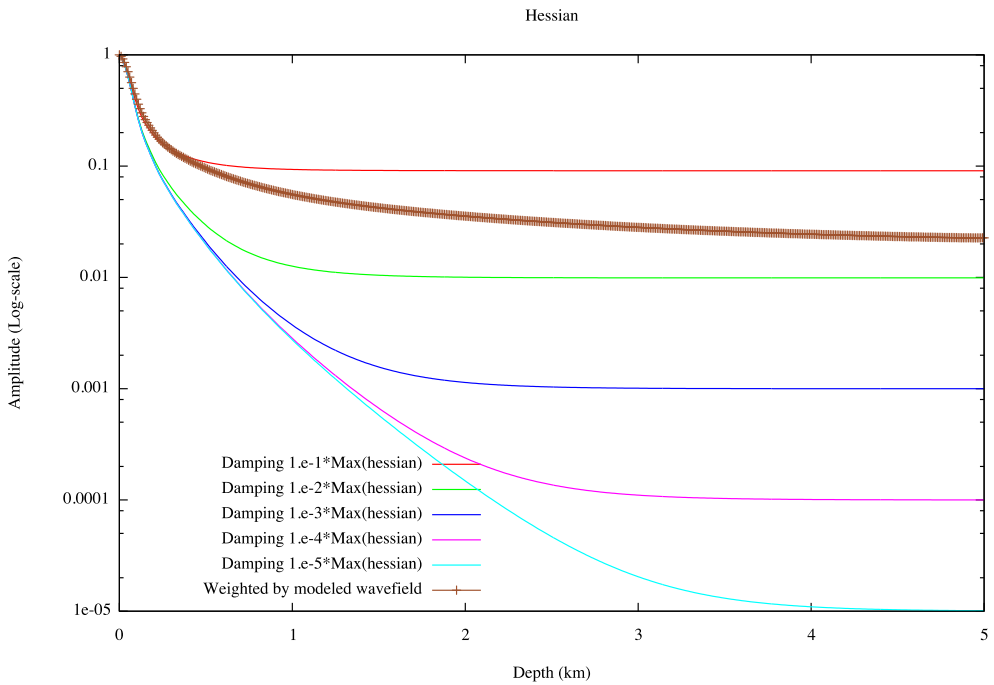

Figure 19. The 1D conventional pseudo-Hessian matrices using various damping factors, $d = 10^{-1}, 10^{-2}, 10^{-3}, 10^{-4}$, and 10^{-5}, and the derived pseudo-Hessian matrix that is regularized using the modeled wavefield.

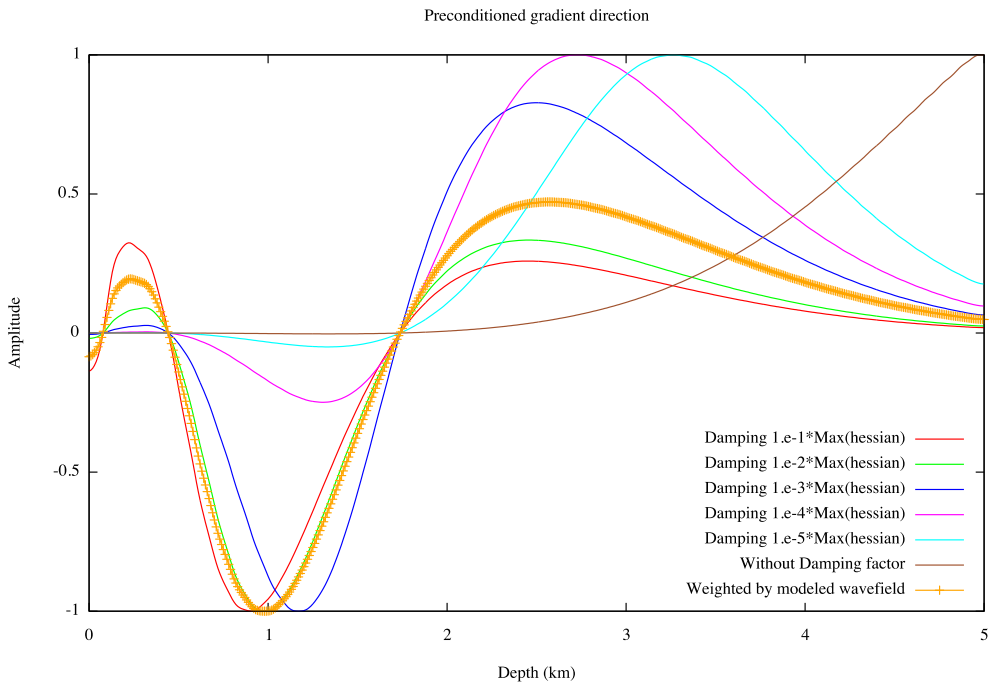

Figure 20.The 1D preconditioned gradient directions obtained using conventional pseudo-Hessians with various damping factors; $d = 10^{-1}, 10^{-2}, 10^{-3}, 10^{-4},$ and 10^{-5}, and using the derived pseudo-Hessian.

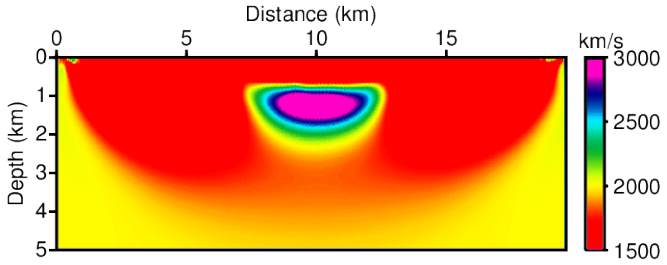

(a)

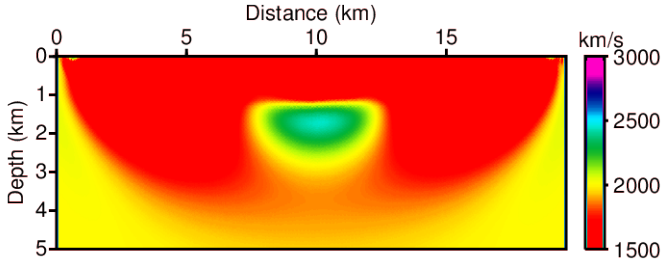

(b)

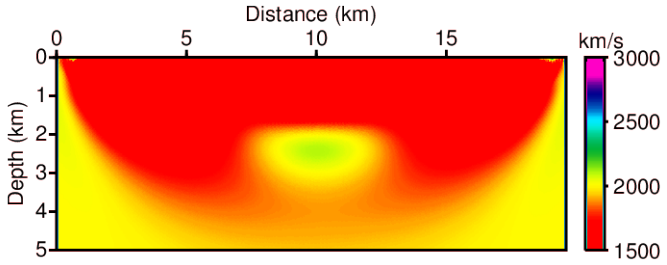

(c)

Figure 21. Inverted P-wave velocity models obtained using the derived pseudo-Hessian for 3 datasets. Inversion results using (a) parameter set 1, (b) parameter set 2 and (c) parameter set 3.

2.4.3 Source-estimation algorithm

The full-Newton method suggested by Shin et al. (2007) is applied to estimate the unknown source wavelet. In this section, it is reviewed.

The Laplace-Fourier-transformed observed data can be defined using the amplitude and phase term as follows,

$$\tilde{d}_j = {A_j}^{obs} e^{i{\phi_j}^{obs}}, \tag{2-65}$$

where ${A_j}^{obs}$ and ${\phi_j}^{obs}$ denote the amplitude and phase, respectively, of the observed data at the location of the j_{th} receiver and an arbitrary source. Similarly, the vertical component of the modeled wavefield for the an arbitrary source in the Laplace-Fourier domain is defined as

$$\tilde{u}_{z,j} = {B_j}^{cal} e^{i{\phi_j}^{cal}} C^{src} e^{i\phi^{src}}, \tag{2-66}$$

where ${B_j}^{cal}$ and ${\phi_j}^{cal}$ denote the amplitude and phase, respectively, of the modeled data at the location of the j_{th} receiver. C^{src} and ϕ^{src} are the amplitude and phase, respectively, of the source wavelet.

The objective function of the source wavelet for the logarithmic wavefield is constructed as follows in equation (2-66). In this thesis, the source-estimation algorithm is applied for each shot independently, instead of applying the one-source-wavelet assumption. The one-source-wavelet assumption is typically applied for the full-waveform inversion, and its applicability is not questioned in the acoustic case, which considers a homogeneous and isotropic medium of water surveyed using an air-gun source. However, for a land survey, the amplitude and phase of the source-wavelet must be assumed differently for each source because of the condition and property of the source triggered position must be different.

The equation (2-67) shows the objective function for the source-wavelet.

$$\mathrm{E}^{s} = \sum_{j}^{n_r} \frac{1}{2} \left(\ln\tilde{u}_{z,j} - \ln\tilde{d}_j\right) \left(\ln\tilde{u}_{z,j} - \ln\tilde{d}_j\right)^{*} \tag{2-67}$$

$$= \sum_{j}^{n_r} \frac{1}{2} \left(\left(\ln \frac{B_j{}^{cal} C^{src}}{A_j{}^{obs}} \right)^2 + \left(\phi_j{}^{cal} + \phi^{src} - \phi_j{}^{obs} \right)^2 \right).$$

The Newton method for an iterative solution can be expressed as

$$\delta m^{s} = -\mathbf{H} \nabla_{m^s} \mathrm{E}^{s}, \tag{2-68}$$

where δm^{s} is the update direction for the source wavelet, which contains both the amplitude and phase of the source. $\mathbf{H}$ is the 2×2 Hessian matrix, which includes 2[nd]-derivative components and is given by

$$\mathbf{H} = \begin{pmatrix} \dfrac{\partial^2 \mathrm{E}^{s}}{\partial C^{src} \partial C^{src}} & \dfrac{\partial^2 \mathrm{E}^{s}}{\partial C^{src} \partial \phi^{src}} \\ \dfrac{\partial^2 \mathrm{E}^{s}}{\partial \phi^{src} \partial C^{src}} & \dfrac{\partial^2 \mathrm{E}^{s}}{\partial \phi^{src} \partial \phi^{src}} \end{pmatrix}. \tag{2-69}$$

With considering of the logarithmic amplitude, the Hessian matrix can be expressed and simply computed as follows:

$$\mathbf{H} = \begin{pmatrix} \dfrac{\partial^2 \mathrm{E}^{s}}{\partial \ln C^{src} \partial \ln C^{src}} & \dfrac{\partial^2 \mathrm{E}^{s}}{\partial \ln C^{src} \partial \phi^{src}} \\ \dfrac{\partial^2 \mathrm{E}^{s}}{\partial \phi^{src} \partial \ln C^{src}} & \dfrac{\partial^2 \mathrm{E}^{s}}{\partial \phi^{src} \partial \phi^{src}} \end{pmatrix}. \tag{2-70}$$

$$= \begin{pmatrix} \sum_{j}^{n_r} 1 & 0 \\ 0 & \sum_{j}^{n_r} 1 \end{pmatrix} = \begin{pmatrix} n_r & 0 \\ 0 & n_r \end{pmatrix}.$$

The gradient-direction vector $\nabla_{m^s}\mathrm{E}^{\mathrm{s}}$ with respect to the parameter can also be computed using the logarithmic amplitudes:

$$\nabla_{m^s}\mathrm{E}^{\mathrm{s}}(\ln C^{src}, \phi^{src}) = \begin{pmatrix} \sum_{j}^{n_s} \ln \frac{{B_j}^{cal} C^{src}}{{A_j}^{obs}} \\ \sum_{j}^{n_s} \left({\phi_j}^{cal} + \phi^{src} - {\phi_j}^{obs}\right) \end{pmatrix}. \tag{2-71}$$

Finally, the update direction of the source-wavelet is obtained as follows:

$$\delta m^s = \frac{1}{n_r} \begin{pmatrix} \sum_{j}^{n_s} \ln \frac{{B_j}^{cal} C^{src}}{{A_j}^{obs}} \\ \sum_{j}^{n_s} \left({\phi_j}^{cal} + \phi^{src} - {\phi_j}^{obs}\right) \end{pmatrix}. \tag{2-72}$$

And the updating algorithm of the source-estimation is such that,

$$m^{s,(l+1)} = m^{s,(l)} + \alpha^{(l)} \delta m^s, \tag{2-73}$$

where $m^{s,(l)}$ is the source wavelet at the l_{th} iteration.

2.4.4 Construction of the mesh

There are many advantages to adopting the unstructured meshes. It is possible to model even complex topography or geological discontinuities almost perfectly, and the mesh size can be locally adapted to the properties of the medium (*h*-adaptivity) or arbitrarily high-order derivatives (*p*-adaptivity) for important regions. However, these advantages can be used only when the properties of the medium are already known.

Full-waveform inversion is applied to determine these properties, so the mesh-construction procedure in this algorithm must be performed without any consideration of the subsurface domain, using only the surface topography information. Moreover, most seismic research has been conducted using structured grids; thus, the compatibility with structured meshes was required for using of previously developed algorithms such as reverse time migration.

Therefore, a mixed-type mesh was used that composed of an unstructured part and a structured part. The unstructured part adopting triangular elements generated using Delaunay refinement algorithm (Shewchuk, 2002) is used to describe the topography, and the structured part is used for the subdomain. This type of mixed mesh allows the error to be minimized when the computed result is need to be moved to a structured grid. Figure 22a and 22b show examples of the fully unstructured mesh and such a mixed-type mesh, respectively.

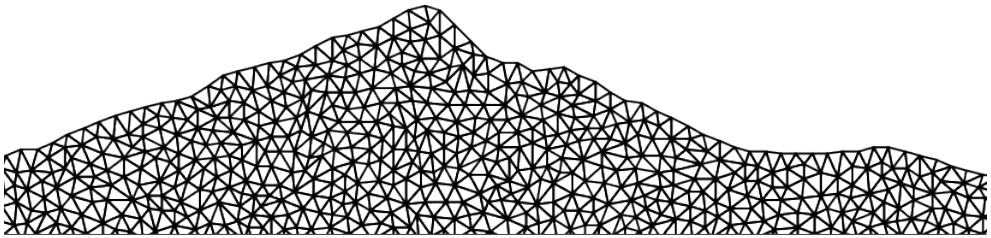

(a)

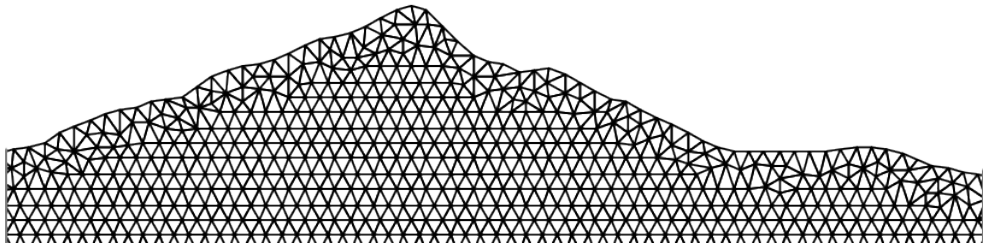

(b)

Figure 22. Examples of (a) unstructured mesh and (b) mixed-type mesh. The surface parts are constructed using unstructured grids, and the inner domain is composed of structured triangular elements for the mixed type mesh.

2.4.5 Stopping criterion using normalized error for the Laplace-Fourier-domain inversion

Full waveform inversion is an indirect method to recover the subsurface parameter by reducing the objective function in an algorithm via iteratively updating the parameters. However, the objective function is not always decreased and it actually begins to get worse again (over-fitting) at some point because of seismic inversion is the problem that always has too many parameters relative to the number of observations. Therefore, the full waveform inversion using fixed number of iterations without considering about it cannot give the best result.

There are basically two ways to fight with over-fitting problem: the first one is reducing the number of parameters and the other is terminating of procedure at proper point (Prechelt, 1997). In this thesis, the developed algorithm was applied the second method from automatically stopping based on stopping criterion with the multi-loop method (Shin et al, 2010).

The following code snippet in Figure 23 shows how the multi-loop algorithm might be implemented. Suppose that there is a routine call `modeling` that computes an impedance matrix for simulating of the wave propagation using current guess model parameter $m^{(l)}$. d denotes Laplace-transformed observed dataset $\ln\tilde{d}_{i,j}$ as presented in equation (2-38), A denotes an inverse of the impedance matrix, $\mathbf{S}^{-1}$ in equation (2-16), and $\mathbf{f}$ is the source vector. For the presented method, the stopping criterion $\epsilon_{obj.}$ was defined based on an objective function and residual. The stopping criterion based on the objective function is the basic method to define it (Prechelt, 1997; Zielinski et al., 2005, 2006).

itermax=... % Limit on the number of iterations
nloop=... % number of loop
d=... % observed dataset

for iloop =1,2,..., nloop
$m^{(1)}$=... % initial guess model parameter
$x^{(1)}$=... % Initial guess source-wavelet model
l =1
While $l \leq$ itermax
$A^{(l)}$=modeling($m^{(l)}$)
$r^{(l)} = A^{(l)}x^{(l)} - d$
$\epsilon_{obj.}^{(l)} = \sum_{i=1}^{n_s}\sum_{j=1}^{n_r} r^{(l)}\left(r^{(l)}\right)^*$
if ($\epsilon_{obj.}^{(l)} > \epsilon_{obj.}^{(l-1)}$ .and. l > 3) then
stop and end or go to the next loop
endif
$\Delta m^{(1)}$=... % Compute the update for model parameter
$\Delta x^{(1)}$=... % Compute the update for source-wavelet
$m^{(l+1)}$=$m^{(l)}$+$\Delta m^{(l)}$
$x^{(l+1)}$=$x^{(l)} + \Delta x^{(l)}$
l= l+1;
end
end

Figure 23. The multi-loop inversion methods using stopping criterion based on the objective function.

A numerical-inversion test using the stopping criterion was applied to the 2 types of dataset; the first dataset contained low-frequency information, while the second did not.

The test model used was the modified Pluto velocity model (Stoughton et al., 2001), which has the complex topography shown in Figure 24. The modified parameter models were reduced in size, but the aspect ratio was maintained. In this test, the S-wave velocity model was generated using a fixed Poisson's ratio (0.21875).

The forward dataset was computed using the 2D elastic IPDG method (described in Appendix A) in the time domain with a 1st-derivative Gaussian source wavelet. The source wavelet was generated with a maximum frequency of 25Hz in the time domain. The number of sources was 100, and the number of receivers was 600. The sources and receivers were located 0.0001 m below the surface. The recording time of the observed dataset was 5 sec with a 2 ms sampling interval. The observed data were obtained using 332,282 triangular elements with P2 shape function (with 6 degrees of freedom per element); thus, the total number of DOF (degrees of freedom) was 1,993,692. The detailed information about synthetic dataset is presented in Table 1.

To remove the low-frequency information for verisimilitude with the real data, a high-pass filter was applied to the observed dataset. Figure 25 shows the designed high-pass filter. Examples of 2 types of datasets with and without low-frequency information were presented in Figure 26 and Figure 27. Figure 26 shows examples of the vertical shot gather of the data from the 51th-source and its frequency spectrum of the low-frequency-containing dataset. Figure 27 shows examples of the shot gather of the filtered data and its frequency spectrum.

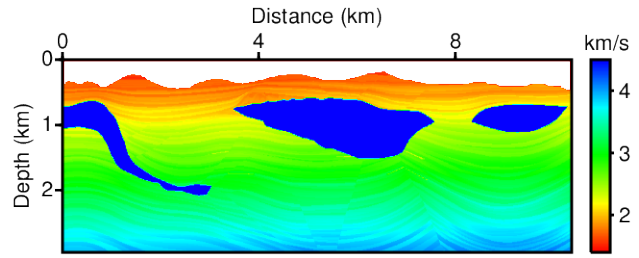

(a)

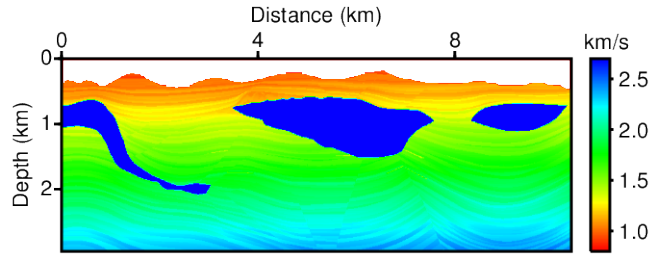

(b)

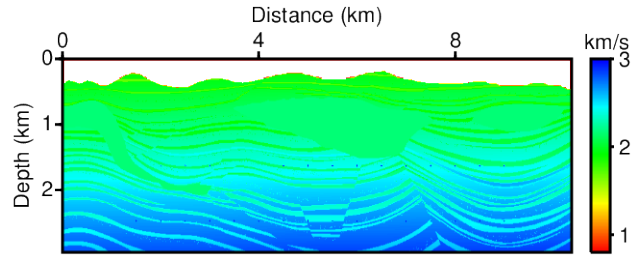

(c)

Figure 24. The modified Pluto parameter set with complex topography: (a) P-wave velocity, (b) S-wave velocity, and (c) density models.

Summary of the information of the synthetic dataset

Domain size	10,380 m × 2,960 m
Far trace offset	10,350 m
Near trace offset	0 m
Number of shots	100
Number of receivers	600
Modeling scheme	IPDG in the time domain
Used number of elements	332,282
Number of total DOF	1,993,692
Recording time	5 sec
Sampling interval	0.002 sec
Source wavelet	1^{st}-derivative Gaussian wavelet
Maximum-frequency of the source wavelet	25 Hz

Table 1. Summary of the information of the generated time-domain synthetic dataset using modified Pluto parameter set.

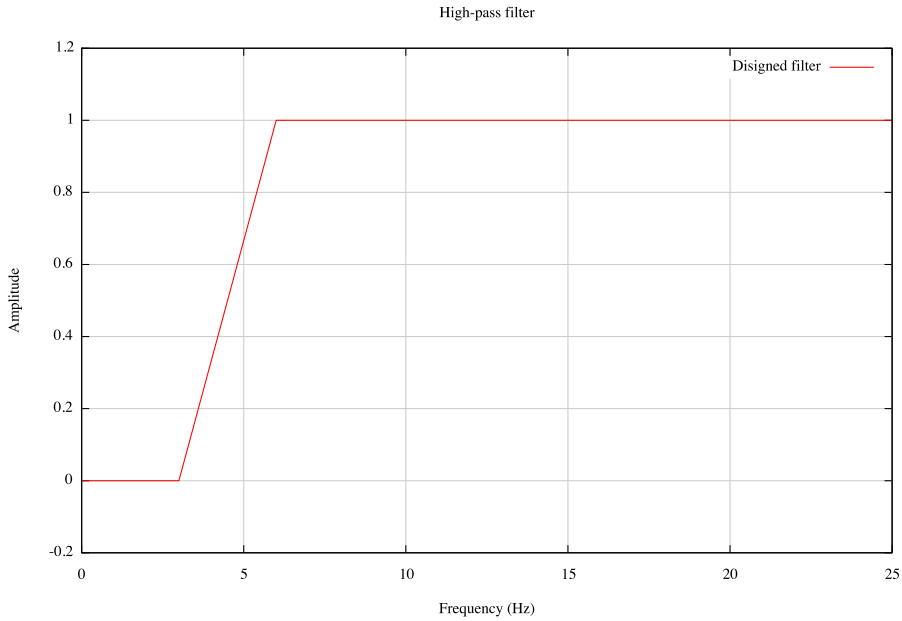

Figure 25. The high-pass filter to remove low-frequency information (frequency=0., 3., 6., and 9. Hz and amplitude=0., 0., 1., and 1.).

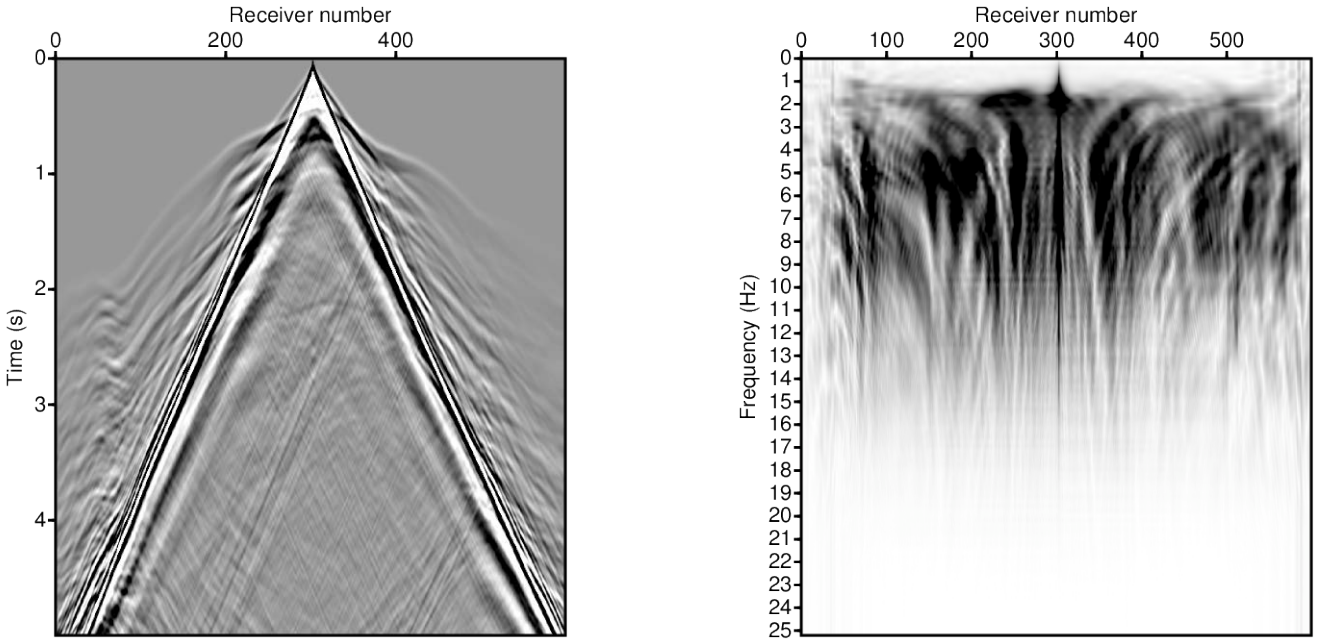

(a) (b)

Figure 26. Examples of the (a) vertical displacement shot gather and its frequency spectrum from the modified Pluto set using the time domain IPDG scheme.

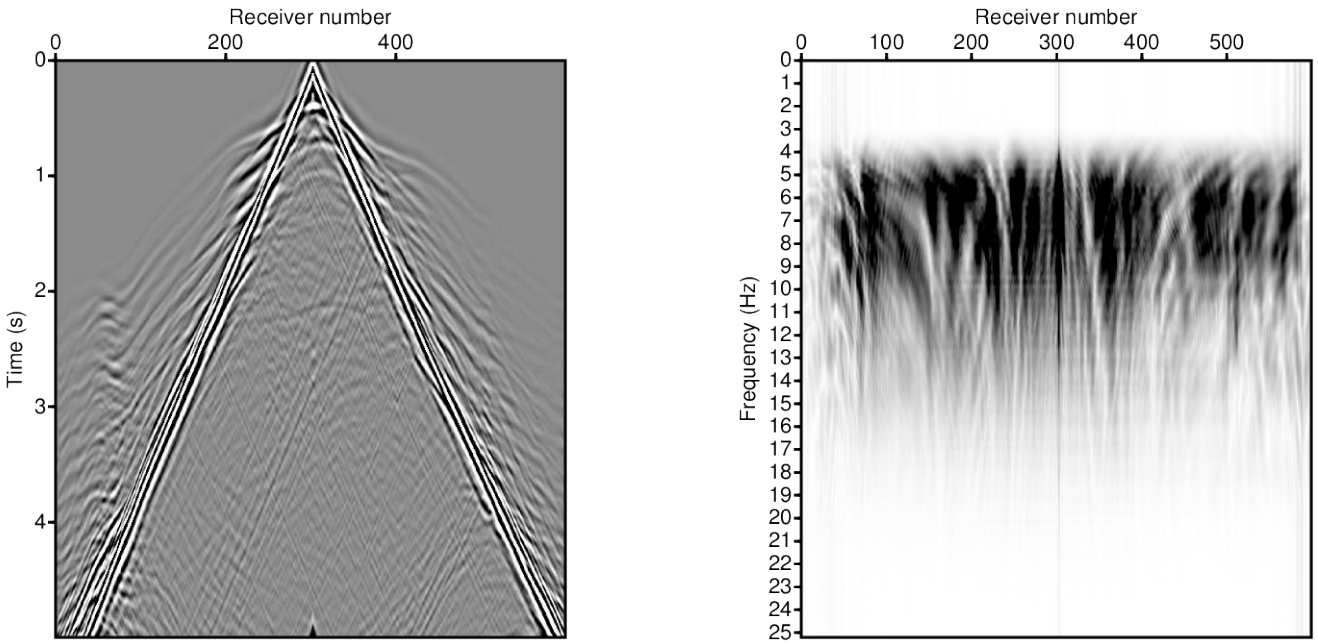

(a) (b)

Figure 27. Examples of the high-pass filtered (a) vertical displacement shot gather and its frequency spectrum from the modified Pluto set using the time domain IPDG scheme.

The Laplace-Fourier-domain inversion was initiated using the linearly increasing velocity models presented in Figure 28, and the density was fixed to 2.3 g/cc. The multistep loops for this test was designed with 21 loops with 500 maximum iteration number for each loop. The modeling in the inversion algorithm was performed via conventional FEM using 85,428 elements with P1 shape functions, and the DOF was 42,950. Detailed summaries of the inversion parameters are presented in Table 2.

The Laplace-Fourier-domain inversion using on the stopping criterion based on objective function computed the P- and S-wave velocities shown in Figure 29 and Figure 30. The inverted P- and S-wave velocities obtained using the low-frequency-containing dataset are successfully show the shape of the salts and the background velocity. However, the inverted results using high-pass filtered dataset seems to over- or under-estimated result in some region as shown in Figure 30.

We considered that it is possible to expect better result by changing the stopping criterion with considering of the characteristics of the logarithmic residual. The logarithmic residual has the property of natural separation into amplitude and phase components, which correspond to the real parts and imaginary parts, respectively, of the complex values as we showed in the theory of the source estimation.

The amplitude and phase error have different and independent meanings. Thus, we supposed that the logarithmic objective function could be treated as the multi-objective function by separating into the amplitude and phase part.

There were studies on frequency inversion using a logarithmic wavefield have considered the amplitude only, the phase only, and both (Shin et al., 2007; Badner et al., 2007; Pyun et al., 2007).

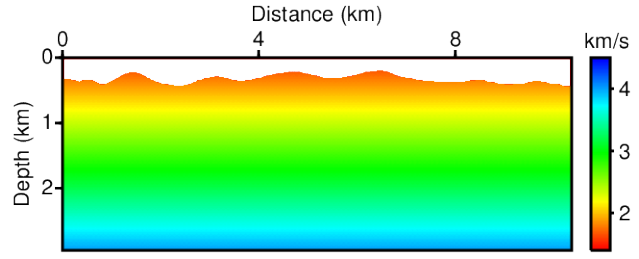

(a)

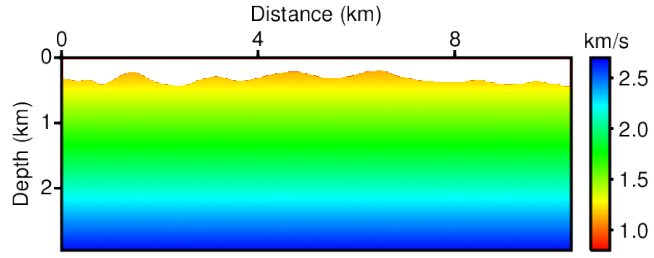

(b)

Figure 28. The initial models for inversion tests with the stopping criterion: (a) initial P-wave velocity model and (b) initial S-wave velocity model.

Summary of the inversion parameters

Loop number	σ	f
1	2, 4, 6, 8, 10,and 12	-
2	2, 4, 6, 8, 10,and 12	0.001 – 2.000 Hz
3	2, 4, 6, 8, 10,and 12	1.000 – 3.000 Hz
4	2, 4, 6, 8, 10,and 12	2.000 – 4.000 Hz
5	2, 4, 6, 8, 10,and 12	3.000 – 5.000 Hz
6	2, 4, 6, 8, 10,and 12	4.000 – 6.000 Hz
7	2, 4, 6, 8, 10,and 12	5.000 – 7.000 Hz
8	2, 4, 6, 8, 10,and 12	6.000 – 8.000 Hz
9	2, 4, 6, 8, 10,and 12	7.000 – 9.000 Hz
10	2, 4, 6, 8, 10,and 12	8.000 – 10.00 Hz
11	2, 4, 6, 8, 10,and 12	9.000– 11.00 Hz
12	2, 4, 6, 8, 10,and 12	10.00– 12.00 Hz
13	2, 4, 6, 8, 10,and 12	11.00– 13.00 Hz
14	2, 4, 6, 8, 10,and 12	12.00– 14.00 Hz
15	2, 4, 6, 8, 10,and 12	13.00– 15.00 Hz
16	2, 4, 6, 8, 10,and 12	14.00– 16.00 Hz
17	2, 4, 6, 8, 10,and 12	15.00– 17.00 Hz
18	2, 4, 6, 8, 10,and 12	16.00– 18.00 Hz
19	2, 4, 6, 8, 10,and 12	17.00– 19.00 Hz
20	2, 4, 6, 8, 10,and 12	18.00– 20.00 Hz
21	2, 4, 6, 8, 10,and 12	19.00– 21.00 Hz

Table 2. Summary of the inversion parameters for each loop. It is designed for the inversion test with modified PLUTO dataset.

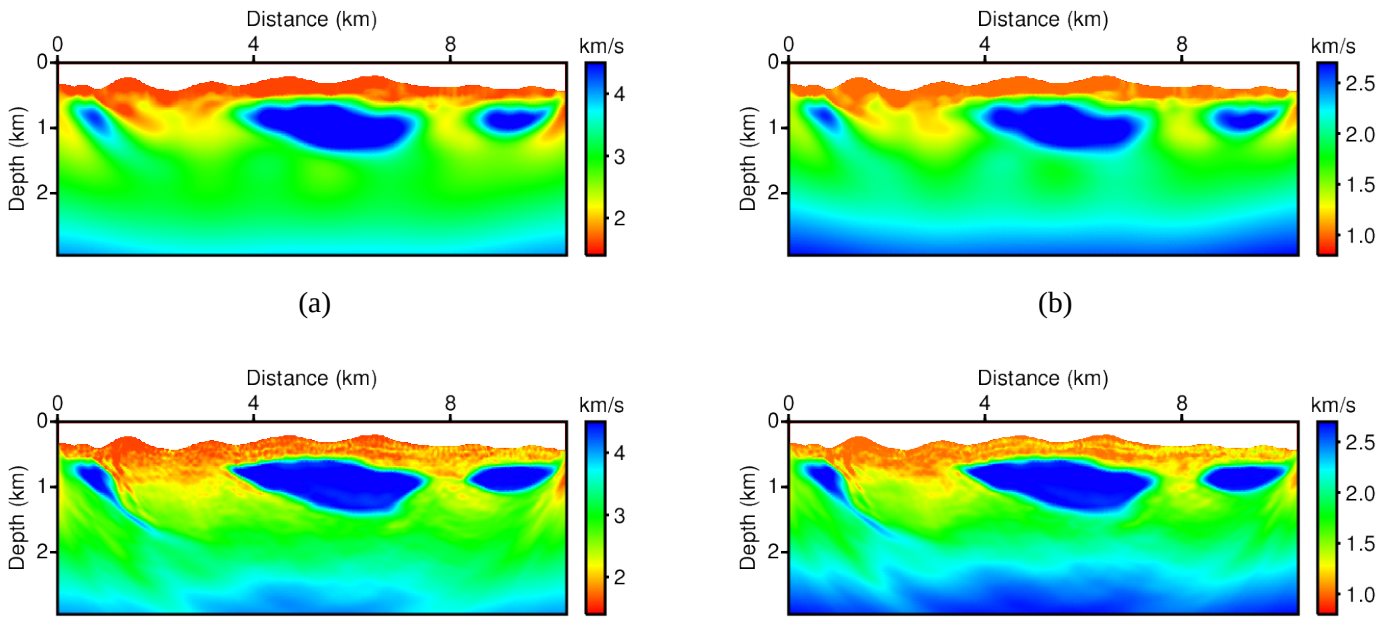

Figure 29. Inverted (a) P-wave and (b) S-wave velocity models obtained using Laplace-domain inversion using the stopping criterion $\epsilon_{obj.}$ and the low-frequency-containing dataset. Inverted (c) P-wave and (d) S-wave velocity models obtained using Laplace-Fourier-domain inversion using the stopping criterion $\epsilon_{obj.}$ and the low-frequency-containing dataset.

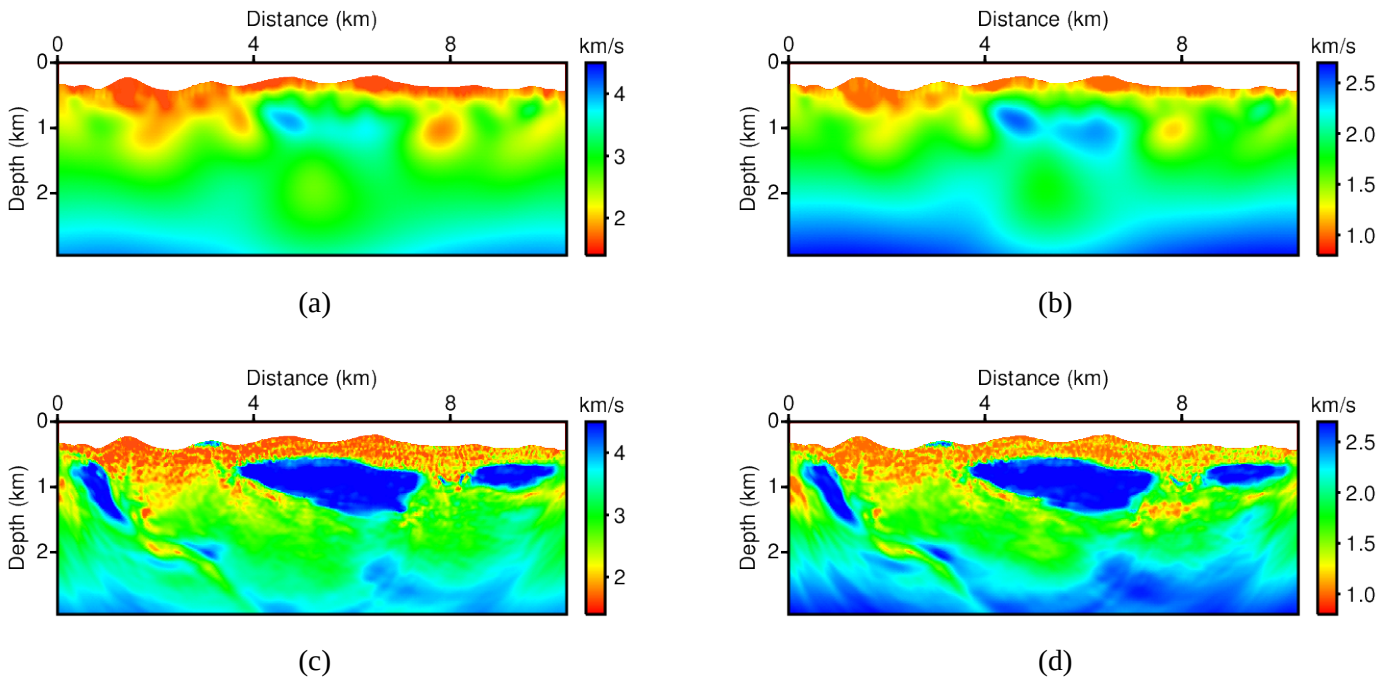

Figure 30. Inverted (a) P-wave and (b) S-wave velocity models obtained using Laplace-domain inversion the stopping criterion $\epsilon_{obj.}$ and the high-pass-filtered dataset. Inverted (c) P-wave and (d) S-wave velocity models obtained using Laplace-Fourier-domain inversion using the stopping criterion $\epsilon_{obj.}$ and the high-pass-filtered dataset.

Of these studies, the logarithmic inversion using both components produced the best result; however, the logarithmic phase inversion yielded a much better inverted result than the amplitude approach. This result indicates that the phase information is more important than the amplitude information for logarithmic frequency inversion. On the other hand, Laplace-domain inversion is an amplitude inversion and amplitude information is the governing parameter.

The Laplace-Fourier-domain inversion is the mixed method of Laplace-domain and frequency-domain inversion and its characteristic is varied with respect to the used Laplace-damping constant and frequency information. For lower-frequency components and higher-Laplace-damping, it is closer to Laplace-domain inversion, while for higher-frequency components and lower-Laplace-damping, the phase information is more important, similar to Fourier-domain inversion.

Firstly to obtain some information about the magnitude of amplitude and phase error, simple test was performed with respect to 7 Laplace damping constants and 6 frequency components using true parameter models shown in Figure 24 and initial parameter models shown in Figure 28. From the simple test, the amplitude-versus-phase error ratios and the phase-versus-amplitude error ratios was obtained with respect to the Laplace damping constants and frequency components as presented in Figure 31. In these plots, it is apparent that the Laplace-Fourier-domain inversion may be dominated by either the amplitude error or the phase error depending on the particular value of the Laplace damping constant and the frequency component. When the logarithmic objective function is considered as the multi-objective problem, then a reasonable solution must be to investigate a set of solutions, each of which objectives at an acceptable level without being dominated by 1 factor.

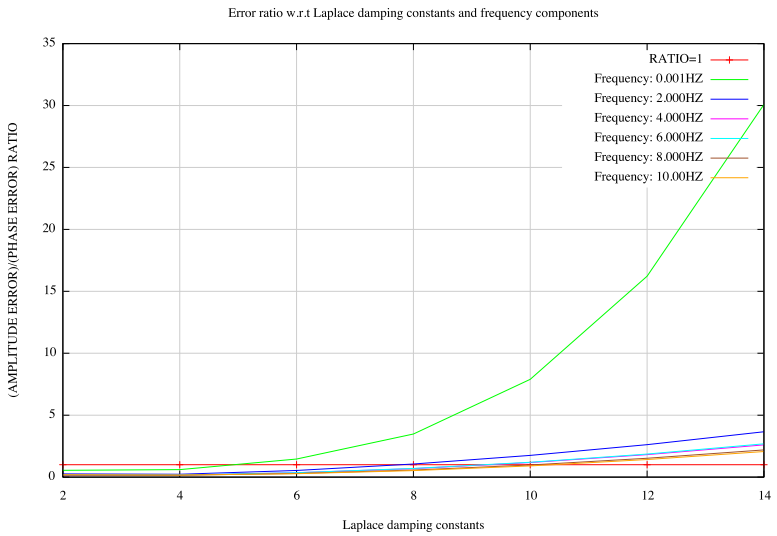

(a)

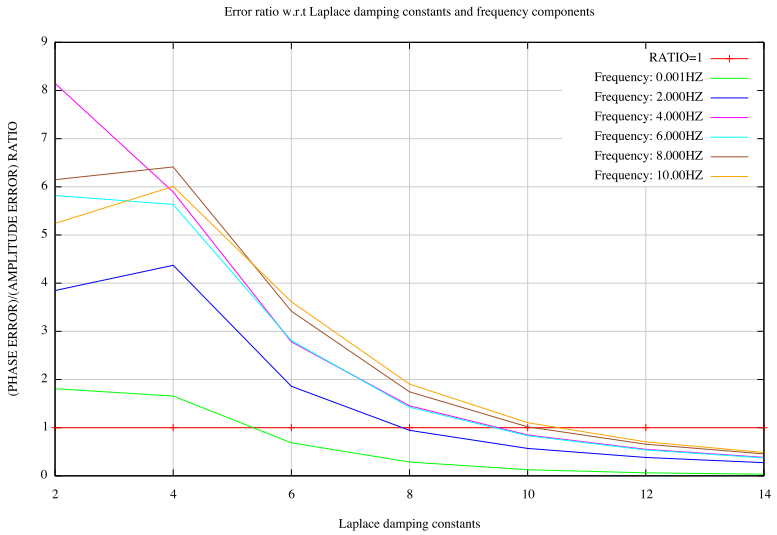

(b)

Figure 31. The magnitude of the (a) amplitude-versus-phase error ratio and (b) phase-versus-amplitude error ratio for 7 Laplace damping constants: σ={2, 4, 6, 8, 10, 12, and 14} and f={0.0, 2.0, 4.0, 6.0, 8.0, and 10.0}.

For the multi-objective assumption, the weighted sum approach was applied to define the stopping for equal contributions of amplitude and phase information and the multi-loop inversion using this criterion is presented in Figure 32 (Konak, 2006; Recktenwald, 2012).

To verify the efficacy of the stopping criterion, the same numerical-inversion test was performed. Figure 33 and Figure 34 show the Laplace-Fourier-domain inverted results for the low-frequency-containing data and the filtered data, respectively. The results obtained for the low-frequency-containing dataset exhibit no improvement in the inverted results with respect to the results obtained using the conventional stopping criterion. However, the inverted results shown in Figure 34 for the high-pass-filtered dataset demonstrate that the Laplace-Fourier-domain inversion using the stopping criterion based on multi-objective assumption was able to recover superior results with respect to the inverted result shown in Figure 30. P-wave velocity residuals between the true models and inverted models are presented in Figure 35 to illustrate the performance of 2 stopping criterions. The residuals and histograms demonstrate the normalized stopping criterion, $\epsilon_{nor.}$, give better result.

Table 3 and Table 4 show the performance of the stopping criterion based on the objective function, i.e. $\epsilon_{obj.}$, and the multi-objective assumption of the logarithmic objective function, i.e. $\epsilon_{nor.}$. In the Table 3 and Table 4Table 3, the first branch point of these tests can be observed at the 2nd loop and it must be returned as a totally different final result for this kind hierarchical multi-loop approach. The Figure 36 shows error curves obtained using 2 different stopping criterions, in the 2nd loop. In this plot, $\epsilon_{obj.}$ made to keep going the inversion procedure until the objective function faced to its terminating point in spite of that the amplitude error was increasing, whereas $\epsilon_{nor.}$ Terminated

the calculation earlier to prevent the large over-fitting of amplitude error.

Here, the stopping criterion tests were performed using 2 types of definition; the first one was defined from the objective function and the second was suggested as the normalized objective function using the assumption of multi-objective problem based on the characteristic of the logarithmic objective function, i.e. natural separation into amplitude and phase components. And in this numerical test, we could obtain better result using the suggested normalized stopping criterion.

itermax=... % Limit on the number of iterations
nloop=... % number of loop
d=... % observed dataset

for iloop =1,2,..., nloop
$m^{(1)}$=... % initial guess model parameter
$x^{(1)}$=... % Initial guess source-wavelet model
l =1
While $l \leq$ itermax
$A^{(l)}$=**modeling**($m^{(l)}$)
$r^{(l)} = A^{(l)}x^{(l)} - d$
if ($l = 1$) then
$r^0 = r^{(l)}$
endif
$\epsilon_{nor.}^{(l)} = \sum_{i=1}^{n_s}\sum_{j=1}^{n_r}\left(\frac{\mathrm{Re}(r^{(l)})^2}{\mathrm{Re}(r^0)^2} + \frac{\mathrm{Im}(r^{(l)})^2}{\mathrm{Im}(r^0)^2}\right)$
if ($\epsilon_{nor.}^{(l)} > \epsilon_{nor.}^{(l-1)}$ .and. l > 3) then
stop and end or go to the next loop
endif
$\Delta m^{(1)}$=... % Compute the update for model parameter
$\Delta x^{(1)}$=... % Compute the update for source-wavelet
$m^{(l+1)}$=$m^{(l)}$+$\Delta m^{(l)}$
$x^{(l+1)}$=$x^{(l)} + \Delta x^{(l)}$
l= l+1;
end
end

Figure 32. The multi-loop inversion methods using stopping criterion based on the multi-objective assumption of the logarithmic objective function.

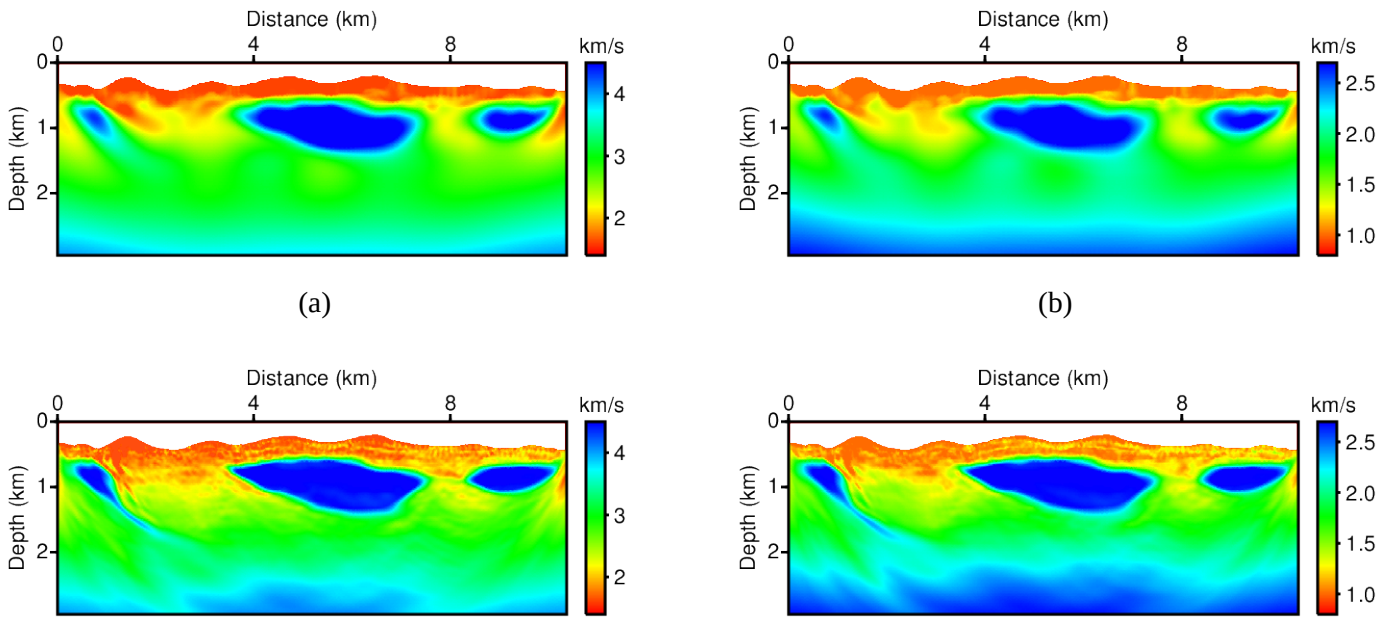

Figure 33. Inverted (a) P-wave and (b) S-wave velocity models obtained using Laplace-domain inversion using the normalized stopping criterion $\epsilon_{nor.}$ and the low-frequency-containing dataset. Inverted (c) P-wave and (d) S-wave velocity models obtained using Laplace-Fourier-domain inversion using the normalized stopping criterion $\epsilon_{nor.}$ and the low-frequency-containing dataset.

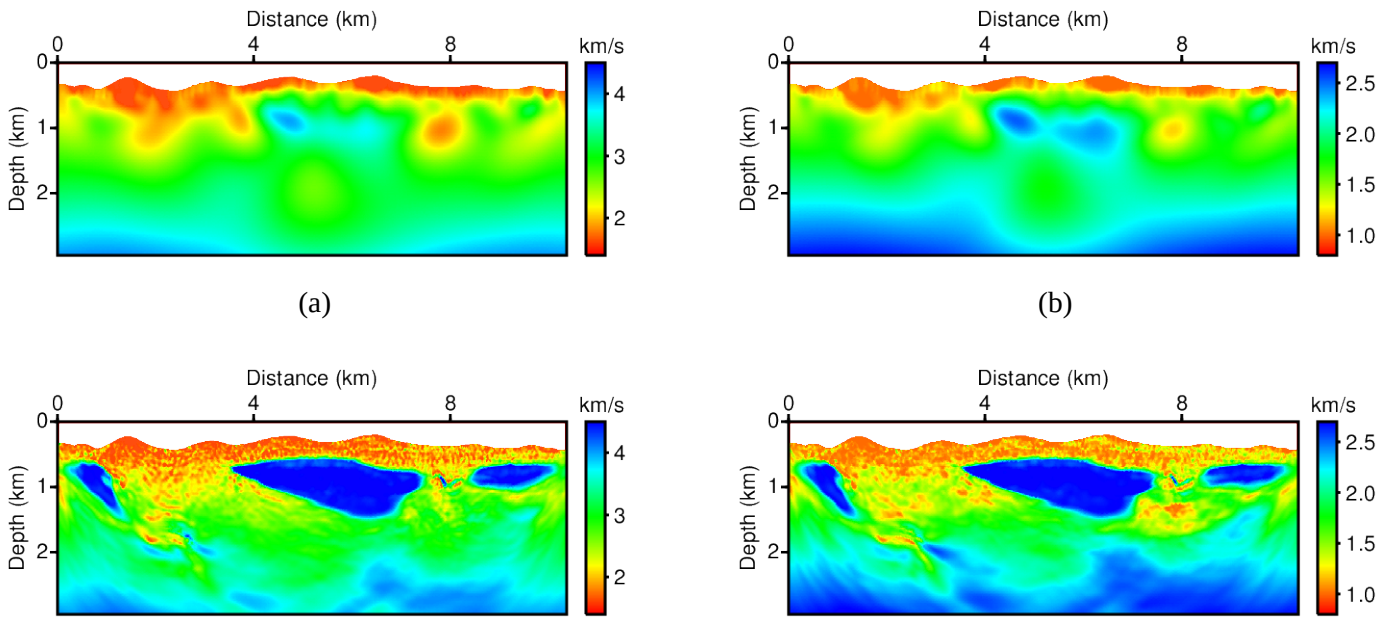

Figure 34. Inverted (a) P-wave and (b) S-wave velocity models obtained using Laplace-domain inversion using the normalized stopping criterion $\epsilon_{nor.}$ and the high-pass-filtered dataset. Inverted (c) P-wave and (d) S-wave velocity models obtained using Laplace-Fourier-domain inversion usisng the normalized stopping criterion $\epsilon_{nor.}$ and the high-pass-filtered dataset.

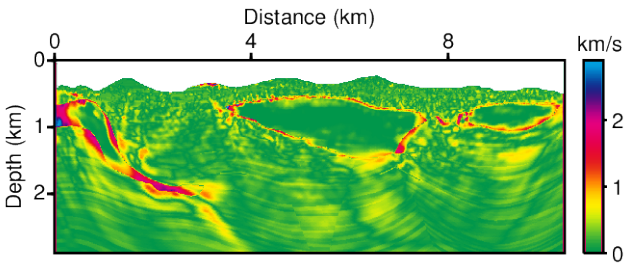

(a)

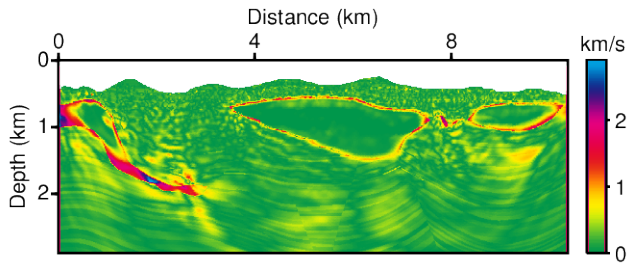

(b)

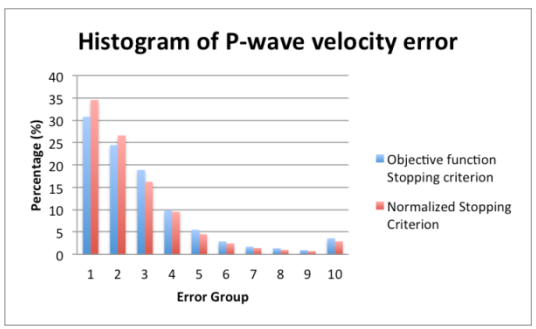

(c)

Figure 35. The P-wave residuals between true models and initial models obtained with (a) $\epsilon_{obj.}$, (b) $\epsilon_{nor.}$, and (c) histogram of the magnitude of the error of P-wave. Error groups defined as (1) 0.0 ~ 0.1, (2) 0.1 ~ 0.2, (3) 0.2 ~ 0.3, (4) 0.3 ~ 0.4, (5) 0.4 ~ 0.5, (6) 0.5 ~ 0.6, (7) 0.6 ~ 0.7, (8) 0.7 ~ 0.8, (9) 0.8 ~ 0.9, and (10) 0.9 ~ km/s.

The number of over-fitting with $\epsilon_{obj.}$

Loop number	Number of Iterations	Objective	Amplitude	Phase
1	75	0	0	0
2	260	0	153	0
3	500	0	51	0
4	500	0	0	0
5	500	0	0	0
6	500	0	0	0
7	500	0	0	0
8	500	0	0	0
9	343	0	0	2
10	500	0	106	1
11	31	0	6	0
12	77	0	25	1
13	50	0	15	1
14	4	0	0	0
15	136	0	2	0
16	23	0	5	0
17	53	0	4	0
18	65	0	14	3
19	31	0	9	0
20	21	0	4	0
21	17	0	4	0
SUM	**4686**	**0**	**398**	**8**

Table 3. The summaries about the number of over-fitting for objective function, amplitude error, and phase error when the stopping criterion $\epsilon_{obj.}$ is applied.

The number of over-fitting with $\epsilon_{nor.}$

Loop number	Number of Iterations	Objective	Amplitude	Phase
1	75	0	0	0
2	64	0	45	0
3	452	0	181	0
4	500	0	1	0
5	500	0	0	0
6	500	0	0	0
7	500	1	0	0
8	144	3	0	3
9	500	1	0	5
10	442	0	0	2
11	64	0	6	5
12	9	0	2	0
13	74	0	2	0
14	4	0	0	0
15	17	0	0	0
16	4	0	0	0
17	33	1	2	3
18	24	0	6	1
19	18	0	2	0
20	38	1	3	2
21	4	0	0	0
SUM	**3966**	**7**	**250**	**21**

Table 4. The summaries about the number of over-fitting for objective function, amplitude error, and phase error when the stopping criterion $\epsilon_{nor.}$ is applied.

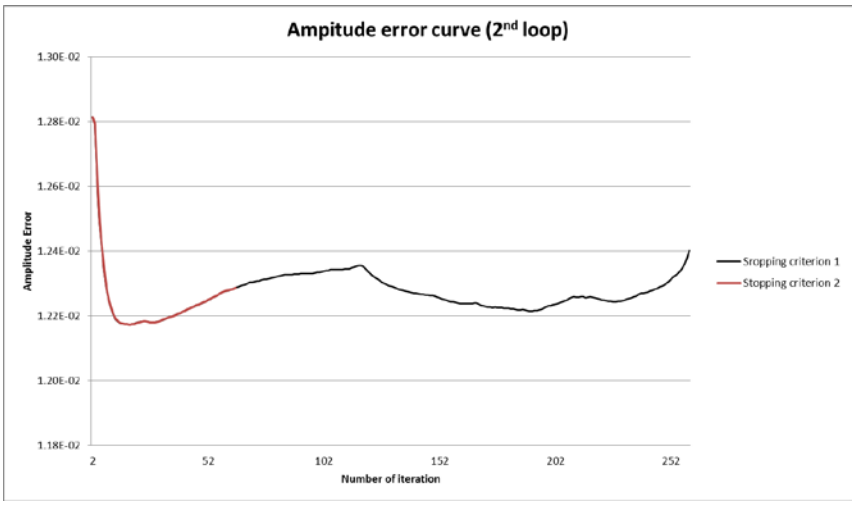

(a)

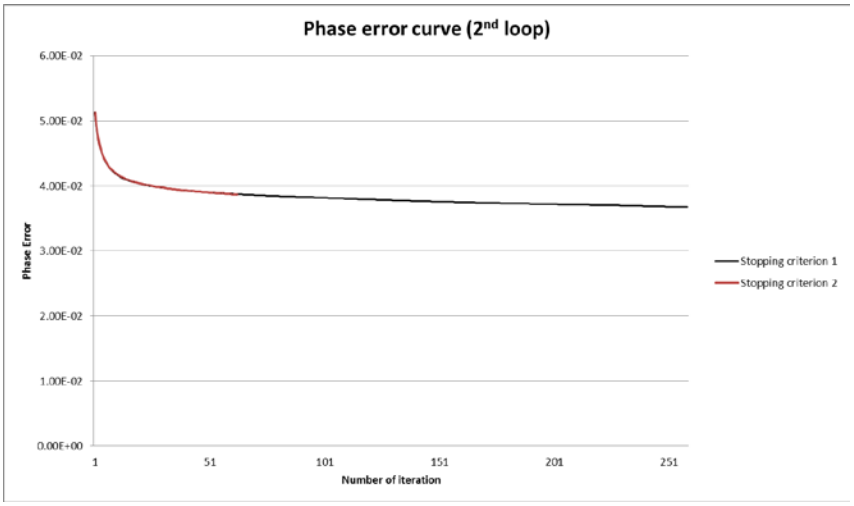

(b)

Figure 36. The error curves at 2nd loop obtained using stopping criterions; (a) amplitude and (b) phase error. Stopping criterion 1 indicates $\epsilon_{nor.}$ and stopping criterion indicates $\epsilon_{nor.}$.

Chapter 3. Examples using synthetic data

The developed elastic full-waveform inversion in the Laplace-Fourier domain was applied to synthetic datasets computed with ‘IPATI model’ as shown in Figure 37. The ‘IPATI model’ is the velocity model that describes the geological structure of the southern Bolivia region. This velocity model represents a folded mountain with complex topography.

The inversion was performed using several datasets treated with different purposes and the same initial parameter models shown in Figure 38 for every test. First, the algorithm was applied to a synthetic dataset generated using the same forward modeling scheme as used in the inversion procedure to verify the algorithm.

Second, the developed algorithm was applied to the synthetic dataset generated with the IPDG scheme in the time domain. In the test using time-domain dataset, the elastic Laplace-Fourier-domain inversion algorithm was applied to several datasets with purpose of the dependency on the low- frequency information and the observation of the performance with a noisy dataset.

And Last, we compared the results of 2D acoustic and 2D elastic inversion in the Laplace-Fourier domain for the same dataset to illustrate why elastic inversion is necessary for a land dataset.

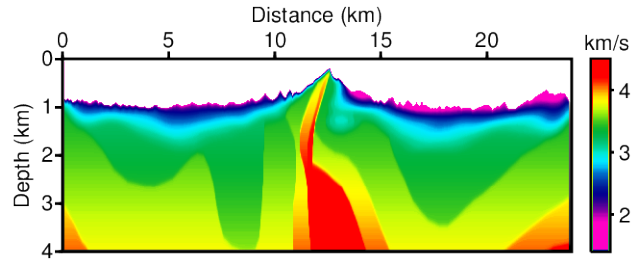

(a)

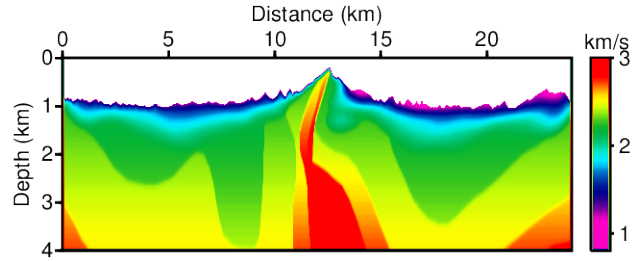

(b)

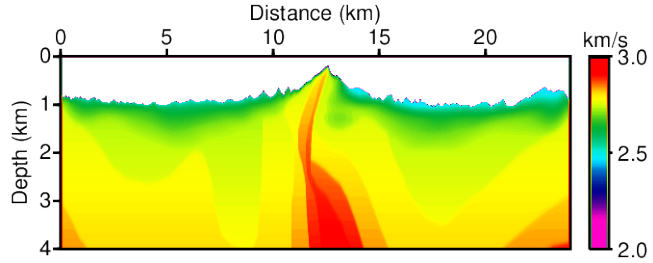

(c)

Figure 37. IPATI parameter set that describes a realistic folded mountain: (a) P-wave velocity, (b) S-wave velocity, and (c) density models.

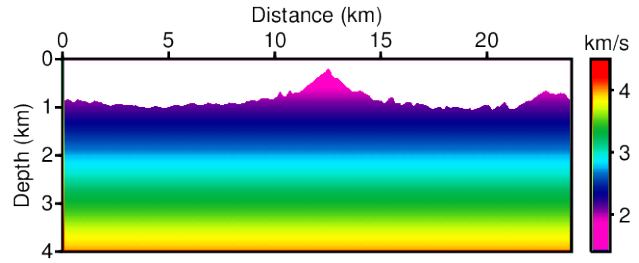

(a)

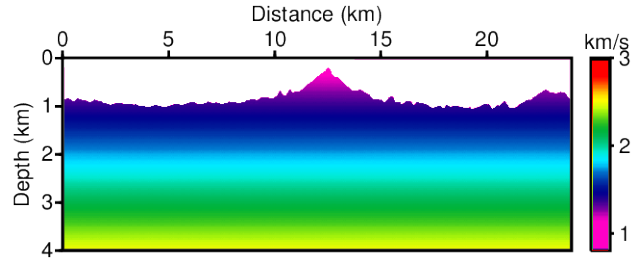

(b)

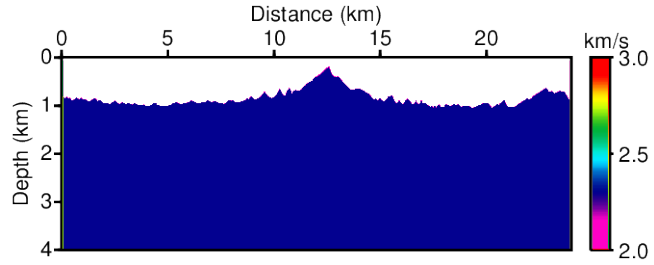

(c)

Figure 38. The initial parameter set for synthetic inversion tests: (a) initial P-wave velocity model, (b) initial S-wave velocity model, and (c) initial density models.

3.1 Laplace-Fourier-domain synthetic dataset

The developed algorithm was applied to the generated synthetic data using the Laplace-Fourier-domain IPDG modeling with the 'IPATI model' shown in Figure 37.

The synthetic model was generated using the IPDG scheme on an unstructured grid with 258,935 elements and 776,805 DOF for a 24 km × 4km domain. The generated synthetic dataset had 960 sources, and the number of the receivers varies from 672 to 1,640 depending on the source position. This distribution of sources and receivers followed the source and receiver placement of the real land acquisition performed by TOTAL at Ipati, Bolivia, in 2003. The far- and near-trace offsets were 6.25 m and 10,256.25 m, respectively. Detailed summaries of the information about the Laplace-Fourier-domain synthetic dataset are presented in Table 5.

The loop strategy of inversion comprised with 9 steps from low- to high-frequency components. Each loop used a different size of mesh. A detailed summary of the inversion strategy is presented in Table 6.

The inversion was initiated with linearly increasing velocity models and homogeneous density model. The initial P-wave velocity model varied from 1.5 km/s to 4.0 km/s, and initial S-wave velocity model varied from 1.0 km/s 2.5 km/s with respect to the depth. The initial density model was a 2.3 g/cc constant model. Throughout the entire inversion step, the density was assumed to be a constant value.

The inversion was performed using the normalized stopping criterion. Figure 39 shows the P-wave and S-wave velocity models recovered via Laplace and Laplace-Fourier inversion.

Summary of the information of the synthetic dataset

Domain size	24,000 m × 4.060 m
Far trace offset	10,256.25 m
Near trace offset	6.25 m
Number of shots	960
Number of receivers	672-1640
Modeling scheme	IPDG in the Laplace-Fourier domain
Used number of elements	258,935
Number of total DOF	776,805
Source wavelet	Impulse source

Table 5. Summary of the information of the generated Laplace-Fourier-domain synthetic dataset using IPATI parameter set.

Summary of the inversion parameters

Loop number	σ	f	Used number of elements
1	2, 4, 6, 8, 10, 12, and 14	0.001 Hz	66,510
2	2, 4, 6, 8, 10, 12, and 14	0.001 – 0.250 Hz	66,510
3	2, 4, 6, 8, 10, 12, and 14	0.250 – 2.750 Hz	66,510
4	2, 4, 6, 8, 10, 12, and 14	3.000 – 5.500 Hz	66,510
5	2, 4, 6, 8, 10, 12, and 14	5.750 – 8.250 Hz	258,935
6	2, 4, 6, 8, 10, 12, and 14	8.500 – 11.00 Hz	258,935
7	2, 4, 6, 8, 10, 12, and 14	11.25 – 13.75 Hz	258,935
8	2, 4, 6, 8, 10, 12, and 14	14.00 – 16.50 Hz	258,935
9	2, 4, 6, 8, 10, 12, and 14	16.75 – 19.25 Hz	258,935

Table 6. Summary of the inversion parameters for each loop. It is designed for the inversion test with the Laplace-Fourier domain IPATI dataset.

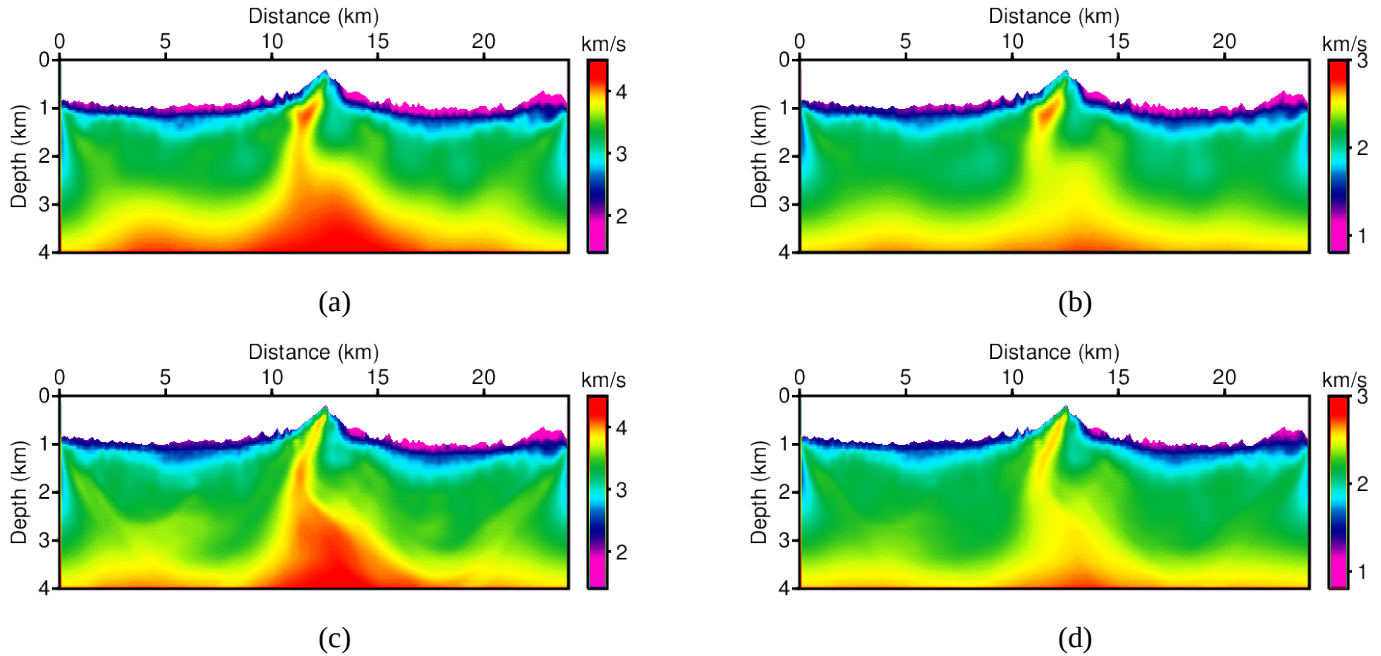

Figure 39. Inverted (a) P-wave and (b) S-wave velocity models obtained using Laplace-domain from IPATI dataset. Inverted (c) P-wave and (d) S-wave velocity models obtained using Laplace-Fourier-domain inversion from Laplace-Fourier domain IPATI dataset.

3.2 Time-domain synthetic dataset

The developed algorithm was applied to synthetic data generated using time-domain 2D elastic wave modeling with the IPDG scheme to verify the algorithm for time-domain datasets for several purposes.

The synthetic model was generated using the same domain size and mesh as used in the first test. However, the DOF of the mesh increased to 1,553,610 with the P2 shape function. The generated synthetic dataset had 240 sources, and the number of receivers varied from 822 to 1,640 depending on the source position. Every source and receiver was located at a 1 m depth below the surface. The far- and near-trace offset were 6.25 m and 10,256.25 m, respectively. The synthetic dataset was recorded in measurement of 8 seconds in duration with 4 ms intervals and it was generated using a first-derivative Gaussian source wavelet with a maximum frequency of 25 Hz. A detailed summary of the time-domain IPATI dataset is presented in Table 7.

The Figure 40 shows an example of a generated seismogram of vertical displacement and its frequency spectrum. The dataset is remade with respect to the 2 different purposes. First, the generated dataset was applied high-pass filter to investigate the dependency of the algorithm on the low-frequency information. And also, the Gaussian white noise was applied to the synthetic dataset for using it to test the algorithm's performance with the noisy dataset.

In the test with the time-domain synthetic dataset, 3 types of inversion-test were performed using the same conditions. The initial velocity models were linearly increasing models, as shown in Figure 38. The inversion loop comprised 12 steps, with frequency components in ranging from 0.001 Hz to 25 Hz and 7 Laplace damping constants (2, 4, 6, 8, 10, 12, and 14). A detailed

summary of the inversion strategy for each loop is presented in Table 8.

Summary of the information of the synthetic dataset

Domain size	24,000 m × 4.060 m
Far trace offset	10,256.25 m
Near trace offset	6.25 m
Number of shots	240
Number of receivers	882-1640
Modeling scheme	IPDG in the time domain
Used number of elements	258,935
Number of total DOF	1,553,610
Recording time	8 sec
Sampling interval	0.004 sec
Source wavelet	1^{st} derivative Gaussian wavelet
Maximum-frequency of the source wavelet	25 Hz

Table 7. Summary of the information of the generated time domain synthetic dataset using IPATI parameter set.

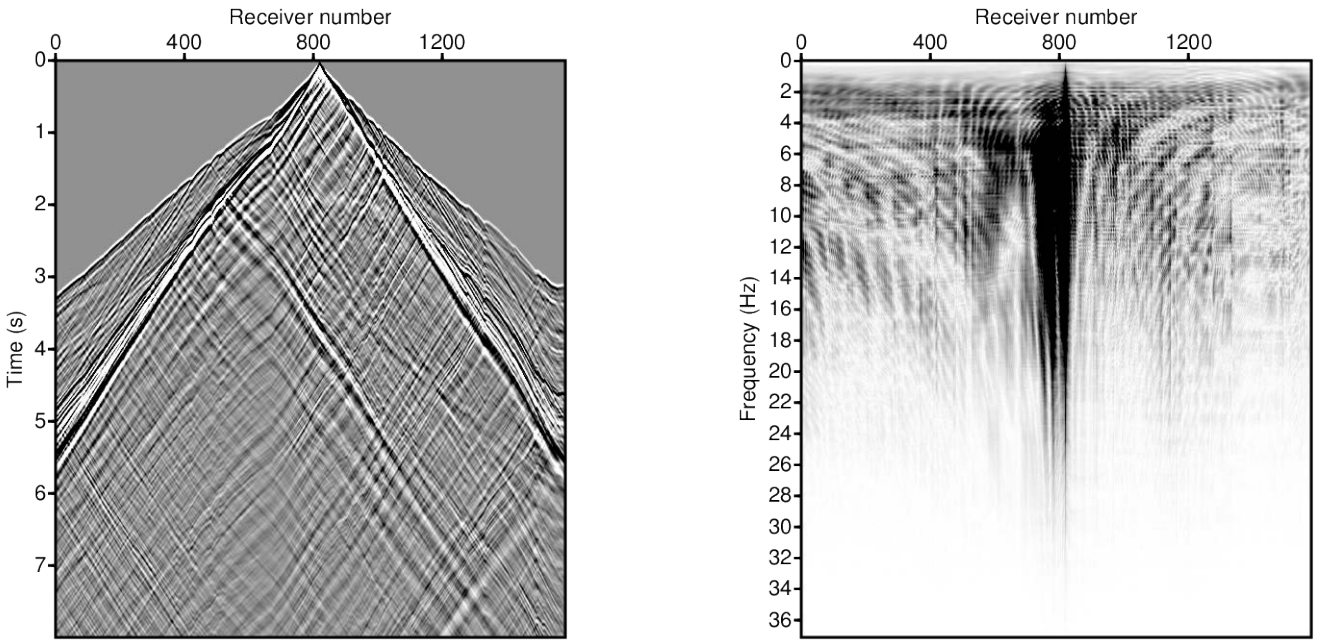

(a) (b)

Figure 40. Examples of the (a) vertical displacement shot gather computed using time-domain IPDG scheme from IPATI parameter set and (b) its frequency spectrum.

Summary of the inversion parameters

Loop number	σ	f	Used number of elements
1	2, 4, 6, 8, 10, 12, and 14	0.001 Hz	66,510
2	2, 4, 6, 8, 10, 12, and 14	0.001-0.250 Hz	66,510
3	2, 4, 6, 8, 10, 12, and 14	0.250-2.750 Hz	66,510
4	2, 4, 6, 8, 10, 12, and 14	3.000-5.250 Hz	258,935
5	2, 4, 6, 8, 10, 12, and 14	5.500-7.750 Hz	258,935
6	2, 4, 6, 8, 10, 12, and 14	8.000-10.25 Hz	258,935
7	2, 4, 6, 8, 10, 12, and 14	10.50-12.75 Hz	258,935
8	2, 4, 6, 8, 10, 12, and 14	13.00-15.25 Hz	258,935
9	2, 4, 6, 8, 10, 12, and 14	15.50-17.75 Hz	258,935
10	2, 4, 6, 8, 10, 12, and 14	18.00-20.25 Hz	258,935
11	2, 4, 6, 8, 10, 12, and 14	20.50-22.75 Hz	258,935
12	2, 4, 6, 8, 10, 12, and 14	23.00-25.00 Hz	258,935

Table 8. Summary of the inversion parameters for each loop. It is designed for the inversion test with the time domain IPATI dataset.

3.2.1 Inversion test for the dependency with respect to the low-frequency information

The absence of low-frequency information in many real datasets is the main hindrance to successful full-waveform inversion. Thus, many geophysicists have commented upon the necessity of a wavelength velocity model for successful inversion (Sirgue, 2006; Brenders and Pratt, 2007; Shin and Cha, 2008; Virieux and Operto, 2009). The algorithm for estimating the initial velocity model must therefore be tested using a dataset that does not contain low-frequency information.

I designed the 2 types of high-pass filters shown in Figure 41 to get rid of the low frequency information. The first high-pass filter removes the low-frequency components below 3 Hz and proportionally suppresses the components in the range of 3 – 6 Hz. And a second high-pass filter was designed for more general condition of the lacking of frequency spectrum of the dataset. The second high-pass filter removes the low-frequency information under below 6 Hz and proportionally suppresses the components in the range 6 – 12 Hz (Latimer et al., 2000).

Figure 42 and Figure 43 show the filtered datasets from which the low-frequency information has been removed and their frequency spectra

The developed 2D elastic Laplace-Fourier-domain inversion algorithm was applied to these 3 datasets: the low-frequency-containing dataset, the first high-pass-filtered dataset and the second high-pass-filtered dataset. As mentioned in the early part of this chapter, the inversion conditions were the same for each test as presented in Table 8. The initial models were used as presented in Figure 38. The density was assumed as a constant value and it was not

updated in this inversion test. The newly derived pseudo-Hessian was applied and the number of iteration was controlled by the normalized stopping criterion for each loop.

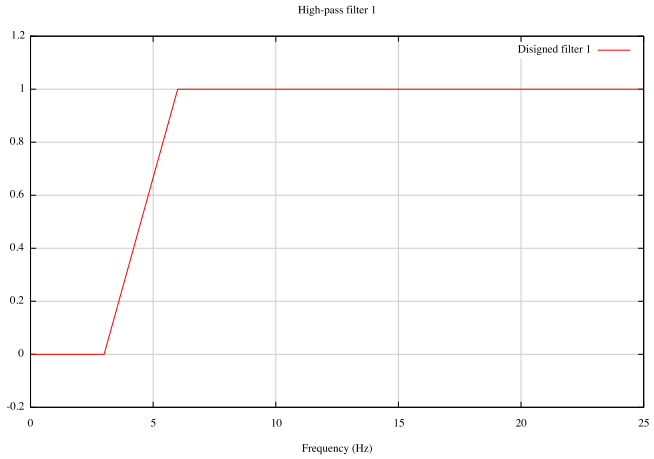

(a)

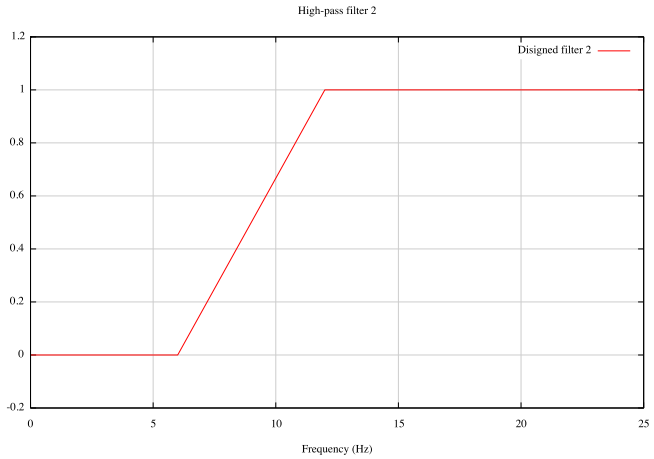

(b)

Figure 41. The high-pass filter to remove low frequency information. (a) High-pass filter 1 (frequency=0., 3., 6., and 9. Hz and amplitude=0., 0., 1., and 1.) (b) High-pass filter 2 (frequency=0., 6., 12., and 18. Hz and amplitude=0., 0., 1., and 1.).

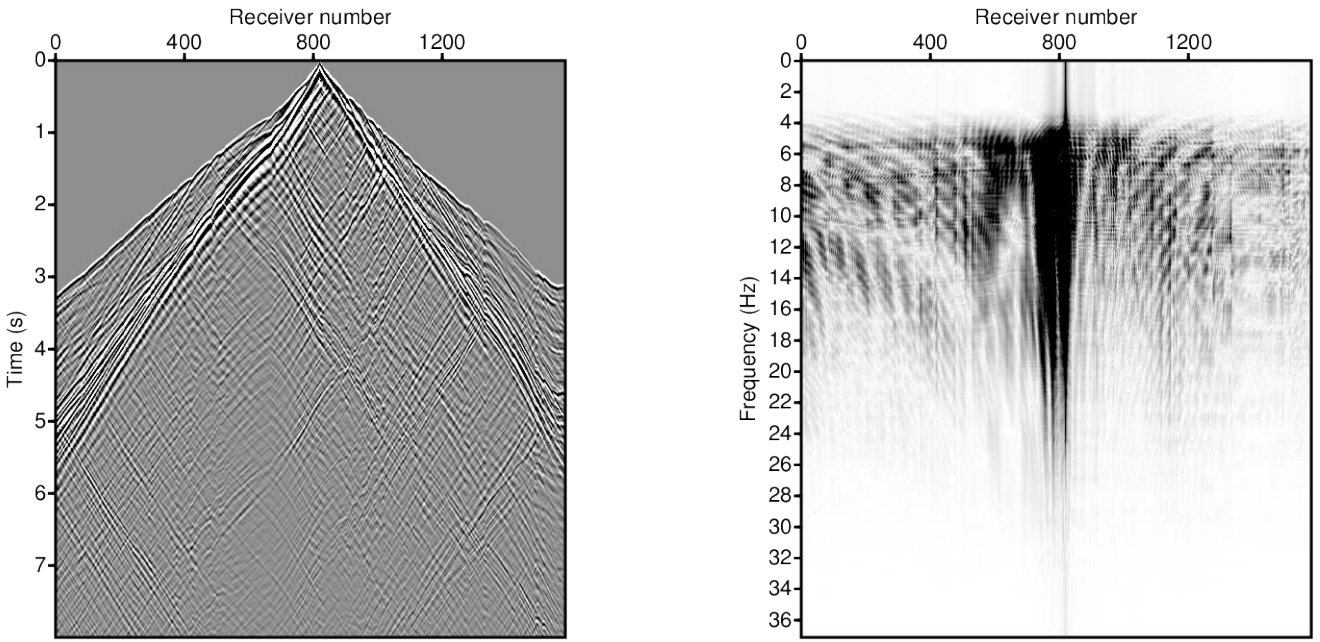

(a) (b)

Figure 42. Examples of the (a) vertical displacement shot gather computed using time-domain IPDG scheme from IPATI parameter set and (b) its frequency spectrum. This dataset is applied the 1st high-pass filter presented in Figure 41a.

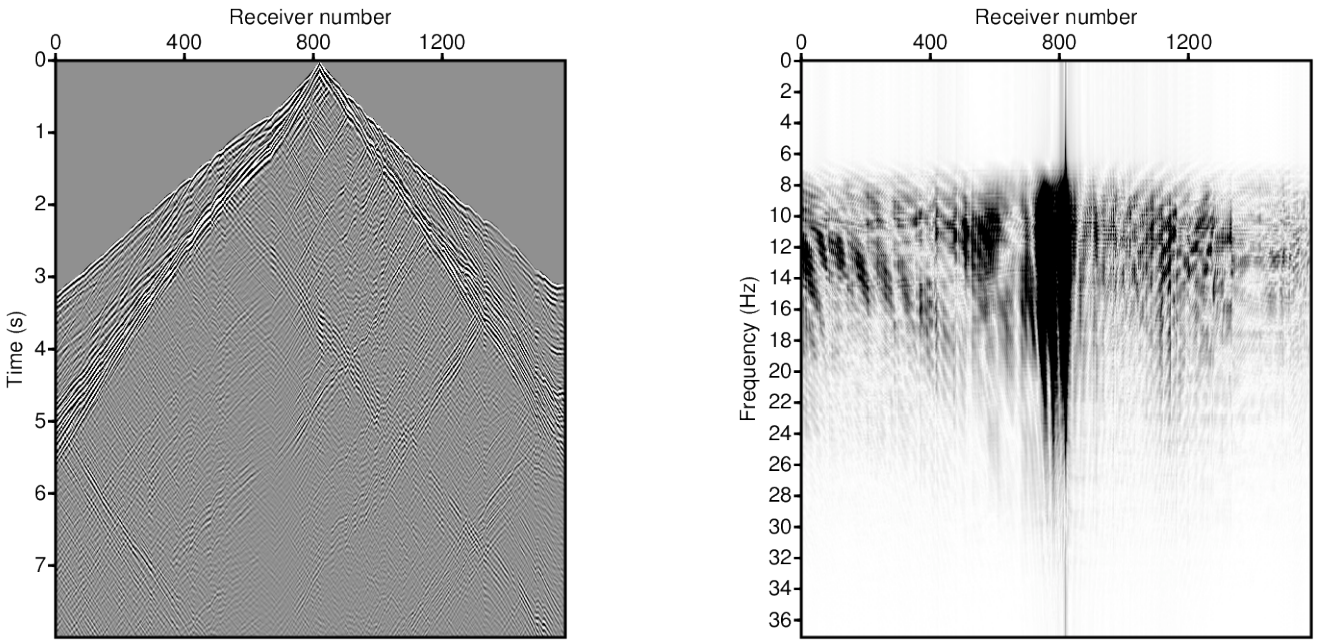

(a) (b)

Figure 43. Examples of the (a) vertical displacement shot gather computed using time-domain IPDG scheme from IPATI parameter set and (b) its frequency spectrum. This dataset is applied the 2nd high-pass filter presented in Figure 41b.

Figure 44, Figure 45, and Figure 46 show the Laplace- and Laplace-Fourier-inverted results for the P-wave velocity and S-wave velocity obtained using the low-frequency-containing dataset, the first high-pass-filtered dataset and the second high-pass-filtered dataset, respectively.

Residuals between the true models and inverted models are presented to illustrate the performance of the developed inversion algorithm. Figure 47a and Figure 47b show the residuals between the true models shown in Figure 37 and the initial models shown in Figure 38. The range of the P-wave velocity residuals is from 0.000016 km/s to 2.143 km/s and the range of the S-wave velocity residuals is from 0.000052 km/s to 1.461 km/s. In Figure 47c and Figure 47d, the distribution of the magnitude of the P-wave and S-wave residuals is presented, the error groups are classified as 10 groups with respect to the absolute magnitude; (1) from 0.0 to 0.1 km/s, (2) from 0.1 to 0.2 km/s, (3) from 0.2 to 0.3 km/s, (4) from 0.3 to 0.4 km/s, (5) from 0.4 to 0.5 km/s, (6) from 0.5 to 0.6 km/s, (7) from 0.6 to 0.7 km/s, (8) from 0.7 to 0.8 km/s, (9) from 0.8 to 0.9 km/s, and (10) over 0.9 km/s.

In these figures, it can be seen that the error due to the initial models is evenly distributed across the entire domain with respect to the true models. The averages of the residual of the P-wave velocity and the S-wave velocity are 0.476 km/s and 0.416 km/s, respectively.

Figure 48 show the residuals computed between the true models and the Laplace-Fourier inverted results using the low-frequency-containing dataset. The presented residuals show that the fitting discrepancy is reduced with respect to the initial models at most points. The range of the P-wave velocity residuals is from 0.00000024 km to 0.866 km/s, and the range of the S-wave velocity residuals is from 0.000004 km/s to 0.703 km/s. The average of the P-

wave velocity residuals is 0.130 km/s, and of the S-wave velocity residuals are 0.176 km/s. The ranges of the residuals and their averages also are considerably decreased. Some discrepancies still remain on each side and in the deeper region.

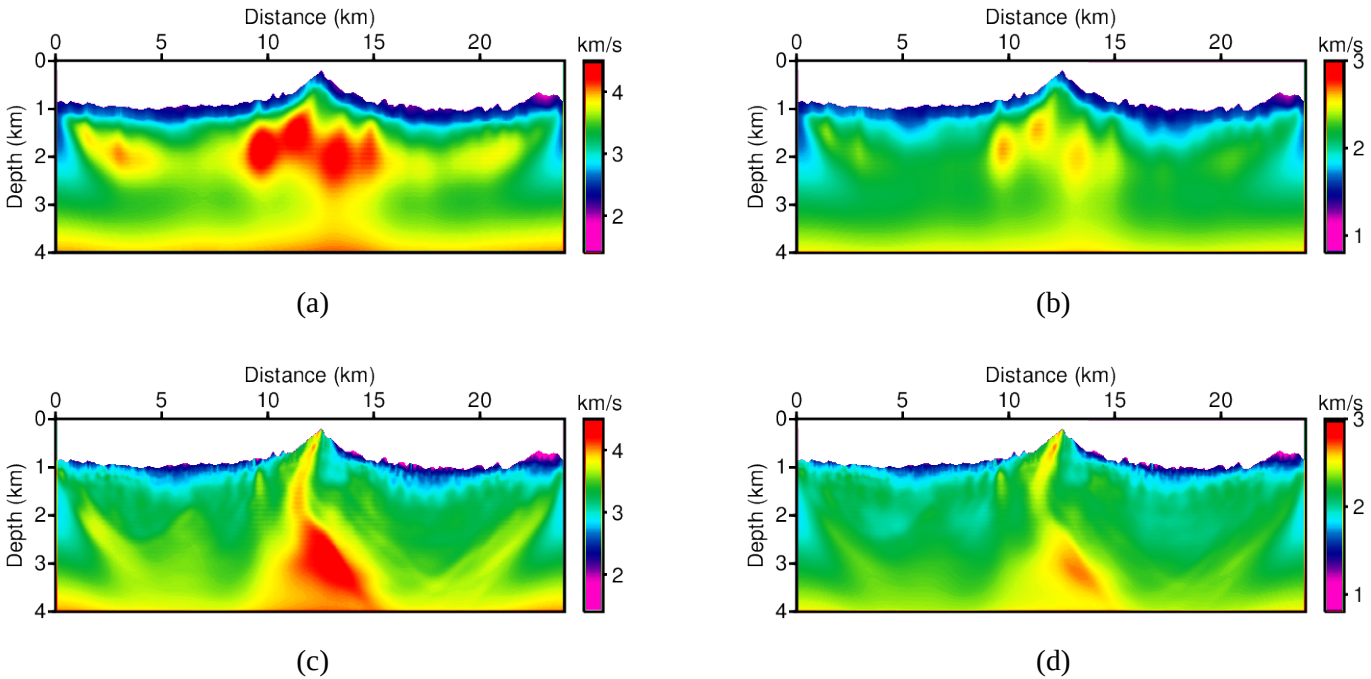

Figure 44. Inverted (a) P-wave and (b) S-wave velocity models obtained using Laplace-domain inversion. Inverted (c) P-wave and (d) S-wave velocity models obtained using Laplace-Fourier-domain inversion with time domain IPATI dataset. The inversion results are obtained with the low frequency contains dataset presented in Figure 40.

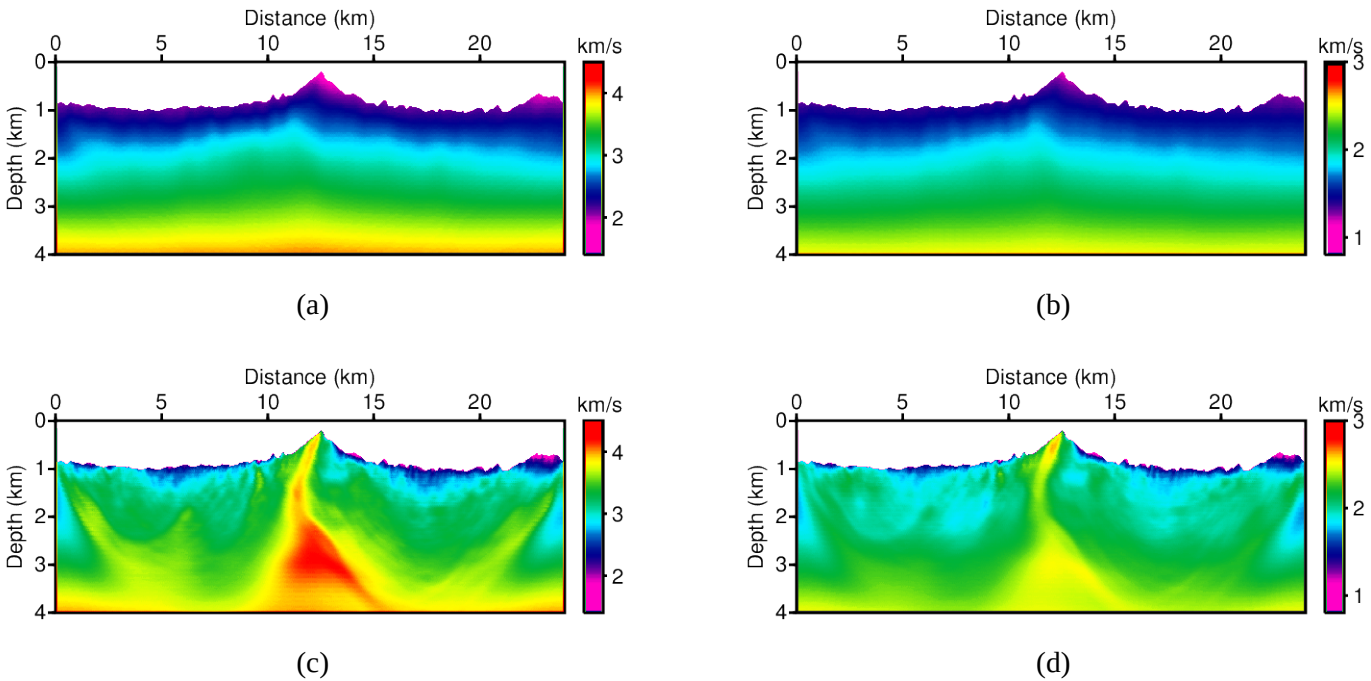

Figure 45. Inverted (a) P-wave and (b) S-wave velocity models obtained using Laplace-domain inversion. Inverted (c) P-wave and (d) S-wave velocity models obtained using Laplace-Fourier-domain inversion with time domain IPATI dataset. The inversion results are obtained with the time domain dataset applied the 1st high-pass filter, thus the dataset is not contains the low-frequency information below 3 Hz as presented in Figure 42.

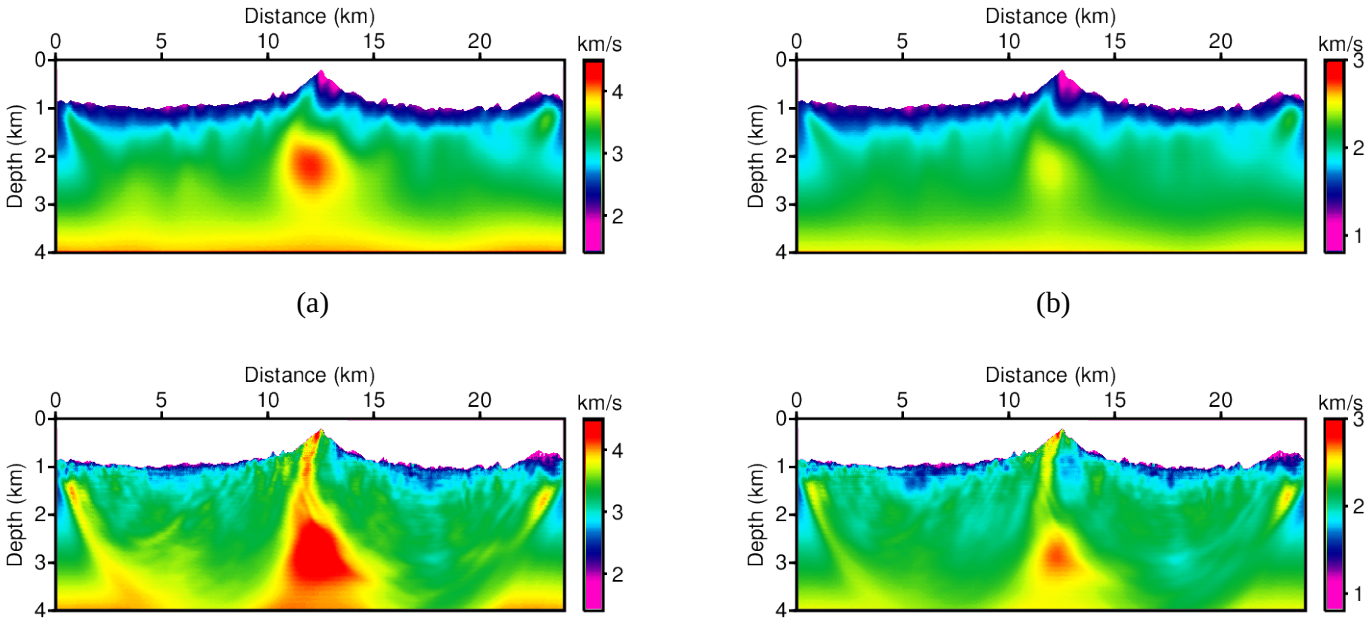

Figure 46. Inverted (a) P-wave and (b) S-wave velocity models obtained using Laplace-domain inversion. Inverted (c) P-wave and (d) S-wave velocity models obtained using Laplace-Fourier-domain inversion with time domain IPATI dataset. The inversion results are obtained with the time domain dataset applied the 2nd high-pass filter, thus the dataset is not contains the low-frequency information below 6 Hz as presented in Figure 43.

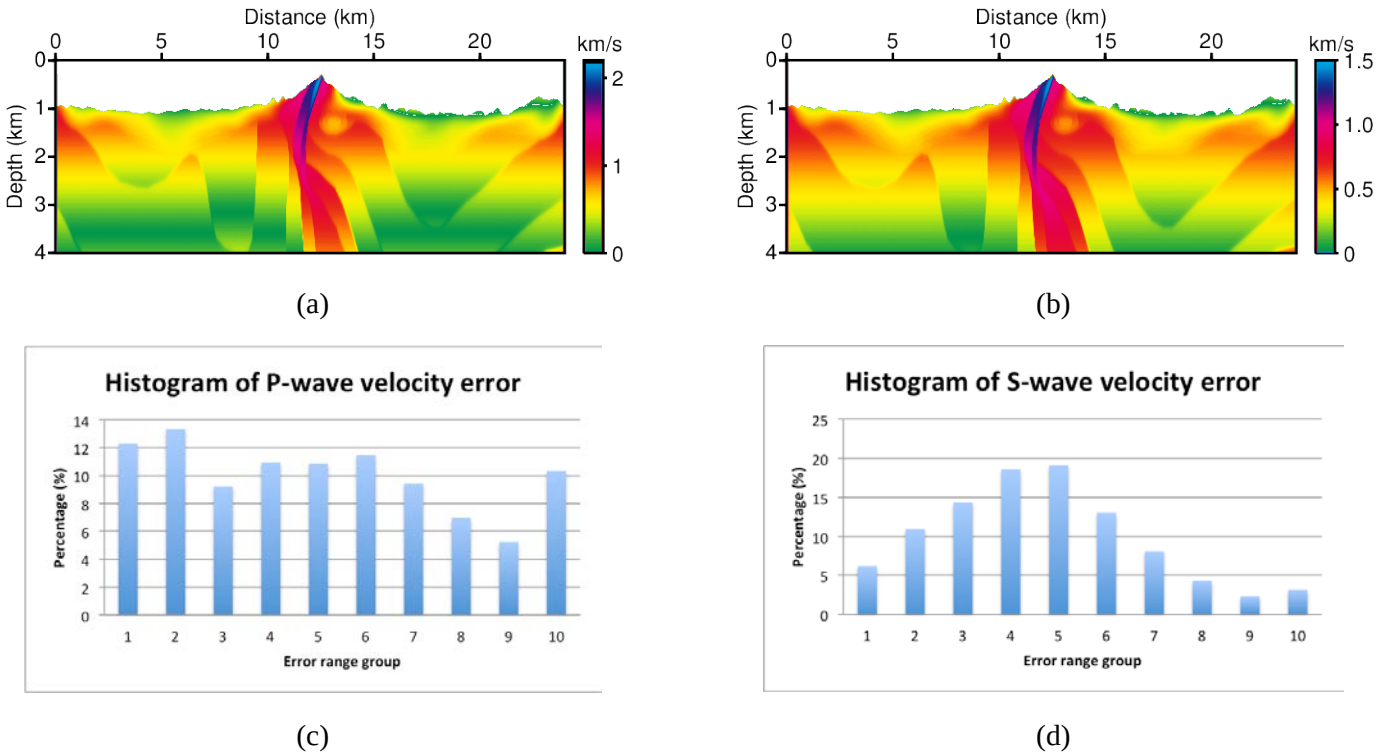

Figure 47. The residuals between true models and initial models: (a) P-wave and (b) S-wave velocity models. Histogram of the magnitude of the error: (c) P-wave and (d) S-wave velocity models. Error range groups defined as (1) 0.0 ~ 0.1, (2) 0.1 ~ 0.2, (3) 0.2 ~ 0.3, (4) 0.3 ~ 0.4, (5) 0.4 ~ 0.5, (6) 0.5 ~ 0.6, (7) 0.6 ~ 0.7, (8) 0.7 ~ 0.8, (9) 0.8 ~ 0.9, and (10) 0.9 ~ km/s.

However we believe that these discrepancies are related to the penetration depth and offset, not a problem of the algorithm. The P-wave velocity appears to have been more properly recovered than the S-wave inverted result. We guess that this difference may be attributable to the use of same step length for both lambda and mu, or the lack of information, the elastic inversion without horizontal observed data. We will study this problem further in the future.

The inverted velocity model could be confirmed with the error distributions in Figure 45c and 45d, the most of population of the residuals are located in group 1 (0.0 ~ 0.1 km/s) and group 2 (0.1 ~ 0.2 km/s).

Second, the Figure 49 and Figure 49b shows the residuals computed between true models and the inverted results obtained using the first high-pass-filtered dataset. The range of the P-wave velocity residuals is from 0.000000238 km/s to 0.904 km/s and the range of the S-wave velocity residuals is from 0.00000596 km/s to 0.786 km/s. The averages of the P-wave and S-wave velocity residuals are 0.142 km/s and 0.224 km/s, respectively. The error is increased compared with the first test results; however, the results still successfully recover the true velocities, even though dataset does not contain the low-frequency information below 3 Hz. The residual histograms in Figure 49 and Figure 49 also show that the inverted results are converged to the true velocities well, but the population of group 1 is decreased with comparison to the first result. In particular, the error at the surface is increased with respect to the first inverted results.

Finally, Figure 50 and Figure 50 show the residuals between the true models and the inverted results computed using the second high-pass-filtered dataset, which does not include the low-frequency data below 6 Hz. The residuals demonstrate that the developed algorithm was able to recover the true

models in the absence of low-frequency information to some degree; as shown in this test, the algorithm was successful at least in the absence of information below 6 Hz. The range of the P-wave velocity residuals is from 0.000000238 km/s to 1.034 km/s, and that of the S-wave velocity residuals is from 0.00000310 km/s to 0.739. The averages of the P-wave and the S-wave residuals are 0.169 km/s and 0.215 km/s, respectively. Figure 50 and Figure 50 show the distribution of the magnitude of the residuals.

In these tests, the developed algorithm was applied to the 3 datasets distinguished in term of the existence of low-frequency information to test the dependency on the low-frequency components. All inverted results generated reasonable inverted models regardless of the presence of low-frequency components. Summaries of the residuals and error distributions of these tests is presented in Table 9 and Table 10.

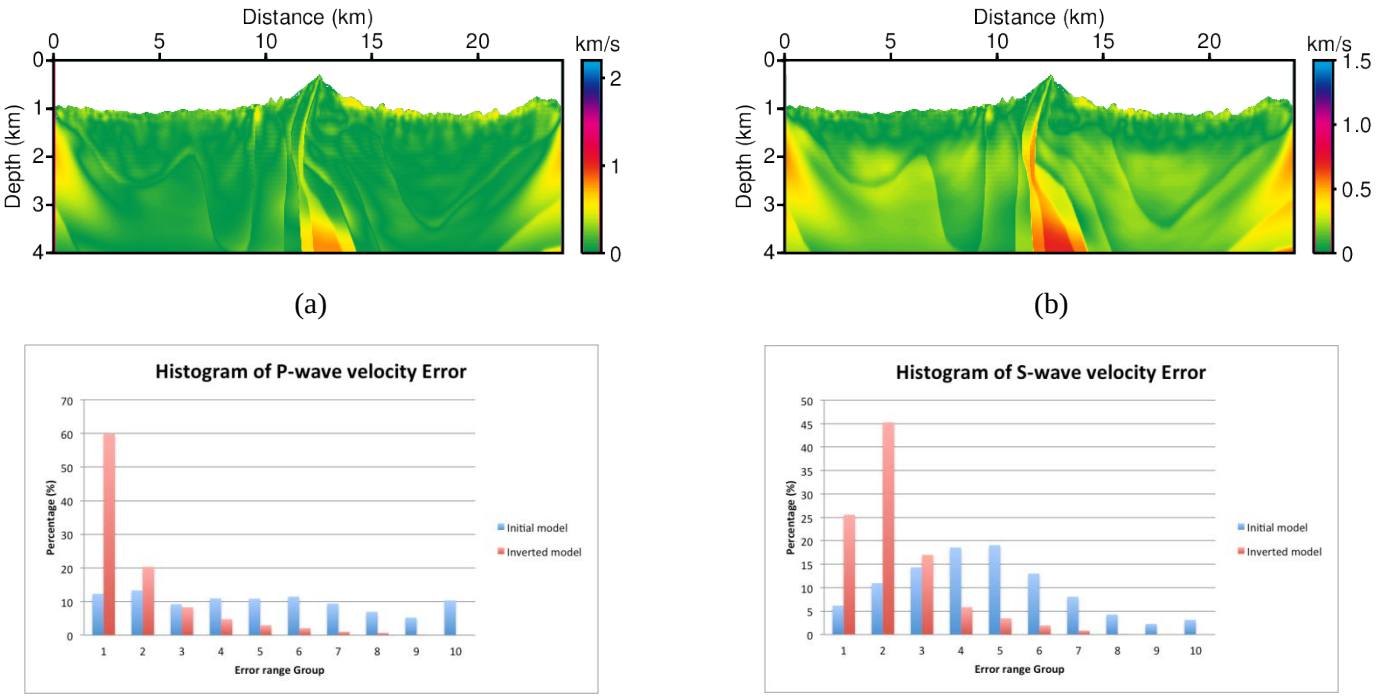

Figure 48. The residuals between the true models and the inverted models with low-frequency-containing dataset as shown in Figure 40: (a) P-wave and (b) S-wave velocity models. Histograms of the magnitude of the residuals of inverted (c) P-wave and (d) S-wave velocity models.

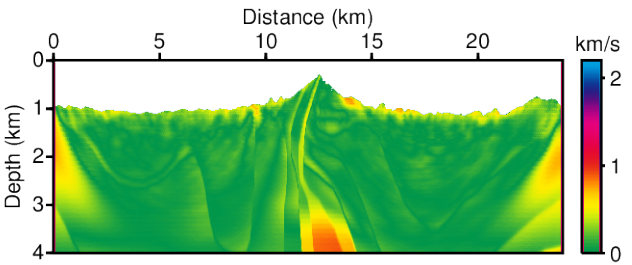

(a)

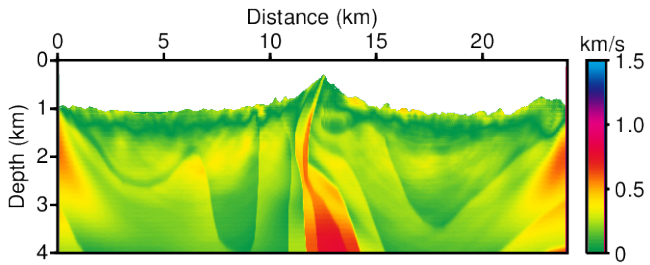

(b)

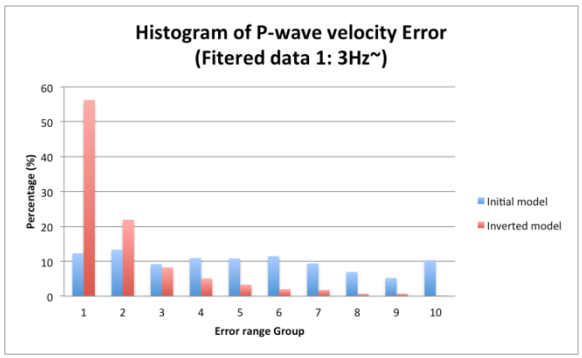

(c)

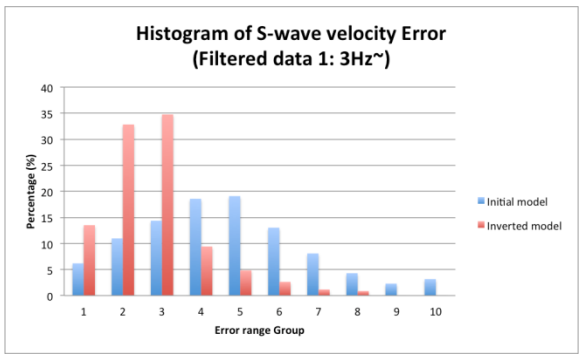

(d)

Figure 49. The residuals between the true models and the inverted models without low-frequency component dataset as shown in Figure 42 (3Hz~): (a) P-wave and (b) S-wave velocity models. Histograms of the magnitude of the residuals of inverted (c) P-wave and (d) S-wave velocity models.

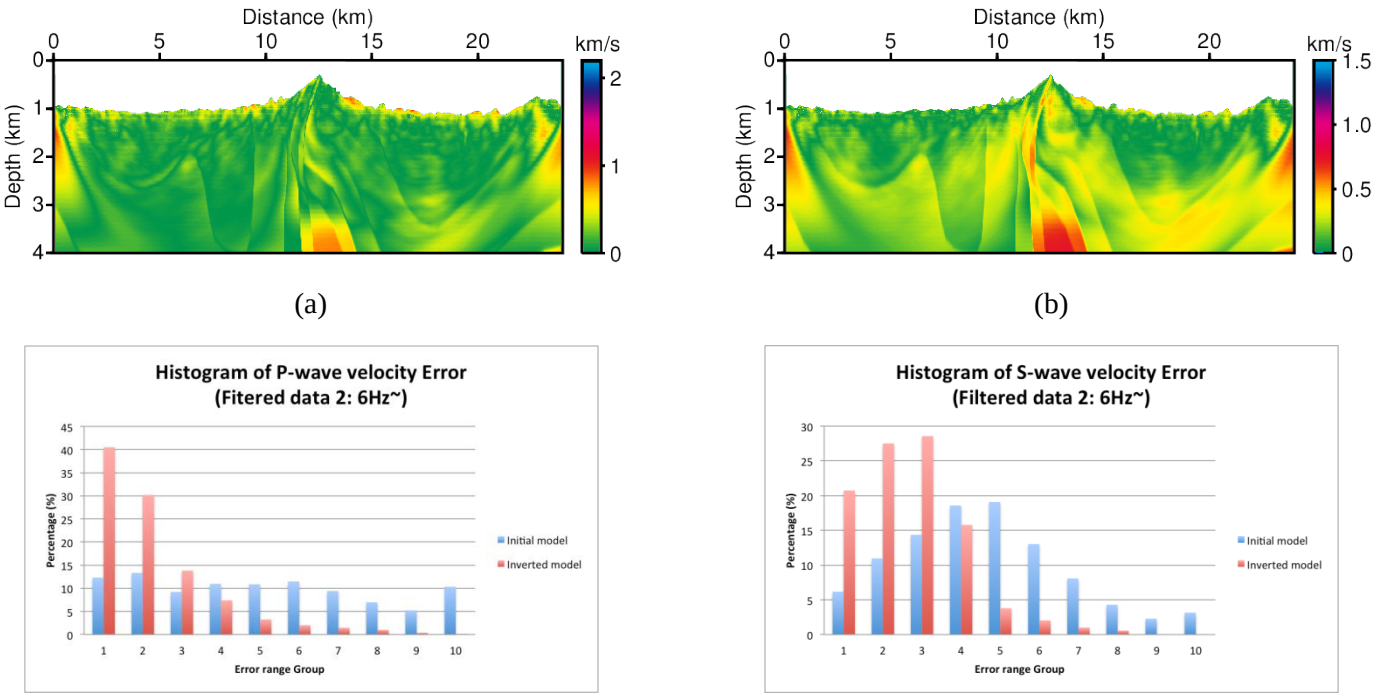

Figure 50. The residuals between the true models and the inverted models without low-frequency component dataset as shown in Figure 43 (6Hz~): (a) P-wave and (b) S-wave velocity models. Histograms of the magnitude of the residuals of inverted (c) P-wave and (d) S-wave velocity models.

The information of the residuals

	Range of P-wave residuals	Range of S-wave residuals	Average of P-wave residuals	Average of S-wave residuals
Initial model	0.000 ~ 2.143 km/s	0.000 ~ 1.460 km/s	0.47587389 km/s	0.41591409 km/s
Inverted model set 1	0.000 ~ 0.866 km/s	0.000 ~ 0.703 km/s	0.12953152 km/s	0.17582294 km/s
Inverted model set 2	0.000 ~ 0.904 km/s	0.000 ~ 0.786 km/s	0.14256380 km/s	0.22438702 km/s
Inverted model set 3	0.000 ~ 1.034 km/s	0.000 ~ 0.739 km/s	0.16885108 km/s	0.21513708 km/s

Table 9. The information of the velocity residuals computed with the true velocity models and initial models and inverted models. Inverted model set 1 denotes the inverted results with low frequency contains dataset, Inverted model set 2 denotes the inverted results with the 1st high pass filter applied dataset (contains: 3 Hz~), and Inverted model set 3 denotes the inverted results with the 2nd high pass filter applied dataset (contains: 6 Hz~).

Distribution of the magnitude of the residuals

	Initial model		Inverted model set 1		Inverted model set 2		Inverted model set 3	
Group	P-wave	S-wave	P-wave	S-wave	P-wave	S-wave	P-wave	S-wave
1	12.30 %	6.179 %	**59.87 %**	**25.56 %**	**56.23 %**	**13.51 %**	**40.48 %**	**20.74 %**
2	13.32 %	10.97 %	**20.33 %**	**45.28 %**	**21.96 %**	**32.83 %**	**30.17 %**	**27.51 %**
3	9.208 %	14.36 %	8.278 %	**17.00 %**	8.214 %	**34.75 %**	**13.82 %**	**28.56 %**
4	10.94 %	18.57 %	4.756%	5.856 %	5.073 %	9.415 %	7.388 %	**15.76 %**
5	10.85 %	19.08 %	2.949 %	3.468 %	3.314 %	4.834 %	3.250 %	3.794 %
6	11.47 %	13.02 %	2.091 %	1.941 %	2.021 %	2.630 %	2.008 %	2.037 %
7	9.405 %	8.081 %	1.032 %	0.869 %	1.818 %	1.163 %	1.460 %	1.007 %
8	6.959 %	4.293 %	0.687 %	0.025 %	0.691 %	0.868 %	1.012 %	0.576 %
9	5.228 %	2.287 %	0.001 %	-	0.710 %	-	0.373 %	-
10	10.32 %	3.158 %	-	-	0.002 %	-	0.005 %	-

Table 10. The distribution of the magnitude of the velocity residuals computed with the true velocity models and initial models and inverted models. Inverted model set 1 denotes the inverted results with low frequency contains dataset, Inverted model set 2 denotes the inverted results with the 1st high pass filter applied dataset (contains: 3 Hz~), and Inverted model set 3 denotes the inverted results with the 2nd high pass filter applied dataset (contains: 6 Hz~).

3.2.2 Inversion test with a noisy dataset

A real dataset always contains not only the seismic response but also noise from the environment of the acquisition site. The noise disturbs the recovery of the parameters of the subsurface via full-waveform inversion. Many researchers have made efforts to increase signal to noise ratio (SN ratio) to improve the quality of the result of seismic methods such as inversion and migration, and so on. Thus, the noise problem must be tested for the algorithm developed with the aim of the real data application.

2 types of noisy datasets were generated using the first high-pass-filtered dataset shown in Figure 42. The Gaussian white noise was added to the synthetic dataset with SN ratios of 100 and 50 in the time domain. Figure 51 show the generated noisy datasets and the plots shown in Figure 52 and Figure 53 show the trace of the noise-free dataset and the 2 types of noisy data recorded at the 400^{th} and 800^{th} receivers. The shot gather energy and SN rations were also presented in Figure 54 and they show that noise is heavily added at low-frequency range.

The developed algorithm was applied to these noisy datasets and the results of Laplace- and Laplace-Fourier-domain inversion are presented in Figure 55 and Figure 56 for each noisy dataset. In terms of clarity of the inverted image, the Laplace-inverted result seems to be less affected by noise than the Laplace-Fourier result, which exhibits many scattered irregularities in the recovered velocity.

I also computed the residuals and distribution of residuals as presented in Figure 57 and Figure 58 for the each case. From these residuals, it can be seen that the noise causes large discrepancies at the surface. However, the inverted

results are reasonable in the other regions, and the high-velocity structure in the center is defined successfully.

The detailed summary of residuals in Table 11 shows conspicuous increased range of the residuals with noisy dataset. Table 12 shows the histogram of the residual of inverted result. In these tables, the interesting point is that the S-wave inverted model with noise added dataset gives better average result than with noise free dataset. This enjoyable result can be assumed that it caused from the more large number of iteration than noise free test (Noise free: 122 iterations; SN ratio 100: 348 iterations; SN ratio 50: 262 iterations) and it requires the study about step lengths for multi parameter inversion.

The Laplace-Fourier inversion algorithm was tested with a noise-added dataset that, moreover, does not contain low-frequency information below 3 Hz. The computed results could not demonstrate that the algorithm is insensitive to the noise. However, the results show that the algorithm is capable of recovering promising initial parameters for Fourier inversion, even using noisy data.

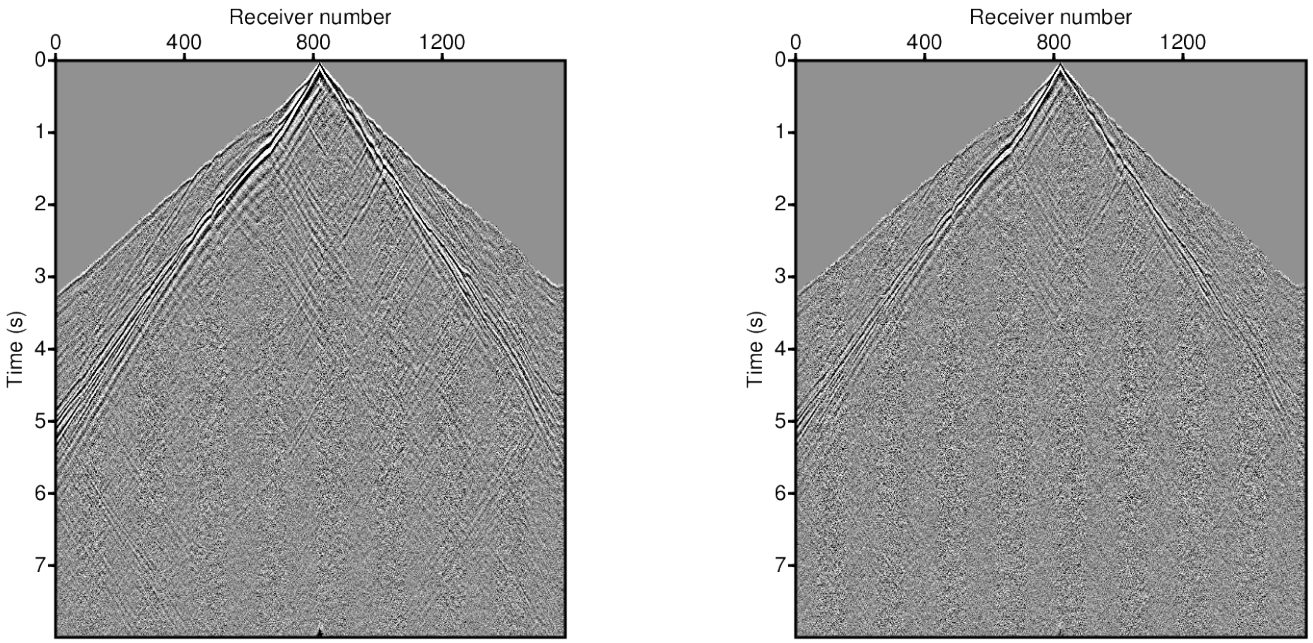

(a) (b)

Figure 51. Examples of the vertical displacement shot gather from the IPATI parameter set. (a) Contains the Gaussian white noise with intensity of SN ratio 100. (b) Contains the Gaussian white noise with intensity of SN ratio 50.

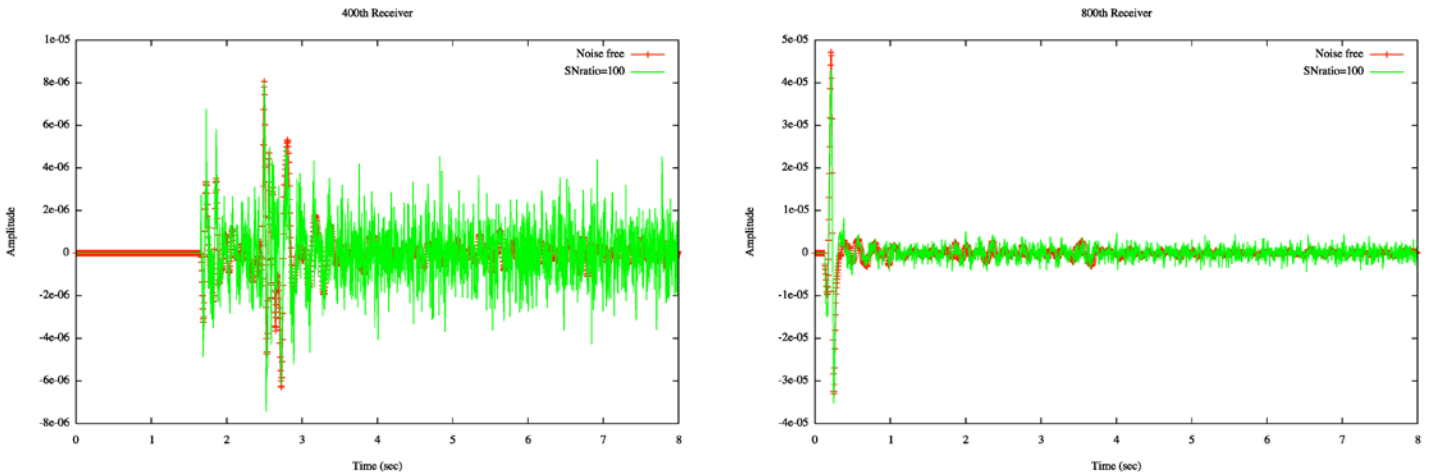

(a) (b)

Figure 52. The comparison of the traces between noise free shot gather and noise applied shot gather (SN ratio: 100) at the (a) 400th and (b) 800th receiver.

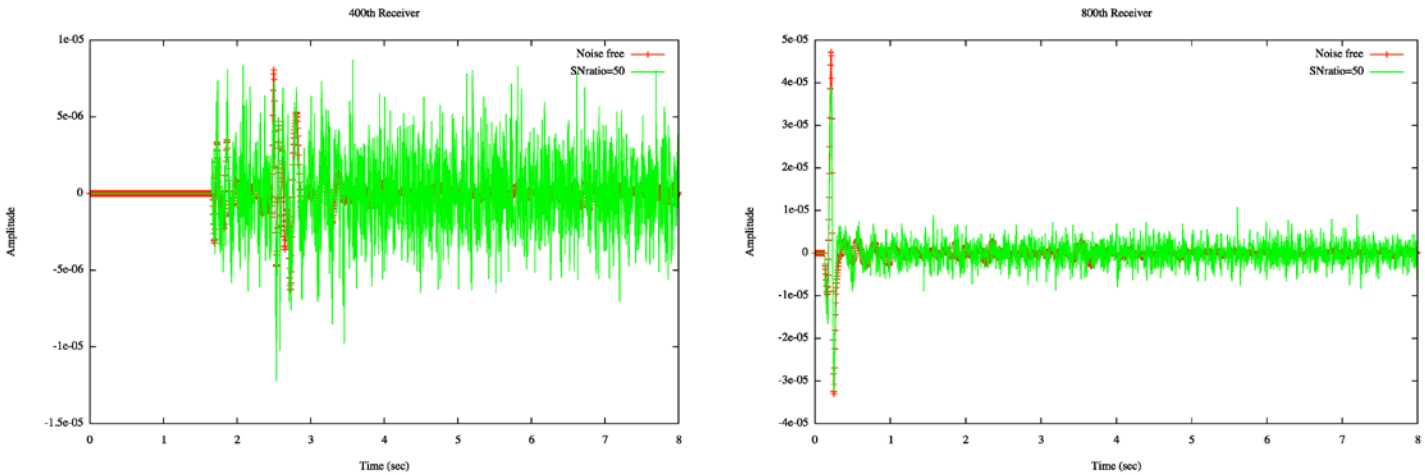

(a) (b)

Figure 53. The comparison of the traces between noise free shot gather and noise applied shot gather (SN ratio: 50) at the (a) 400th and (b) 800th receiver.

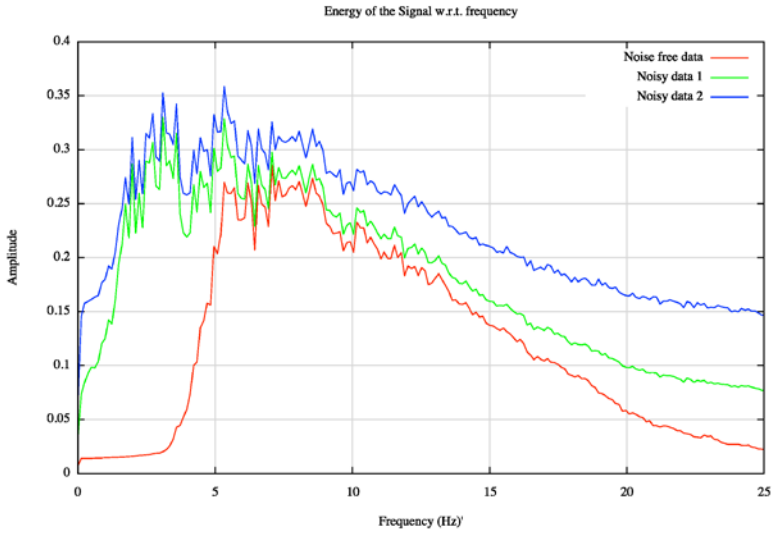

(a)

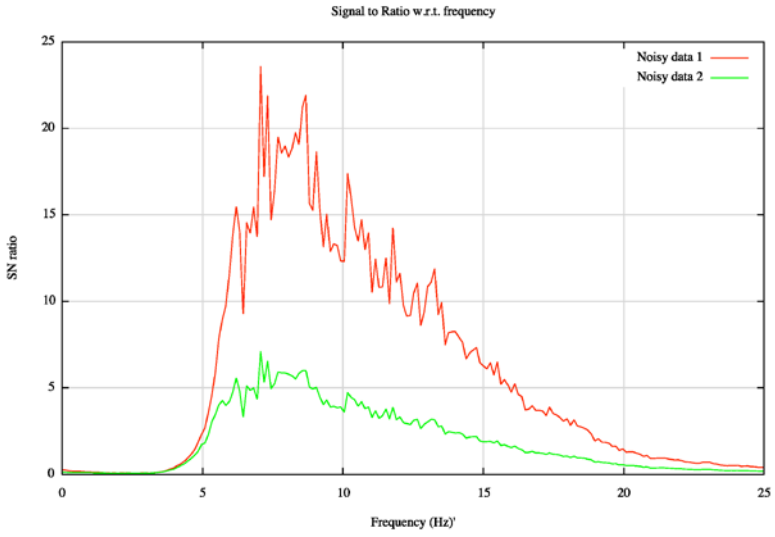

(b)

Figure 54. (a) The comparison of the energy of noise-free, noisy 1, and noisy 2 dataset shown in Figure 42, Figure 51, and Figure 51, with respect to the frequency. (b) SN ratios of noisy datasets with respect to the frequency.

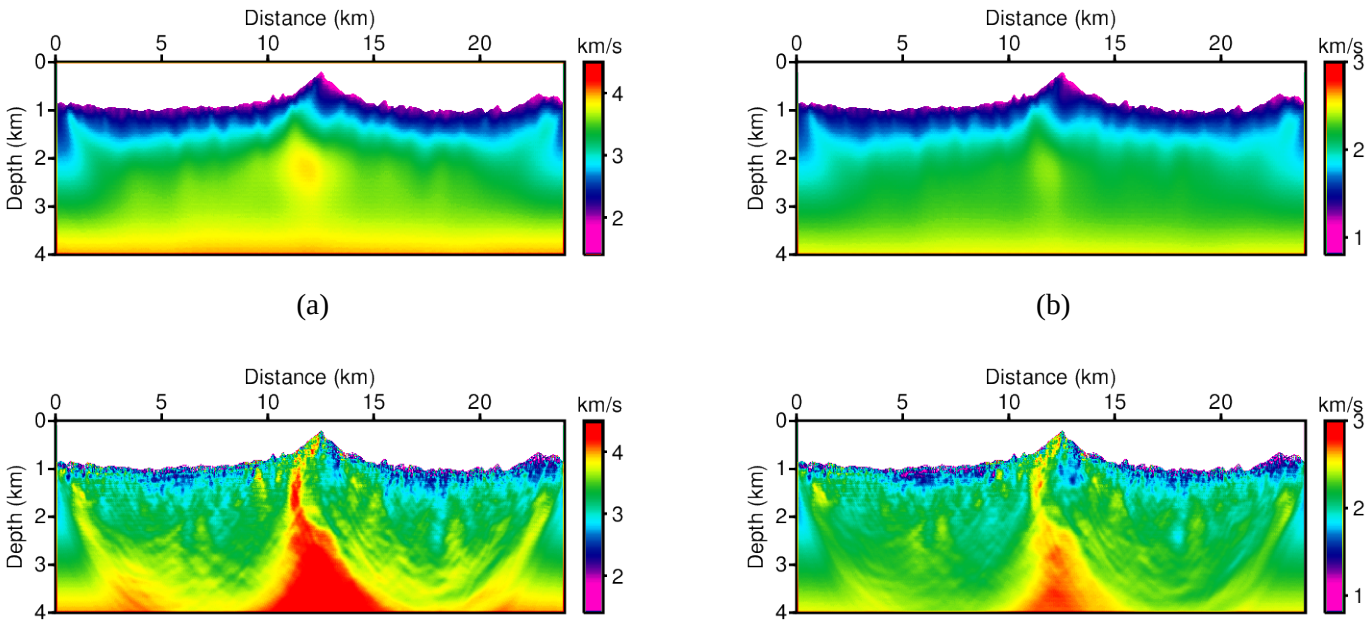

Figure 55. Inverted (a) P-wave and (b) S-wave velocity models obtained using Laplace-domain inversion with time domain IPATI dataset. Inverted (c) P-wave and (d) S-wave velocity models obtained using Laplace-Fourier-domain inversion with time domain IPATI dataset. The inversion results are obtained with the time domain dataset applied the 1st high-pass filter and the Gaussian white noise with intensity of SN ratio 100 as presented in Figure 51a.

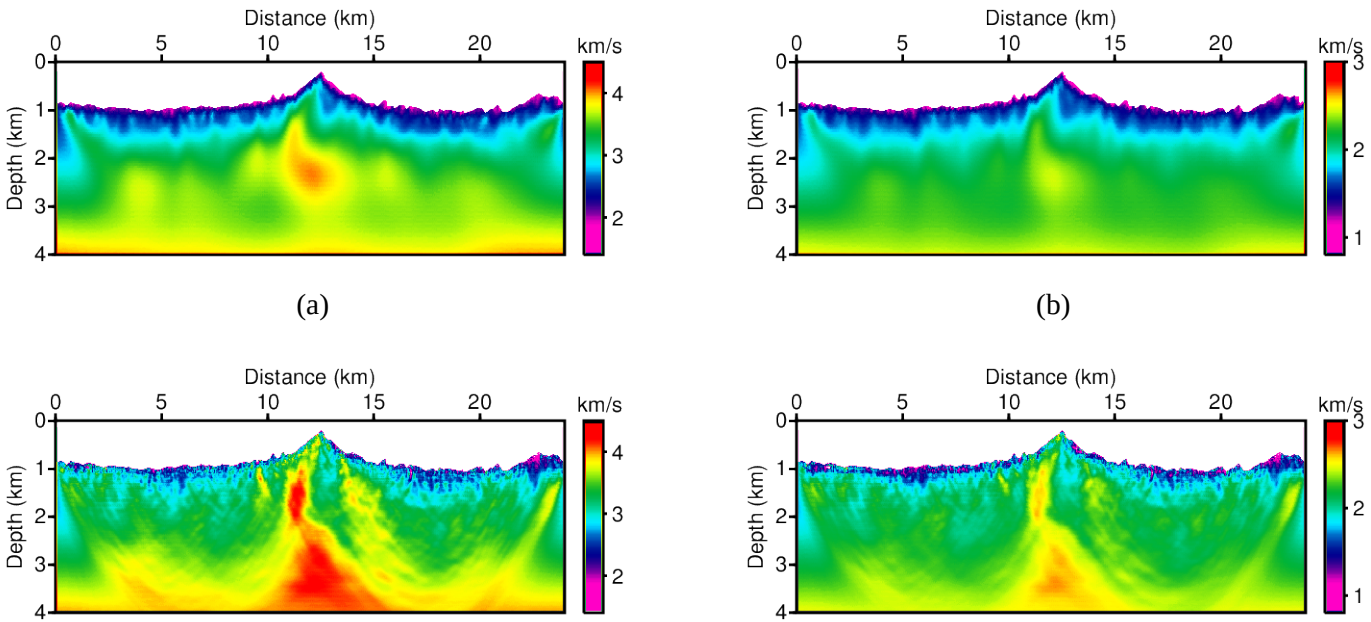

Figure 56. Inverted (a) P-wave and (b) S-wave velocity models obtained using Laplace-domain inversion with time domain IPATI dataset. Inverted (c) P-wave and (d) S-wave velocity models obtained using Laplace-Fourier-domain inversion with time domain IPATI dataset. The inversion results are obtained with the time domain dataset applied the 1st high-pass filter and the Gaussian white noise with intensity of SN ratio 50 as presented in Figure 51b.

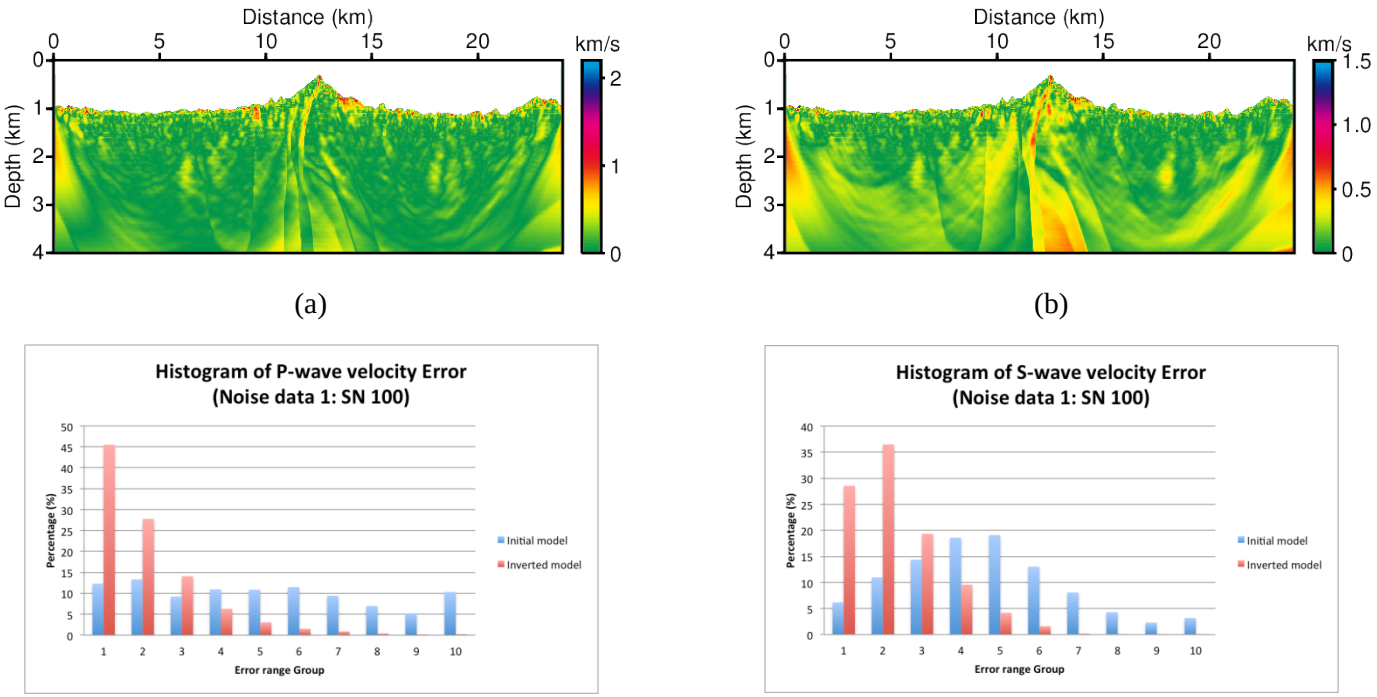

Figure 57. The residuals between true models and the inverted models with noise added dataset as shown in Figure 51a (SN ratio 100): (a) P-wave and (b) S-wave velocity models. Histogram of the magnitude of the residuals of inverted (c) P-wave and (d) S-wave velocity models.

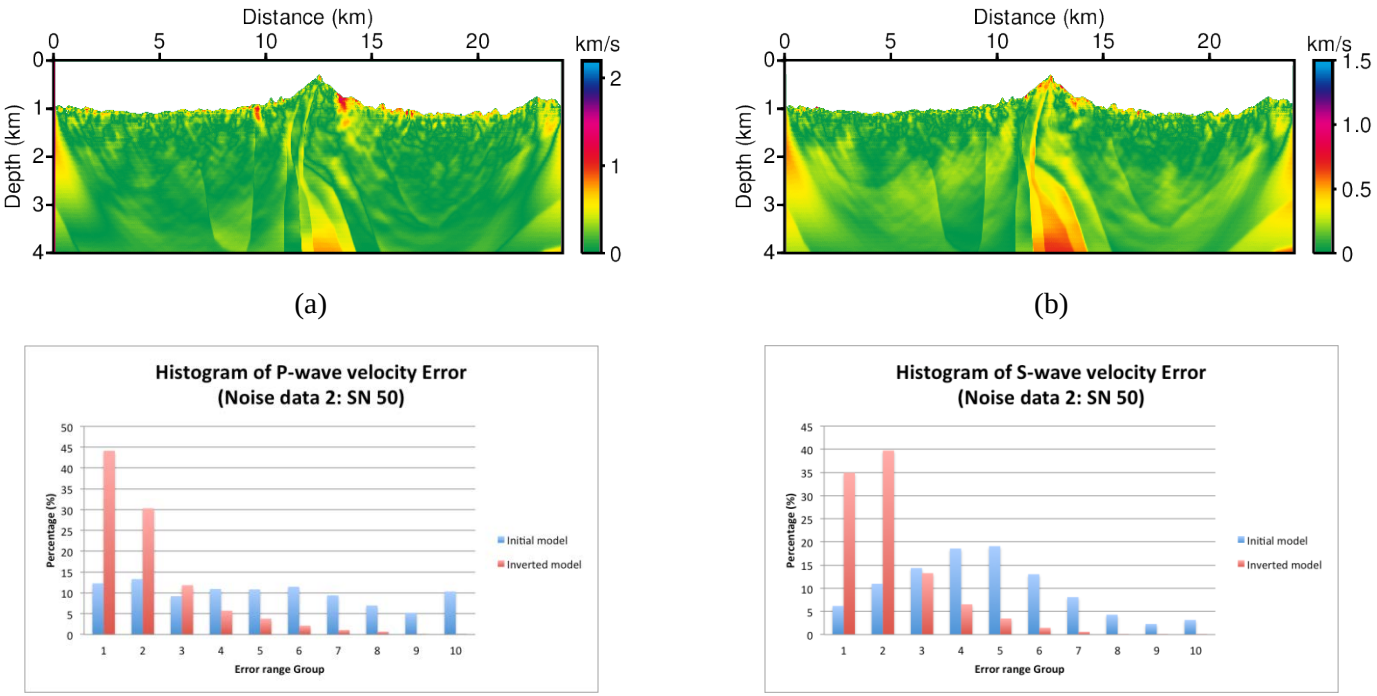

Figure 58. The residuals between true models and the inverted models with noise added dataset as shown in Figure 51b (SN ratio 50): (a) P-wave and (b) S-wave velocity models. Histogram of the magnitude of the residuals of inverted (c) P-wave and (d) S-wave velocity models.

The information of the residuals

	Range of P-wave residuals	Range of S-wave residuals	Average of P-wave residuals	Average of S-wave residuals
Initial model	0.000 ~ 2.143 km/s	0.000 ~ 1.460 km/s	0.47587389 km/s	0.41591409 km/s
Inverted model set 1	0.000 ~ 0.904 km/s	0.000 ~ 0.786 km/s	0.14256380 km/s	0.22438702 km/s
Inverted model set 2	0.000 ~ 1.962 km/s	0.000 ~ 1.330 km/s	0.15310143 km/s	0.17840558 km/s
Inverted model set 3	0.000 ~ 1.552 km/s	0.000 ~ 1.003 km/s	0.15749350 km/s	0.15841290 km/s

Table 11. The information of the velocity residuals computed with the true velocity models and initial models and inverted models. Inverted model set 1 denotes the inverted results with noise free dataset, Inverted model set 2 denotes the inverted results with the noise applied dataset 1 (SN ratio: 100), and Inverted model set 3 denotes the inverted results with the noise added dataset 2 (SN ratio: 50).

Distribution of the magnitude of the residuals

	Initial model		Inverted model set 1		Inverted model set 2		Inverted model set 3	
Group	P-wave	S-wave	P-wave	S-wave	P-wave	S-wave	P-wave	S-wave
1	12.30 %	6.179 %	**56.23 %**	**13.51 %**	**45.47 %**	**28.55 %**	**44.13 %**	**34.93 %**
2	13.32 %	10.97 %	**21.96 %**	**32.83 %**	**27.78 %**	**36.47 %**	**30.31 %**	**39.73 %**
3	9.208 %	14.36 %	8.214 %	**34.75 %**	**14.09 %**	**19.33 %**	**11.84 %**	**13.26 %**
4	10.94 %	18.57 %	5.073 %	9.415 %	6.315 %	9.575 %	5.737 %	6.532 %
5	10.85 %	19.08 %	3.314 %	4.834 %	3.063 %	4.180 %	3.800 %	3.468 %
6	11.47 %	13.02 %	2.021 %	2.630 %	1.539 %	1.613 %	2.112 %	1.458 %
7	9.405 %	8.081 %	1.818 %	1.163 %	0.891 %	0.201 %	1.087 %	0.605 %
8	6.959 %	4.293 %	0.691 %	0.868 %	0.414 %	0.042 %	0.687 %	0.015 %
9	5.228 %	2.287 %	0.710 %	-	0.179 %	0.023 %	0.127 %	0.007 %
10	10.32 %	3.158 %	0.002 %	-	0.250 %	0.024 %	0.169 %	0.005 %

Table 12. The distribution of the magnitude of the velocity residuals computed with the true velocity models and initial models and inverted models. Inverted model set 1 denotes the inverted results with noise free dataset, Inverted model set 2 denotes the inverted results with the noise applied dataset 1 (SN ratio: 100), and Inverted model set 3 denotes the inverted results with the noise added dataset 2 (SN ratio: 50).

3.2.3 Acoustic approach for an elastic dataset

The two different signals, especially at the later times can be made equal by applying a damped function with respect to time. Thus, the Laplace transform, the integral of the damped signal with respect to time, is able to ignore seismic signals to some degree. Ha et al., in 2010, applied the 2D acoustic Laplace-domain inversion algorithm to an elastic dataset with the expectation that the damping factor could reduce the differences between the wave propagation of the acoustic and elastic surface waves. Their approach recovered a reasonable velocity model for an elastic CCSS dataset (Zelt et al., 2005).

Their algorithm was applied to the 1st filtered synthetic dataset shown in Figure 39 to compare the inverted results obtaining using the elastic and acoustic approaches. For the inversion test, all inversion parameters and conditions were the same as those used for the elastic inversion, except hessian matrix. The acoustic inversion was performed with the acoustic pseudo-Hessian introduced by Ha et al., in 2012.

Figure 55 shows the inverted P-wave results obtained via Laplace- and Laplace-Fourier-domain inversion. The recovered velocity model by acoustic approach seems to agree well with the true P-wave velocity model in overall shape. Especially the Laplace-domain inverted result is not worse than elastic Laplace-domain inverted result.

However for the Laplace-Fourier-domain results, the elastic inverted P-wave velocity result presented in Figure 42c shows much more detailed subsurface structures than acoustic result shown in Figure 55b. From the residual in Figure 56a, we believe the surface wave disturbs to recover proper parameters in near surface region in the Laplace-Fourier domain. The detailed infor-

mation of residuals and its distribution of this test are presented in Table 11 and Table 12, respectively.

The results of this test demonstrate that although the acoustic approach can effectively compute the inverted velocity for land dataset, the elastic approach can yield superior results.

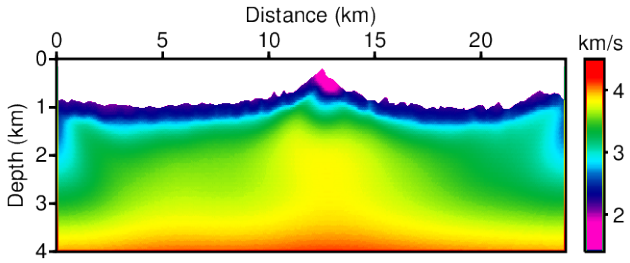

(a)

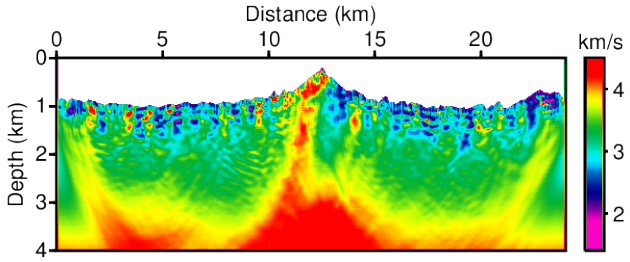

(b)

Figure 59. Inverted P-wave models via acoustic (a) Laplace-domain inversion and (b) Laplace-Fourier-domain inversion.

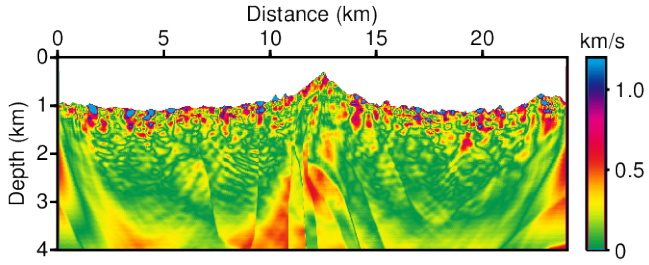

(a)

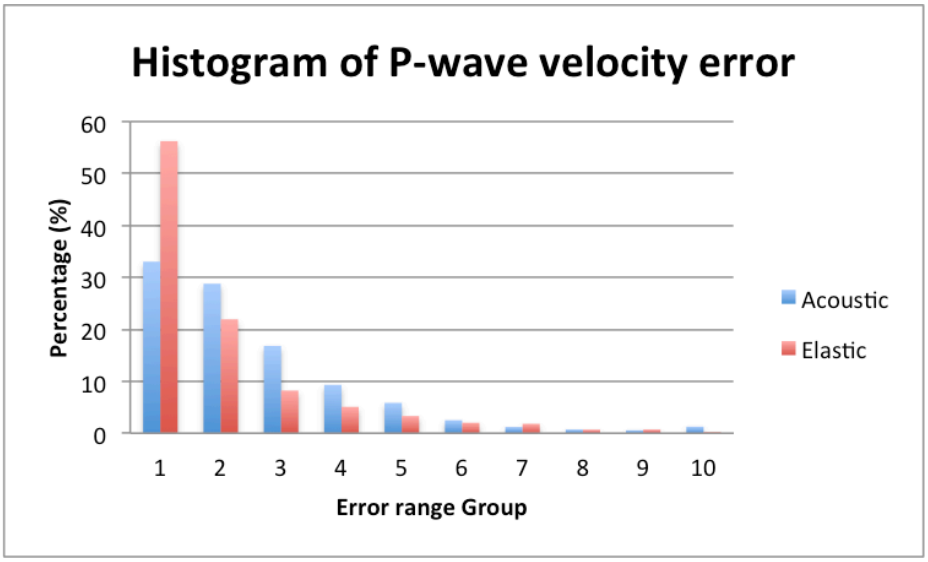

(b)

Figure 60. (a) The residuals between the true P-wave model and the inverted P-wave models via acoustic approach Laplace-Fourier-domain inversion shown in Figure 59b. (b) Histogram of the magnitude of the residuals of acoustic inverted and elastic inverted P-wave velocity models.

The information of the residuals (P-wave velocity)

	Range of P-wave residuals	Average of P-wave residuals
Initial model	0.000 ~ 2.143 km/s	0.47587389 km/s
Elastic inversion	0.000 ~ 0.904 km/s	0.14256380 km/s
Acoustic inversion	0.000 ~ 2.264 km/s	0.19696705 km/s

Table 13. The information of the P-wave velocity residuals computed with the true velocity model, initial model and inverted models with the elastic approach shown in Figure 45c and the acoustic approach shown in Figure 59b.

Distribution of the magnitude of the residuals (P-wave velocity)

Group	Initial model	Elastic inversion	Acoustic inversion
1	12.30 %	**56.23 %**	**33.02 %**
2	13.32 %	**21.96 %**	**28.77 %**
3	9.208 %	8.214 %	**16.82 %**
4	10.94 %	5.073 %	9.312 %
5	10.85 %	3.314 %	5.835 %
6	11.47 %	2.021 %	2.503 %
7	9.405 %	1.818 %	1.967 %
8	6.959 %	0.691 %	0.710 %
9	5.228 %	0.710 %	0.565 %
10	10.32 %	0.002 %	1.264 %

Table 14. The distribution of the magnitude of the P-wave velocity residuals computed with true P-wave velocity model and initial P-wave model and inverted models with the elastic and acoustic approaches.

Chapter 4. Conclusion

In this thesis, we introduced a 2D elastic Laplace-Fourier inversion algorithm on unstructured grids. The Laplace- and Laplace-Fourier-domain inversion methods have been studied with respect to their characteristics, limitations, and use for various media, such as acoustic, elastic, and acoustic-elastic coupled media, by many geophysicists (Shin et al., 2008; Shin el., 2009; Cha et al., 2010; Ha et al., 2010; Chung et al., 2010; Bae et al., 2010; Kim et al., 2013).

This study began with the simple extension from elastic Laplace-domain inversion to elastic Laplace-Fourier-domain inversion and the application of the unstructured grid. However, we encountered many problems, not those related to the choice of a structured or unstructured grid, but those originating from the complex-topography effect. For instance, for elastic Laplace-domain inversion with a flat surface it is possible to adopt the one-source assumption; thus, the source-estimation algorithm can be performed using a single source wavelet. However for an elastic inversion with complex topography, the source wavelets must be estimated independently for each shot because the different surface conditions encompassed by the topography lead to different source amplitudes and phases.

Moreover, irregular surface conditions make the regularized steepest-gradient direction more sensitive to damping factor in the flat surface case; thus, we were obliged to suggest a modified pseudo-Hessian matrix to address this issue. In this paper, it was derived using the difference in the definition of the pseudo-Hessian matrix based on the l_2 norm by Shin et al., 2001, and the

log norm by Ha et al., 2012.

In addition, the increased non-linearity in the signal caused by complex topography requires reasonable stopping criterion instead of the empirically determined number of iterations to guarantee accurate results. This type of multi-loop inversion is easy to yield an over- or underestimated velocity, depending on the number of iterations.

First, the stopping criterion based on the objective function was applied for the Laplace-Fourier-domain inversion. However, it was unable to obtain satisfactory results. Thus, the normalized stopping criterion was suggested based on studies of the characteristics of the logarithmic objective function (Shin et al, 2007; Bednar et al., 2007; Pyun et al., 2007). This stopping criterion was defined with the multi-objective assumption of real part amplitude error and imaginary part phase error, and it ensures the equal weighting of the influence of the two by assigning a normalized error to each. Numerical experiment successfully demonstrated the improvement in the results that was obtained using this approach. In this study, we imposed equal weighting for the phase and amplitude; however, we believe that an optimized weighting between the two exists that is a function of the frequency and Laplace damping constant and it will be studied in the future.

The developed algorithms are verified with synthetic and land dataset. For the time-domain synthetic test, 3 numerical tests was performed with different purposes, and the results demonstrated that the developed elastic Laplace-Fourier inversion algorithm is not entirely dependent to the low-frequency information, can recover an appropriate inversion result using a noisy dataset, and yields better results than the acoustic approach.

This research is a preliminary step in a promising line of investigation and

we plan to continuously improve this algorithm by applying it to many land datasets that represent many different conditions. In this study, we used only the vertical displacement as the observed but in the future, we wish to study elastic inversion using multi-component datasets and also for anisotropic media.

Appendix A. The 2D elastic wave simulation using interior penalty discontinuous Galerkin method in the time domain

The interior penalty discontinuous Galerkin finite element method (IPDG-FEM) is a type of FEM has been proven to yield accurate results using every type of mesh. This method relies on the exchange of numerical fluxes between adjacent elements. It is illustrated in Figure A.1. In contrast to classical FEMs, no continuity of a basis functions is imposed between elements, and therefore, the method supports discontinuities in the seismic wavefield between at the nodal points of two neighboring elements. Thus, this method does not suffer from spurious reflections, unlike classical FEMs, which generate unexpected reflection when applied to a changeable mesh.

Not only does the IPDG-FEM accommodate elements of various types and shapes, irregular non-matching grids, and even locally varying polynomial order, hence offering significant flexibility in mesh design, but it also produces block-diagonal mass matrices and therefore yields fully explicit, inherently parallel methods when coupled with explicit time stepping. The mass matrix that arises from a DG discretization is always block diagonal, with a block size equal to the number of degrees of freedom per element; hence, it can be computed at low computational cost without using the FEM lumping method (Marfurt, 1984).

The DG methods for the 2D elastic wave equation have been derived and applied by many geophysicists in recent years (Mercerat et al. 2006; Dumbser et al., 2006; Frey et al., 2008; Delcourte et al, 2009; Tago et al., 2012). Here, we derive the DG formulation from the 2^{nd}-order elastic equation, which dif-

fers from the 1st-order velocity-stress elastic equation that has previously been utilized.

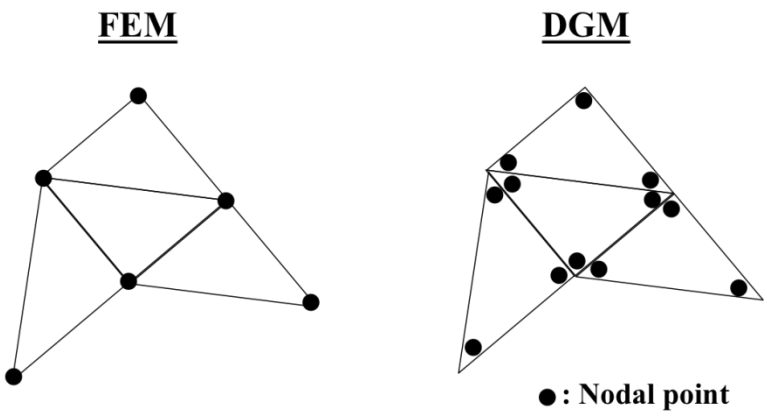

A 1. The comparison of the nodal point between FEM and DGM.

A.1 The notations

For a given domain Ω, we consider shape-irregular meshes Γ_h that partitions the domain Ω into disjointed triangular elements K, such that $\overline{\Omega} = \sum k$. $\overline{\Omega}$ is the domain for computation. k^- denotes neighboring elements of the element k^+. In addition, the following notation is used in this appendix.

- F_i represents the set of all interior edges, i.e., $F_i \coloneqq \partial K^+ \cap \partial K^-$;
- F_b represents the set of all boundary edges, i.e., $F_b \coloneqq \partial K^+ \cap \partial \overline{\Omega}$;
- F represents the set of all edges, i.e., $F \coloneqq F_i \cup F_b$;
- $\boldsymbol{n}^{\pm}$ denotes the unit normal vector of $K^{\pm}$;
- $[\![\ \ ]\!]$ is the jump function, i.e., $[\![\phi]\!] := \begin{cases} \phi^+\boldsymbol{n}^+ + \phi^-\boldsymbol{n}^- & f \in F_i \\ \phi\boldsymbol{n} & , f \in F_b \end{cases}$;
- $\{\{\ \ \}\}$ is the mean function, i.e., $\{\{\phi\}\} \coloneqq \begin{cases} (\phi^+ + \phi^-)/2 & f \in F_i \\ \phi & , f \in F_b \end{cases}$.

Where f denotes the edge at each element.

A.2 The IPDG formulation of the 2D elastic wave equation

The 2nd-order elastic wave equation in the time domain has already been presented in equations (2-2) to (2-6); however, for convenience in deriving the IPDG formulation from the beginning, we present it here again. Note that the notations used here are different from those used in the main article. The 2D elastic equation in the time domain can be expressed as

$$-\rho\frac{\partial^2}{\partial t^2}u = \frac{\partial}{\partial x}\sigma_{xx} + \frac{\partial}{\partial z}\sigma_{xz}, \tag{A.1}$$

$$-\rho\frac{\partial^2}{\partial t^2}v = \frac{\partial}{\partial x}\sigma_{zx} + \frac{\partial}{\partial z}\sigma_{zz}, \tag{A.2}$$

$$\sigma_{xx} = \lambda\Delta + 2\mu\varepsilon_{xx}, \tag{A.3}$$

$$\sigma_{zz} = \lambda\Delta + 2\mu\varepsilon_{zz},$$

$$\sigma_{xz} = \sigma_{zx} = \mu\varepsilon_{zx},$$

$$\Delta = \frac{\partial u}{\partial x} + \frac{\partial v}{\partial z}, \tag{A.4}$$

$$\varepsilon_{xx} = \frac{\partial u}{\partial x}, \tag{A.5}$$

$$\varepsilon_{zz} = \frac{\partial v}{\partial z},$$

$$\varepsilon_{zx}\frac{\partial v}{\partial x} + \frac{\partial u}{\partial z}.$$

Where u and v represent the horizontal displacement and vertical displacement, respectively. Equation (A.1) and (A.2) can be expressed using the Galerkin approximation as follows:

$$-\rho\frac{\partial^2}{\partial t^2}\int_{\bar{\Omega}}(u,\phi_x)d\bar{\Omega} = \int_{\bar{\Omega}}\left(\frac{\partial}{\partial x}\sigma_{xx},\phi_x\right)d\bar{\Omega} + \int_{\bar{\Omega}}\left(\frac{\partial}{\partial z}\sigma_{xz},\phi_x\right)d\bar{\Omega}, \tag{A.6}$$

$$-\rho\frac{\partial^2}{\partial t^2}\int_{\bar{\Omega}}(v,\phi_z)d\bar{\Omega} = \int_{\bar{\Omega}}\left(\frac{\partial}{\partial x}\sigma_{zx},\phi_z\right)d\bar{\Omega} + \int_{\bar{\Omega}}\left(\frac{\partial}{\partial z}\sigma_{zz},\phi_z\right)d\bar{\Omega}, \tag{A.7}$$

where (a,b) denotes the inner product of a and b. ϕ_x and ϕ_z are test functions for u and v, respectively.

The IPDG formulation for the horizontal displacement given by equation (A.6) will be presented in below, term by term. The 1st term on the right-hand side of it can be derived using Green's 1st identity and the jump and mean relations as follows:

$$\int_{\bar{\Omega}}\left(\frac{\partial}{\partial x}\sigma_{xx},\phi_x\right)d\bar{\Omega} \tag{A.8}$$

$$= \int_F(\sigma_{xx}\boldsymbol{n}_x,\phi_x)dF - \int_{\bar{\Omega}}\left(\sigma_{xx},\frac{\partial}{\partial x}\phi_x\right)d\bar{\Omega}$$

$$= \int_F\{\{\sigma_{xx}\}\}\cdot[\![\phi_x]\!] + [\![\sigma_{xx}]\!]\cdot\{\{\phi_x\}\}dF - \int_{\bar{\Omega}}\left(\sigma_{xx},\frac{\partial}{\partial x}\phi_x\right)d\bar{\Omega} + \gamma$$

(Because of $\sigma_{xx}\boldsymbol{n}_x$ is continuous; $[\![\sigma_{xx}]\!]$ is zero)

$$= \int_F\{\{\sigma_{xx}\}\}\cdot[\![\phi_x]\!]dF - \int_{\bar{\Omega}}\left(\sigma_{xx},\frac{\partial}{\partial x}\phi_x\right)d\bar{\Omega} + \gamma$$

$$= \int_F \frac{1}{2}(\sigma_{xx}{}^{+} + \sigma_{xx}{}^{-}) \cdot \left(\phi_x{}^{+}\boldsymbol{n}_x{}^{+} + \phi_x{}^{-}\boldsymbol{n}_x{}^{-}\right) dF - \int_{\bar{\Omega}} \left(\sigma_{xx}, \frac{\partial}{\partial x}\phi_x\right) d\bar{\Omega}$$

$$+\gamma.$$

Where, F is all edges. γ is the interior penalty constant and it will be defined later. The stress term in equation (A.8) can be replaced by the relationship expressed by equation (A.3). Then, equation (A.8) can be rewritten as follows,

$$\int_{\bar{\Omega}} \left(\frac{\partial}{\partial x}\sigma_{xx}, \phi_x\right) d\bar{\Omega} \tag{A.9}$$

$$= \int_F \frac{1}{2}\left(\lambda^{+}\Delta^{+} + 2\mu^{+}\frac{\partial u^{+}}{\partial x} + \lambda^{-}\Delta^{-} + 2\mu^{-}\frac{\partial u^{-}}{\partial x}\right) \cdot \left(\phi_x{}^{+}\boldsymbol{n}_x{}^{+} + \phi_x{}^{-}\boldsymbol{n}_x{}^{-}\right) dF$$

$$- \int_{\bar{\Omega}} \left(\lambda\Delta + 2\mu\frac{\partial u}{\partial x}, \frac{\partial}{\partial x}\phi_x\right) d\bar{\Omega} \; + \gamma$$

Similarly, the 2nd term on the right-hand side of equation (A.6) can be written as

$$\int_{\bar{\Omega}} \left(\frac{\partial}{\partial z}\sigma_{xz}, \phi_x\right) d\bar{\Omega} \tag{A.10}$$

$$= \int_F \frac{1}{2}\left(\mu^{+}\frac{\partial u^{+}}{\partial z} + \mu^{+}\frac{\partial v^{+}}{\partial x} + \mu^{-}\frac{\partial u^{-}}{\partial z} + \mu^{-}\frac{\partial v^{-}}{\partial x}\right) \cdot \left(\phi_x{}^{+}\boldsymbol{n}_z{}^{+} + \phi_x{}^{-}\boldsymbol{n}_z{}^{-}\right) dF$$

$$- \int_{\bar{\Omega}} \left(\mu\frac{\partial u}{\partial z} + \mu\frac{\partial v}{\partial x}, \frac{\partial}{\partial z}\phi_x\right) d\bar{\Omega} \; + \gamma$$

Thus, the horizontal displacement equation (A.6) can be transformed into equation (A.11), which does not contain the stress term, using equations (A.9) and (A.10).

$$-\rho\frac{\partial^2}{\partial t^2}\int_{\bar{\Omega}}(u,\phi_x)d\bar{\Omega} \tag{A.11}$$

$$=-\int_{\bar{\Omega}}\left(\lambda\Delta+2\mu\frac{\partial u}{\partial x},\frac{\partial}{\partial x}\phi_x\right)d\bar{\Omega}-\int_{\bar{\Omega}}\left(\mu\frac{\partial u}{\partial z}+\mu\frac{\partial v}{\partial x},\frac{\partial}{\partial z}\phi_x\right)d\bar{\Omega}$$

$$+\int_F\frac{1}{2}\left(\lambda^+\Delta^++2\mu^+\frac{\partial u^+}{\partial x}+\lambda^-\Delta^-+2\mu^-\frac{\partial u^-}{\partial x}\right)\cdot\left({\phi_x}^+\boldsymbol{n}_x{}^++{\phi_x}^-\boldsymbol{n}_x{}^-\right)dF$$

$$+\int_F\frac{1}{2}\left(\mu^+\frac{\partial u^+}{\partial z}+\mu^+\frac{\partial v^+}{\partial x}+\mu^-\frac{\partial u^-}{\partial z}+\mu^-\frac{\partial v^-}{\partial x}\right)\cdot\left({\phi_x}^+\boldsymbol{n}_z{}^++{\phi_x}^-\boldsymbol{n}_z{}^-\right)dF$$

$$+\gamma.$$

The vertical displacement equation can be rewritten as equation (A.12) using the same procedure.

$$-\rho\frac{\partial^2}{\partial t^2}\int_{\bar{\Omega}}(v,\phi_z)d\bar{\Omega} \tag{A.12}$$

$$=-\int_{\bar{\Omega}}\left(\lambda\Delta+2\mu\frac{\partial v}{\partial z},\frac{\partial}{\partial z}\phi_z\right)d\bar{\Omega}-\int_{\bar{\Omega}}\left(\mu\frac{\partial v}{\partial x}+\mu\frac{\partial u}{\partial z},\frac{\partial}{\partial x}\phi_z\right)d\bar{\Omega}$$

$$+\int_F\frac{1}{2}\left(\lambda^+\Delta^++2\mu^+\frac{\partial v^+}{\partial z}+\lambda^-\Delta^-+2\mu^-\frac{\partial v^-}{\partial z}\right)\cdot\left({\phi_z}^+\boldsymbol{n}_z{}^++{\phi_z}^-\boldsymbol{n}_z{}^-\right)dF$$

$$+\int_F\frac{1}{2}\left(\mu^+\frac{\partial v^+}{\partial x}+\mu^+\frac{\partial u^+}{\partial z}+\mu^-\frac{\partial v^-}{\partial x}+\mu^-\frac{\partial u^-}{\partial z}\right)\cdot\left({\phi_z}^+\boldsymbol{n}_x{}^++{\phi_z}^-\boldsymbol{n}_x{}^-\right)dF$$

$$+\gamma.$$

The 2nd order elastic wave equation can be expressed as a system of equations by considering the source term.

$$-\rho\frac{\partial^2}{\partial t^2}\mathbf{Ma}=\mathbf{Ka}+\mathbf{f}, \tag{A.13}$$

where **M** is the mass matrix; **a** is the displacement vector, which contains both horizontal and vertical components; **K** is the stiffness matrix; and **f** is the source vector.

$$\mathbf{M} = \begin{pmatrix} m_{11} & 0 \\ 0 & m_{22} \end{pmatrix}, \tag{A.14}$$

$$m_{11} = m_{22} = \sum_{K} \int_{k} \phi_I \phi_J d\,k, \tag{A.15}$$

$$\mathbf{a} = \begin{pmatrix} \boldsymbol{u} \\ \boldsymbol{v} \end{pmatrix}, \tag{A.16}$$

$$\mathbf{K} = \begin{pmatrix} k_{11} & k_{12} \\ k_{21} & k_{22} \end{pmatrix}. \tag{A.17}$$

The components of the stiffness matrix k_{11}, k_{12}, k_{21}, and k_{22} can be derived from the relations expressed in equations (A.11) and (A.12).

$$\begin{aligned} k_{11} = \sum_{K} \Bigg[& -\int_{k} (\lambda_k + 2\mu_k) \frac{\partial \phi_i}{\partial x} \frac{\partial \phi_j}{\partial x} dk - \int_{k} \mu_k \frac{\partial \phi_i}{\partial z} \frac{\partial \phi_j}{\partial z} dk \\ & + \sum_{F \in \partial k} \int_{f} \frac{1}{2} \left(\left(\lambda_k{}^{+} + 2\mu_k{}^{+}\right) \frac{\partial \phi_i{}^{+}}{\partial x} \phi_j{}^{+} \boldsymbol{n}_x{}^{+} + \left(\lambda_k{}^{-} + 2\mu_k{}^{-}\right) \frac{\partial \phi_i{}^{-}}{\partial x} \phi_j{}^{+} \boldsymbol{n}_x{}^{+} \right) df \\ & + \sum_{F \in \partial k} \int_{f} \frac{1}{2} \left(\mu_k{}^{+} \frac{\partial \phi_i{}^{+}}{\partial z} \phi_j{}^{+} \boldsymbol{n}_z{}^{+} + \mu_k{}^{-} \frac{\partial \phi_i{}^{-}}{\partial z} \phi_j{}^{+} \boldsymbol{n}_z{}^{+} \right) df \\ & + \sum_{F \in \partial k} \int_{f} \gamma_f \left(\phi_i{}^{+} \boldsymbol{n}^{+} \phi_j{}^{+} \boldsymbol{n}^{+} + \phi_i{}^{-} \boldsymbol{n}^{-} \phi_j{}^{+} \boldsymbol{n}^{+} \right) df \Bigg], \end{aligned} \tag{A.18}$$

(A.19)

$$k_{12} = \sum_K \left[-\int_k \lambda_k \frac{\partial \phi_i}{\partial z}\frac{\partial \phi_j}{\partial x} dk - \int_k \mu_k \frac{\partial \phi_i}{\partial x}\frac{\partial \phi_j}{\partial z} dk \right.$$

$$+ \sum_{F\in\partial k} \int_f \frac{1}{2}\left({\lambda_k}^+ \frac{\partial {\phi_i}^+}{\partial z} {\phi_j}^+ {\boldsymbol{n}_x}^+ + {\lambda_k}^- \frac{\partial {\phi_i}^-}{\partial z} {\phi_j}^+ {\boldsymbol{n}_x}^+ \right) df$$

$$\left. + \sum_{F\in\partial k} \int_f \frac{1}{2}\left({\mu_k}^+ \frac{\partial {\phi_i}^+}{\partial x} {\phi_j}^+ {\boldsymbol{n}_z}^+ + {\mu_k}^- \frac{\partial {\phi_i}^-}{\partial x} {\phi_j}^+ {\boldsymbol{n}_z}^+ \right) df, \right.$$

(A.20)

$$k_{21} = \sum_K \left[-\int_k \lambda_k \frac{\partial \phi_i}{\partial x}\frac{\partial \phi_j}{\partial z} dk - \int_k \mu_k \frac{\partial \phi_i}{\partial z}\frac{\partial \phi_j}{\partial x} dk \right.$$

$$+ \sum_{F\in\partial k} \int_f \frac{1}{2}\left({\lambda_k}^+ \frac{\partial {\phi_i}^+}{\partial x} {\phi_j}^+ {\boldsymbol{n}_z}^+ + {\lambda_k}^- \frac{\partial {\phi_i}^-}{\partial x} {\phi_j}^+ {\boldsymbol{n}_z}^+ \right) df$$

$$\left. + \sum_{F\in\partial k} \int_f \frac{1}{2}\left({\mu_k}^+ \frac{\partial {\phi_i}^+}{\partial z} {\phi_j}^+ {\boldsymbol{n}_x}^+ + {\mu_k}^- \frac{\partial {\phi_i}^-}{\partial z} {\phi_j}^+ {\boldsymbol{n}_x}^+ \right) df, \right.$$

(A.21)

$$k_{22} = \sum_K \left[-\int_k (\lambda_k + 2\mu_k) \frac{\partial \phi_i}{\partial z}\frac{\partial \phi_j}{\partial z} dk - \int_k \mu_k \frac{\partial \phi_i}{\partial x}\frac{\partial \phi_j}{\partial x} dk \right.$$

$$+ \sum_{F\in\partial k} \int_f \frac{1}{2}\left(\left({\lambda_k}^+ + 2{\mu_k}^+ \right) \frac{\partial {\phi_i}^+}{\partial z} {\phi_j}^+ {\boldsymbol{n}_z}^+ \right.$$

$$\left. \left. + \left({\lambda_k}^- + 2{\mu_k}^- \right) \frac{\partial {\phi_i}^-}{\partial z} {\phi_j}^+ {\boldsymbol{n}_z}^+ \right) df \right.$$

$$+ \sum_{F\in\partial k} \int_f \frac{1}{2}\left({\mu_k}^+ \frac{\partial {\phi_i}^+}{\partial x} {\phi_j}^+ {\boldsymbol{n}_x}^+ + {\mu_k}^- \frac{\partial {\phi_i}^-}{\partial x} {\phi_j}^+ {\boldsymbol{n}_x}^+ \right) df$$

$$+\sum_{F\in\partial k}\int_{f}\gamma_f\left(\phi_i{}^{+}\boldsymbol{n}^{+}\phi_j{}^{+}\boldsymbol{n}^{+}+\phi_i{}^{-}\boldsymbol{n}^{-}\phi_j{}^{+}\boldsymbol{n}^{+}\right)df\Bigg],$$

where the γ_f is the interior penalty constant for stabilization and it is defined on each edge of the element as (Baldassari, 2009)

$$\gamma_f = ac_{max}h_{min}, \tag{A.22}$$

$$a = \frac{1}{2}l(l+1), \tag{A.23}$$

$$c_{max} = \begin{cases} max(c_{k^+}, c_{k^-}) & f \in F_i \\ c_k & f \in F_b \end{cases}, \tag{A.24}$$

$$h_{min} = \begin{cases} min(h_{k^+}, h_{k^-}) & f \in F_i \\ h_k & f \in F_b \end{cases}, \tag{A.25}$$

Finally, the IPDG formulation of the 2D elastic wave equation can be presented as in equation (A.26) via the central FDM scheme for a 2nd-derivative displacement vector with respect to time.

$$\mathbf{a}^{i+1} = 2\mathbf{a}^{i} - \mathbf{a}^{i-1} - \mathbf{M}^{-1}\frac{(dt)^2}{\rho}\left(\mathbf{K}\mathbf{a}^{i} + \mathbf{f}\right), \tag{A.26}$$

where, i is the number of discrete time samples with the interval dt.

Figure A 2 presents the modeling results computed using the parameters shown in Figure 8, 9 and the time-domain IPDG scheme, and it shows the horizontal and vertical displacement after 1 sec.

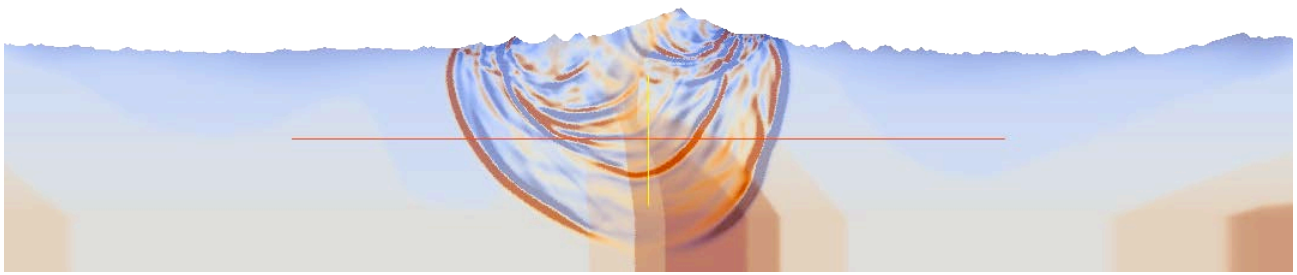

(a)

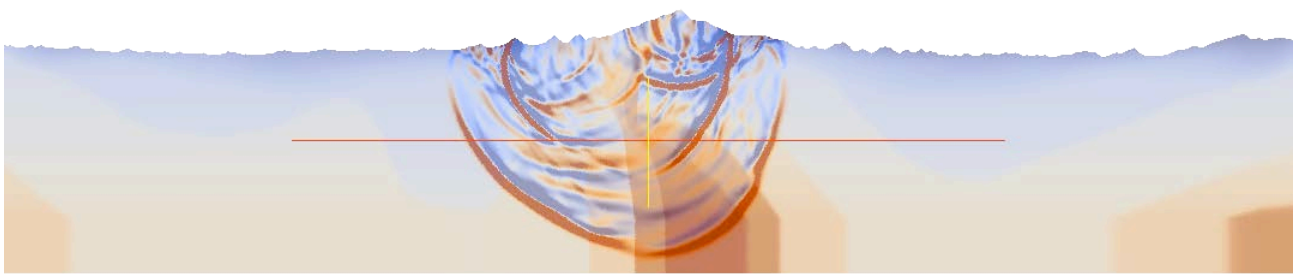

(b)

A 2. Snap shots after 1sec of the (a) horizontal and (b) vertical displacements obtained using IPDG method.

REFERENCES

Bae, Ho Seuk, Sukjoon Pyun, Wookeen Chung, Seung-Goo Kang, and Changsoo Shin. "Frequency-domain acoustic-elastic coupled waveform inversion using the Gauss-Newton conjugate gradient method." Geophysical Prospecting 60, no. 3 (2012): 413-432.

Baeten, Guido, Jan Willem de Maag, René-Edouard Plessix, Rini Klaassen, Tahira Qureshi, Maren Kleemeyer, Fons ten Kroode, and Zhang Rujie. "The use of low frequencies in a full-waveform inversion and impedance inversion land seismic case study." Geophysical Prospecting (2013).

Baldassari, Caroline. "Modélisation et simulation numérique pour la migration terrestre par équation d'ondes." PhD diss., Université de Pau et des Pays de l'Adour, 2009.

Bleibinhaus, Florian, and Stéphane Rondenay. "Effects of surface scattering in full-waveform inversion." Geophysics 74, no. 6 (2009): WCC69-WCC77.

Brenders, A. J., and R. G. Pratt. "Full waveform tomography for lithospheric imaging: results from a blind test in a realistic crustal model." Geophysical Journal International 168, no. 1 (2007): 133-151.

Brossier, Romain. "Imagerie sismique à deux dimensions des milieux visco-élastiques par inversion des formes d'ondes: développements méthodologiques et applications." PhD diss., Université de Nice Sophia-Antipolis, 2009.

Brossier, Romain. "Two-dimensional frequency-domain visco-elastic full waveform inversion: Parallel algorithms, optimization and performance." Computers & Geosciences 37, no. 4 (2011): 444-455.

Bunks, Carey, Fatimetou M. Saleck, S. Zaleski, and G. Chavent. "Multiscale seismic waveform inversion." Geophysics 60, no. 5 (1995): 1457-1473.

Cha, Young Ho, and Changsoo Shin. "Two-dimensional Laplace-domain waveform inversion using adaptive meshes: an experience of the 2004 BP velocity-analysis benchmark data set." Geophysical Journal International 182, no. 2 (2010): 865-879.

Chung, Wookeen, Changsoo Shin, and Sukjoon Pyun. "2D elastic waveform inversion in the Laplace domain." Bulletin of the Seismological Society of America 100, no. 6 (2010): 3239-3249.

Cohen, Gary. Higher-order numerical methods for transient wave equations. Springer, 2002.

Delcourte, Sarah, and Nathalie Glinsky. "ANALYSIS OF A DISCONTINUOUS GALERKIN METHOD FOR ELASTODYNAMIC EQUATIONS. APPLICATION TO 3D WAVE PROPAGATION." (2013).

Dumbser, Michael, and Martin Käser. "An arbitrary high-order discontinuous Galerkin method for elastic waves on unstructured meshes–II. The three-dimensional isotropic case." Geophysical Journal International 167, no. 1 (2006): 319-336.

Gélis, Céline, Jean Virieux, and Gilles Grandjean. "Two-dimensional elastic full waveform inversion using Born and Rytov formulations in the frequency domain." Geophysical Journal International 168, no. 2 (2007): 605-633.

Wansoo Ha, Wookeen Chung, and Changsoo Shin. “Pseudo-Hessian matrix for the logarithmic objective function in full wave inversion.”Journal of Seismic Exploration, vol.21, no.3, (2012) 201-214

Ha, Wansoo, Sukjoon Pyun, Jewoo Yoo, and Changsoo Shin. "Acoustic full waveform inversion of synthetic land and marine data in the Laplace domain." Geophysical Prospecting 58, no. 6 (2010): 1033-1048.

Jeong, Woodon, Ho-Yong Lee, and Dong-Joo Min. "Full waveform inversion strategy for density in the frequency domain." Geophysical Journal International 188.3 (2012): 1221-1242.

Kim, Youngseo, et al. "An algorithm for 3D acoustic time-Laplace-Fourier-domain hybrid full waveform inversion." Geophysics 78.4 (2013): R151-R166.

Konak, Abdullah, David W. Coit, and Alice E. Smith. "Multi-objective optimization using genetic algorithms: A tutorial." Reliability Engineering & System Safety 91.9 (2006): 992-1007.

Lailly, Patrick. "The seismic inverse problem as a sequence of before stack migrations." In Conference on inverse scattering: theory and application, pp.

206-220. Society for Industrial and Applied Mathematics, Philadelphia, PA, 1983.

Latimer, Rebecca Buxton, Rick Davidson, and Paul Van Riel. "An interpreter's guide to understanding and working with seismic-derived acoustic impedance data." The leading edge 19.3 (2000): 242-256.

Lee, Ho-Yong, June Mo Koo, Dong-Joo Min, Byung-Doo Kwon, and Hai Soo Yoo. "Frequency-domain elastic full waveform inversion for VTI media." Geophysical Journal International 183, no. 2 (2010): 884-904.

Lee, Shiann-Jong, Dimitri Komatitsch, Bor-Shouh Huang, and Jeroen Tromp. "Effects of topography on seismic-wave propagation: an example from Northern Taiwan." Bulletin of the Seismological Society of America 99, no. 1 (2009): 314-325.

Marfurt, Kurt J. "Accuracy of finite-difference and finite-element modeling of the scalar and elastic wave equations." Geophysics 49.5 (1984): 533-549.

Mercerat, E. D., J. P. Vilotte, and F. J. Sánchez-Sesma. "Triangular Spectral Element simulation of two-dimensional elastic wave propagation using unstructured triangular grids." Geophysical Journal International 166.2 (2006): 679-698.

Mora, Peter. "Nonlinear two-dimensional elastic inversion of multioffset seismic data." Geophysics 52.9 (1987): 1211-1228.

Operto, S., C. Ravaut, L. Improta, J. Virieux, A. Herrero, and P. Dell'Aversana. "Quantitative imaging of complex structures from dense wide-aperture seismic data by multiscale traveltime and waveform inversions: a case study." Geophysical Prospecting 52, no. 6 (2004): 625-651.

Plessix, René-Édouard, Guido Baeten, Jan Willem de Maag, Fons ten Kroode, and Zhang Rujie. "Full waveform inversion and distance separated simultaneous sweeping: a study with a land seismic data set." Geophysical Prospecting 60, no. 4 (2012): 733-747.

Pratt, Gerhard, and Changsoo Shin. "Gauss–Newton and full Newton methods in frequency–space seismic waveform inversion." Geophysical Journal International 133.2 (1998): 341-362.

Prechelt, Lutz. "Automatic early stopping using cross validation: quantifying the criteria." Neural Networks 11.4 (1998): 761-767.

Pyun, Sukjoon, Changsoo Shin, and J. B. Bednar. "Comparison of waveform inversion, part 3: amplitude approach." Geophysical prospecting 55.4 (2007): 477-485.

Recktenwald, Gerald. "Stopping Criteria for Iterative Solution Methods." (2012).

Romdhane, Anouar, Gilles Grandjean, Romain Brossier, Fayçal Rejiba, Stéphane Operto, and Jean Virieux. "Shallow-structure characterization by 2D elastic full-waveform inversion." Geophysics 76, no. 3 (2011): R81-R93.

Shewchuk, Jonathan Richard. "Delaunay refinement algorithms for triangular mesh generation." Computational geometry 22.1 (2002): 21-74.

Shin, Changsoo, Sukjoon Pyun, and J. Bednar. "Comparison of waveform inversion, part 1: conventional wavefield vs logarithmic wavefield." Geophysical Prospecting 55.4 (2007): 449-464.

Shin, Changsoo, Nam-Hyung Koo, Young Ho Cha, and Keun-Pil Park. "Sequentially ordered single-frequency 2-D acoustic waveform inversion in the Laplace–Fourier domain." Geophysical Journal International 181, no. 2 (2010): 935-950.

Shin, Changsoo, Seonghyung Jang, and Dong-Joo Min. "Improved amplitude preservation for prestack depth migration by inverse scattering theory." Geophysical prospecting 49.5 (2001): 592-606.

Shin, Changsoo, and Dong-Joo Min. "Waveform inversion using a logarithmic wavefield." Geophysics 71.3 (2006): R31-R42.

Shin, Changsoo, Sukjoon Pyun, and J. Bednar. "Comparison of waveform inversion, part 1: conventional wavefield vs logarithmic wavefield." Geophysical Prospecting 55.4 (2007): 449-464.

Shin, Changsoo, and Young Ho Cha. "Waveform inversion in the Laplace domain." Geophysical Journal International 173.3 (2008): 922-931.

Shin, Changsoo, and Wansoo Ha. "A comparison between the behavior of objective functions for waveform inversion in the frequency and Laplace domains." Geophysics 73.5 (2008): VE119-VE133.

Shin, Changsoo, and Young Ho Cha. "Waveform inversion in the Laplace—Fourier domain." Geophysical Journal International 177.3 (2009): 1067-1079.

Shipp, Richard M., and Satish C. Singh. "Two-dimensional full wavefield inversion of wide-aperture marine seismic streamer data." Geophysical Journal International 151.2 (2002): 325-344.

Stoughton, D., J. Stefani, and S. Michell. "2D elastic model for wavefield investigations of subsalt objectives, deep water Gulf of Mexico." 63rd EAGE Conference & Exhibition. 2001.

Tago, J., V. M. Cruz-Atienza, J. Virieux, V. Etienne, and F. J. Sánchez-Sesma. "A 3D hp-adaptive discontinuous Galerkin method for modeling earthquake dynamics." Journal of Geophysical Research: Solid Earth (1978–2012) 117, no. B9 (2012).

Tarantola, Albert. "Linearized inversion of seismic reflection data." Geophysical prospecting 32.6 (1984): 998-1015.

Tarantola, Albert. Inverse problem theory: Methods for data fitting and model parameter estimation. Elsevier Science, 2002.

Virieux, Jean, and Stéphane Operto. "An overview of full-waveform inversion

in exploration geophysics." Geophysics 74.6 (2009): WCC1-WCC26.

Zielinski, Karin, Dagmar Peters, and Rainer Laur. "Stopping criteria for single-objective optimization." Proceedings of the Third International Conference on Computational Intelligence, Robotics and Autonomous Systems. 2005.

Zielinski, Karin, and Rainer Laur. "Stopping criteria for a constrained single-objective particle swarm optimization algorithm." Informatica (Slovenia) 31.1 (2007): 51-59.

Zelt, C. A., et al. "Advancements in long-offset seismic imaging: A blind test of traveltime and waveform tomography." AGU Spring Meeting Abstracts. Vol. 1. 2005.

초 록

현재 탄성파 자료 획득분야에서의 놀라운 발전은 지금까지 완전 파형역산의 현장자료에 대한 적용을 어렵게 해온 저주파수 성분의 부재 문제를 해결할 수 있는 가능성을 보여준다. 그러나 아직까지 대부분의 현장 탄성파 자료에서 저주파수 성분을 기대하기는 어려운 상황이다. 따라서 저주파수의 부재 문제를 해결해 줄 수 있는 좋은 장파장 속도 모델을 구축 하는 것은 푸리에 영역에서의 파형역산을 통해 고해상도의 속도모델을 구축하거나 구조보정을 통한 지하영상 획득에 있어서 매우 중요한 의미를 갖는다.

본 논문에서는 라플라스-푸리에 영역에서 2차원 탄성 파동방정식을 이용하여 육상탐사에 적용 가능한 파형역산 기법을 개발하였다. 이 기술은 비정규 격자를 이용한 유한요소법에 기반하여 개발되었다. 비정규 격자를 적용함으로써 육상 탐사 자료가 획득된 지형을 정확하게 묘사하는 것이 가능해졌고, 이를 통해 불규칙한 지표면에 의해 발생되는 자료의 비선형성을 줄이는 효과를 기대 할 수 있다.

탄성 매질에서 적용할 수 있는 수정된 헤시안 매트릭스를 정의함으로써 라플라스-푸리에 완전 파형 역산의 결과가 지금까지 유사 헤시안을 적용할시에 함께 정의된 감쇄상 없이 이전의 방법에 비해 깊은 탐사심도와 정확성을 동시에 가질 수 있게 만들었다.

또한 로그 목적함수가 진폭 오차와 위상 오차를 자연적으로 분리해내는 특성에 착안하여 라플라스-푸리에 영역 완전파형 역산에서 잔차의 진폭정보와 위상정보를 균형 있게 이용할 수 있는

진폭 오차와 위상 오차를 정규화 시켜 이용하는 반복중단 알고리즘을 소개하였다. 이를 적용함으로 잘못된 역산 반복횟수 결정이나 과대적합에 의해 야기될 수 있는 부적절한 파형역산 결과 획득을 막고자 하였다.

본 논문을 통해 개발된 알고리즘의 실제 탐사자료에 대한 적용 가능성을 실험하기 위해 현장자료가 가질 수 있는 대표적인 문제점인 저주파수가 없는 경우와 잡음이 가해진 시간영역 인공합성 자료를 이용하여 수치실험을 수행하였다. 그 결과 저주파수 성분에 의존하지 않고 성공적으로 장파장 속도모델을 구축할 수 있었고, 잡음이 섞인 자료에 대해서도 만족할 만한 결과를 보여주었다.

주요어: 2차원 탄성 매질, 완전 파형 역산, 비정규 격자요소, 반복중단 알고리듬, 유사 헤시안, 라플라스-푸리에 영역

학 번: 2009-22977

공학박사 학위논문

The velocity-construction algorithm using the Laplace-Fourier-domain inversion for a land dataset

- 라플라스-푸리에 영역 역산기법을 이용한 육상탐사자료에 대한 속도 모델 구축 알고리즘-

2014년 2월

서울대학교 대학원

계산과학 협동과정

유 제 우

Abstract

Currently, brilliant advances in the acquisition offer the possibility of solving the problem of the absence of low-frequency components that hinders the full-waveform inversion, yet, most real datasets do not contain these components. Thus, the long-wavelength velocity model that can be obtained using the Laplace- or Laplace-Fourier-domain inversion should be conducive to delineating the subsurface structure via migration or Fourier-domain inversion starting from this algorithm.

In this thesis, the 2D elastic Laplace-Fourier inversion algorithm was developed for the application to a land dataset could recover the long-wavelength velocity models. This velocity-estimation algorithm adopts the finite element method on an unstructured grid with expectation of mitigating the high nonlinearity observed in datasets that originate from topography via accurate depiction of an irregular surface.

For the inversion methodology, the novel pseudo-Hessian matrix is suggested in this thesis. This modified pseudo-Hessian matrix allows for a deeper penetration depth of the inverted result and promises a more convergent result regardless of damping factor that generally required for pseudo-Hessian matrix. Also, the normalized stopping criterion was introduced using multi-objective assumption based on the property of the logarithmic objective function, the natural separation of the phase and amplitude error, to ensure that the phase and amplitude information contribute to the inversion result with parity. This method could help to prevent the result of an acquiring of an over- or under-inverted result caused by over-fitting or an unsuitable determination of

the number of inversion iterations.

The developed inverse algorithm was tested using a time domain synthetic dataset generated with a realistic foothill model. The results of the test demonstrate that this algorithm can recover an adequate velocity model without requiring low-frequency information and with the dataset containing an expected noise.

Keywords: 2D elastic domain, Full-waveform inversion, Unstructured grid, Stopping criterion, Pseudo-Hessian matrix, Laplace-Fourier domain

Student Number: 2009-22977

Contents

List of Tables

List of Figures

Chapter 1. Introduction

Full-waveform inversion (FWI) has been used as a reasonable tool for recovering subsurface parameters using pre-stack seismic data since Laily and Tarantola introduced the back-propagation algorithm (Laily, 1983; Tarantola, 1984). In the past 30 years, seismic inversion has dramatically developed with the advancement of inversion theories and computational environments (Tarantola, 1984; Tarantola, 1986; Mora, 1987; Bunks et al., 1995; Pratt, 1998, Operto et al., 2004; Shin and Min, 2006; Shin et al., 2007; Shin and Cha, 2008, 2009). Also, the advance of the FWI strategy could be possible to apply the FWI to the real dataset has been suffered from the lack of low-frequency information via inversion starting from a long wavelength velocity model computed using reflection tomography (Brenders and Pratt, 2007; Virieux and Operto, 2009) or the Laplace inversion algorithm (Shin and Cha, 2008; Shin and Cha, 2009; Ha et al., 2012). In recent years, the brilliant developments in the acquisition field have demonstrated success in obtaining good land datasets that contain sufficient low-frequency information and wide-aperture long-offset data (Plessix, 2012; Baeten, 2013), and these developments are promising for the use of FWI for velocity-model building in production lines in the future. However, most of the FWI research has been performed using an acoustic environment, and the application of FWI using the elastic wave equation remains a topic of future work.

FWI using the elastic wave equation must be a more appropriate algorithm than the acoustic assumption for land datasets because the earth supports both P- and S- waves; however, the successful case studies using elastic FWI with

real datasets are not easy to find.

Elastic full-waveform inversions have been studied by many geo-physicists. They have presented partially successful results and have explained why elastic FWI encounters more difficulties than acoustic FWI (Mora, 1987, 1988; Tarantola, 1987; Shipp and Singh, 2002; Gelis et al., 2007). For instance, multiple parameters of elastic FWI are interdependent on one another. This interdependency causes the inversion to converge more easily to a local minimum than in the acoustic case (Brossier et al., 2009, 2010; Bae et al., 2010; Lee et al., 2010). The complex topography of an acquisition region produces extremely complex seismic signals, especially for surface waves of large amplitude energy, and this complexity disturbs the convergence of the inverse problem by increasing the nonlinearity (Anouar et al., 2011). Moreover, the difference in surface-wave propagation between the 2D and 3D elastic wave equations is one of the most critical hindrances to attempt to perform a land inversion using the elastic approach. In addition, the problem of the lack of low-frequency components is still extant for most real land datasets. Because the novel acquisition method that is capable of obtaining low-frequency information suffers from limitations concerning applicable sites and for sources, it is not possible to apply this method for every land acquisition site.

This research was started with the purpose of recovering a proper velocity model from a real land dataset using the Laplace-Fourier inverse algorithm suggested by Shin and Cha, 2009.

The Laplace-Fourier algorithm offers some advantages for elastic inversion. Most importantly, this method does not suffer from the absence of the low-frequency components, as has been verified in many studies (Shin et al., 2008, 2009; Cha et al., 2010; Ha et al., 2010; Chung et al., 2010; Bae et al., 2010;

Kim et al., 2013). Additionally, especially for the elastic case, this method allows the use of the 2D elastic wave equation for the inversion of a 3D land dataset. The most critical difference between the 2D and 3D elastic equations is the damped (3D) or un-damped (2D) surface waves. This difference means that the discrepancy increases with increasing offset distance between the modeled data and the observed data when the 2D modeling scheme is used. However, the existence of time damping constant in the Laplace or Laplace-Fourier approach could effectively reduce this discrepancy. Ha et al. (2010) have inverted synthetic elastic data using the acoustic wave equation without removing the Rayleigh waves in the Laplace domain by exploiting this characteristic. They were able to suppress the Rayleigh wave via the damping applied in the Laplace transformation. Therefore, we believe that the 2D Laplace-Fourier-domain inversion could mitigate this difference in surface-wave propagation.

Elastic inversion using a Laplace-transformed dataset has already been performed by Chung et al., in 2010. They successfully demonstrated that the Laplace inversion method has the ability to recover long-wavelength velocity for the elastic parameters. However, this study was performed using the assumption of an upper flat surface; thus, their algorithm does not have the ability to handle with real data that of complex topography. For realistic elastic wave propagation, the presence of the complex topography is one of the most predominant factors that affect successful inversion (Gelis et al., 2007; Romdhane et al., 2011). Several studied have indicated that complex topography drastically influences the amplitudes and phases of the seismic signal (Bleibinhaus and Rondenay, 2009; Shiann-Jong et al., 2009; Romdhane et al, 2011).

Thus, this FWI algorithm adopts unstructured grids to describe the complex topography of a land acquisition site. The modeling algorithm, gradient calculation, and updating are performed on unstructured grids, and only the output result is mapped to a structured grid to apply a seismic inversion method such as reverse time migration after the inversion is completed.

Also in this paper, a novel gradient-scaling method for elastic Laplace-Fourier inversion is introduced which is obtained by modifying the pseudo-Hessian matrix derived by Shin et al., 2001. The newly introduced pseudo-Hessian matrix could increases the penetration depth of the inverted result, and it also could give proper preconditioning to the steepest descent gradient direction without a damping factor defined in the original pseudo-Hessian with the purpose of stabilization. In addition, the stopping criterion using normalized amplitude and phase error is suggested. The amplitude and phase error can be extracted from the error of logarithmic objective function and the new stopping criterion could prevent a biased inversion to the amplitude or phase.

To address the problem of the interdependency among elastic parameters, the density was assumed as a constant value; thus it was not included in the updating process, following the approach taken in other studies (Brossier et al., 2009, 2010; Bae et al., 2010; Lee et al., 2010, Romdhane, 2011; Jeong et al, 2012), and this conventional density assumption did not disturb the recovery of the velocity model in numerical tests using a synthetic dataset.

This work begins with the definition of the Laplace and Laplace-Fourier-transformed datasets. And then, the simulation algorithm of the 2D elastic wave propagation was reviewed. The finite element method was used on unstructured grid for complex topography. The perfectly matched layer (PML)

boundary condition is applied for this modeling algorithm (Cohen, 2002).

In chapter 2.4, some theories of full-waveform inversion was described, such as the computation of the steepest-gradient direction, how to estimate source wavelets, some details concerning the novel pseudo-Hessian matrix, and the normalized stopping criterion.

In chapter 3, the developed elastic Laplace-Fourier-domain FWI is applied to a synthetic dataset. The first test was performed using the same modeling algorithm in the forward and inverse problems to confirm the performance of the developed inversion algorithm. The second test was performed with 3 different purposes; the observation of the dependency on low-frequency information in the dataset, the robustness against noisy data, and the performance with respect to the results of the acoustic approach. The synthetic dataset used in this study was generated using the time-domain 2D elastic interior penalty discontinuous Galerkin method on an unstructured grid (Appendix A). This time-domain dataset was computed using realistic foothill velocity models with complex topography.

Chapter 2. Theory

2.1 The elastic wavefield in the Laplace and Laplace-Fourier domains

The Laplace-Fourier transform of a time domain wavefield is given by (Shin and Cha, 2009)

$$\tilde{u}(s) = \int_0^\infty u(t)e^{-st}dt, \qquad (2\text{-}1)$$
$$s = i\omega + \sigma,$$

where s is a complex number, σ is the real Laplace damping constant, ω is the real angular frequency (given by $2\pi f$, where f is the frequency), t is the time, $u(t)$ is the time-domain wavefield, and $\tilde{u}(t)$ is the Laplace-Fourier transform of $u(t)$.

In equation (2-1), we can observe that the Laplace-Fourier-transformed wavefield is the same as the Laplace-transformed wavefield when ω is zero. The Laplace-transformed wavefield is the integral of the damped time-domain wavefield with respect to time and the damping constant σ, and it can take on only real values. The Laplace transform for large σ turns the time-domain signal into a delta-like signal that shows the first arrival event, and the transform for small σ contains a larger contribution from late-arrival signals and is expected to include the reflections from deeper regions.

In contrast, the Laplace-Fourier-transformed wavefield contains both an amplitude term and a phase term, and it contributes to the acquisition of high-resolution parameter models when it is used for inversion.

For the observation of the properties of the Laplace-Fourier-transformed wavefield with respect to the damping constant and angular frequency, *the* amplitude of the Green's function of the elastic wave equation in the Laplace-Fourier domain is presented in Figure 2 and 3, calculated with 3 damping constants ($\sigma = 1, 5, \text{and } 10$), 3 angular frequencies ($\omega = 0, 10\pi, \text{and } 20\pi$), and the modeling parameters shown in Figure 1.

From Figure 2 and Figure 3, an estimation of some characteristics of the Laplace-Fourier-domain inversion is possible. First, we can see that the amplitude of the Laplace-Fourier wavefield becomes concentrated at the source point as the damping constant is increased, and this property is related to the penetration depth of the inversion.

Figure 4 and 5 show the phase component of the Laplace-Fourier-domain Green's function. In these figures, it is possible to confirm that the Laplace transform does not contain the phase information; thus, the Laplace-domain inversion can be considered to be a purely dynamic algorithm (Pyun et al., 2007). Therefore, the Laplace-domain inversion might be sensitive to impedance variations in the subsurface. On the other hand, the Laplace-Fourier wavefield contains both amplitude and phase information. It is interesting to note that the amplitude spectrum varies drastically with respect to the Laplace damping constant, but the phase spectrum seems to be influenced little or not at all by Laplace damping.

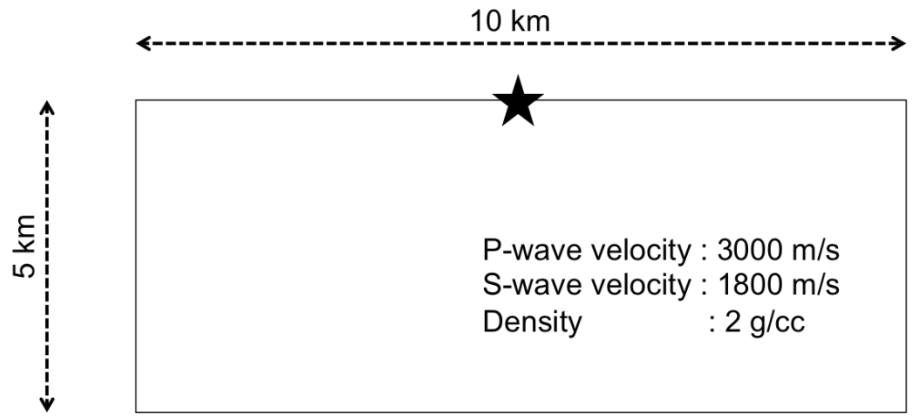

Figure 1. The geometry and homogeneous elastic parameters for computing the Green's function in the Laplace-Fourier domain.

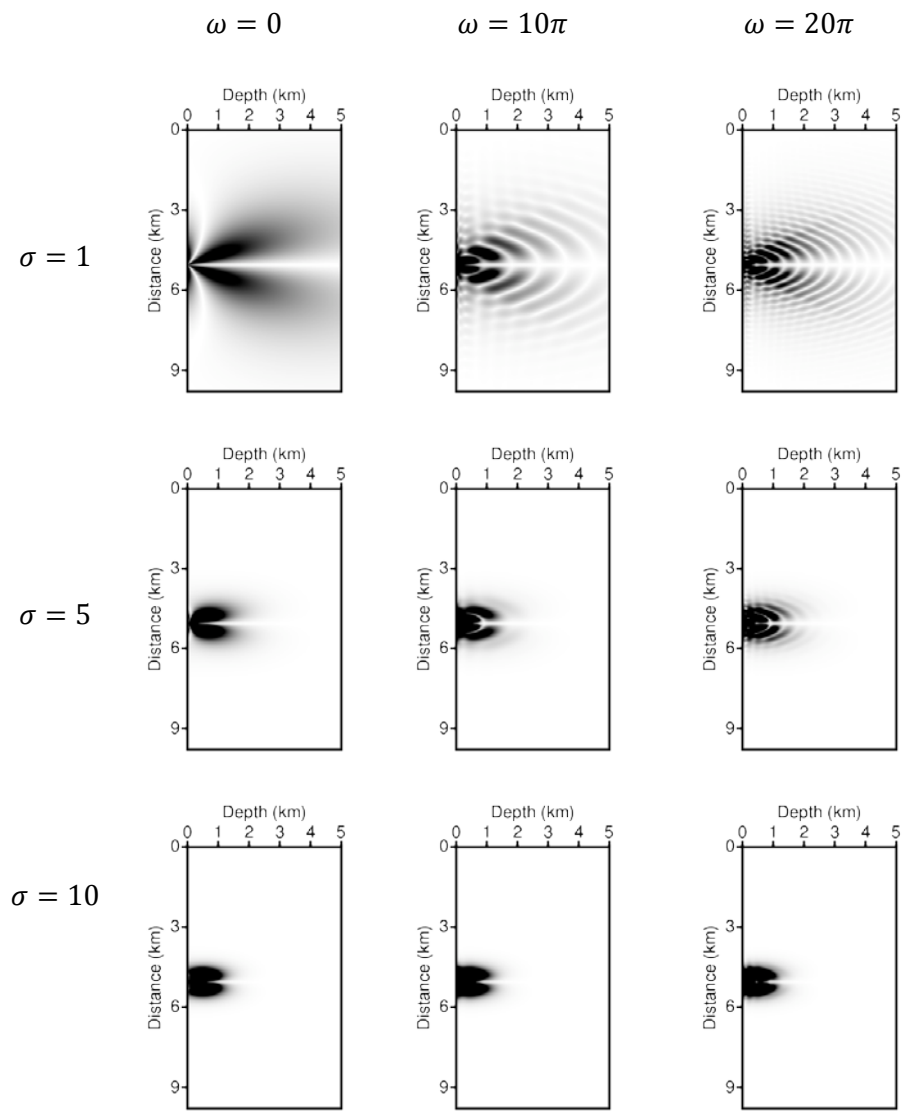

Figure 2. The amplitude spectrum of the horizontal Green's function in the Laplace-Fourier domain with respect to the 3 Laplace damping constants and 3 angular-frequency components.

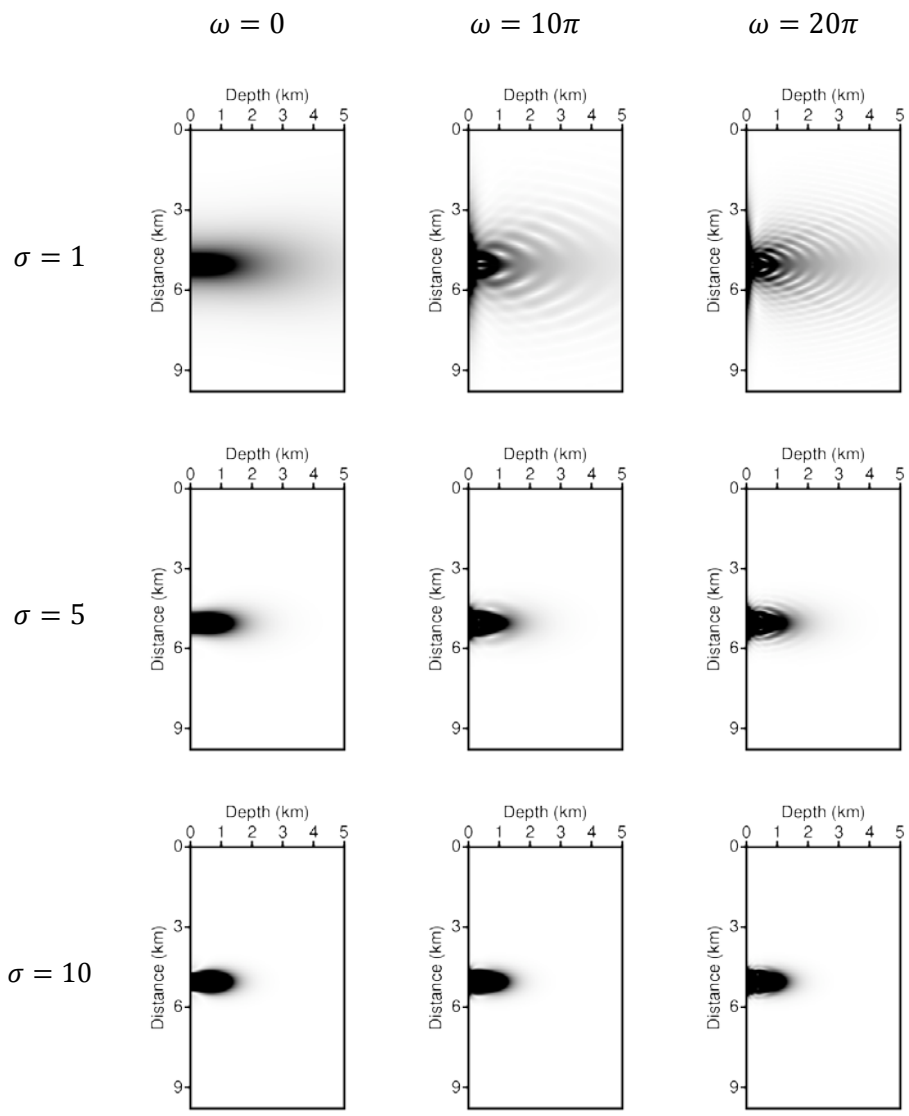

Figure 3. The amplitude spectrum of the vertical Green's function in the Laplace-Fourier domain with respect to the 3 Laplace damping constants and 3 angular-frequency components.

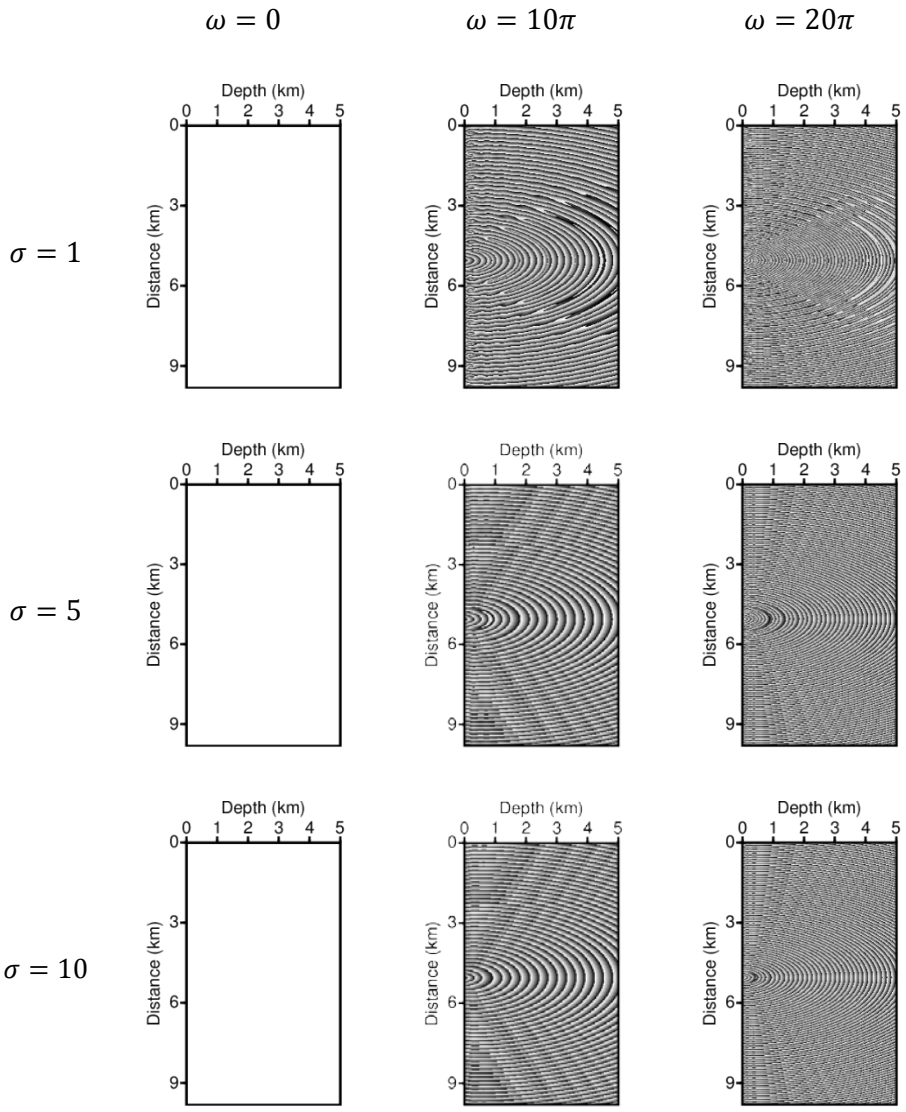

Figure 4. The phase spectrum of the vertical Green's function in the Laplace-Fourier domain with respect to the 3 Laplace damping constants and 3 angular-frequency components.

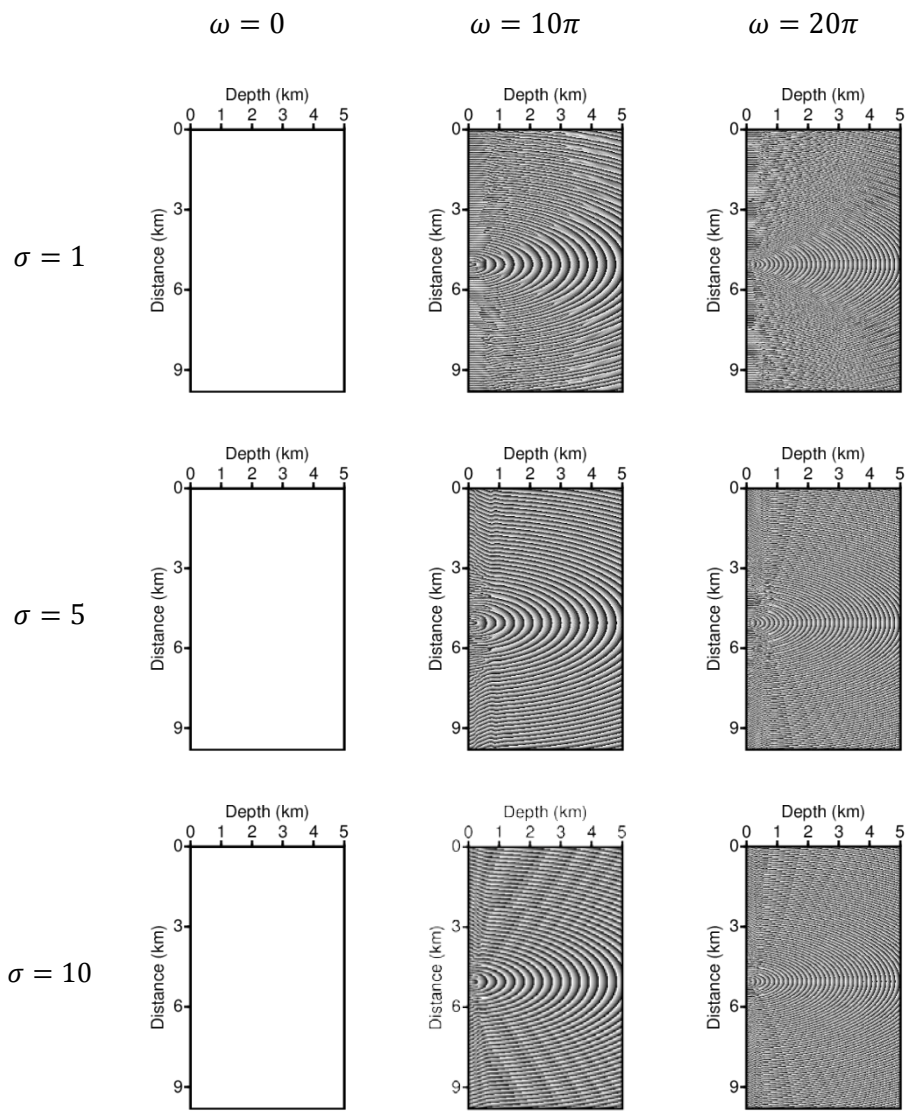

Figure 5. The phase spectrum of the vertical Green's function in the Laplace-Fourier domain with respect to the 3 Laplace damping constants and 3 angular-frequency components.

2.2 The elastic wave equation in the Laplace-Fourier domain

The elastic wave equation in the time domain for an isotropic and heterogeneous medium is defined as (Officer, 1958)

$$\rho \frac{d^2}{dt^2} u_x(\boldsymbol{x}, t) = \frac{\partial}{\partial x} \sigma_{xx}(\boldsymbol{x}, t) + \frac{\partial}{\partial z} \sigma_{xz}(\boldsymbol{x}, t), \tag{2-2}$$

$$\rho \frac{d^2}{dt^2} u_z(\boldsymbol{x}, t) = \frac{\partial}{\partial x} \sigma_{zx}(\boldsymbol{x}, t) + \frac{\partial}{\partial z} \sigma_{zz}(\boldsymbol{x}, t), \tag{2-3}$$

with

$$\sigma_{xx} = (\lambda + 2\mu) \frac{\partial u_x}{\partial x} + \lambda \frac{\partial u_z}{\partial z}, \tag{2-4}$$

$$\sigma_{xz} = \sigma_{zx} = \mu \left(\frac{\partial u_z}{\partial x} + \frac{\partial u_x}{\partial z} \right), \tag{2-5}$$

$$\sigma_{zz} = \lambda \frac{\partial u_x}{\partial x} + (\lambda + 2\mu) \frac{\partial u_z}{\partial z}, \tag{2-6}$$

where $\boldsymbol{x}$ denotes position vector (x, z), $u_x(\boldsymbol{x}, t)$ is the horizontal displacement, and $u_z(\boldsymbol{x}, t)$ is the vertical displacement in the time domain. σ_{xx}, σ_{xz}, and σ_{zz} are stresses. λ, μ, and ρ are the Lamé parameters, which have a particular relation to the P-wave and S-wave velocities.

$$\alpha = \sqrt{\frac{(\lambda + 2\mu)}{\rho}}, \tag{2-7}$$

$$\beta = \sqrt{\frac{\mu}{\rho}}, \tag{2-8}$$

where α is the P-wave velocity, and β is the S-wave velocity.

The elastic wave equation in the Laplace-Fourier domain can be obtained by taking the Laplace-Fourier transforms of equations (2-2) - (2-3), yielding

$$\rho s^2 \tilde{u}_x(\boldsymbol{x}, s) = \frac{\partial}{\partial x}\left(\lambda\Delta + 2\mu\frac{\partial \tilde{u}_x(\boldsymbol{x}, s)}{\partial x}\right) + \frac{\partial}{\partial z}\left(\mu\frac{\partial \tilde{u}_z(\boldsymbol{x}, s)}{\partial x} + \mu\frac{\partial \tilde{u}_x(\boldsymbol{x}, s)}{\partial z}\right), \tag{2-9}$$

$$\rho s^2 \tilde{u}_z(\boldsymbol{x}, s) = \frac{\partial}{\partial x}\left(\mu\frac{\partial \tilde{u}_z(\boldsymbol{x}, s)}{\partial x} + \mu\frac{\partial \tilde{u}_x(\boldsymbol{x}, s)}{\partial z}\right) + \frac{\partial}{\partial z}\left(\lambda\Delta + 2\mu\frac{\partial \tilde{u}_z(\boldsymbol{x}, s)}{\partial z}\right), \tag{2-10}$$

$$\Delta = \frac{\partial \tilde{u}_x(\boldsymbol{x}, s)}{\partial x} + \frac{\partial \tilde{u}_z(\boldsymbol{x}, s)}{\partial z}, \tag{2-11}$$

where,

$$\tilde{u}_x(\boldsymbol{x}, s) = \int_0^\infty u_x(\boldsymbol{x}, t)e^{-st}dt, \tag{2-12}$$

$$\tilde{u}_z(\boldsymbol{x}, s) = \int_0^\infty u_z(\boldsymbol{x}, t)e^{-st}dt. \tag{2-13}$$

2.3 Simulation of the elastic wave propagation using the FEM

The accurate simulation of wave propagation is the one of the most important factors that could make successful full-waveform inversion possible. For the elastic case, the exact simulation of elastic wave propagation for a land dataset depends on a description of complex topography of the acquisition site.

Many prior studies have been conducted regarding elastic inversion; however, most of them have used Cartesian grids for simulation, the flat-surface assumption and the 2D elastic wave equation. They have produced well-inverted results and promising algorithms. However, the flat-surface assumption makes that their studies are not suitable for the application to land datasets.

The flat-surface assumption imposes the different seismic responses with the acquired data. The most energetic signal of the elastic wave equation is the ground roll, which propagates along the surface, and an irregular surface generates much more complexity in this phenomenon. Thus, in this study, we tried to describe the complex topography by using the finite element method (FEM), which can easily handle complex boundaries and unstructured grids meshes, even when higher-order discretization is applied.

2.3.1 The finite element method for the 2D elastic wave equation

The simulation of the elastic wave propagation was computed in the domain shown in Figure 6. The symbol Ω represents the domain of elastic modeling. The symbol Ω_{pml} denotes the absorbing zone for the application of the perfectly matched boundary condition, and it is included in Ω. The Neumann boundary condition is applied to all outer boundaries, $\partial\Omega$.

For the given domain Ω, we consider shape-irregular meshes Γ_h that partitions the domain Ω into a triangular elements K, such that $\Omega = \sum K$. The 2D elastic wave equation in the Laplace-Fourier domain, equations (2-9) and (2-10), can then be express in the FEM formulation.

$$\rho s^2 \int_\Omega {u_x}^h v^h \mathrm{d}\Omega = \int_\Omega \frac{\partial}{\partial x}\left(\lambda \frac{\partial {u_x}^h}{\partial x} + \lambda \frac{\partial {u_z}^h}{\partial z} + 2\mu \frac{\partial {u_x}^h}{\partial x}\right) v^h d\Omega + \int_\Omega \frac{\partial}{\partial z}\left(\mu \frac{\partial {u_z}^h}{\partial x} + \mu \frac{\partial {u_x}^h}{\partial z}\right) v^h d\Omega, \tag{2-14}$$

$$\rho s^2 \int_\Omega {u_z}^h v^h \mathrm{d}\Omega = \int_\Omega \frac{\partial}{\partial x}\left(\mu \frac{\partial {u_z}^h}{\partial x} + \mu \frac{\partial {u_x}^h}{\partial z}\right) v^h d\Omega + \int_\Omega \frac{\partial}{\partial z}\left(\lambda \frac{\partial {u_x}^h}{\partial x} + \lambda \frac{\partial {u_z}^h}{\partial z} + 2\mu \frac{\partial {u_z}^h}{\partial x}\right) v^h d\Omega, \tag{2-15}$$

where, ${u_x}^h = \sum_i^{n_{dof}} \hat{u}_i \phi_i$, ${u_z}^h = \sum_i^{n_{dof}} \hat{v}_i \phi_i$, $v^h = \sum_j^{n_{dof}} \phi_j$, ϕ is the shape function, and i and j are nodal points, n_{dof} denotes total degree of freedom.

The equation (2-14) and (2-15) can be rewritten in a matrix form as follows (Marfurt, 1984),

$$\mathbf{Su} = (\mathbf{M} + \mathbf{K})\mathbf{u} = \mathbf{f}, \tag{2-16}$$

where, $\mathbf{S}$ is the complex impedence matrix composed of $\mathbf{M}$, the mass matrix, and $\mathbf{K}$, the stiffness matrix. $\mathbf{f}$ denotes the source vector.

$$\mathbf{u} = \begin{pmatrix} \hat{u} \\ \hat{v} \end{pmatrix}, \tag{2-17}$$

$$\mathbf{M} = \begin{pmatrix} m_{11} & 0 \\ 0 & m_{22} \end{pmatrix}, \tag{2-18}$$

$$\mathbf{K} = \begin{pmatrix} k_{11} & k_{12} \\ k_{21} & k_{22} \end{pmatrix}, \tag{2-19}$$

$$\mathbf{f} = \begin{pmatrix} f_x \\ f_z \end{pmatrix}, \tag{2-20}$$

where f_x and f_z are the horizontal and vertical source vector, respectively. The components of the mass matrix and the stiffness matrix are expressed as follows,

$$m_{11} = m_{22} = \sum_K \int_k \rho_k \, s^2 \, {a_k}^x {a_k}^z \phi_i \phi_j dk, \tag{2-21}$$

$$k_{11} = \sum_K \int_k \left\{ (\lambda_k + 2\mu_k) \frac{{a_k}^z}{{a_k}^x} \frac{\partial \phi_i}{\partial x} \frac{\partial \phi_j}{\partial x} + \mu_k \frac{{a_k}^x}{{a_k}^z} \frac{\partial \phi_i}{\partial z} \frac{\partial \phi_j}{\partial z} \right\} dk, \tag{2-22}$$

$$k_{12} = \sum_K \int_k \left\{ \lambda_k \frac{\partial \phi_i}{\partial z} \frac{\partial \phi_j}{\partial x} + \mu_k \frac{\partial \phi_i}{\partial x} \frac{\partial \phi_j}{\partial z} dk \right\}, \tag{2-23}$$

$$k_{21} = \sum_K \int_k \left\{ \lambda_k \frac{\partial \phi_i}{\partial x} \frac{\partial \phi_j}{\partial z} + \mu_k \frac{\partial \phi_i}{\partial z} \frac{\partial \phi_j}{\partial x} dk \right\}, \tag{2-24}$$

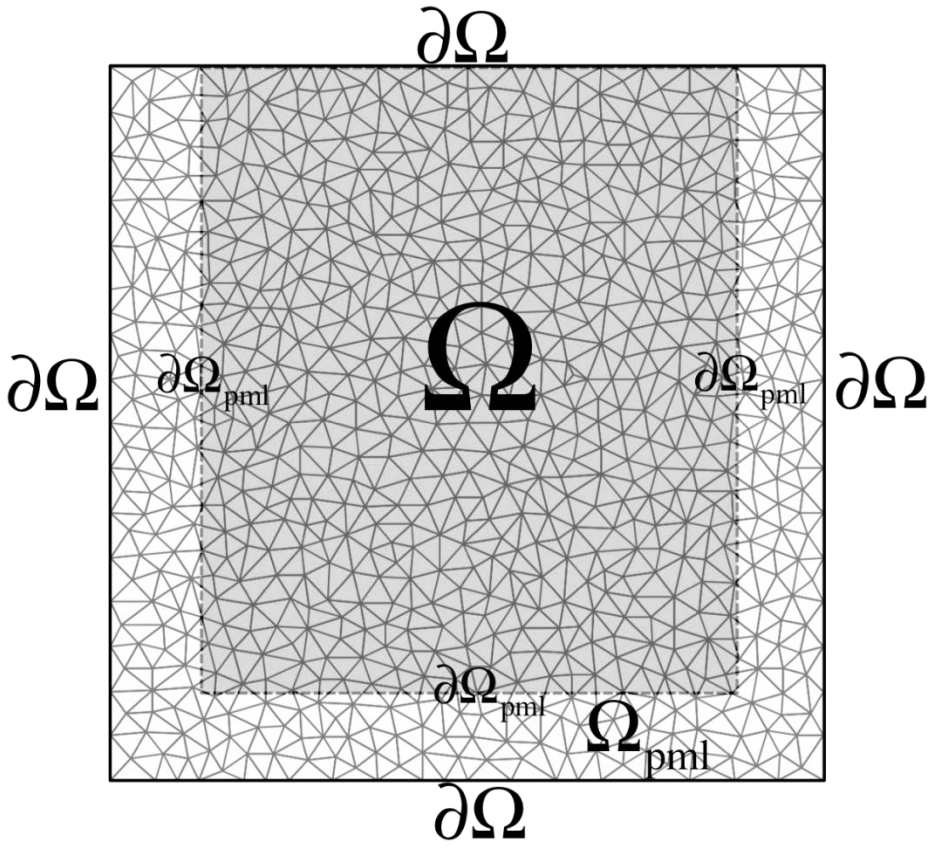

Figure 6. An elastic modeling domain for wave propagation. Ω is the entire domain, and ∂Ω is the Neumann boundary condition. Ω_{pml} denotes the domain for absorbing boundary condition, and $\partial\Omega_{pml}$ represents the boundaries of PML zone.

$$k_{22} = \sum_{K} \int_{k} \left\{ \mu_k \frac{{a_k}^z}{{a_k}^x} \frac{\partial \phi_i}{\partial x} \frac{\partial \phi_j}{\partial x} + (\lambda_k + 2\mu_k) \frac{{a_k}^x}{{a_k}^z} \frac{\partial \phi_i}{\partial z} \frac{\partial \phi_j}{\partial z} dk \right\}. \tag{2-25}$$

Where, k is an element and K is a finite set of element. The number of the local node point for an arbitrary element k is defined with respect to the shape function order (l_k) of each element.

$${n_{dof}}^k = (l_k + 1)(l_k + 2)/2 \tag{2-26}$$

${a_k}^x$ and ${a_k}^z$ is equation (2-21) are the PML constants that are defined for each element. For the unstructured-grids model, the PML constants is computed using the center coordinate of the element and the distance from the PML boundary $\partial\Omega_{pml}$. The practical definitions of the PML constants can be written in the forms

$${a_k}^x = \begin{cases} 1 & (k \notin \Omega_{pml}) \\ 1 + i\varsigma_x/s & (k \in \Omega_{pml}) \end{cases}, \tag{2-27}$$

$$\varsigma_x = \frac{3c_0}{2a} \log R \left(\frac{x'}{a} \right)^2, \tag{2-28}$$

$${a_k}^z = \begin{cases} 1 & (k \notin \Omega_{pml}) \\ 1 + i\varsigma_z/s & (k \in \Omega_{pml}) \end{cases} \tag{2-29}$$

$$\varsigma_z = \frac{3c_0}{2a} \log R \left(\frac{z'}{a} \right)^2, \tag{2-30}$$

where a is the thickness of the boundary layer, c_0 is the velocity of the PML zone, R=1000, x′ is the x-axis distance from the $\partial\Omega_{pml}$, and z´ is the z-axis distance from the $\partial\Omega_{pml}$ (Cohen, 2002).

The components of the mass matrix in equation (2-21) can be computed using the shape function $\hat{\phi}$ of the master element $\hat{K}$; F_k, which is the mapping

function of the k element; and the relationship $\phi_i = \hat{\phi}_I \circ {F_k}^{-1}$ between ϕ and $\hat{\phi}$.

$$
\begin{aligned}
m_{11} &= \sum_K \int_k \rho_k s^2 {a_k}^x {a_k}^z \phi_i \phi_j dk \\
&= s^2 \sum_K \rho_k {a_k}^x {a_k}^z \int_k \hat{\phi}_I \circ {F_k}^{-1} \hat{\phi}_J \circ {F_k}^{-1} dk \\
&= s^2 \sum_K \rho_k {a_k}^x {a_k}^z \int_k \left(\hat{\phi}_I \hat{\phi}_J\right) \circ {F_k}^{-1} dk \\
&= s^2 \sum_K \rho_k {a_k}^x {a_k}^z |det J_k| \int_{\hat{K}} \left(\hat{\phi}_I \hat{\phi}_J\right) d\hat{K} \\
&= m_{22}.
\end{aligned}
\tag{2-31}
$$

The mapping function is shown in Figure 7, and it is defined for a triangular element as follows:

$$
\begin{aligned}
F_k(\hat{x}, \hat{y}) &= \begin{pmatrix} x_1 \\ y_1 \end{pmatrix} + \begin{pmatrix} x_2 - x_1 & x_3 - x_1 \\ y_2 - y_1 & y_3 - x_1 \end{pmatrix} \begin{pmatrix} \hat{x} \\ \hat{y} \end{pmatrix}, \\
&= b_k + J_k \begin{pmatrix} \hat{x} \\ \hat{y} \end{pmatrix},
\end{aligned}
\tag{2-32}
$$

where, (x_1, y_1), (x_2, y_2), and (x_3, y_3) are the global coordinates of the vertex of the triangular element k. $(\hat{x}, \hat{y})$ represents its corresponding coordinates on the master triangular element $\hat{K}$.

For the stiffness matrix, all components of it can be computed the components using the quantities above and the relationship $\nabla\phi_i = {J_k}^{-\mathrm{T}} \nabla\hat{\phi}_I \circ {F_k}^{-1}$ between ϕ and $\hat{\phi}$.

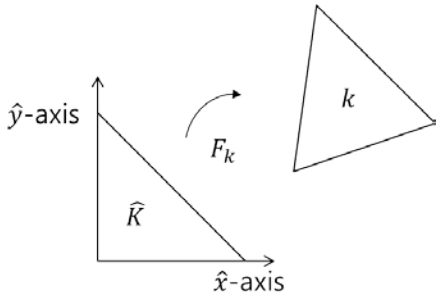

Figure 7. Illustration of the mapping from the master to the global element via F_k.

$$k_{11} = \sum_K \int_k \left\{ (\lambda_k + 2\mu_k) \frac{{a_k}^z}{{a_k}^x} \frac{\partial \phi_i}{\partial x} \frac{\partial \phi_j}{\partial x} + \mu_k \frac{{a_k}^x}{{a_k}^z} \frac{\partial \phi_i}{\partial z} \frac{\partial \phi_j}{\partial z} \right\} dk \tag{2-33}$$

$$= \sum_K (\lambda_k + 2\mu_k) \frac{{a_k}^z}{{a_k}^x} |detJ_k| \int_{\widehat{K}} \nabla \hat{\phi}_I {J_k}^{-1} \begin{pmatrix} 1 & 0 \\ 0 & 0 \end{pmatrix} {J_k}^{-\mathrm{T}} \nabla \hat{\phi}_J d\widehat{K}$$

$$+ \sum_K \mu_k \frac{{a_k}^x}{{a_k}^z} |detJ_k| \int_{\widehat{K}} \nabla \hat{\phi}_I {J_k}^{-1} \begin{pmatrix} 0 & 0 \\ 0 & 1 \end{pmatrix} {J_k}^{-\mathrm{T}} \nabla \hat{\phi}_J d\widehat{K},$$

$$k_{12} = \sum_K \int_k \left\{ \lambda_k \frac{\partial \phi_i}{\partial z} \frac{\partial \phi_j}{\partial x} + \mu_k \frac{\partial \phi_i}{\partial x} \frac{\partial \phi_j}{\partial z} \right\} dk \tag{2-34}$$

$$= \sum_K \lambda_k |detJ_k| \int_{\widehat{K}} \nabla \hat{\phi}_I {J_k}^{-1} \begin{pmatrix} 0 & 0 \\ 1 & 0 \end{pmatrix} {J_k}^{-\mathrm{T}} \nabla \hat{\phi}_J d\widehat{K}$$

$$+ \sum_K \mu_k |detJ_k| \int_{\widehat{K}} \nabla \hat{\phi}_I {J_k}^{-1} \begin{pmatrix} 0 & 1 \\ 0 & 0 \end{pmatrix} {J_k}^{-\mathrm{T}} \nabla \hat{\phi}_J d\widehat{K},$$

$$k_{21} = \sum_K \int_k \left\{ \lambda_k \frac{\partial \phi_i}{\partial x} \frac{\partial \phi_j}{\partial z} + \mu_k \frac{\partial \phi_i}{\partial z} \frac{\partial \phi_j}{\partial x} \right\} dk \tag{2-35}$$

$$= \sum_K \lambda_k |detJ_k| \int_{\widehat{K}} \nabla \hat{\phi}_I {J_k}^{-1} \begin{pmatrix} 0 & 1 \\ 0 & 0 \end{pmatrix} {J_k}^{-\mathrm{T}} \nabla \hat{\phi}_J d\widehat{K}$$

$$+ \sum_K \mu_k |detJ_k| \int_{\widehat{K}} \nabla \hat{\phi}_I {J_k}^{-1} \begin{pmatrix} 0 & 0 \\ 1 & 0 \end{pmatrix} {J_k}^{-\mathrm{T}} \nabla \hat{\phi}_J d\widehat{K},$$

$$k_{22} = \sum_K \int_k \left\{ \mu_k \frac{{a_k}^z}{{a_k}^x} \frac{\partial \phi_i}{\partial x} \frac{\partial \phi_j}{\partial x} + (\lambda_k + 2\mu_k) \frac{{a_k}^x}{{a_k}^z} \frac{\partial \phi_i}{\partial z} \frac{\partial \phi_j}{\partial z} \right\} dk \tag{2-36}$$

$$= \sum_K \mu_k \frac{{a_k}^z}{{a_k}^x} |detJ_k| \int_{\widehat{K}} \nabla \hat{\phi}_I {J_k}^{-1} \begin{pmatrix} 1 & 0 \\ 0 & 0 \end{pmatrix} {J_k}^{-\mathrm{T}} \nabla \hat{\phi}_J d\widehat{K}$$

$$+ \sum_K (\lambda_k + 2\mu_k) \frac{{a_k}^x}{{a_k}^z} |detJ_k| \int_{\widehat{K}} \nabla \hat{\phi}_I {J_k}^{-1} \begin{pmatrix} 0 & 0 \\ 0 & 1 \end{pmatrix} {J_k}^{-\mathrm{T}} \nabla \hat{\phi}_J d\widehat{K},$$

where ∇ is the gradient operator.

The forward modeling was performed using the derived FEM algorithm with the heterogeneous velocity model that has the complex surface shown in Figure 8. Figure 8, 9a, and 9b show the P-wave and S-wave velocity models and the density model, respectively. The size of the domain is 20,000 m $\times$ 3,700 m. The unstructured grid was showed in the P-wave velocity model. Figure 10 shows the horizontal and vertical displacements obtained via the forward-problem algorithm with the given models, a Laplace-damping value of 1.0, and a frequency value of 20π. In this modeling example, the complication of the elastic wave propagation caused by the topography was able to observe. And it can be an example why the inversion approach using the flat-surface assumption and the corrected dataset, which considers only the time delay that originates from differences in elevation, is highly susceptible to failure when applied to a land dataset that was acquired in a region with complex topography.

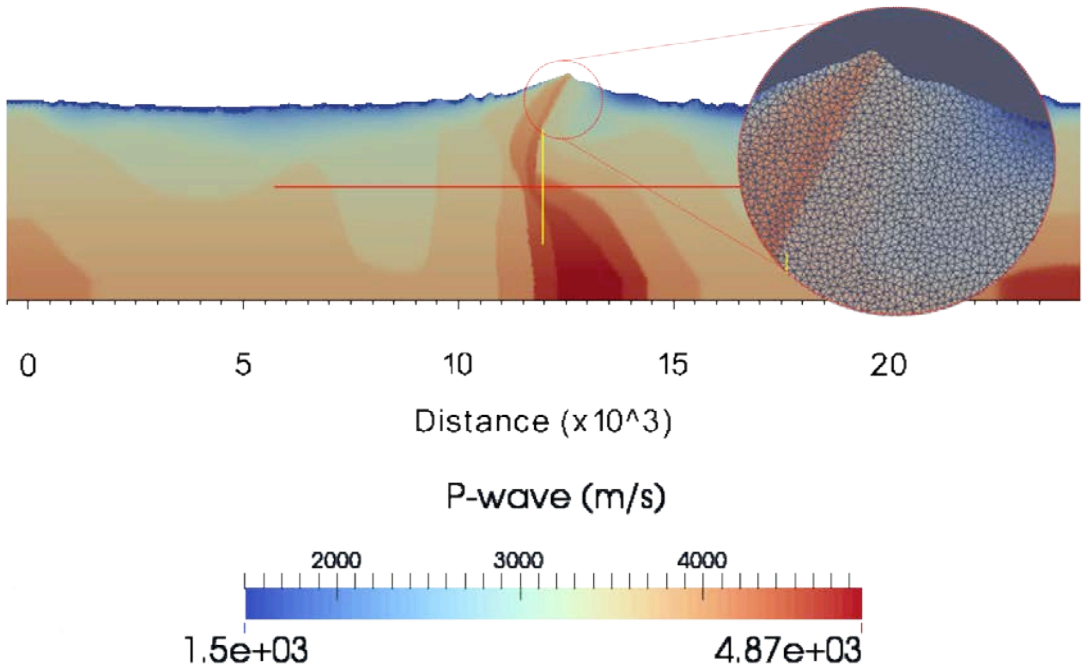

Figure 8. P-wave velocity model defined on the unstructured grids for a modeling test.

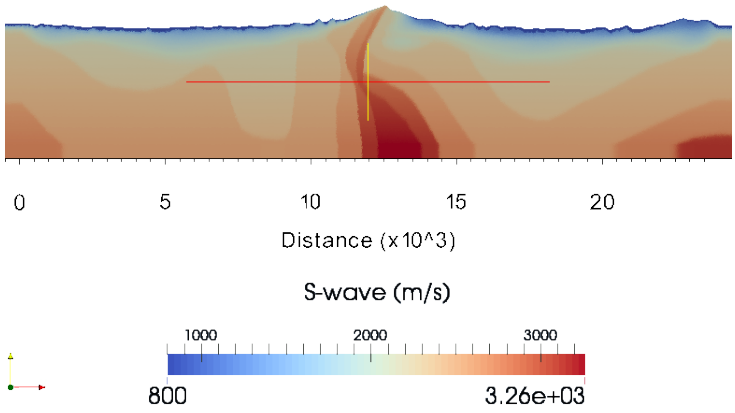

(a)

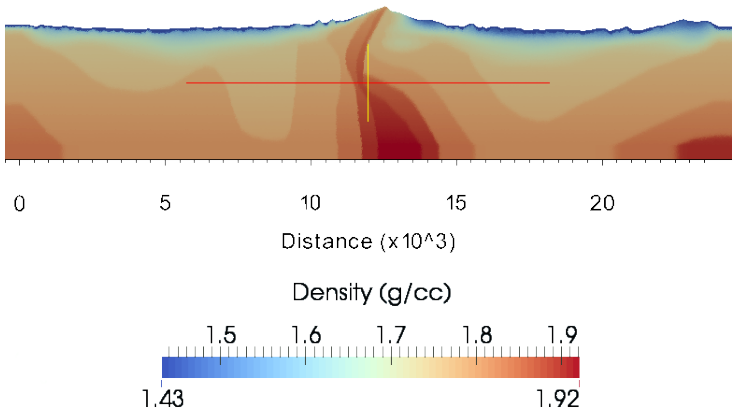

(b)

Figure 9. Parameters defined on unstructured grids for a modeling test: (a) S-wave velocity and (b) density.

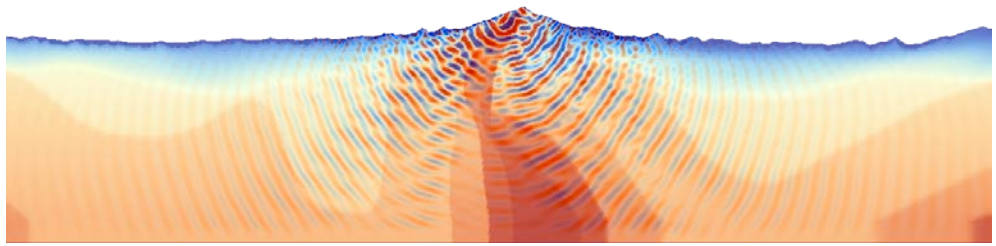

(a)

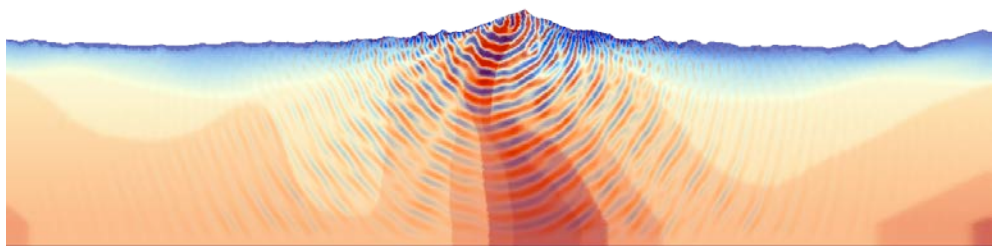

(b)

Figure 10. The (a) horizontal and (b) vertical displacement computed in the Laplace-Fourier domain using the parameters given in Figure 8 and 9, $\sigma = 1$ for and $\omega = 20\pi$.

2.3.2 Source and receiver distributions

A simulation of the wave equation using FEM in the Laplace and Laplace-Fourier domains can compute a stable numerical solution using a grid size ten times coarser grid size than that required for similar simulations using time- or frequency-domain FEM (Shin and Cha, 2008). However, this advantage cannot be exploited when the exact nodal positions of the sources and receivers are applied during the meshing procedure. Thus, the original coordinates of the sources and receivers changed to the distributed coordinates with weighting at the corresponding locations, as shown in Figure 11.

This approach allows for the control of the mesh size and shape without any consideration for the coordinates of the original sources and receivers, based on the definitions of the integral of the delta function, the mapping function F_k and its determinant. A point source located at $\boldsymbol{x}_s$ in the inner region of element k_{src}, an element that contains a source, can be expressed in terms of the distributed sources that are located at the coordinates of the nodal points of the master element. The source vector in equation (2-20) can be written as follows,

$$\begin{aligned} \mathbf{f} &= \sum_{K} \int_{k} \delta(\boldsymbol{x} - \boldsymbol{x}_s) A \phi_j dk \\ &= \int_{k_s} \delta(\boldsymbol{x} - \boldsymbol{x}_s) A \phi_j dk \\ &= \sum_{j}^{{n_{dof}}^{k_s}} A \phi_j (\boldsymbol{x} - \boldsymbol{x}_s) \end{aligned} \tag{2-37}$$

$$= \left|detJ_{k_s}\right| A \sum_{J}^{n_{dof}^{\hat{K}}} \hat{\phi}_J(\boldsymbol{x}_s)$$

where A is the amplitude of the source vector in the Laplace-Fourier domain, j represents the local nodal points on the source element k_s, and J represents the local nodal points on the master element $\hat{K}$. Examples of simulation of the vertical and horizontal wavefields using distributed coordinate are presented in Figure 12 to verify the feasibility of using distributed sources and receivers. The 1st test was performed using the exact source and receiver positions, and the 2nd was performed using distributed sources and receivers. The Figure 12b and Figure 12c show that the calculated wavefields are perfectly consistent.

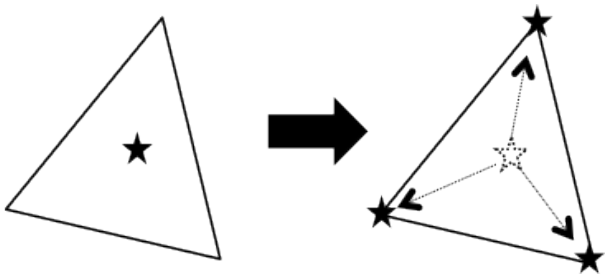

Figure 11. Illustration of the mapping of an arbitrary position to a nodal position.

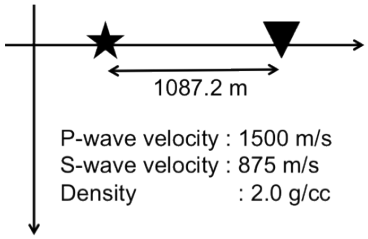

(a)

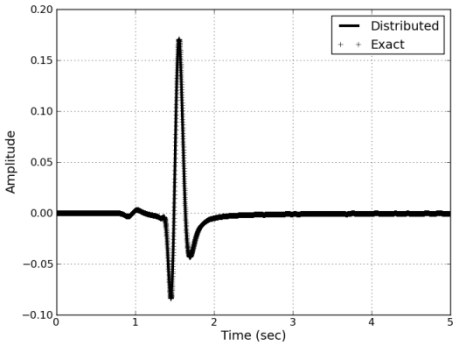

(b)

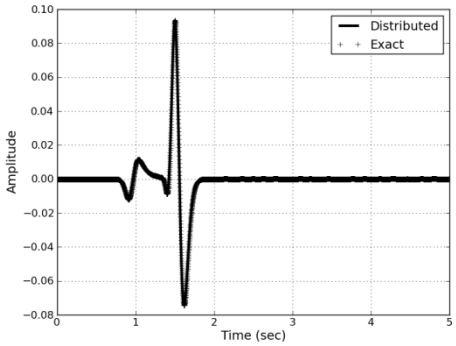

(c)

Figure 12. (a) Domain for testing the elastic wave propagation using the exact and distributed positions of the sources and receivers. (b) Vertical displacement and (c) horizontal displacement.

2.4 Full waveform inversion in the Laplace-Fourier domain

In this section, the Laplace-Fourier-domain inversion algorithm is presented using the steepest descent method introduced by Shin and Cha in 2009 with the logarithmic objective function suggested by Shin and Min (2006). The logarithm objective function must be used for Laplace and Laplace-Fourier-domain inversion because the amplitude of a Laplace-Fourier-transformed wavefield has such a large amplitude range with respect to the offset; thus, no other widely used objective function, such as the l_1 or l_2 norm, is suitable (Shin and Ha, 2008).

The source-estimation algorithm of logarithmic wavefield is also reviewed in this chapter. The full Newton method suggested by Shin et al. (2007) is applied for an estimating of the source wavelet and it is performed for each source, independently.

Next, it is showed that how to distribute the source and receiver position from their original coordinate to node point of mesh. The mixed type mesh is applied to minimize the error originated from mapping the result obtained on unstructured grid to the structured grid.

The novel pseudo-Hessian matrix and stopping criterion using normalized amplitude and phase error were proposed in this chapter. The suggested pseudo-Hessian matrix could promise proper regularized gradient direction than the original one for elastic inversion. Also, the stopping criterion could prevent to be partial inversion toward the amplitude or phase. These methods were introduced with numerical examples.

2.4.1 Determination of gradient direction in the Laplace-Fourier domain using the steepest descent

The Laplace and Laplace-Fourier domain wavefields can be obtained via frequency-domain modeling using a Laplace damping constant and an angular-frequency constants; thus, the inversion algorithm can be implemented in the same manner as in the frequency-domain method using a logarithmic wavefield.

The residual is defined in terms of the ratio of the logarithmic modeled wavefield and the observed wavefields based on the l_2 norm, as follows:

$$\tilde{r}_{i,j} = \ln\tilde{u}_{i,j} - \ln\tilde{d}_{i,j} = \ln\frac{\tilde{u}_{i,j}}{\tilde{d}_{i,j}}, \tag{2-38}$$

where $\tilde{u}_{i,j}$ and $\tilde{d}_{i,j}$ are the modeled and observed wavefields in the Laplace-Fourier domain at the location of the j_{th} receiver of the i_{th} source. In particular, the observed dataset was assumed that it contains only a vertical component, as this assumption is consistent with many real land datasets. Thus, the modeled data $\tilde{u}_{i,j}$ also contains a vertical component. The objective function E can be defined as

$$E = \sum_{i}^{n_s}\sum_{j}^{n_r}\frac{1}{2}\tilde{r}_{i,j}\left(\tilde{r}_{i,j}\right)^{*}, \tag{2-39}$$

where n_s and n_r are the numbers of sources and receivers, respectively. The notation * indicates a complex conjugated value.

The steepest-decent method is an iterative method of minimizing the objective function using the gradient directions for the various unknown parameters.

$$\mathbf{m}^{(l+1)} = \mathbf{m}^{(l)} - \alpha^{(l)}\nabla_{\boldsymbol{m}}E, \tag{2-40}$$

where $\mathbf{m}^{(l)}$ is the model parameter vector at the l_{th} iteration, and $\nabla_{\boldsymbol{m}} E$ is the steepest-decent gradient direction. α is the step length for updating.

The steepest-descent gradient direction for the k element can be computed from the partial derivative of the logarithmic objective function with respect to the model parameter m_k.

$$\nabla_{m_k} E = \frac{\partial E}{\partial m_k} = \sum_{i}^{n_s} \sum_{j}^{n_r} \frac{1}{\tilde{u}_{i,j}} \frac{\partial \tilde{u}_{i,j}}{\partial m_k} \left(\tilde{r}_{i,j}\right)^* \tag{2-41}$$

The partial derivative of the modeled wavefield can be computed by taking the partial derivative of equation (2-16) with respect to the model parameter m_k, and then the following equation can be obtained:

$$\frac{\partial \mathbf{S}}{\partial m_k}\mathbf{u} + \mathbf{S}\frac{\partial \mathbf{u}}{\partial m_k} = 0 \tag{2-42}$$

$$\frac{\partial \mathbf{u}}{\partial m_k} = \mathbf{S}^{-1}\left(-\frac{\partial \mathbf{S}}{\partial m_k}\mathbf{u}\right) \text{ or } \frac{\partial \mathbf{u}}{\partial m_k} = \mathbf{S}^{-1}(\mathbf{v}_k) \tag{2-43}$$

where $\mathbf{v}_k$ is the virtual source vector with respect to the parameter m_k (Pratt et al., 1998), expressed as

$$\mathbf{v}_k = -\frac{\partial \mathbf{S}}{\partial m_k}\mathbf{u} \tag{2-44}$$

Now, the steepest-descent gradient direction of a model parameter for the k element can be calculated using back propagation algorithm (Shin and Min, 2006), and it can be expressed as

$$\nabla_{m_k} E = \sum_{i}^{n_s} \mathbf{v}_k{}^{\mathrm{T}} \mathbf{S}^{-\mathrm{T}} \mathbf{r}_i \tag{2-45}$$

where $\mathbf{S}^{-\mathrm{T}}$ is the inverse of the transposed impedance matrix, and it can be replaced by $\mathbf{S}^{-1}$ because of its symmetry. The residual vector $\mathbf{r}_i$ can be expressed as

$$\mathbf{r}_i = \begin{pmatrix} 0 \\ \vdots \\ 0 \\ \frac{1}{\tilde{u}_{i,1}} \frac{\partial \tilde{u}_{i,1}}{\partial m_k} \left(\tilde{r}_{i,1}\right)^* \\ \vdots \\ \frac{1}{\tilde{u}_{i,n_r}} \frac{\partial \tilde{u}_{i,n_r}}{\partial m_k} \left(\tilde{r}_{i,n_r}\right)^* \\ 0 \\ \vdots \\ 0 \end{pmatrix}. \tag{2-46}$$

2.4.2 Preconditioning of the gradient direction using pseudo-Hessian matrix

The gradient direction computed using the steepest-descent method of equation (2-45) requires preconditioning because it is computed without consideration of the geometrical spreading effect. Pratt et al. suggested the Gauss-Newton method and the full-Newton method for regularizing the gradient direction in 1998, and Shin et al. introduced the pseudo-Hessian matrix, which uses only the diagonal component of the approximated Hessian in Gauss-Newton method, to reduce the computational cost of this task in 2001.

Researches on Laplace- or Laplace-Fourier-domain inversion usually used the diagonal element of the pseudo-Hessian matrix using the virtual source vector, defined in equation (2-47), for preconditioning of the steepest descent gradient.

$$\mathbf{H}^{p} = \mathrm{Re}\left(\sum_{i}^{n_s} \mathbf{v}^{\mathrm{T}}(\mathbf{v})^{*}\right). \tag{2-47}$$

The preconditioned gradient direction for updating is obtained using steepest decent direction normalized by the diagonal element of the pseudo-Hessian matrix, as follows,

$$\delta m_k = \frac{\sum_i^{n_s} \mathbf{v}_k{}^{\mathrm{T}} \mathbf{S}^{-\mathrm{T}} \mathbf{r}_i}{\mathrm{Re}\left(\sum_i^{n_s} \mathbf{v}_k{}^{\mathrm{T}} (\mathbf{v}_k)^{*}\right) + \eta} \tag{2-48}$$

where δm_k is the preconditioned gradient direction for the model parameter of the k element and η is the damping factor to stabilize the normalization. Now, the updating method in equation (2-40) is need to be changed with the preconditioned gradient direction, as follows

$$\mathbf{m}^{(l+1)} = \mathbf{m}^{(l)} + \alpha^{(l)}\delta m, \tag{2-49}$$

In some numerical tests, the pseudo-Hessian matrix presented in equation (2-47) could not be reasonably preconditioned because of the damping factor. The damping factor η is applied to stabilize the gradient direction. In this context, the damping factor must solely stabilize the gradient, and it must not affect to the global trend of the gradient direction. However, it was contributed to the inverted result.

A simple test was performed to investigate the effect of the damping factor on the pseudo-Hessian matrix. Figure 13 shows the 3 types of true model sets that were used for this test. The P-wave velocity models were constructed using a 1500 m/s background velocity and a 3000 m/s box-shaped structure at depths of 1000 m to 2000 m, 1500 m to 2500 m, and 2000 m to 3000 m. The S-wave velocity models were constructed using a 866 m/s background velocity and a 1732 m/s box-shaped structure at depths of 1000 m to 2000 m, 1500 m to 2500 m, and 2000 m to 3000 m, relatively. The density model was a 2 g/cc homogeneous model. Figure 14 shows the initial velocity models; the initial P-wave model was a 2000 m/s constant model, and the initial S-wave model was a 1200 m/s constant model. The density was assumed to be 2 g/cc.

The inversion was performed using 6 Laplace damping constants (2, 4, 6, 8, 10, and 12) and 3 different damping factors. The damping factor was determined as a proportion of the maximum of the pseudo-Hessian matrix as follows:

$$\eta = d \times \max(\mathbf{H}^{p}) \tag{2-50}$$

In Figure 15, the inverted P-wave results was presented using the 3 types of datasets with 3 different damping factors after 30 iterations. The results

demonstrate that the damping factor affects the determination of the inverted depth. The inverted result for $d = 10^{-1}$ is biased in the upwind direction, and the result for $d = 10^{-5}$ is biased in the downward direction. These results indicate that elastic Laplace-Fourier-domain inversion cannot always yield a reasonable result because of the effect of the damping factor.

For a more detailed analysis, the 1D steepest-descent direction and the pseudo-Hessian was extracted at 10,000 m from the left origin for the 1st test, with a high-velocity structure located at a depth of 1000 m to 2000m and for a Laplace damping constant of 2. First, in Figure 16, the steepest gradient, pseudo-Hessian without the damping factor, and the gradient direction were presented and the gradient direction was preconditioned using a pseudo-Hessian without a damping factor.

The preconditioned gradient using a pseudo-Hessian without a damping factor cannot compensate for the geometrical-spreading effect in this analysis. Second, Figure 17 shows the pseudo-Hessian matrixes are computed using the 5 damping factors $d = 10^{-1}, 10^{-2}, 10^{-3}, 10^{-4}, \text{and } 10^{-5}$ to illustrate how the matrix changes with respect to the damping factor. In this plot, it is apparent that the value of the applied damping factor plays a role in the minimum tolerance limit for the Hessian, and it causes unexpected changes in the preconditioned gradient, as shown in Figure 18. The preconditioned gradient direction is tend to emphasize a deeper region following as the damping factor goes to small. From results of this analysis, it seems to that the pseudo-Hessian matrix derived using the conventional l_2 norm is not appropriate for applying to this algorithm.

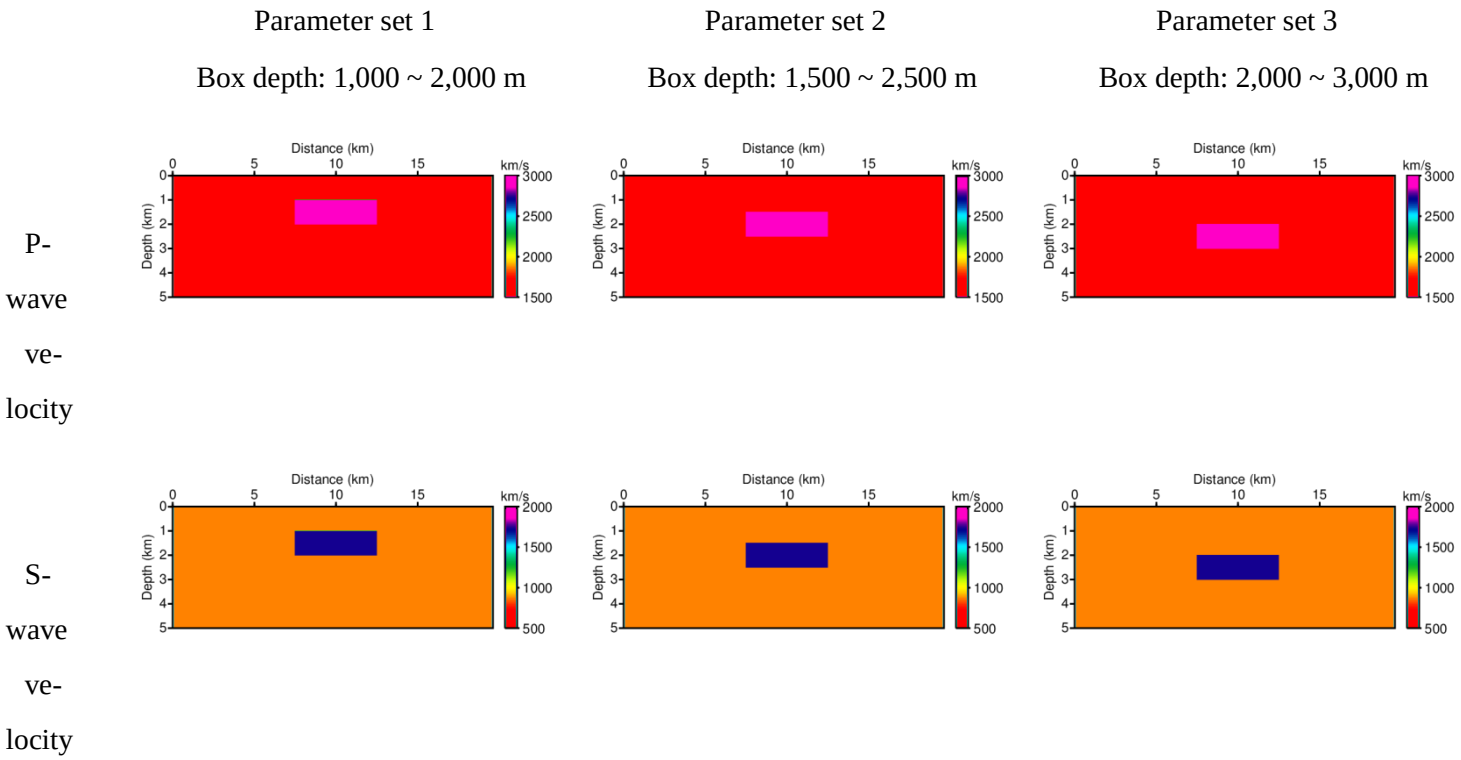

Figure 13. Parameter sets containing the box-shaped structures at different depths for testing the pseudo-Hessian matrix.

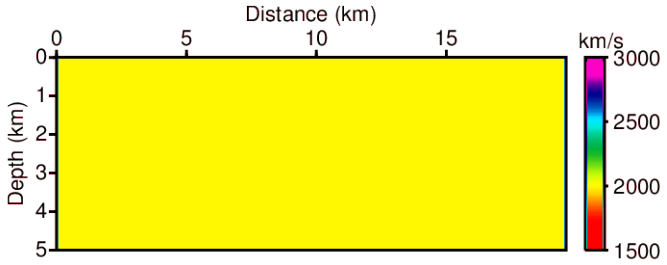

(a)

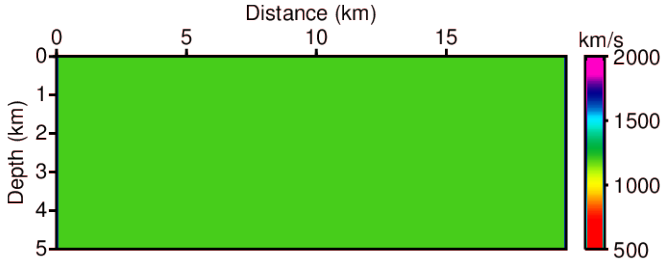

(b)

Figure 14. The initial models for the tests of the pseudo-Hessian matrix: (a) 2000 m/s homogeneous P-wave velocity model and (b) 1200 m/s homogeneous S-wave velocity model.

In 2012, Ha et al. introduced a modified pseudo-Hessian matrix that was derived for the logarithmic objective function. Presented below is the modified pseudo-Hessian matrix for the logarithmic objective function.

$$\mathbf{H}^p = \mathrm{Re}\left(\sum_i^{n_s}\left(-\frac{\partial \mathbf{S}}{\partial m}\mathbf{c}\right)^{\mathrm{T}}\left(-\frac{\partial \mathbf{S}}{\partial m}\mathbf{c}\right)^{*}\right), \tag{2-51}$$

where $\mathbf{c}^{\mathrm{T}} = (1, 1, \cdots, 1)$. This pseudo-Hessian matrix does not contain the information about the modeled wavefield. They have demonstrated that their pseudo-Hessian matrix properly preconditions the steepest-descent gradient direction in the acoustic inversion problem. From here, to prevent confusing names, the pseudo-Hessian matrix derived from the conventional l_2 norm is indicated with $\mathbf{H}_{l_2}{}^p$, while the other is expressed as $\mathbf{H}_{log}{}^p$.

$\mathbf{H}_{log}{}^p$ is applied to the elastic equation. First, the partial-derivative of the impedance matrix for arbitrary element *k* with respect to the model parameters of the elastic wave equation ($\lambda, \mu,$ and ρ) can be expressed using the following equations:

$$-\frac{\partial \mathbf{S}}{\partial \lambda_k}\mathbf{c} = |detJ_k|\begin{pmatrix} a^{k,1} & a^{k,2} \\ a^{k,3} & a^{k,4} \end{pmatrix}\mathbf{c}, \tag{2-52}$$

$$-\frac{\partial \mathbf{S}}{\partial \mu_k}\mathbf{c} = |detJ_k|\begin{pmatrix} 2a^{k,1} + a^{k,4} & a^{k,3} \\ a^{k,2} & a^{k,1} + 2a^{k,4} \end{pmatrix}\mathbf{c}, \tag{2-53}$$

$$-\frac{\partial \mathbf{S}}{\partial \rho_k}\mathbf{c} = |detJ_k|\begin{pmatrix} \int_{\widehat{K}} (\hat{\phi}_I\hat{\phi}_J)d\widehat{K} & 0 \\ 0 & \int_{\widehat{K}} (\hat{\phi}_I\hat{\phi}_J)d\widehat{K} \end{pmatrix}\mathbf{c}, \tag{2-54}$$

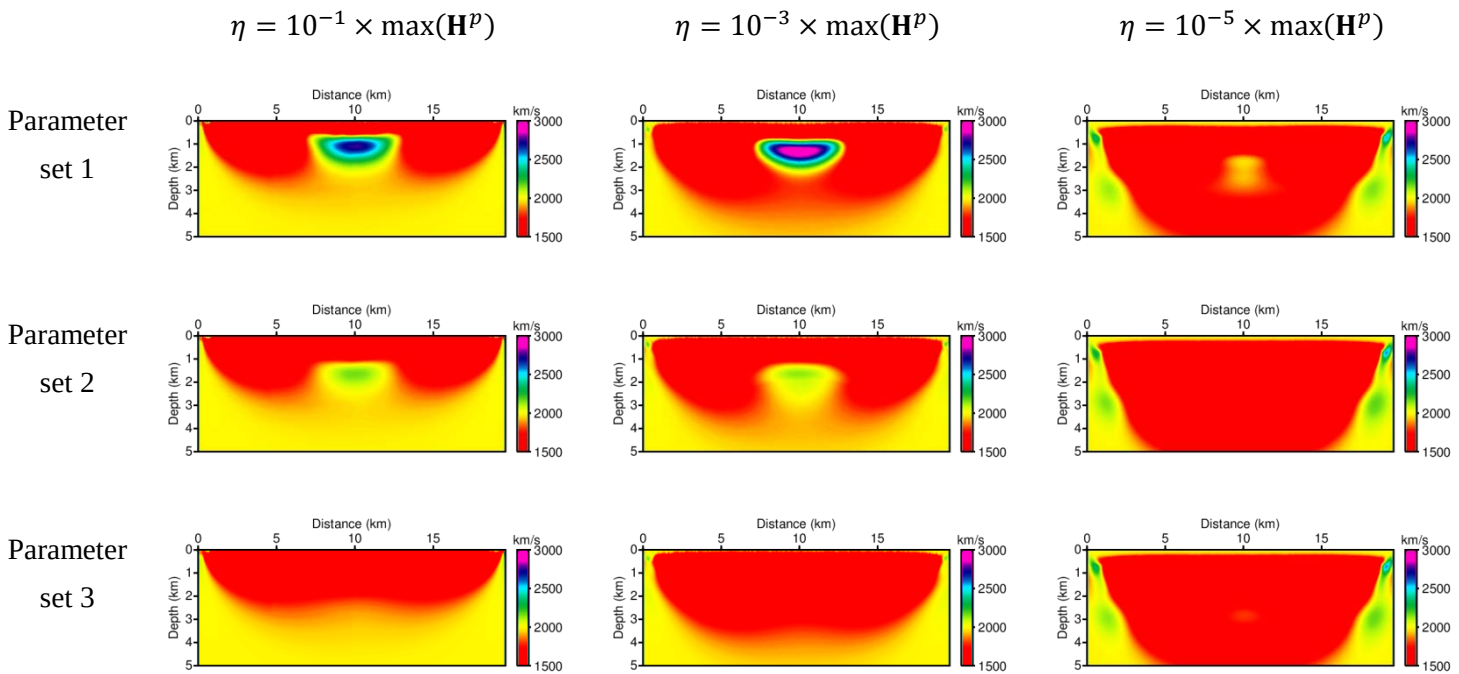

Figure 15. Inverted P-wave velocity using 3 types of damping factors for 3 datasets.

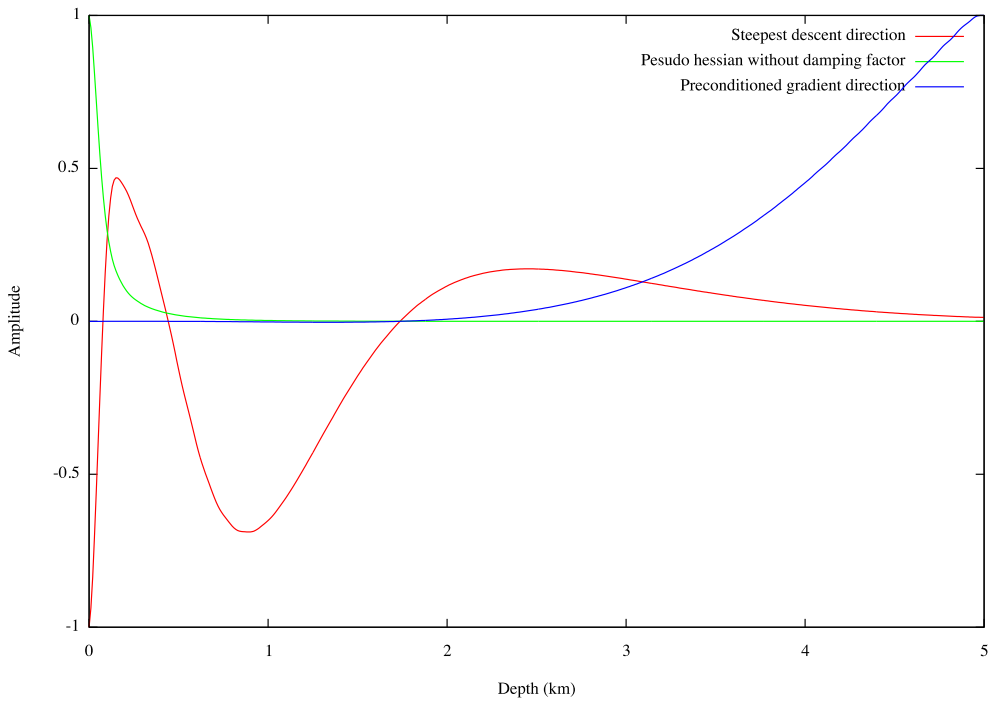

Figure 16. The plots of the 1D steepest-descent direction, the pseudo-Hessian without the damping factor, and the gradient direction obtained when preconditioned using the pseudo-Hessian without damping. These 1D plots were extracted for the location 10,000 m from the left origin for the Hessian test using 1st dataset.

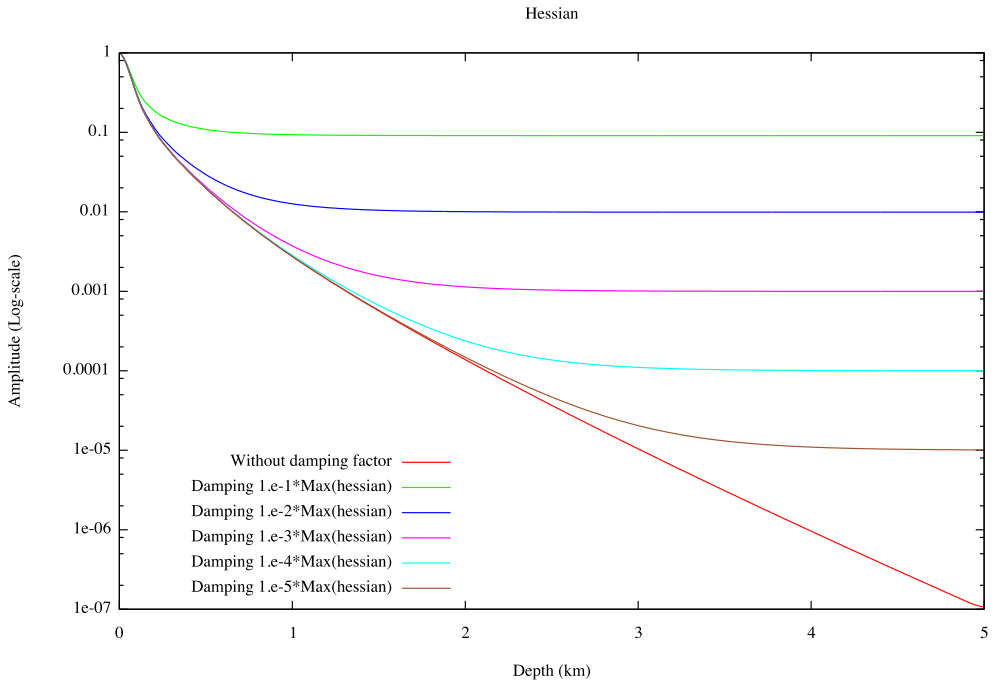

Figure 17. The 1D Hessian matrix without a damping factor and with the various damping factors The 1D pseudo-Hessian matrix without a damping factor and with the various damping factors $d = 10^{-1}, 10^{-2}, 10^{-3}, 10^{-4},$ and 10^{-5}.

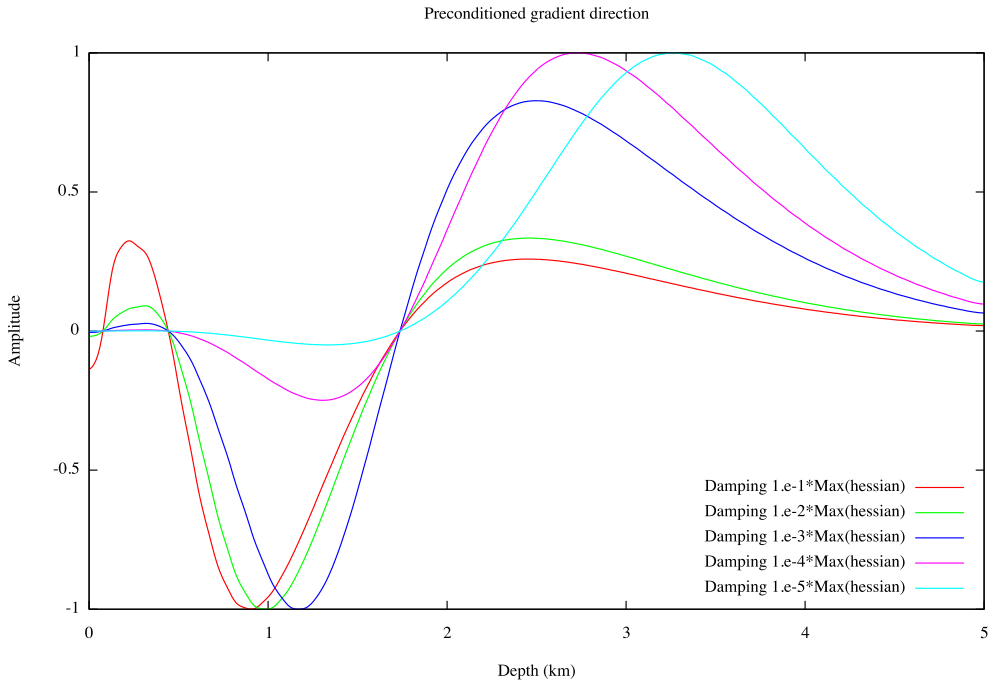

Figure 18. The 1D preconditioned gradient directions obtained using pseudo-Hessians with various damping factors: $\boldsymbol{d = 10^{-1}, 10^{-2}, 10^{-3}, 10^{-4},}$ **and** $\boldsymbol{10^{-5}}$.

Where a^k matrix is consist of ${a_{I,J}}^k$ with size of ${n_{dof}}^k \times {n_{dof}}^k$. The matrix size of partial derivatives is $2{n_{dof}}^k \times 2{n_{dof}}^k$ and the size of vector $\mathbf{c}$ is $2{n_{dof}}^k$.

$$ {a_{I,J}}^{k,1} = \int_{\widehat{K}} \nabla\phi_I {J_k}^{-1} \begin{pmatrix} 1 & 0 \\ 0 & 0 \end{pmatrix} {J_k}^{-\mathrm{T}} \nabla\phi_J d\widehat{K}, \tag{2-55} $$

$$ {a_{I,J}}^{k,2} = \int_{\widehat{K}} \nabla\phi_I {J_k}^{-1} \begin{pmatrix} 0 & 0 \\ 1 & 0 \end{pmatrix} {J_k}^{-\mathrm{T}} \nabla\phi_J d\widehat{K}, \tag{2-56} $$

$$ {a_{I,J}}^{k,3} = \int_{\widehat{K}} \nabla\phi_I {J_k}^{-1} \begin{pmatrix} 0 & 1 \\ 0 & 0 \end{pmatrix} {J_k}^{-\mathrm{T}} \nabla\phi_J d\widehat{K}, \tag{2-57} $$

$$ {a_{I,J}}^{k,4} = \int_{\widehat{K}} \nabla\phi_I {J_k}^{-1} \begin{pmatrix} 0 & 0 \\ 0 & 1 \end{pmatrix} {J_k}^{-\mathrm{T}} \nabla\phi_J d\widehat{K}, \tag{2-58} $$

From these derivatives demonstrate that ${\mathbf{H}_{log}}^p$ are computed using the values of $|detJ_k|$ and J_k for each element k. It means that it contains only information of the element; thus, it cannot compensate for the geometrical-spreading effect for the elastic case. For example, ${\mathbf{H}_{log}}^p$ gives a constant value when the mesh is a structured grid.

Now, we propose that another pseudo-Hessian matrix for the logarithmic objective function can be used for the elastic inversion. This novel Hessian matrix is derived from the difference between ${\mathbf{H}_{l_2}}^p$ and ${\mathbf{H}_{log}}^p$. The difference is whether the modeled wavefield $\boldsymbol{u}$ is contained in the matrix. The virtual source of the ${\mathbf{H}_{l_2}}^p$ with respect to the model parameters, for the each element, can be expressed as follows:

$$ -\frac{\partial \mathbf{S}}{\partial \lambda_k}\boldsymbol{u}_k = |detJ_k| \begin{pmatrix} a^{k,1} & a^{k,2} \\ a^{k,3} & a^{k,4} \end{pmatrix} \boldsymbol{u}_k, \tag{2-59} $$

$$-\frac{\partial \mathbf{S}}{\partial \mu_k}\boldsymbol{u}_k = |detJ_k|\begin{pmatrix} 2a^{k,1}+a^{k,4} & a^{k,3} \\ a^{k,2} & a^{k,1}+2a^{k,4} \end{pmatrix}\boldsymbol{u}_k, \tag{2-60}$$

$$-\frac{\partial \mathbf{S}}{\partial \rho_k}\boldsymbol{u}_k = |detJ_k|\begin{pmatrix} \int_{\widehat{K}} (\hat{\phi}_I\hat{\phi}_J)d\widehat{K} & 0 \\ 0 & \int_{\widehat{K}} (\hat{\phi}_I\hat{\phi}_J)d\widehat{K} \end{pmatrix}\boldsymbol{u}_k, \tag{2-61}$$

where the modeled wavefield $\boldsymbol{u}_k$ contains the horizontal and vertical wavefield on the nodes of element k and the size of this vector is $2{n_{dof}}^k$. And then, the ${\mathbf{H}_{l_2}}^p$ can be expressed by substitute these virtual sources to the equation (2-47).

To derive it, we assume that the energy level for the geometrical spreading of the modeled wavefield is similar for each nodal point on the same element; thus, it can be replaced by certain representable value g_k as follows:

$$\begin{aligned} {\mathbf{H}_{l_2}}^p &= \mathrm{Re}\left(\sum_i^{n_s}\left(-\frac{\partial \mathbf{S}}{\partial m}\boldsymbol{u}\right)^{\mathrm{T}}\left(-\frac{\partial \mathbf{S}}{\partial m}\boldsymbol{u}\right)^*\right) \\ &= \mathrm{Re}\left(\sum_i^{n_s}\left(-\frac{\partial \mathbf{S}}{\partial m}\mathbf{c}g_k\right)^{\mathrm{T}}\left(-\frac{\partial \mathbf{S}}{\partial m}\mathbf{c}g_k\right)^*\right) \\ &= \mathrm{Re}\left(\sum_i^{n_s}\left(-\frac{\partial \mathbf{S}}{\partial m}\mathbf{c}g_k\right)^{\mathrm{T}}\left(-\frac{\partial \mathbf{S}}{\partial m}\mathbf{c}g_k\right)^*\right) \\ &= g_k(g_k)^*\mathrm{Re}\left(\sum_i^{n_s}\left(-\frac{\partial \mathbf{S}}{\partial m}\mathbf{c}\right)^{\mathrm{T}}\left(-\frac{\partial \mathbf{S}}{\partial m}\mathbf{c}\right)^*\right) \\ &= g_k(g_k)^*{\mathbf{H}_{log}}^p. \end{aligned} \tag{2-62}$$

Here, the geometrical energy term $g_k(g_k)^*$ for an element k is defined as the following equation:

$$g_k(g_k)^* = \sum_{i}^{{n_{dof}}^k} \left({u_{x,i}}^k \left({u_{x,i}}^k\right)^* + {u_{z,i}}^k \left({u_{z,i}}^k\right)^*\right) / 2{n_{dof}}^k \tag{2-63}$$

From the relationship in equations (2-62), the new pseudo-Hessian matrix for the logarithmic objective function can be obtained as follows,

$$\mathbf{H}_{log}{}^p = \mathbf{H}_{l_2}{}^p / \, g_k(g_k)^* \tag{2-64}$$

The Figure 19 shows the newly derived Hessian matrix, and Figure 20 shows the preconditioned gradient directions. These figures demonstrate that the derived Hessian can compensate the geometrical-spreading effect without damping factor, reasonably.

The same inversion tests were performed using 3 types of datasets and the derived pseudo-Hessian matrix. Figure 21 shows the inverted P-wave results for each dataset after 30 iterations. The inverted results seem to recover successfully the high-velocity structures at the exact positions at which they were located.

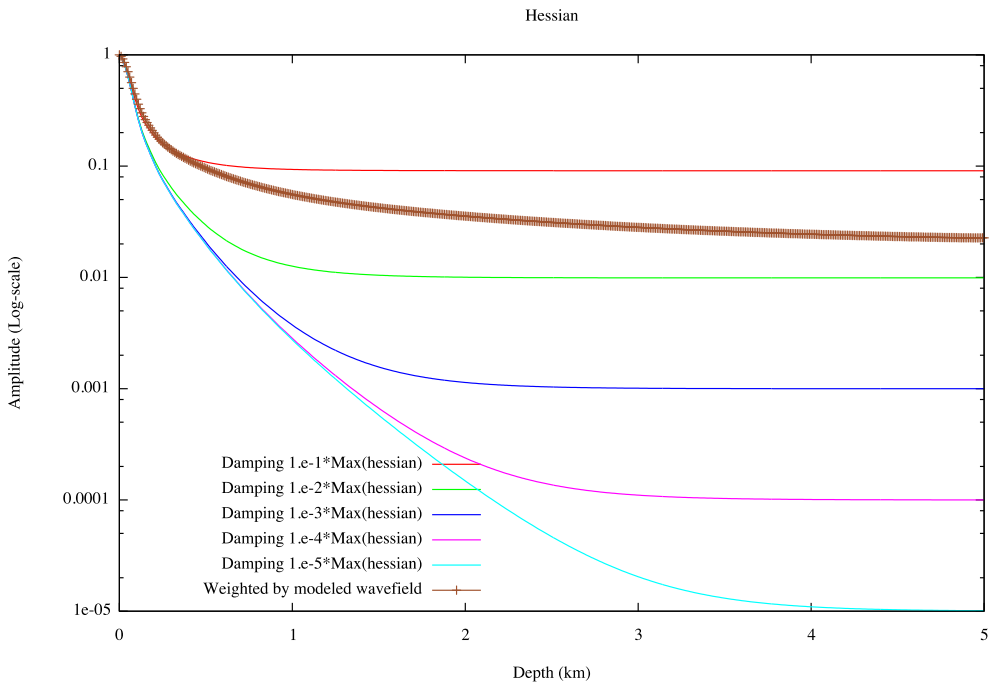

Figure 19. The 1D conventional pseudo-Hessian matrices using various damping factors, $d = 10^{-1}, 10^{-2}, 10^{-3}, 10^{-4}$, and 10^{-5}, and the derived pseudo-Hessian matrix that is regularized using the modeled wavefield.

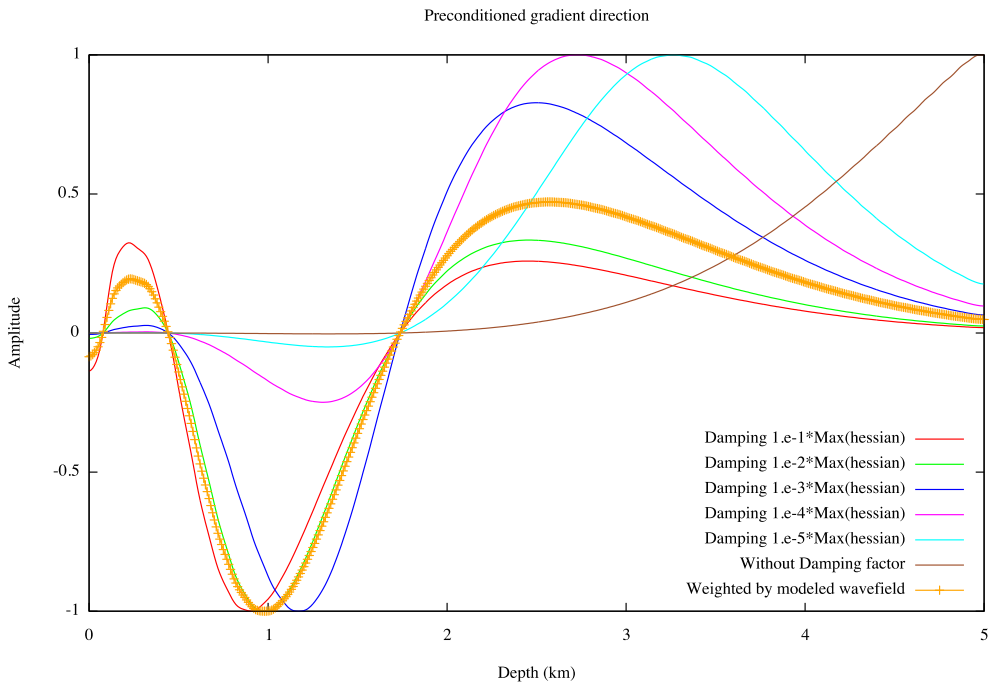

Figure 20.The 1D preconditioned gradient directions obtained using conventional pseudo-Hessians with various damping factors; $d = 10^{-1}, 10^{-2}, 10^{-3}, 10^{-4},$ and 10^{-5}, and using the derived pseudo-Hessian.

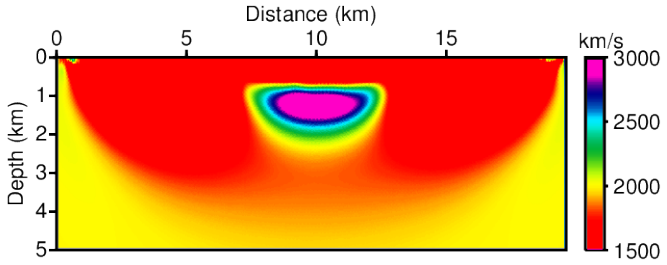

(a)

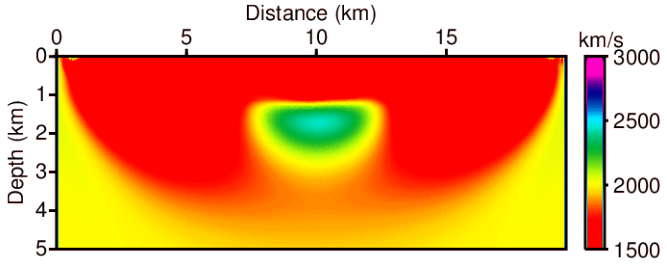

(b)

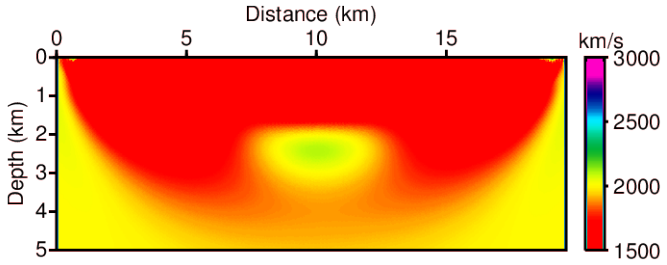

(c)

Figure 21. Inverted P-wave velocity models obtained using the derived pseudo-Hessian for 3 datasets. Inversion results using (a) parameter set 1, (b) parameter set 2 and (c) parameter set 3.

2.4.3 Source-estimation algorithm

The full-Newton method suggested by Shin et al. (2007) is applied to estimate the unknown source wavelet. In this section, it is reviewed.

The Laplace-Fourier-transformed observed data can be defined using the amplitude and phase term as follows,

$$\tilde{d}_j = {A_j}^{obs} e^{i{\phi_j}^{obs}}, \tag{2-65}$$

where ${A_j}^{obs}$ and ${\phi_j}^{obs}$ denote the amplitude and phase, respectively, of the observed data at the location of the j_{th} receiver and an arbitrary source. Similarly, the vertical component of the modeled wavefield for the an arbitrary source in the Laplace-Fourier domain is defined as

$$\tilde{u}_{z,j} = {B_j}^{cal} e^{i{\phi_j}^{cal}} C^{src} e^{i\phi^{src}}, \tag{2-66}$$

where ${B_j}^{cal}$ and ${\phi_j}^{cal}$ denote the amplitude and phase, respectively, of the modeled data at the location of the j_{th} receiver. C^{src} and ϕ^{src} are the amplitude and phase, respectively, of the source wavelet.

The objective function of the source wavelet for the logarithmic wavefield is constructed as follows in equation (2-66). In this thesis, the source-estimation algorithm is applied for each shot independently, instead of applying the one-source-wavelet assumption. The one-source-wavelet assumption is typically applied for the full-waveform inversion, and its applicability is not questioned in the acoustic case, which considers a homogeneous and isotropic medium of water surveyed using an air-gun source. However, for a land survey, the amplitude and phase of the source-wavelet must be assumed differently for each source because of the condition and property of the source triggered position must be different.

The equation (2-67) shows the objective function for the source-wavelet.

$$\mathrm{E}^{s} = \sum_{j}^{n_r} \frac{1}{2} \left(\ln\tilde{u}_{z,j} - \ln\tilde{d}_j\right) \left(\ln\tilde{u}_{z,j} - \ln\tilde{d}_j\right)^{*} \tag{2-67}$$

$$= \sum_{j}^{n_r} \frac{1}{2} \left(\left(\ln \frac{B_j{}^{cal} C^{src}}{A_j{}^{obs}} \right)^2 + \left(\phi_j{}^{cal} + \phi^{src} - \phi_j{}^{obs} \right)^2 \right).$$

The Newton method for an iterative solution can be expressed as

$$\delta m^{s} = -\mathbf{H} \nabla_{m^s} \mathrm{E}^{s}, \tag{2-68}$$

where δm^{s} is the update direction for the source wavelet, which contains both the amplitude and phase of the source. $\mathbf{H}$ is the 2×2 Hessian matrix, which includes 2[nd]-derivative components and is given by

$$\mathbf{H} = \begin{pmatrix} \dfrac{\partial^2 \mathrm{E}^{s}}{\partial C^{src} \partial C^{src}} & \dfrac{\partial^2 \mathrm{E}^{s}}{\partial C^{src} \partial \phi^{src}} \\ \dfrac{\partial^2 \mathrm{E}^{s}}{\partial \phi^{src} \partial C^{src}} & \dfrac{\partial^2 \mathrm{E}^{s}}{\partial \phi^{src} \partial \phi^{src}} \end{pmatrix}. \tag{2-69}$$

With considering of the logarithmic amplitude, the Hessian matrix can be expressed and simply computed as follows:

$$\mathbf{H} = \begin{pmatrix} \dfrac{\partial^2 \mathrm{E}^{s}}{\partial \ln C^{src} \partial \ln C^{src}} & \dfrac{\partial^2 \mathrm{E}^{s}}{\partial \ln C^{src} \partial \phi^{src}} \\ \dfrac{\partial^2 \mathrm{E}^{s}}{\partial \phi^{src} \partial \ln C^{src}} & \dfrac{\partial^2 \mathrm{E}^{s}}{\partial \phi^{src} \partial \phi^{src}} \end{pmatrix}. \tag{2-70}$$

$$= \begin{pmatrix} \sum_{j}^{n_r} 1 & 0 \\ 0 & \sum_{j}^{n_r} 1 \end{pmatrix} = \begin{pmatrix} n_r & 0 \\ 0 & n_r \end{pmatrix}.$$

The gradient-direction vector $\nabla_{m^s}\mathrm{E}^{\mathrm{s}}$ with respect to the parameter can also be computed using the logarithmic amplitudes:

$$\nabla_{m^s}\mathrm{E}^{\mathrm{s}}(\ln C^{src}, \phi^{src}) = \begin{pmatrix} \sum_{j}^{n_s} \ln \frac{{B_j}^{cal} C^{src}}{{A_j}^{obs}} \\ \sum_{j}^{n_s} \left({\phi_j}^{cal} + \phi^{src} - {\phi_j}^{obs}\right) \end{pmatrix}. \tag{2-71}$$

Finally, the update direction of the source-wavelet is obtained as follows:

$$\delta m^s = \frac{1}{n_r} \begin{pmatrix} \sum_{j}^{n_s} \ln \frac{{B_j}^{cal} C^{src}}{{A_j}^{obs}} \\ \sum_{j}^{n_s} \left({\phi_j}^{cal} + \phi^{src} - {\phi_j}^{obs}\right) \end{pmatrix}. \tag{2-72}$$

And the updating algorithm of the source-estimation is such that,

$$m^{s,(l+1)} = m^{s,(l)} + \alpha^{(l)} \delta m^s, \tag{2-73}$$

where $m^{s,(l)}$ is the source wavelet at the l_{th} iteration.

2.4.4 Construction of the mesh

There are many advantages to adopting the unstructured meshes. It is possible to model even complex topography or geological discontinuities almost perfectly, and the mesh size can be locally adapted to the properties of the medium (*h*-adaptivity) or arbitrarily high-order derivatives (*p*-adaptivity) for important regions. However, these advantages can be used only when the properties of the medium are already known.

Full-waveform inversion is applied to determine these properties, so the mesh-construction procedure in this algorithm must be performed without any consideration of the subsurface domain, using only the surface topography information. Moreover, most seismic research has been conducted using structured grids; thus, the compatibility with structured meshes was required for using of previously developed algorithms such as reverse time migration.

Therefore, a mixed-type mesh was used that composed of an unstructured part and a structured part. The unstructured part adopting triangular elements generated using Delaunay refinement algorithm (Shewchuk, 2002) is used to describe the topography, and the structured part is used for the subdomain. This type of mixed mesh allows the error to be minimized when the computed result is need to be moved to a structured grid. Figure 22a and 22b show examples of the fully unstructured mesh and such a mixed-type mesh, respectively.

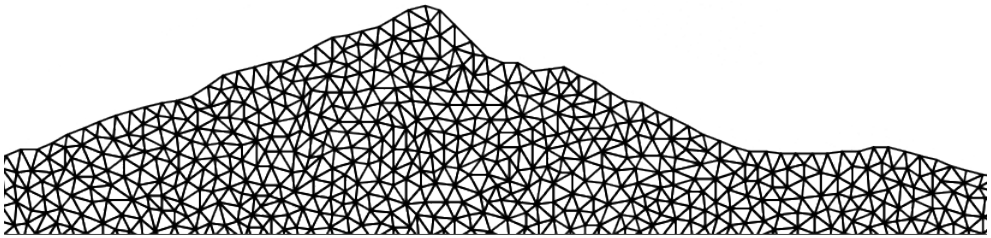

(a)

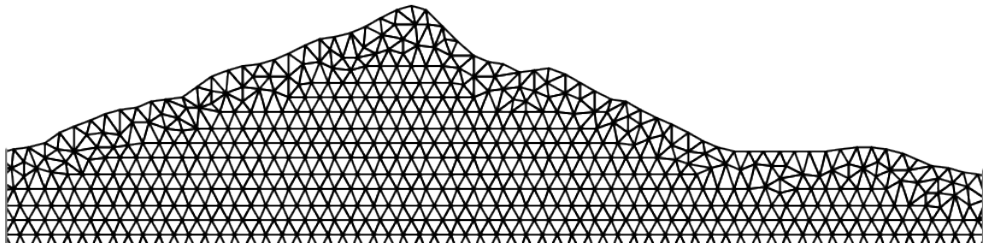

(b)

Figure 22. Examples of (a) unstructured mesh and (b) mixed-type mesh. The surface parts are constructed using unstructured grids, and the inner domain is composed of structured triangular elements for the mixed type mesh.

2.4.5 Stopping criterion using normalized error for the Laplace-Fourier-domain inversion

Full waveform inversion is an indirect method to recover the subsurface parameter by reducing the objective function in an algorithm via iteratively updating the parameters. However, the objective function is not always decreased and it actually begins to get worse again (over-fitting) at some point because of seismic inversion is the problem that always has too many parameters relative to the number of observations. Therefore, the full waveform inversion using fixed number of iterations without considering about it cannot give the best result.

There are basically two ways to fight with over-fitting problem: the first one is reducing the number of parameters and the other is terminating of procedure at proper point (Prechelt, 1997). In this thesis, the developed algorithm was applied the second method from automatically stopping based on stopping criterion with the multi-loop method (Shin et al, 2010).

The following code snippet in Figure 23 shows how the multi-loop algorithm might be implemented. Suppose that there is a routine call `modeling` that computes an impedance matrix for simulating of the wave propagation using current guess model parameter $m^{(l)}$. d denotes Laplace-transformed observed dataset $\ln\tilde{d}_{i,j}$ as presented in equation (2-38), A denotes an inverse of the impedance matrix, $\mathbf{S}^{-1}$ in equation (2-16), and $\mathbf{f}$ is the source vector. For the presented method, the stopping criterion $\epsilon_{obj.}$ was defined based on an objective function and residual. The stopping criterion based on the objective function is the basic method to define it (Prechelt, 1997; Zielinski et al., 2005, 2006).

itermax=... % Limit on the number of iterations
nloop=... % number of loop
d=... % observed dataset

for iloop =1,2,..., nloop
$m^{(1)}$=... % initial guess model parameter
$x^{(1)}$=... % Initial guess source-wavelet model
l =1
While $l \leq$ itermax
$A^{(l)}$=modeling($m^{(l)}$)
$r^{(l)} = A^{(l)}x^{(l)} - d$
$\epsilon_{obj.}^{(l)} = \sum_{i=1}^{n_s}\sum_{j=1}^{n_r} r^{(l)}\left(r^{(l)}\right)^*$
if ($\epsilon_{obj.}^{(l)} > \epsilon_{obj.}^{(l-1)}$ .and. l > 3) then
stop and end or go to the next loop
endif
$\Delta m^{(1)}$=... % Compute the update for model parameter
$\Delta x^{(1)}$=... % Compute the update for source-wavelet
$m^{(l+1)}$=$m^{(l)}$+$\Delta m^{(l)}$
$x^{(l+1)}$=$x^{(l)} + \Delta x^{(l)}$
l= l+1;
end
end

Figure 23. The multi-loop inversion methods using stopping criterion based on the objective function.

A numerical-inversion test using the stopping criterion was applied to the 2 types of dataset; the first dataset contained low-frequency information, while the second did not.

The test model used was the modified Pluto velocity model (Stoughton et al., 2001), which has the complex topography shown in Figure 24. The modified parameter models were reduced in size, but the aspect ratio was maintained. In this test, the S-wave velocity model was generated using a fixed Poisson's ratio (0.21875).

The forward dataset was computed using the 2D elastic IPDG method (described in Appendix A) in the time domain with a 1st-derivative Gaussian source wavelet. The source wavelet was generated with a maximum frequency of 25Hz in the time domain. The number of sources was 100, and the number of receivers was 600. The sources and receivers were located 0.0001 m below the surface. The recording time of the observed dataset was 5 sec with a 2 ms sampling interval. The observed data were obtained using 332,282 triangular elements with P2 shape function (with 6 degrees of freedom per element); thus, the total number of DOF (degrees of freedom) was 1,993,692. The detailed information about synthetic dataset is presented in Table 1.

To remove the low-frequency information for verisimilitude with the real data, a high-pass filter was applied to the observed dataset. Figure 25 shows the designed high-pass filter. Examples of 2 types of datasets with and without low-frequency information were presented in Figure 26 and Figure 27. Figure 26 shows examples of the vertical shot gather of the data from the 51th-source and its frequency spectrum of the low-frequency-containing dataset. Figure 27 shows examples of the shot gather of the filtered data and its frequency spectrum.

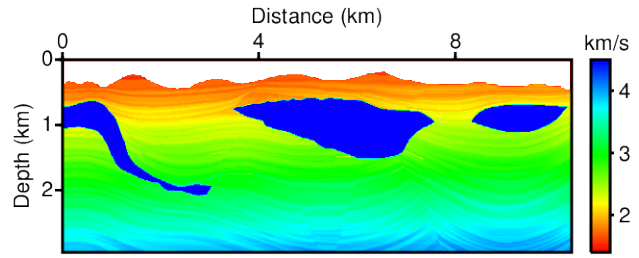

(a)

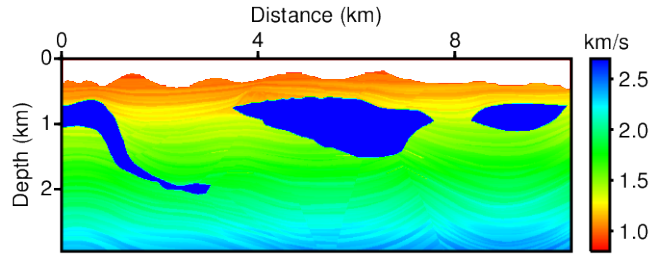

(b)

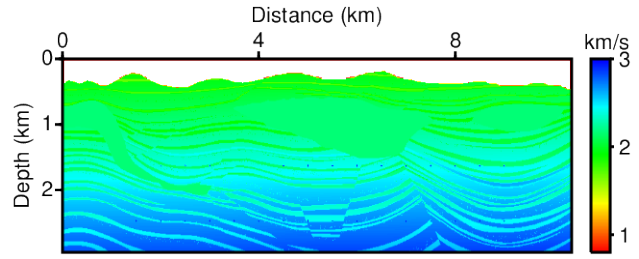

(c)

Figure 24. The modified Pluto parameter set with complex topography: (a) P-wave velocity, (b) S-wave velocity, and (c) density models.

Summary of the information of the synthetic dataset

Domain size	10,380 m × 2,960 m
Far trace offset	10,350 m
Near trace offset	0 m
Number of shots	100
Number of receivers	600
Modeling scheme	IPDG in the time domain
Used number of elements	332,282
Number of total DOF	1,993,692
Recording time	5 sec
Sampling interval	0.002 sec
Source wavelet	1^{st}-derivative Gaussian wavelet
Maximum-frequency of the source wavelet	25 Hz

Table 1. Summary of the information of the generated time-domain synthetic dataset using modified Pluto parameter set.

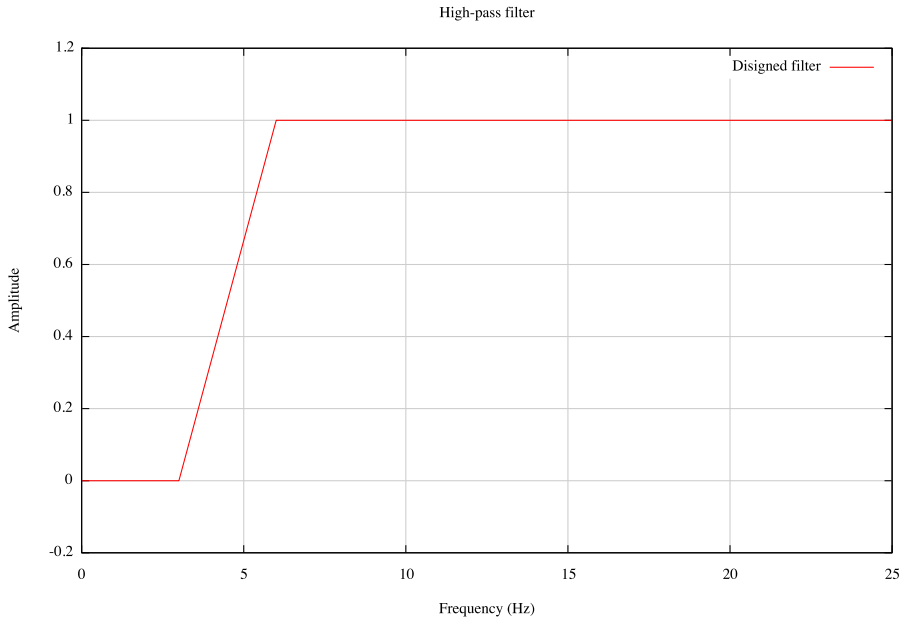

Figure 25. The high-pass filter to remove low-frequency information (frequency=0., 3., 6., and 9. Hz and amplitude=0., 0., 1., and 1.).

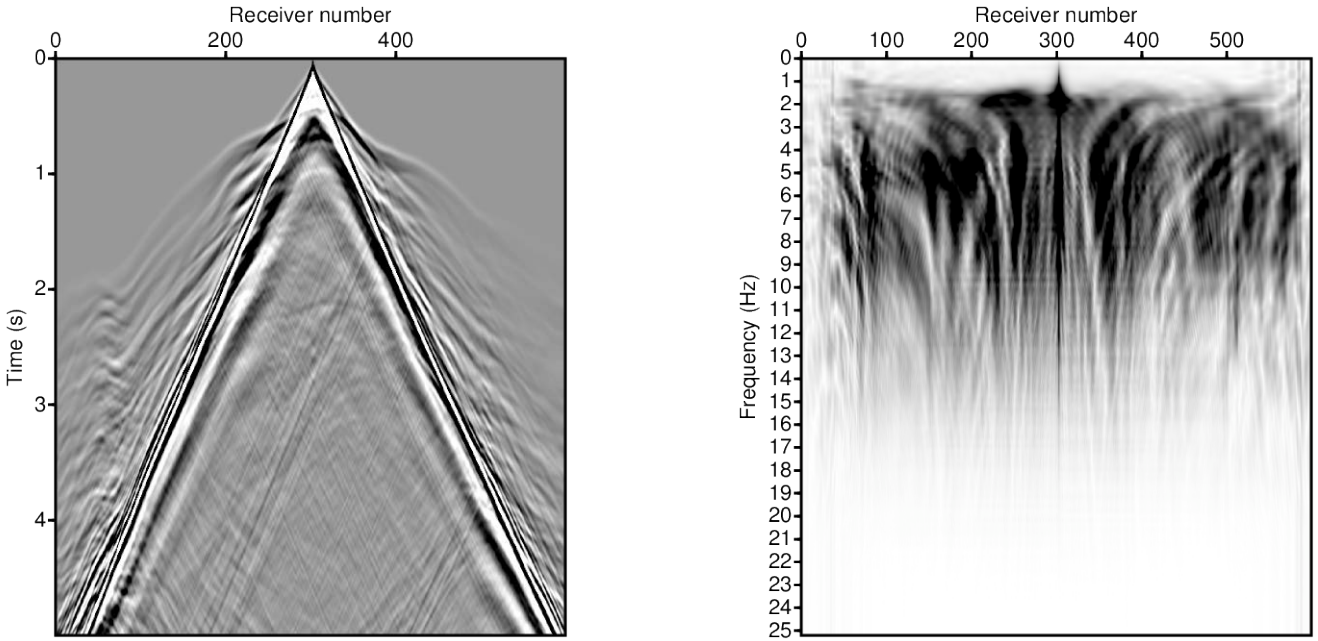

(a) (b)

Figure 26. Examples of the (a) vertical displacement shot gather and its frequency spectrum from the modified Pluto set using the time domain IPDG scheme.

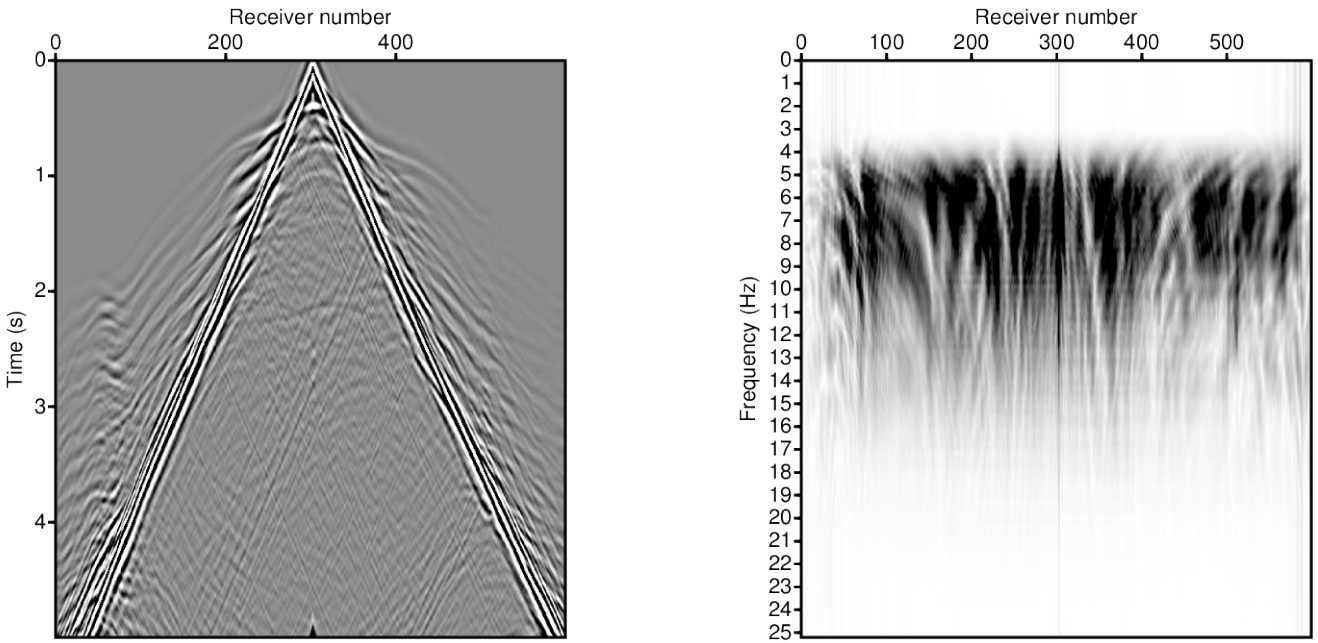

(a) (b)

Figure 27. Examples of the high-pass filtered (a) vertical displacement shot gather and its frequency spectrum from the modified Pluto set using the time domain IPDG scheme.

The Laplace-Fourier-domain inversion was initiated using the linearly increasing velocity models presented in Figure 28, and the density was fixed to 2.3 g/cc. The multistep loops for this test was designed with 21 loops with 500 maximum iteration number for each loop. The modeling in the inversion algorithm was performed via conventional FEM using 85,428 elements with P1 shape functions, and the DOF was 42,950. Detailed summaries of the inversion parameters are presented in Table 2.

The Laplace-Fourier-domain inversion using on the stopping criterion based on objective function computed the P- and S-wave velocities shown in Figure 29 and Figure 30. The inverted P- and S-wave velocities obtained using the low-frequency-containing dataset are successfully show the shape of the salts and the background velocity. However, the inverted results using high-pass filtered dataset seems to over- or under-estimated result in some region as shown in Figure 30.

We considered that it is possible to expect better result by changing the stopping criterion with considering of the characteristics of the logarithmic residual. The logarithmic residual has the property of natural separation into amplitude and phase components, which correspond to the real parts and imaginary parts, respectively, of the complex values as we showed in the theory of the source estimation.

The amplitude and phase error have different and independent meanings. Thus, we supposed that the logarithmic objective function could be treated as the multi-objective function by separating into the amplitude and phase part.

There were studies on frequency inversion using a logarithmic wavefield have considered the amplitude only, the phase only, and both (Shin et al., 2007; Badner et al., 2007; Pyun et al., 2007).

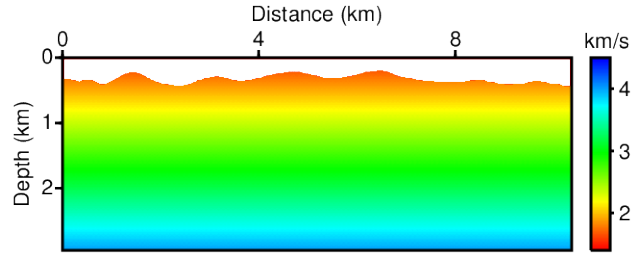

(a)

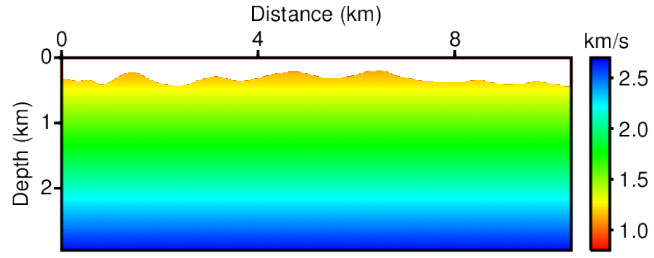

(b)

Figure 28. The initial models for inversion tests with the stopping criterion: (a) initial P-wave velocity model and (b) initial S-wave velocity model.

Summary of the inversion parameters

Loop number	σ	f
1	2, 4, 6, 8, 10,and 12	-
2	2, 4, 6, 8, 10,and 12	0.001 – 2.000 Hz
3	2, 4, 6, 8, 10,and 12	1.000 – 3.000 Hz
4	2, 4, 6, 8, 10,and 12	2.000 – 4.000 Hz
5	2, 4, 6, 8, 10,and 12	3.000 – 5.000 Hz
6	2, 4, 6, 8, 10,and 12	4.000 – 6.000 Hz
7	2, 4, 6, 8, 10,and 12	5.000 – 7.000 Hz
8	2, 4, 6, 8, 10,and 12	6.000 – 8.000 Hz
9	2, 4, 6, 8, 10,and 12	7.000 – 9.000 Hz
10	2, 4, 6, 8, 10,and 12	8.000 – 10.00 Hz
11	2, 4, 6, 8, 10,and 12	9.000– 11.00 Hz
12	2, 4, 6, 8, 10,and 12	10.00– 12.00 Hz
13	2, 4, 6, 8, 10,and 12	11.00– 13.00 Hz
14	2, 4, 6, 8, 10,and 12	12.00– 14.00 Hz
15	2, 4, 6, 8, 10,and 12	13.00– 15.00 Hz
16	2, 4, 6, 8, 10,and 12	14.00– 16.00 Hz
17	2, 4, 6, 8, 10,and 12	15.00– 17.00 Hz
18	2, 4, 6, 8, 10,and 12	16.00– 18.00 Hz
19	2, 4, 6, 8, 10,and 12	17.00– 19.00 Hz
20	2, 4, 6, 8, 10,and 12	18.00– 20.00 Hz
21	2, 4, 6, 8, 10,and 12	19.00– 21.00 Hz

Table 2. Summary of the inversion parameters for each loop. It is designed for the inversion test with modified PLUTO dataset.

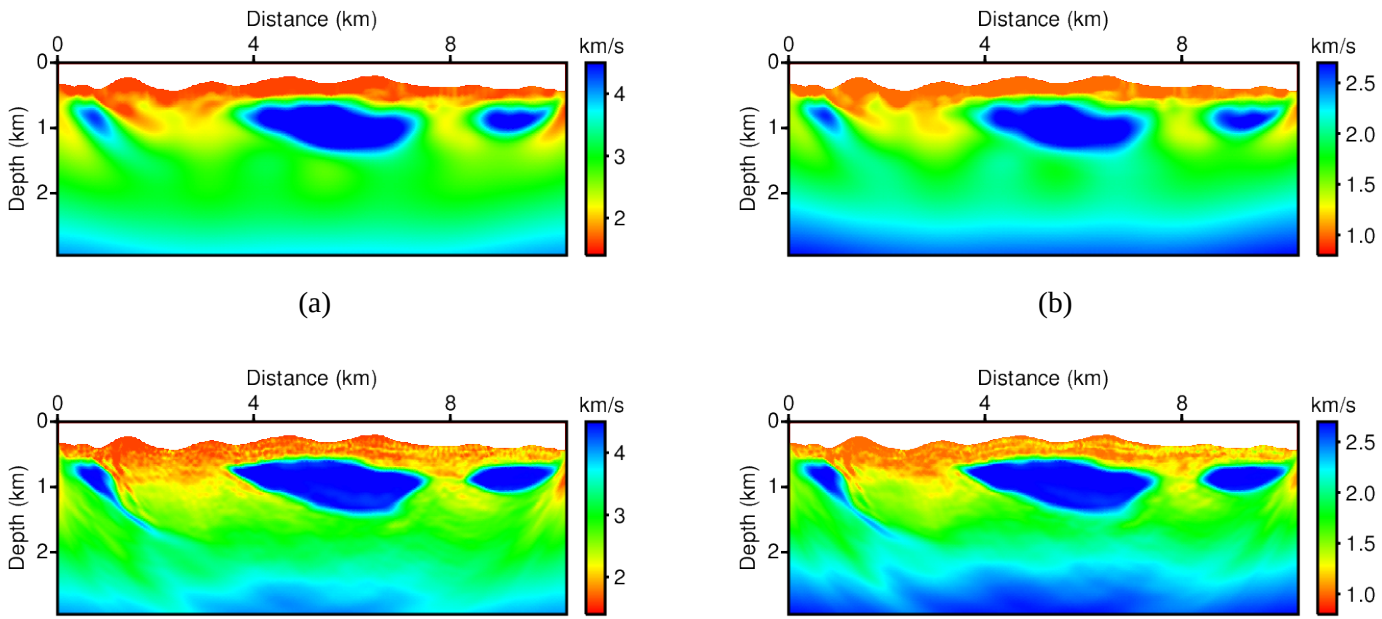

Figure 29. Inverted (a) P-wave and (b) S-wave velocity models obtained using Laplace-domain inversion using the stopping criterion $\epsilon_{obj.}$ and the low-frequency-containing dataset. Inverted (c) P-wave and (d) S-wave velocity models obtained using Laplace-Fourier-domain inversion using the stopping criterion $\epsilon_{obj.}$ and the low-frequency-containing dataset.

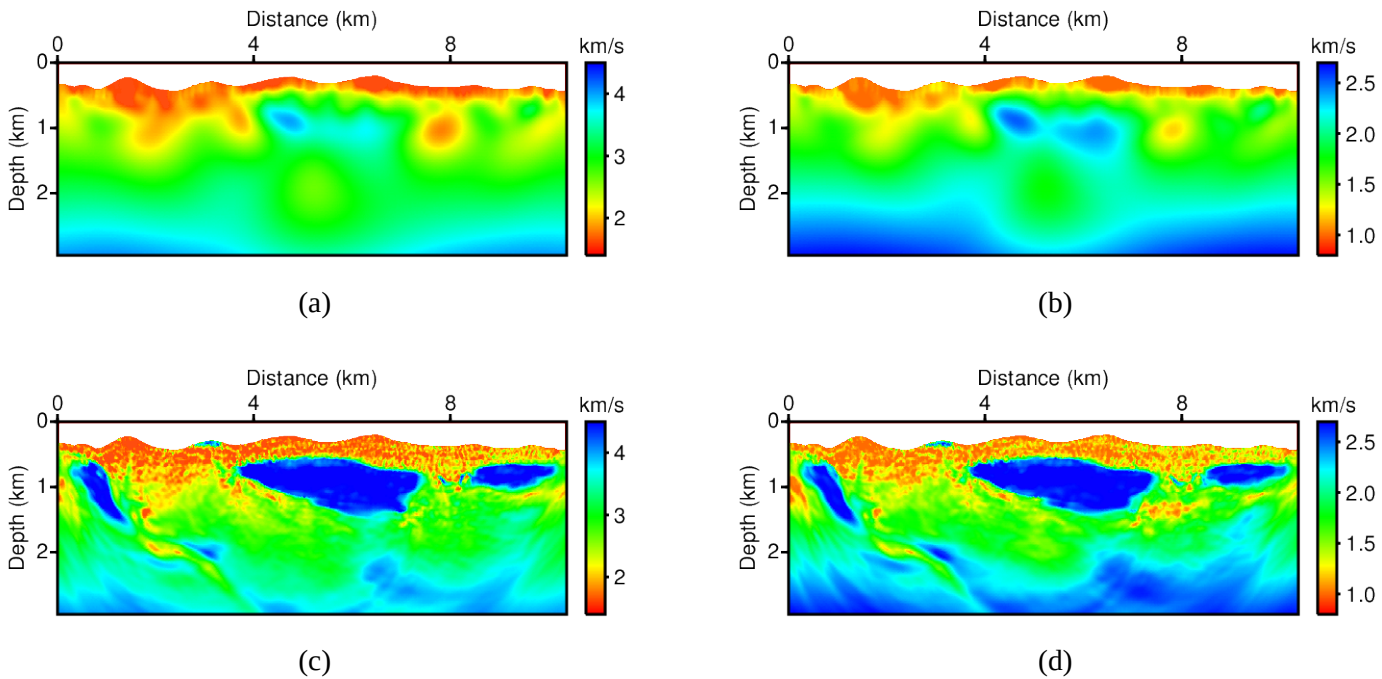

Figure 30. Inverted (a) P-wave and (b) S-wave velocity models obtained using Laplace-domain inversion the stopping criterion $\epsilon_{obj.}$ and the high-pass-filtered dataset. Inverted (c) P-wave and (d) S-wave velocity models obtained using Laplace-Fourier-domain inversion using the stopping criterion $\epsilon_{obj.}$ and the high-pass-filtered dataset.

Of these studies, the logarithmic inversion using both components produced the best result; however, the logarithmic phase inversion yielded a much better inverted result than the amplitude approach. This result indicates that the phase information is more important than the amplitude information for logarithmic frequency inversion. On the other hand, Laplace-domain inversion is an amplitude inversion and amplitude information is the governing parameter.

The Laplace-Fourier-domain inversion is the mixed method of Laplace-domain and frequency-domain inversion and its characteristic is varied with respect to the used Laplace-damping constant and frequency information. For lower-frequency components and higher-Laplace-damping, it is closer to Laplace-domain inversion, while for higher-frequency components and lower-Laplace-damping, the phase information is more important, similar to Fourier-domain inversion.

Firstly to obtain some information about the magnitude of amplitude and phase error, simple test was performed with respect to 7 Laplace damping constants and 6 frequency components using true parameter models shown in Figure 24 and initial parameter models shown in Figure 28. From the simple test, the amplitude-versus-phase error ratios and the phase-versus-amplitude error ratios was obtained with respect to the Laplace damping constants and frequency components as presented in Figure 31. In these plots, it is apparent that the Laplace-Fourier-domain inversion may be dominated by either the amplitude error or the phase error depending on the particular value of the Laplace damping constant and the frequency component. When the logarithmic objective function is considered as the multi-objective problem, then a reasonable solution must be to investigate a set of solutions, each of which objectives at an acceptable level without being dominated by 1 factor.

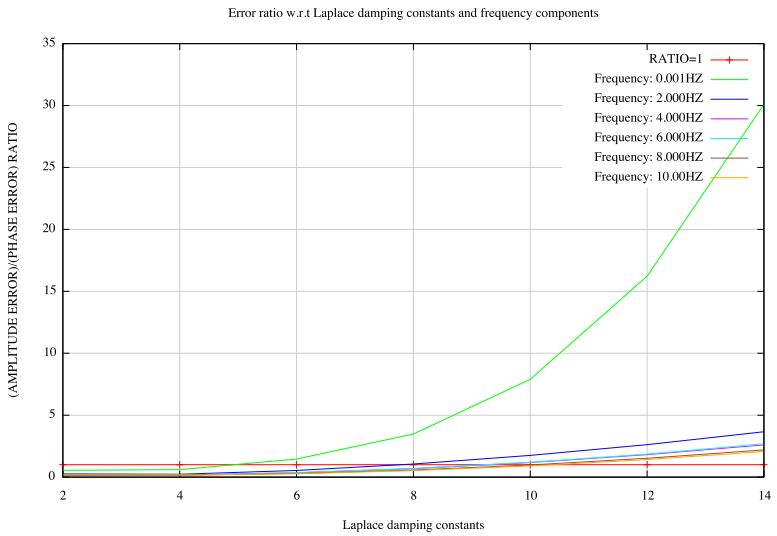

(a)

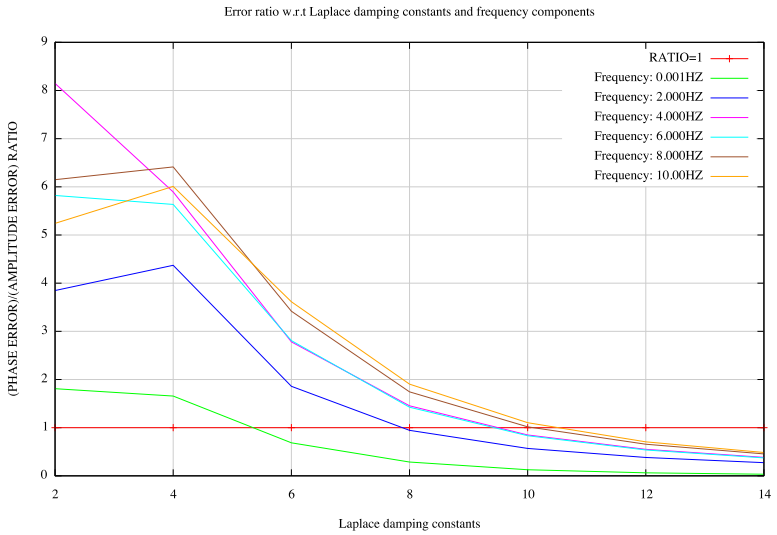

(b)

Figure 31. The magnitude of the (a) amplitude-versus-phase error ratio and (b) phase-versus-amplitude error ratio for 7 Laplace damping constants: σ={2, 4, 6, 8, 10, 12, and 14} and f={0.0, 2.0, 4.0, 6.0, 8.0, and 10.0}.

For the multi-objective assumption, the weighted sum approach was applied to define the stopping for equal contributions of amplitude and phase information and the multi-loop inversion using this criterion is presented in Figure 32 (Konak, 2006; Recktenwald, 2012).

To verify the efficacy of the stopping criterion, the same numerical-inversion test was performed. Figure 33 and Figure 34 show the Laplace-Fourier-domain inverted results for the low-frequency-containing data and the filtered data, respectively. The results obtained for the low-frequency-containing dataset exhibit no improvement in the inverted results with respect to the results obtained using the conventional stopping criterion. However, the inverted results shown in Figure 34 for the high-pass-filtered dataset demonstrate that the Laplace-Fourier-domain inversion using the stopping criterion based on multi-objective assumption was able to recover superior results with respect to the inverted result shown in Figure 30. P-wave velocity residuals between the true models and inverted models are presented in Figure 35 to illustrate the performance of 2 stopping criterions. The residuals and histograms demonstrate the normalized stopping criterion, $\epsilon_{nor.}$, give better result.

Table 3 and Table 4 show the performance of the stopping criterion based on the objective function, i.e. $\epsilon_{obj.}$, and the multi-objective assumption of the logarithmic objective function, i.e. $\epsilon_{nor.}$. In the Table 3 and Table 4Table 3, the first branch point of these tests can be observed at the 2nd loop and it must be returned as a totally different final result for this kind hierarchical multi-loop approach. The Figure 36 shows error curves obtained using 2 different stopping criterions, in the 2nd loop. In this plot, $\epsilon_{obj.}$ made to keep going the inversion procedure until the objective function faced to its terminating point in spite of that the amplitude error was increasing, whereas $\epsilon_{nor.}$ Terminated

the calculation earlier to prevent the large over-fitting of amplitude error.

Here, the stopping criterion tests were performed using 2 types of definition; the first one was defined from the objective function and the second was suggested as the normalized objective function using the assumption of multi-objective problem based on the characteristic of the logarithmic objective function, i.e. natural separation into amplitude and phase components. And in this numerical test, we could obtain better result using the suggested normalized stopping criterion.

itermax=... % Limit on the number of iterations
nloop=... % number of loop
d=... % observed dataset

for iloop =1,2,..., nloop
$m^{(1)}$=... % initial guess model parameter
$x^{(1)}$=... % Initial guess source-wavelet model
l =1
While $l \leq$ itermax
$A^{(l)}$=**modeling**($m^{(l)}$)
$r^{(l)} = A^{(l)}x^{(l)} - d$
if ($l = 1$) then
$r^0 = r^{(l)}$
endif
$\epsilon_{nor.}^{(l)} = \sum_{i=1}^{n_s}\sum_{j=1}^{n_r}\left(\frac{\mathrm{Re}(r^{(l)})^2}{\mathrm{Re}(r^0)^2} + \frac{\mathrm{Im}(r^{(l)})^2}{\mathrm{Im}(r^0)^2}\right)$
if ($\epsilon_{nor.}^{(l)} > \epsilon_{nor.}^{(l-1)}$ .and. l > 3) then
stop and end or go to the next loop
endif
$\Delta m^{(1)}$=... % Compute the update for model parameter
$\Delta x^{(1)}$=... % Compute the update for source-wavelet
$m^{(l+1)}$=$m^{(l)}$+$\Delta m^{(l)}$
$x^{(l+1)}$=$x^{(l)} + \Delta x^{(l)}$
l= l+1;
end
end

Figure 32. The multi-loop inversion methods using stopping criterion based on the multi-objective assumption of the logarithmic objective function.

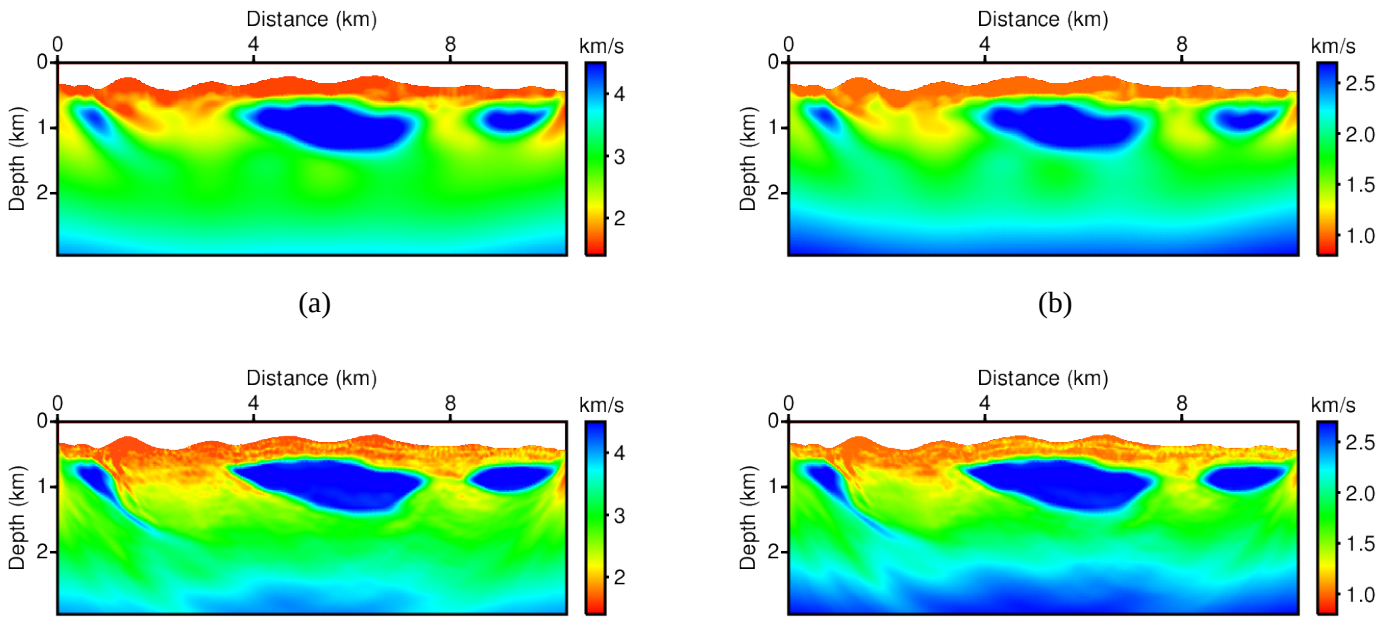

Figure 33. Inverted (a) P-wave and (b) S-wave velocity models obtained using Laplace-domain inversion using the normalized stopping criterion $\epsilon_{nor.}$ and the low-frequency-containing dataset. Inverted (c) P-wave and (d) S-wave velocity models obtained using Laplace-Fourier-domain inversion using the normalized stopping criterion $\epsilon_{nor.}$ and the low-frequency-containing dataset.

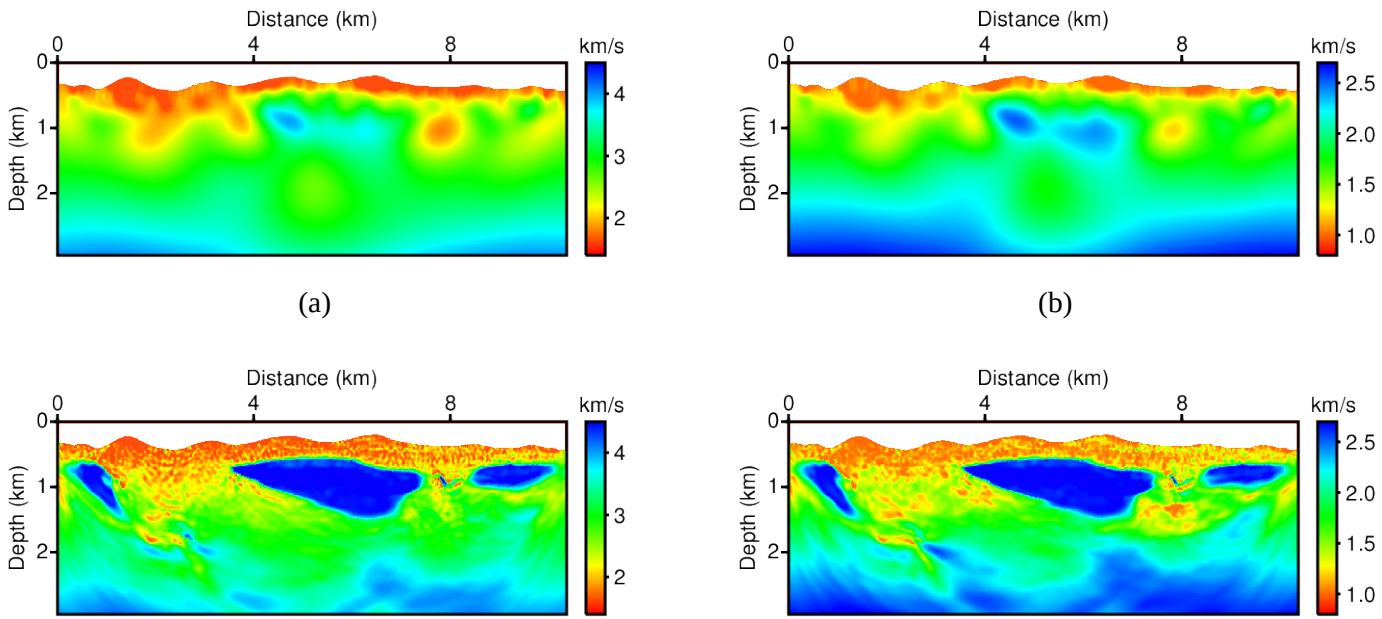

Figure 34. Inverted (a) P-wave and (b) S-wave velocity models obtained using Laplace-domain inversion using the normalized stopping criterion $\epsilon_{nor.}$ and the high-pass-filtered dataset. Inverted (c) P-wave and (d) S-wave velocity models obtained using Laplace-Fourier-domain inversion usisng the normalized stopping criterion $\epsilon_{nor.}$ and the high-pass-filtered dataset.

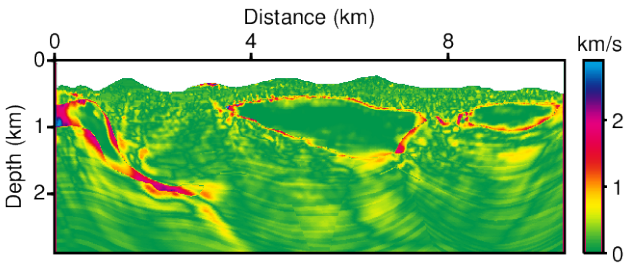

(a)

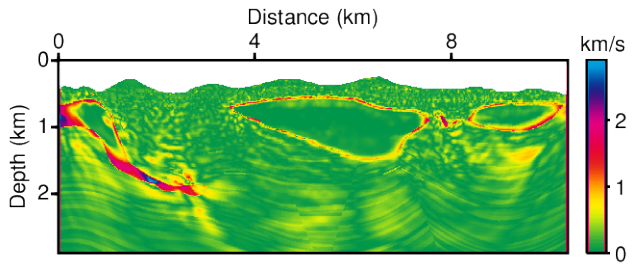

(b)

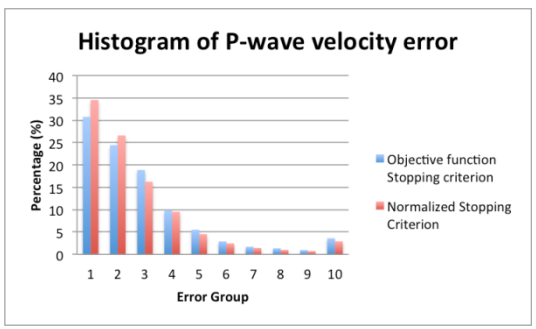

(c)

Figure 35. The P-wave residuals between true models and initial models obtained with (a) $\epsilon_{obj.}$, (b) $\epsilon_{nor.}$, and (c) histogram of the magnitude of the error of P-wave. Error groups defined as (1) 0.0 ~ 0.1, (2) 0.1 ~ 0.2, (3) 0.2 ~ 0.3, (4) 0.3 ~ 0.4, (5) 0.4 ~ 0.5, (6) 0.5 ~ 0.6, (7) 0.6 ~ 0.7, (8) 0.7 ~ 0.8, (9) 0.8 ~ 0.9, and (10) 0.9 ~ km/s.

The number of over-fitting with $\epsilon_{obj.}$

Loop number	Number of Iterations	Objective	Amplitude	Phase
1	75	0	0	0
2	260	0	153	0
3	500	0	51	0
4	500	0	0	0
5	500	0	0	0
6	500	0	0	0
7	500	0	0	0
8	500	0	0	0
9	343	0	0	2
10	500	0	106	1
11	31	0	6	0
12	77	0	25	1
13	50	0	15	1
14	4	0	0	0
15	136	0	2	0
16	23	0	5	0
17	53	0	4	0
18	65	0	14	3
19	31	0	9	0
20	21	0	4	0
21	17	0	4	0
SUM	**4686**	**0**	**398**	**8**

Table 3. The summaries about the number of over-fitting for objective function, amplitude error, and phase error when the stopping criterion $\epsilon_{obj.}$ is applied.

The number of over-fitting with $\epsilon_{nor.}$

Loop number	Number of Iterations	Objective	Amplitude	Phase
1	75	0	0	0
2	64	0	45	0
3	452	0	181	0
4	500	0	1	0
5	500	0	0	0
6	500	0	0	0
7	500	1	0	0
8	144	3	0	3
9	500	1	0	5
10	442	0	0	2
11	64	0	6	5
12	9	0	2	0
13	74	0	2	0
14	4	0	0	0
15	17	0	0	0
16	4	0	0	0
17	33	1	2	3
18	24	0	6	1
19	18	0	2	0
20	38	1	3	2
21	4	0	0	0
SUM	**3966**	**7**	**250**	**21**

Table 4. The summaries about the number of over-fitting for objective function, amplitude error, and phase error when the stopping criterion $\epsilon_{nor.}$ is applied.

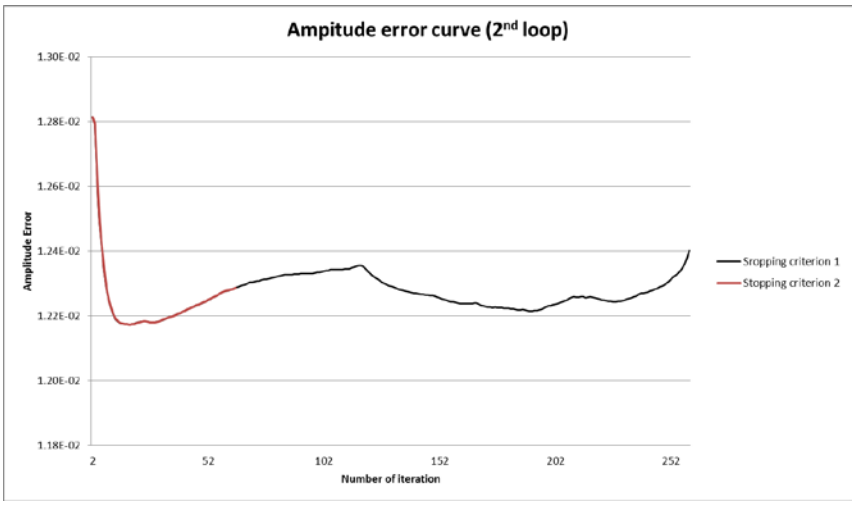

(a)

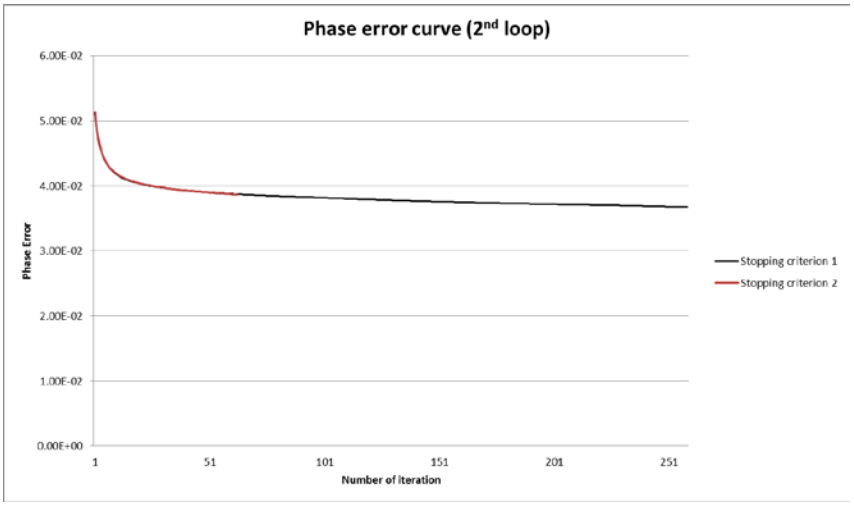

(b)

Figure 36. The error curves at 2nd loop obtained using stopping criterions; (a) amplitude and (b) phase error. Stopping criterion 1 indicates $\epsilon_{nor.}$ and stopping criterion indicates $\epsilon_{nor.}$.

Chapter 3. Examples using synthetic data

The developed elastic full-waveform inversion in the Laplace-Fourier domain was applied to synthetic datasets computed with ‘IPATI model’ as shown in Figure 37. The ‘IPATI model’ is the velocity model that describes the geological structure of the southern Bolivia region. This velocity model represents a folded mountain with complex topography.

The inversion was performed using several datasets treated with different purposes and the same initial parameter models shown in Figure 38 for every test. First, the algorithm was applied to a synthetic dataset generated using the same forward modeling scheme as used in the inversion procedure to verify the algorithm.

Second, the developed algorithm was applied to the synthetic dataset generated with the IPDG scheme in the time domain. In the test using time-domain dataset, the elastic Laplace-Fourier-domain inversion algorithm was applied to several datasets with purpose of the dependency on the low- frequency information and the observation of the performance with a noisy dataset.

And Last, we compared the results of 2D acoustic and 2D elastic inversion in the Laplace-Fourier domain for the same dataset to illustrate why elastic inversion is necessary for a land dataset.

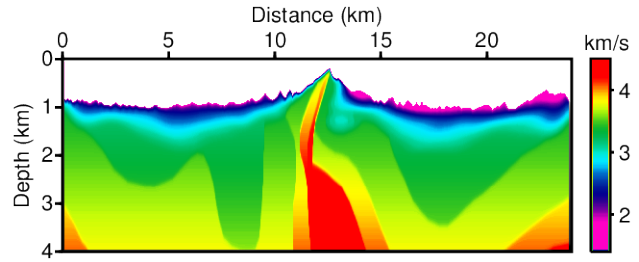

(a)

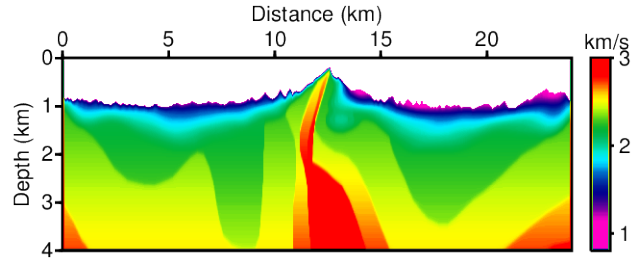

(b)

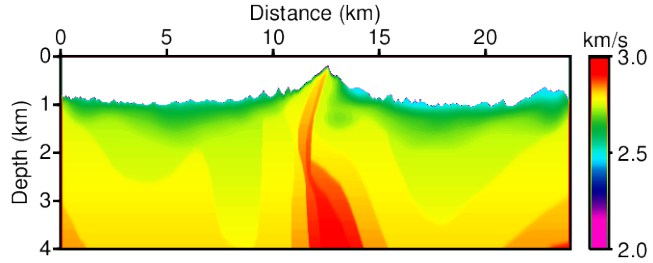

(c)

Figure 37. IPATI parameter set that describes a realistic folded mountain: (a) P-wave velocity, (b) S-wave velocity, and (c) density models.

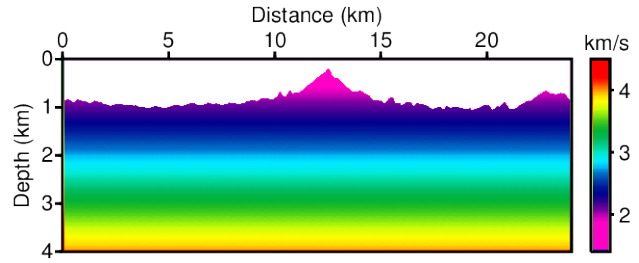

(a)

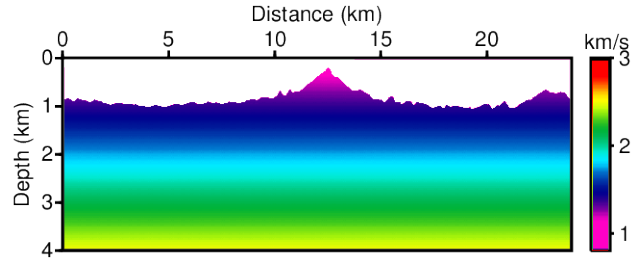

(b)

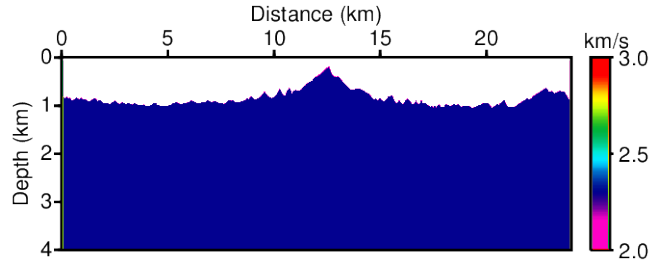

(c)

Figure 38. The initial parameter set for synthetic inversion tests: (a) initial P-wave velocity model, (b) initial S-wave velocity model, and (c) initial density models.

3.1 Laplace-Fourier-domain synthetic dataset

The developed algorithm was applied to the generated synthetic data using the Laplace-Fourier-domain IPDG modeling with the 'IPATI model' shown in Figure 37.

The synthetic model was generated using the IPDG scheme on an unstructured grid with 258,935 elements and 776,805 DOF for a 24 km × 4km domain. The generated synthetic dataset had 960 sources, and the number of the receivers varies from 672 to 1,640 depending on the source position. This distribution of sources and receivers followed the source and receiver placement of the real land acquisition performed by TOTAL at Ipati, Bolivia, in 2003. The far- and near-trace offsets were 6.25 m and 10,256.25 m, respectively. Detailed summaries of the information about the Laplace-Fourier-domain synthetic dataset are presented in Table 5.

The loop strategy of inversion comprised with 9 steps from low- to high-frequency components. Each loop used a different size of mesh. A detailed summary of the inversion strategy is presented in Table 6.

The inversion was initiated with linearly increasing velocity models and homogeneous density model. The initial P-wave velocity model varied from 1.5 km/s to 4.0 km/s, and initial S-wave velocity model varied from 1.0 km/s 2.5 km/s with respect to the depth. The initial density model was a 2.3 g/cc constant model. Throughout the entire inversion step, the density was assumed to be a constant value.

The inversion was performed using the normalized stopping criterion. Figure 39 shows the P-wave and S-wave velocity models recovered via Laplace and Laplace-Fourier inversion.

Summary of the information of the synthetic dataset

Domain size	24,000 m × 4.060 m
Far trace offset	10,256.25 m
Near trace offset	6.25 m
Number of shots	960
Number of receivers	672-1640
Modeling scheme	IPDG in the Laplace-Fourier domain
Used number of elements	258,935
Number of total DOF	776,805
Source wavelet	Impulse source

Table 5. Summary of the information of the generated Laplace-Fourier-domain synthetic dataset using IPATI parameter set.

Summary of the inversion parameters

Loop number	σ	f	Used number of elements
1	2, 4, 6, 8, 10, 12, and 14	0.001 Hz	66,510
2	2, 4, 6, 8, 10, 12, and 14	0.001 – 0.250 Hz	66,510
3	2, 4, 6, 8, 10, 12, and 14	0.250 – 2.750 Hz	66,510
4	2, 4, 6, 8, 10, 12, and 14	3.000 – 5.500 Hz	66,510
5	2, 4, 6, 8, 10, 12, and 14	5.750 – 8.250 Hz	258,935
6	2, 4, 6, 8, 10, 12, and 14	8.500 – 11.00 Hz	258,935
7	2, 4, 6, 8, 10, 12, and 14	11.25 – 13.75 Hz	258,935
8	2, 4, 6, 8, 10, 12, and 14	14.00 – 16.50 Hz	258,935
9	2, 4, 6, 8, 10, 12, and 14	16.75 – 19.25 Hz	258,935

Table 6. Summary of the inversion parameters for each loop. It is designed for the inversion test with the Laplace-Fourier domain IPATI dataset.

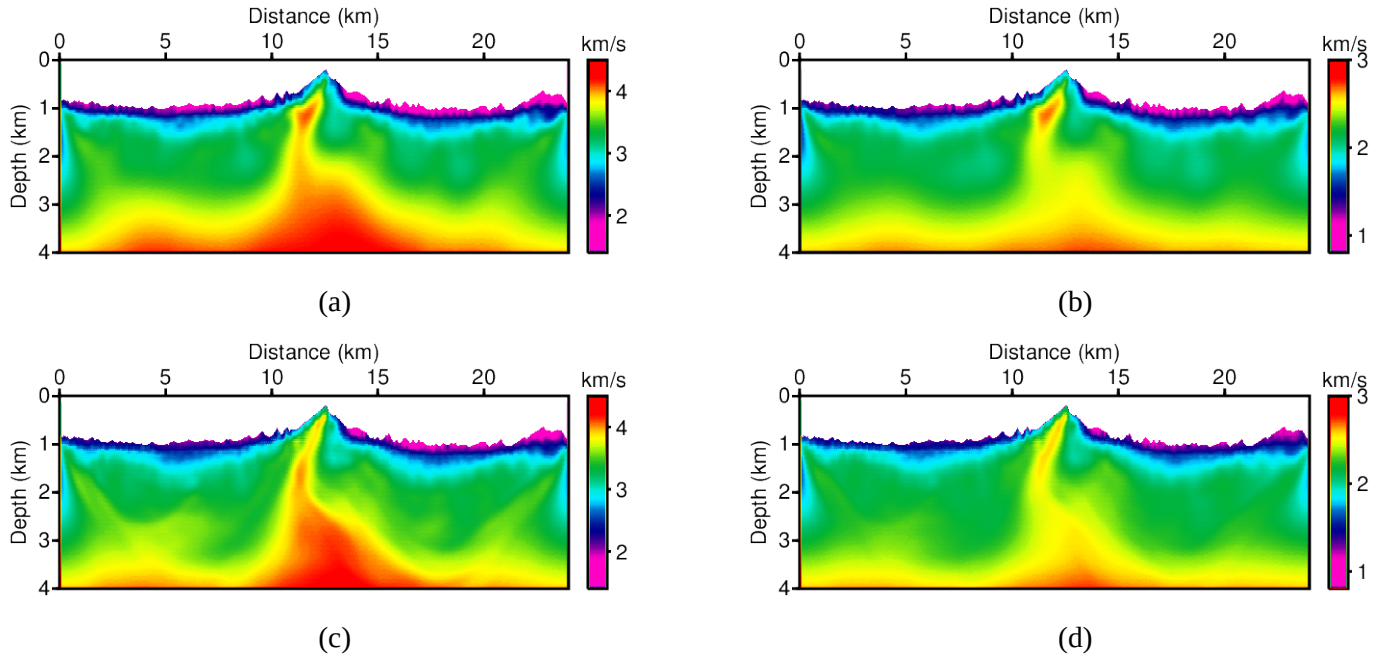

Figure 39. Inverted (a) P-wave and (b) S-wave velocity models obtained using Laplace-domain from IPATI dataset. Inverted (c) P-wave and (d) S-wave velocity models obtained using Laplace-Fourier-domain inversion from Laplace-Fourier domain IPATI dataset.

3.2 Time-domain synthetic dataset

The developed algorithm was applied to synthetic data generated using time-domain 2D elastic wave modeling with the IPDG scheme to verify the algorithm for time-domain datasets for several purposes.

The synthetic model was generated using the same domain size and mesh as used in the first test. However, the DOF of the mesh increased to 1,553,610 with the P2 shape function. The generated synthetic dataset had 240 sources, and the number of receivers varied from 822 to 1,640 depending on the source position. Every source and receiver was located at a 1 m depth below the surface. The far- and near-trace offset were 6.25 m and 10,256.25 m, respectively. The synthetic dataset was recorded in measurement of 8 seconds in duration with 4 ms intervals and it was generated using a first-derivative Gaussian source wavelet with a maximum frequency of 25 Hz. A detailed summary of the time-domain IPATI dataset is presented in Table 7.

The Figure 40 shows an example of a generated seismogram of vertical displacement and its frequency spectrum. The dataset is remade with respect to the 2 different purposes. First, the generated dataset was applied high-pass filter to investigate the dependency of the algorithm on the low-frequency information. And also, the Gaussian white noise was applied to the synthetic dataset for using it to test the algorithm's performance with the noisy dataset.

In the test with the time-domain synthetic dataset, 3 types of inversion-test were performed using the same conditions. The initial velocity models were linearly increasing models, as shown in Figure 38. The inversion loop comprised 12 steps, with frequency components in ranging from 0.001 Hz to 25 Hz and 7 Laplace damping constants (2, 4, 6, 8, 10, 12, and 14). A detailed

summary of the inversion strategy for each loop is presented in Table 8.

Summary of the information of the synthetic dataset

Domain size	24,000 m × 4.060 m
Far trace offset	10,256.25 m
Near trace offset	6.25 m
Number of shots	240
Number of receivers	882-1640
Modeling scheme	IPDG in the time domain
Used number of elements	258,935
Number of total DOF	1,553,610
Recording time	8 sec
Sampling interval	0.004 sec
Source wavelet	1^{st} derivative Gaussian wavelet
Maximum-frequency of the source wavelet	25 Hz

Table 7. Summary of the information of the generated time domain synthetic dataset using IPATI parameter set.

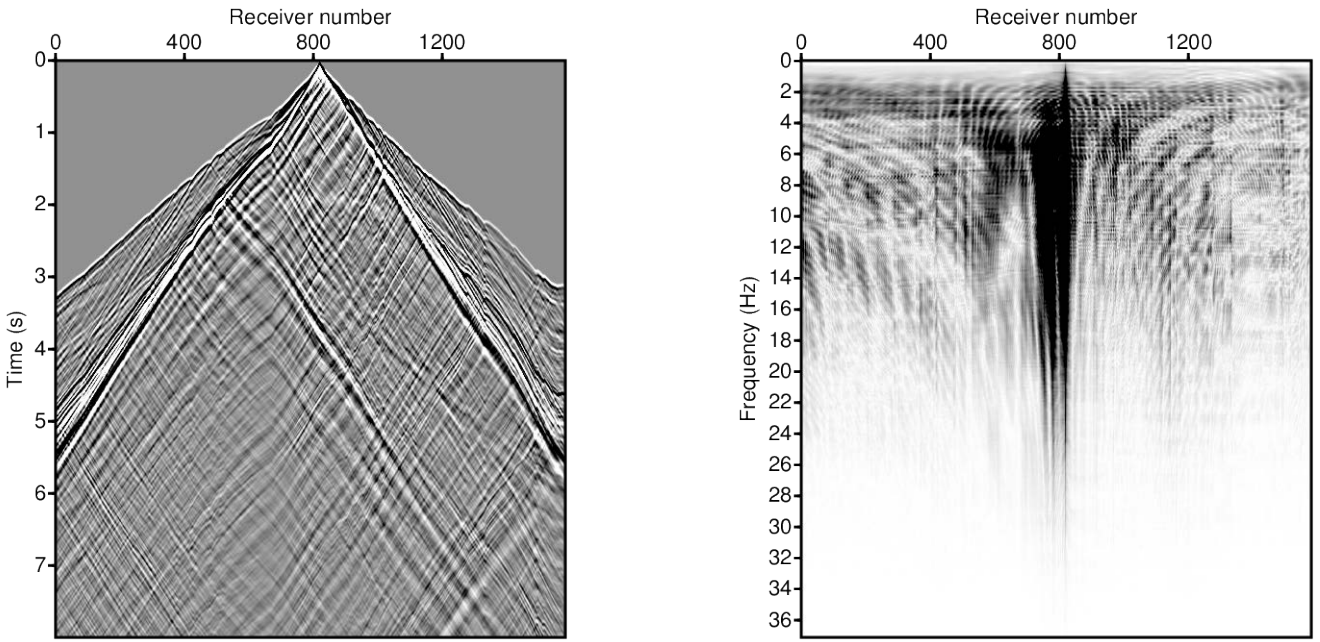

(a) (b)

Figure 40. Examples of the (a) vertical displacement shot gather computed using time-domain IPDG scheme from IPATI parameter set and (b) its frequency spectrum.

Summary of the inversion parameters

Loop number	σ	f	Used number of elements
1	2, 4, 6, 8, 10, 12, and 14	0.001 Hz	66,510
2	2, 4, 6, 8, 10, 12, and 14	0.001-0.250 Hz	66,510
3	2, 4, 6, 8, 10, 12, and 14	0.250-2.750 Hz	66,510
4	2, 4, 6, 8, 10, 12, and 14	3.000-5.250 Hz	258,935
5	2, 4, 6, 8, 10, 12, and 14	5.500-7.750 Hz	258,935
6	2, 4, 6, 8, 10, 12, and 14	8.000-10.25 Hz	258,935
7	2, 4, 6, 8, 10, 12, and 14	10.50-12.75 Hz	258,935
8	2, 4, 6, 8, 10, 12, and 14	13.00-15.25 Hz	258,935
9	2, 4, 6, 8, 10, 12, and 14	15.50-17.75 Hz	258,935
10	2, 4, 6, 8, 10, 12, and 14	18.00-20.25 Hz	258,935
11	2, 4, 6, 8, 10, 12, and 14	20.50-22.75 Hz	258,935
12	2, 4, 6, 8, 10, 12, and 14	23.00-25.00 Hz	258,935

Table 8. Summary of the inversion parameters for each loop. It is designed for the inversion test with the time domain IPATI dataset.

3.2.1 Inversion test for the dependency with respect to the low-frequency information

The absence of low-frequency information in many real datasets is the main hindrance to successful full-waveform inversion. Thus, many geophysicists have commented upon the necessity of a wavelength velocity model for successful inversion (Sirgue, 2006; Brenders and Pratt, 2007; Shin and Cha, 2008; Virieux and Operto, 2009). The algorithm for estimating the initial velocity model must therefore be tested using a dataset that does not contain low-frequency information.

I designed the 2 types of high-pass filters shown in Figure 41 to get rid of the low frequency information. The first high-pass filter removes the low-frequency components below 3 Hz and proportionally suppresses the components in the range of 3 – 6 Hz. And a second high-pass filter was designed for more general condition of the lacking of frequency spectrum of the dataset. The second high-pass filter removes the low-frequency information under below 6 Hz and proportionally suppresses the components in the range 6 – 12 Hz (Latimer et al., 2000).

Figure 42 and Figure 43 show the filtered datasets from which the low-frequency information has been removed and their frequency spectra

The developed 2D elastic Laplace-Fourier-domain inversion algorithm was applied to these 3 datasets: the low-frequency-containing dataset, the first high-pass-filtered dataset and the second high-pass-filtered dataset. As mentioned in the early part of this chapter, the inversion conditions were the same for each test as presented in Table 8. The initial models were used as presented in Figure 38. The density was assumed as a constant value and it was not

updated in this inversion test. The newly derived pseudo-Hessian was applied and the number of iteration was controlled by the normalized stopping criterion for each loop.

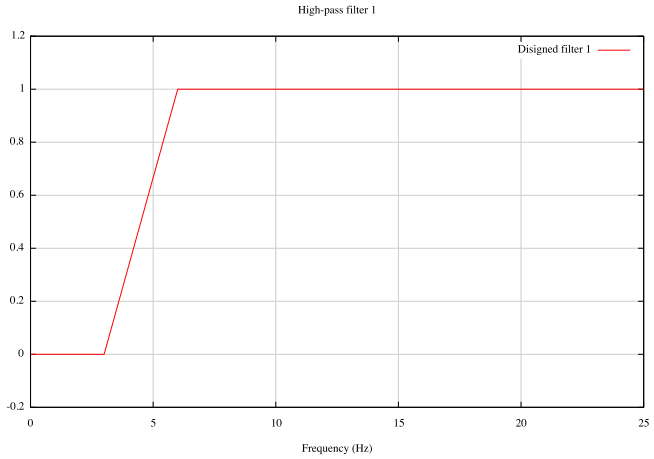

(a)

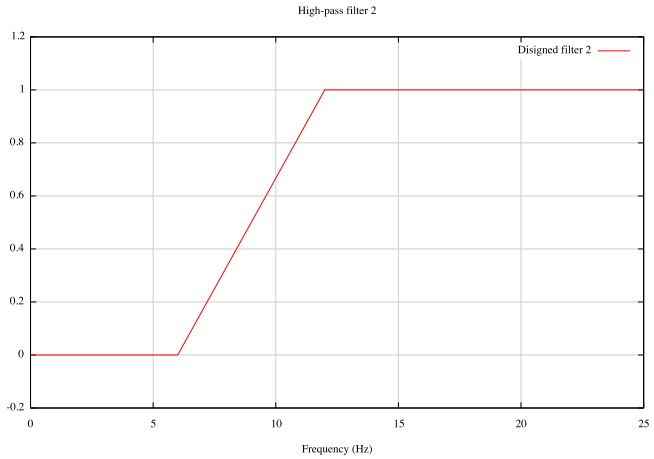

(b)

Figure 41. The high-pass filter to remove low frequency information. (a) High-pass filter 1 (frequency=0., 3., 6., and 9. Hz and amplitude=0., 0., 1., and 1.) (b) High-pass filter 2 (frequency=0., 6., 12., and 18. Hz and amplitude=0., 0., 1., and 1.).

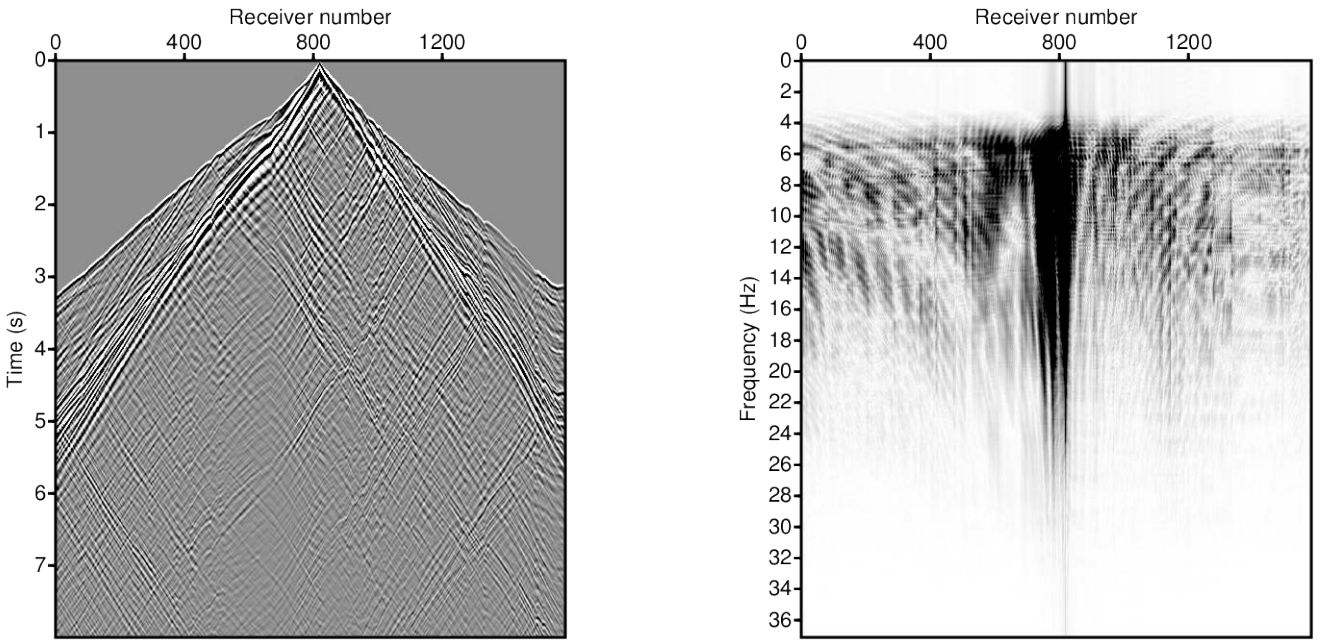

(a) (b)

Figure 42. Examples of the (a) vertical displacement shot gather computed using time-domain IPDG scheme from IPATI parameter set and (b) its frequency spectrum. This dataset is applied the 1st high-pass filter presented in Figure 41a.

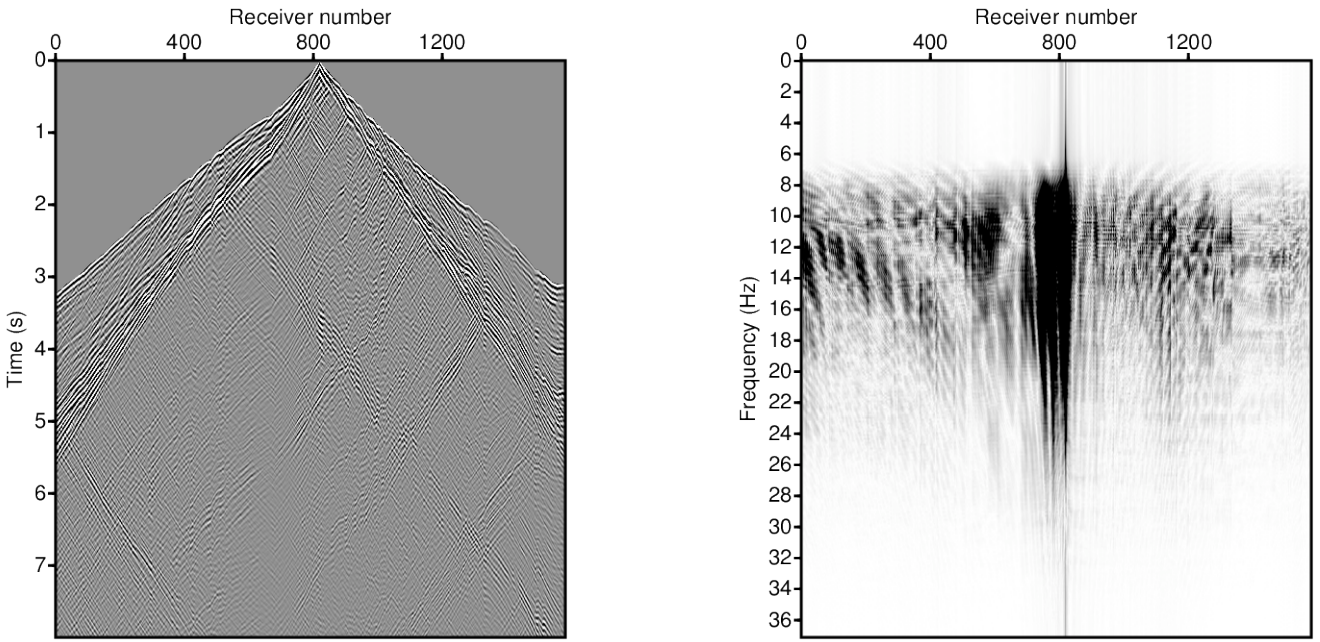

(a) (b)

Figure 43. Examples of the (a) vertical displacement shot gather computed using time-domain IPDG scheme from IPATI parameter set and (b) its frequency spectrum. This dataset is applied the 2nd high-pass filter presented in Figure 41b.

Figure 44, Figure 45, and Figure 46 show the Laplace- and Laplace-Fourier-inverted results for the P-wave velocity and S-wave velocity obtained using the low-frequency-containing dataset, the first high-pass-filtered dataset and the second high-pass-filtered dataset, respectively.

Residuals between the true models and inverted models are presented to illustrate the performance of the developed inversion algorithm. Figure 47a and Figure 47b show the residuals between the true models shown in Figure 37 and the initial models shown in Figure 38. The range of the P-wave velocity residuals is from 0.000016 km/s to 2.143 km/s and the range of the S-wave velocity residuals is from 0.000052 km/s to 1.461 km/s. In Figure 47c and Figure 47d, the distribution of the magnitude of the P-wave and S-wave residuals is presented, the error groups are classified as 10 groups with respect to the absolute magnitude; (1) from 0.0 to 0.1 km/s, (2) from 0.1 to 0.2 km/s, (3) from 0.2 to 0.3 km/s, (4) from 0.3 to 0.4 km/s, (5) from 0.4 to 0.5 km/s, (6) from 0.5 to 0.6 km/s, (7) from 0.6 to 0.7 km/s, (8) from 0.7 to 0.8 km/s, (9) from 0.8 to 0.9 km/s, and (10) over 0.9 km/s.

In these figures, it can be seen that the error due to the initial models is evenly distributed across the entire domain with respect to the true models. The averages of the residual of the P-wave velocity and the S-wave velocity are 0.476 km/s and 0.416 km/s, respectively.

Figure 48 show the residuals computed between the true models and the Laplace-Fourier inverted results using the low-frequency-containing dataset. The presented residuals show that the fitting discrepancy is reduced with respect to the initial models at most points. The range of the P-wave velocity residuals is from 0.00000024 km to 0.866 km/s, and the range of the S-wave velocity residuals is from 0.000004 km/s to 0.703 km/s. The average of the P-

wave velocity residuals is 0.130 km/s, and of the S-wave velocity residuals are 0.176 km/s. The ranges of the residuals and their averages also are considerably decreased. Some discrepancies still remain on each side and in the deeper region.

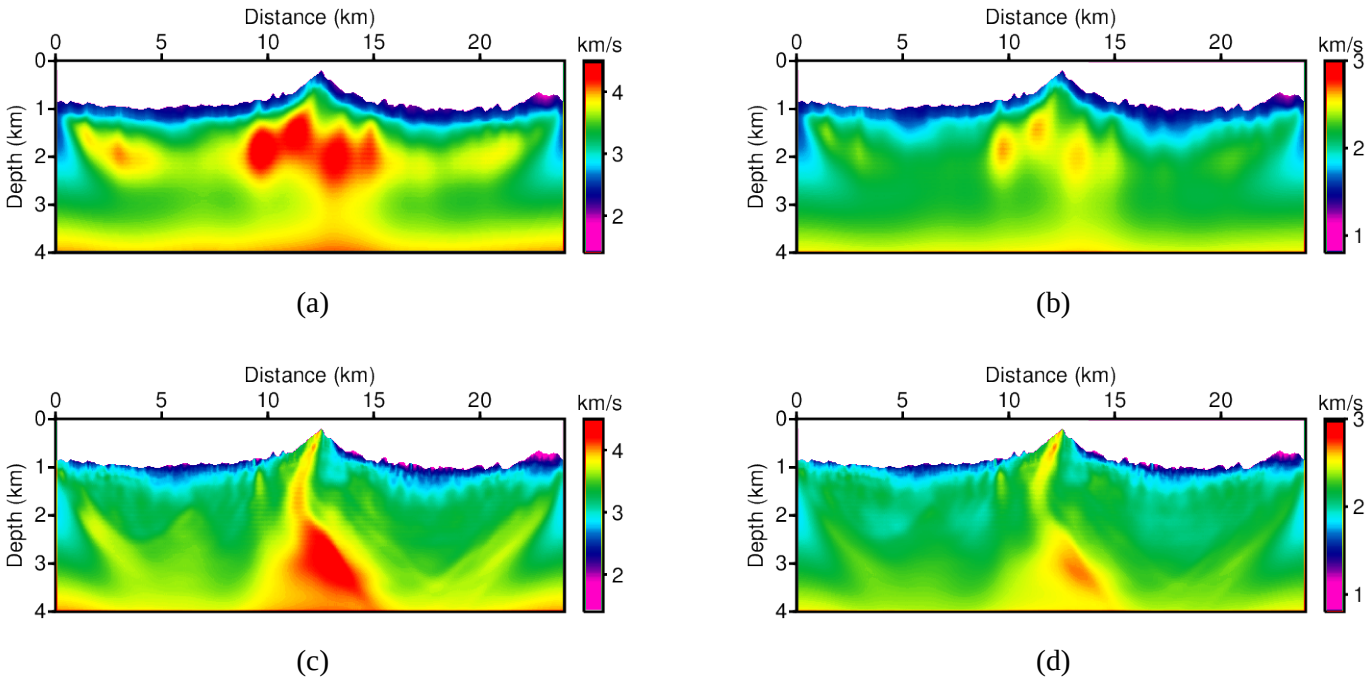

Figure 44. Inverted (a) P-wave and (b) S-wave velocity models obtained using Laplace-domain inversion. Inverted (c) P-wave and (d) S-wave velocity models obtained using Laplace-Fourier-domain inversion with time domain IPATI dataset. The inversion results are obtained with the low frequency contains dataset presented in Figure 40.

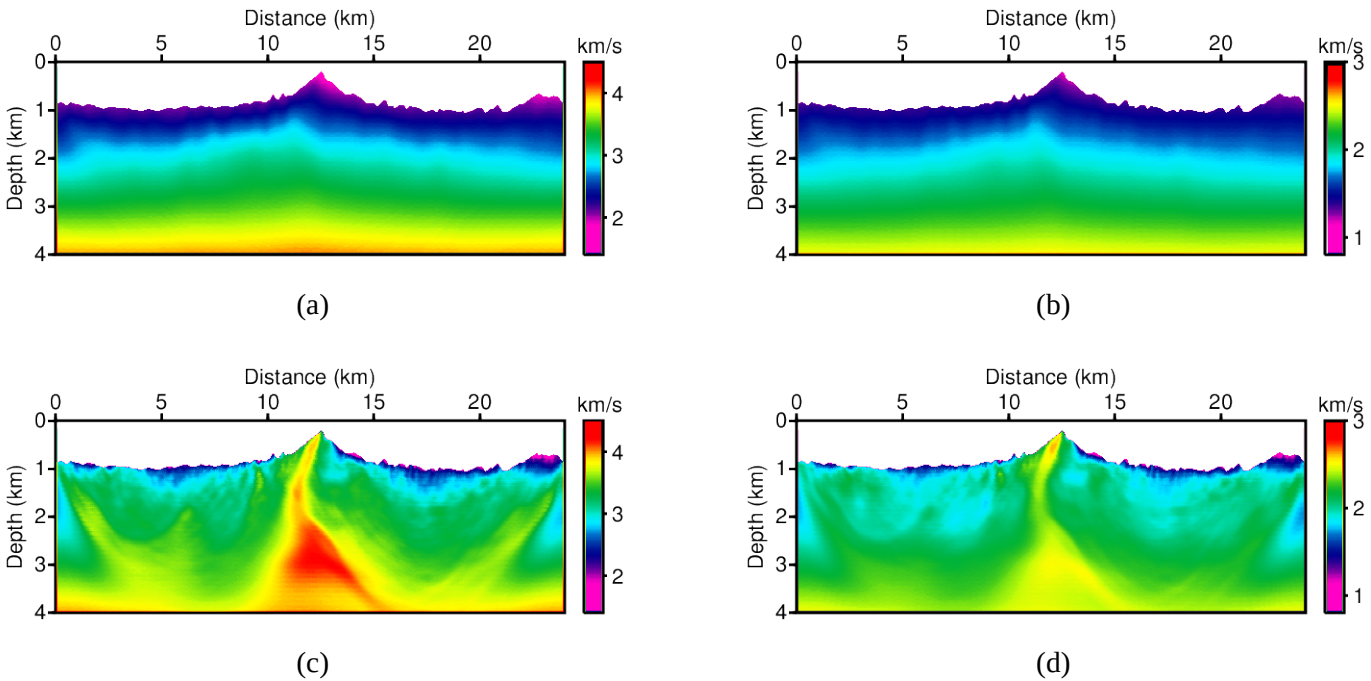

Figure 45. Inverted (a) P-wave and (b) S-wave velocity models obtained using Laplace-domain inversion. Inverted (c) P-wave and (d) S-wave velocity models obtained using Laplace-Fourier-domain inversion with time domain IPATI dataset. The inversion results are obtained with the time domain dataset applied the 1st high-pass filter, thus the dataset is not contains the low-frequency information below 3 Hz as presented in Figure 42.

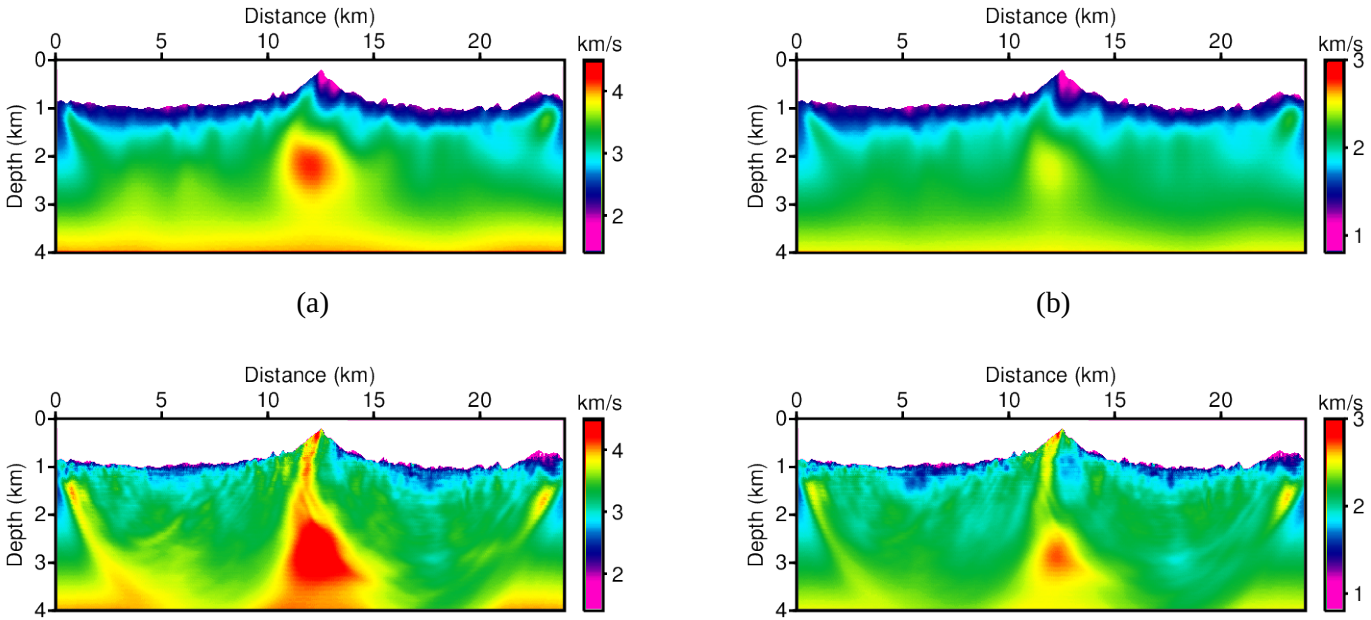

Figure 46. Inverted (a) P-wave and (b) S-wave velocity models obtained using Laplace-domain inversion. Inverted (c) P-wave and (d) S-wave velocity models obtained using Laplace-Fourier-domain inversion with time domain IPATI dataset. The inversion results are obtained with the time domain dataset applied the 2nd high-pass filter, thus the dataset is not contains the low-frequency information below 6 Hz as presented in Figure 43.

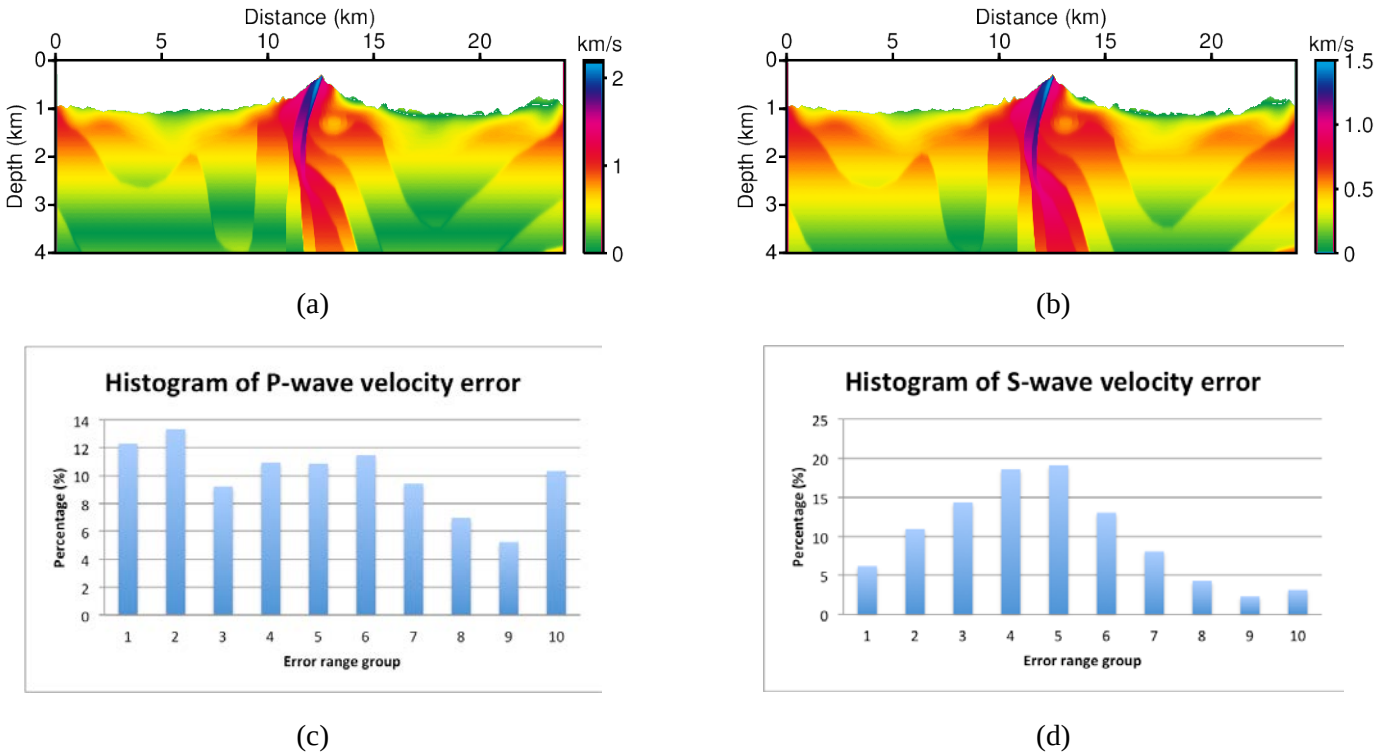

Figure 47. The residuals between true models and initial models: (a) P-wave and (b) S-wave velocity models. Histogram of the magnitude of the error: (c) P-wave and (d) S-wave velocity models. Error range groups defined as (1) 0.0 ~ 0.1, (2) 0.1 ~ 0.2, (3) 0.2 ~ 0.3, (4) 0.3 ~ 0.4, (5) 0.4 ~ 0.5, (6) 0.5 ~ 0.6, (7) 0.6 ~ 0.7, (8) 0.7 ~ 0.8, (9) 0.8 ~ 0.9, and (10) 0.9 ~ km/s.

However we believe that these discrepancies are related to the penetration depth and offset, not a problem of the algorithm. The P-wave velocity appears to have been more properly recovered than the S-wave inverted result. We guess that this difference may be attributable to the use of same step length for both lambda and mu, or the lack of information, the elastic inversion without horizontal observed data. We will study this problem further in the future.

The inverted velocity model could be confirmed with the error distributions in Figure 45c and 45d, the most of population of the residuals are located in group 1 (0.0 ~ 0.1 km/s) and group 2 (0.1 ~ 0.2 km/s).

Second, the Figure 49 and Figure 49b shows the residuals computed between true models and the inverted results obtained using the first high-pass-filtered dataset. The range of the P-wave velocity residuals is from 0.000000238 km/s to 0.904 km/s and the range of the S-wave velocity residuals is from 0.00000596 km/s to 0.786 km/s. The averages of the P-wave and S-wave velocity residuals are 0.142 km/s and 0.224 km/s, respectively. The error is increased compared with the first test results; however, the results still successfully recover the true velocities, even though dataset does not contain the low-frequency information below 3 Hz. The residual histograms in Figure 49 and Figure 49 also show that the inverted results are converged to the true velocities well, but the population of group 1 is decreased with comparison to the first result. In particular, the error at the surface is increased with respect to the first inverted results.

Finally, Figure 50 and Figure 50 show the residuals between the true models and the inverted results computed using the second high-pass-filtered dataset, which does not include the low-frequency data below 6 Hz. The residuals demonstrate that the developed algorithm was able to recover the true

models in the absence of low-frequency information to some degree; as shown in this test, the algorithm was successful at least in the absence of information below 6 Hz. The range of the P-wave velocity residuals is from 0.000000238 km/s to 1.034 km/s, and that of the S-wave velocity residuals is from 0.00000310 km/s to 0.739. The averages of the P-wave and the S-wave residuals are 0.169 km/s and 0.215 km/s, respectively. Figure 50 and Figure 50 show the distribution of the magnitude of the residuals.

In these tests, the developed algorithm was applied to the 3 datasets distinguished in term of the existence of low-frequency information to test the dependency on the low-frequency components. All inverted results generated reasonable inverted models regardless of the presence of low-frequency components. Summaries of the residuals and error distributions of these tests is presented in Table 9 and Table 10.

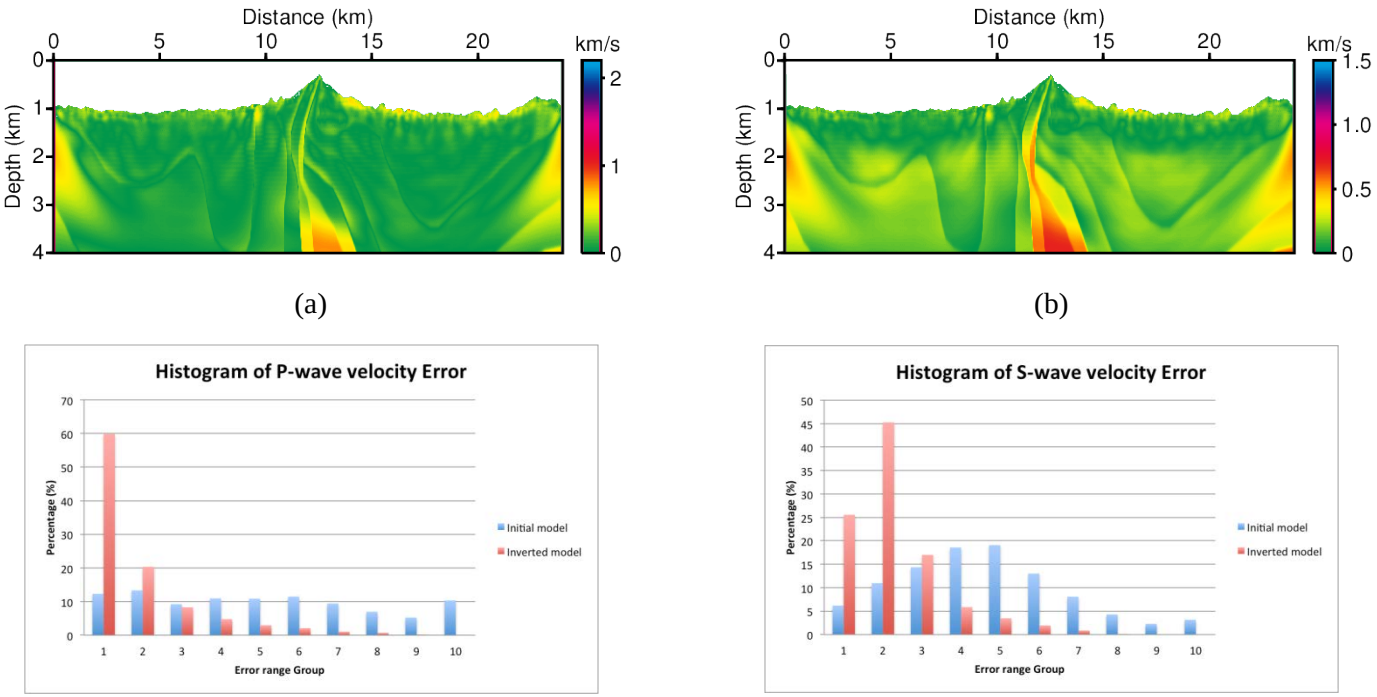

Figure 48. The residuals between the true models and the inverted models with low-frequency-containing dataset as shown in Figure 40: (a) P-wave and (b) S-wave velocity models. Histograms of the magnitude of the residuals of inverted (c) P-wave and (d) S-wave velocity models.

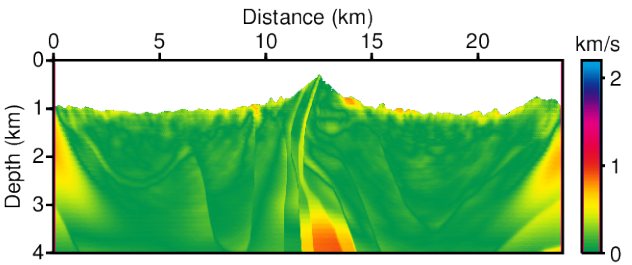

(a)

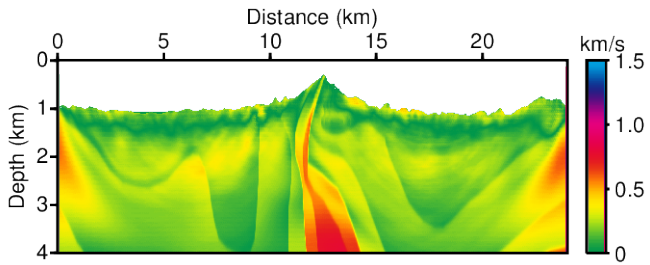

(b)

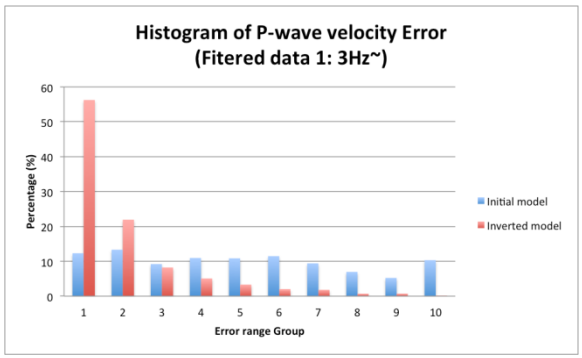

(c)

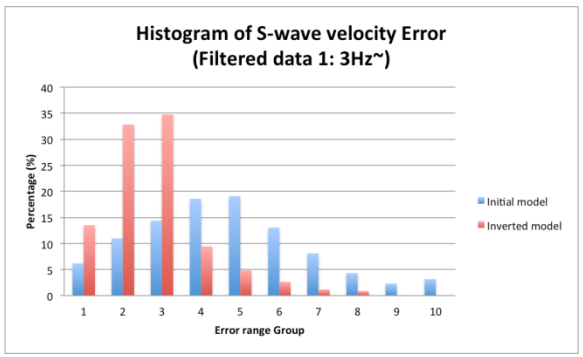

(d)

Figure 49. The residuals between the true models and the inverted models without low-frequency component dataset as shown in Figure 42 (3Hz~): (a) P-wave and (b) S-wave velocity models. Histograms of the magnitude of the residuals of inverted (c) P-wave and (d) S-wave velocity models.

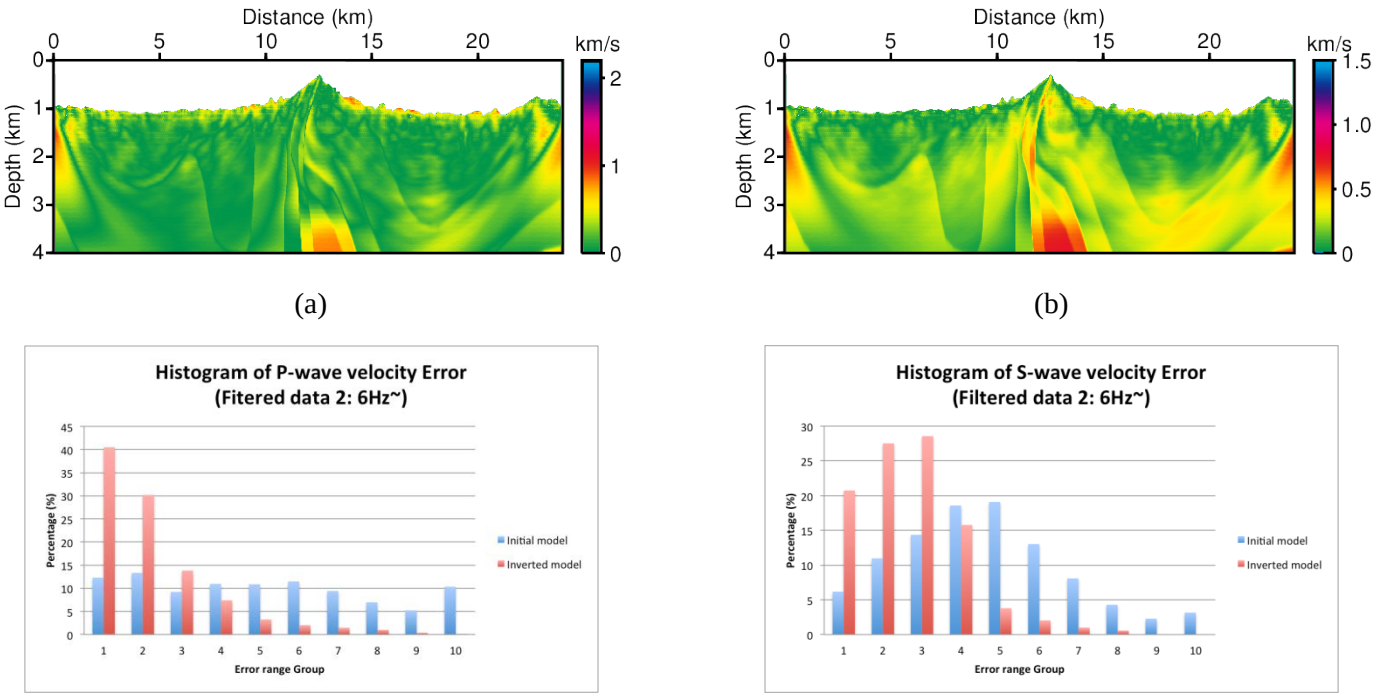

Figure 50. The residuals between the true models and the inverted models without low-frequency component dataset as shown in Figure 43 (6Hz~): (a) P-wave and (b) S-wave velocity models. Histograms of the magnitude of the residuals of inverted (c) P-wave and (d) S-wave velocity models.

The information of the residuals

	Range of P-wave residuals	Range of S-wave residuals	Average of P-wave residuals	Average of S-wave residuals
Initial model	0.000 ~ 2.143 km/s	0.000 ~ 1.460 km/s	0.47587389 km/s	0.41591409 km/s
Inverted model set 1	0.000 ~ 0.866 km/s	0.000 ~ 0.703 km/s	0.12953152 km/s	0.17582294 km/s
Inverted model set 2	0.000 ~ 0.904 km/s	0.000 ~ 0.786 km/s	0.14256380 km/s	0.22438702 km/s
Inverted model set 3	0.000 ~ 1.034 km/s	0.000 ~ 0.739 km/s	0.16885108 km/s	0.21513708 km/s

Table 9. The information of the velocity residuals computed with the true velocity models and initial models and inverted models. Inverted model set 1 denotes the inverted results with low frequency contains dataset, Inverted model set 2 denotes the inverted results with the 1st high pass filter applied dataset (contains: 3 Hz~), and Inverted model set 3 denotes the inverted results with the 2nd high pass filter applied dataset (contains: 6 Hz~).

Distribution of the magnitude of the residuals

	Initial model		Inverted model set 1		Inverted model set 2		Inverted model set 3	
Group	P-wave	S-wave	P-wave	S-wave	P-wave	S-wave	P-wave	S-wave
1	12.30 %	6.179 %	**59.87 %**	**25.56 %**	**56.23 %**	**13.51 %**	**40.48 %**	**20.74 %**
2	13.32 %	10.97 %	**20.33 %**	**45.28 %**	**21.96 %**	**32.83 %**	**30.17 %**	**27.51 %**
3	9.208 %	14.36 %	8.278 %	**17.00 %**	8.214 %	**34.75 %**	**13.82 %**	**28.56 %**
4	10.94 %	18.57 %	4.756%	5.856 %	5.073 %	9.415 %	7.388 %	**15.76 %**
5	10.85 %	19.08 %	2.949 %	3.468 %	3.314 %	4.834 %	3.250 %	3.794 %
6	11.47 %	13.02 %	2.091 %	1.941 %	2.021 %	2.630 %	2.008 %	2.037 %
7	9.405 %	8.081 %	1.032 %	0.869 %	1.818 %	1.163 %	1.460 %	1.007 %
8	6.959 %	4.293 %	0.687 %	0.025 %	0.691 %	0.868 %	1.012 %	0.576 %
9	5.228 %	2.287 %	0.001 %	-	0.710 %	-	0.373 %	-
10	10.32 %	3.158 %	-	-	0.002 %	-	0.005 %	-

Table 10. The distribution of the magnitude of the velocity residuals computed with the true velocity models and initial models and inverted models. Inverted model set 1 denotes the inverted results with low frequency contains dataset, Inverted model set 2 denotes the inverted results with the 1st high pass filter applied dataset (contains: 3 Hz~), and Inverted model set 3 denotes the inverted results with the 2nd high pass filter applied dataset (contains: 6 Hz~).

3.2.2 Inversion test with a noisy dataset

A real dataset always contains not only the seismic response but also noise from the environment of the acquisition site. The noise disturbs the recovery of the parameters of the subsurface via full-waveform inversion. Many researchers have made efforts to increase signal to noise ratio (SN ratio) to improve the quality of the result of seismic methods such as inversion and migration, and so on. Thus, the noise problem must be tested for the algorithm developed with the aim of the real data application.

2 types of noisy datasets were generated using the first high-pass-filtered dataset shown in Figure 42. The Gaussian white noise was added to the synthetic dataset with SN ratios of 100 and 50 in the time domain. Figure 51 show the generated noisy datasets and the plots shown in Figure 52 and Figure 53 show the trace of the noise-free dataset and the 2 types of noisy data recorded at the 400^{th} and 800^{th} receivers. The shot gather energy and SN rations were also presented in Figure 54 and they show that noise is heavily added at low-frequency range.

The developed algorithm was applied to these noisy datasets and the results of Laplace- and Laplace-Fourier-domain inversion are presented in Figure 55 and Figure 56 for each noisy dataset. In terms of clarity of the inverted image, the Laplace-inverted result seems to be less affected by noise than the Laplace-Fourier result, which exhibits many scattered irregularities in the recovered velocity.

I also computed the residuals and distribution of residuals as presented in Figure 57 and Figure 58 for the each case. From these residuals, it can be seen that the noise causes large discrepancies at the surface. However, the inverted

results are reasonable in the other regions, and the high-velocity structure in the center is defined successfully.

The detailed summary of residuals in Table 11 shows conspicuous increased range of the residuals with noisy dataset. Table 12 shows the histogram of the residual of inverted result. In these tables, the interesting point is that the S-wave inverted model with noise added dataset gives better average result than with noise free dataset. This enjoyable result can be assumed that it caused from the more large number of iteration than noise free test (Noise free: 122 iterations; SN ratio 100: 348 iterations; SN ratio 50: 262 iterations) and it requires the study about step lengths for multi parameter inversion.

The Laplace-Fourier inversion algorithm was tested with a noise-added dataset that, moreover, does not contain low-frequency information below 3 Hz. The computed results could not demonstrate that the algorithm is insensitive to the noise. However, the results show that the algorithm is capable of recovering promising initial parameters for Fourier inversion, even using noisy data.

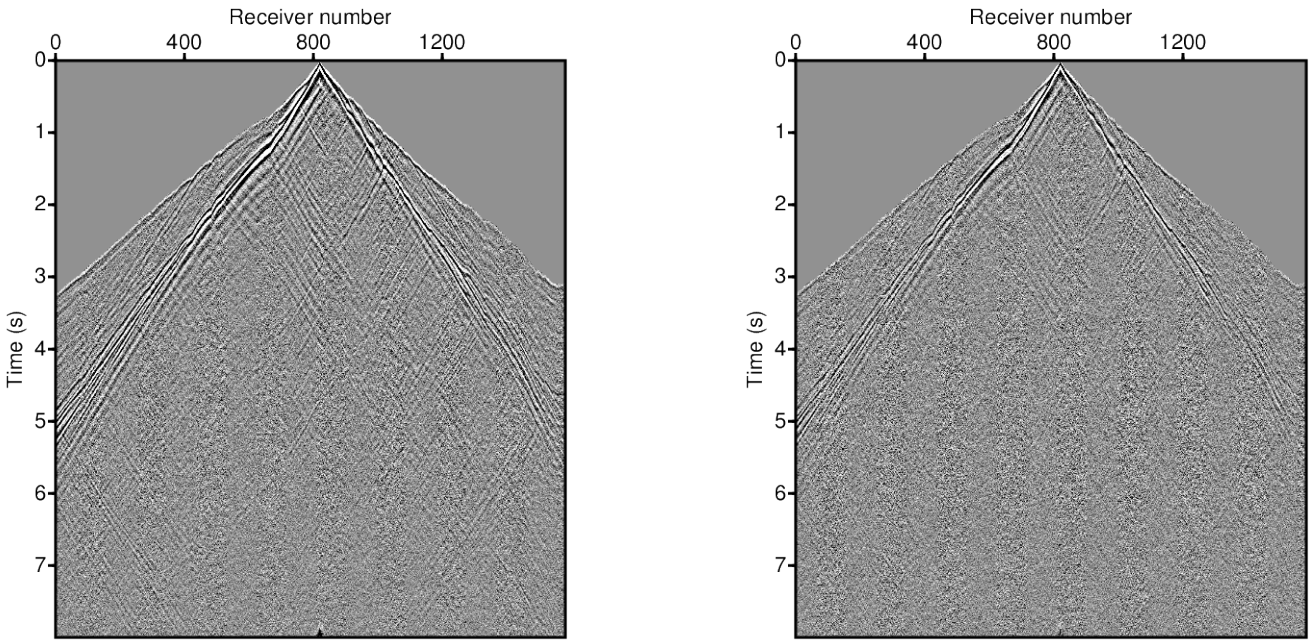

(a) (b)

Figure 51. Examples of the vertical displacement shot gather from the IPATI parameter set. (a) Contains the Gaussian white noise with intensity of SN ratio 100. (b) Contains the Gaussian white noise with intensity of SN ratio 50.

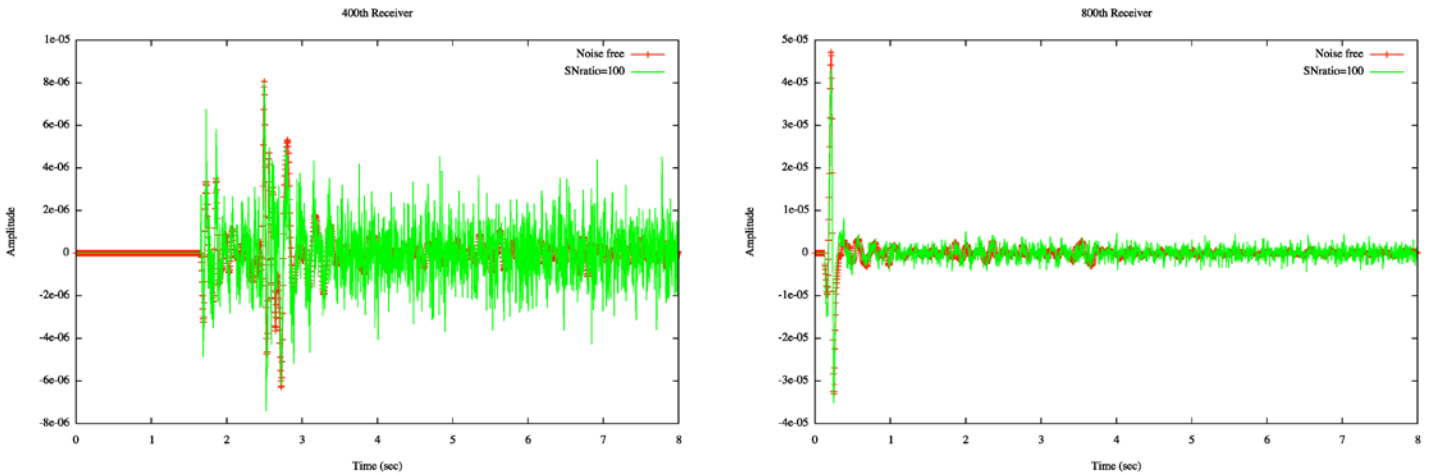

(a) (b)

Figure 52. The comparison of the traces between noise free shot gather and noise applied shot gather (SN ratio: 100) at the (a) 400th and (b) 800th receiver.

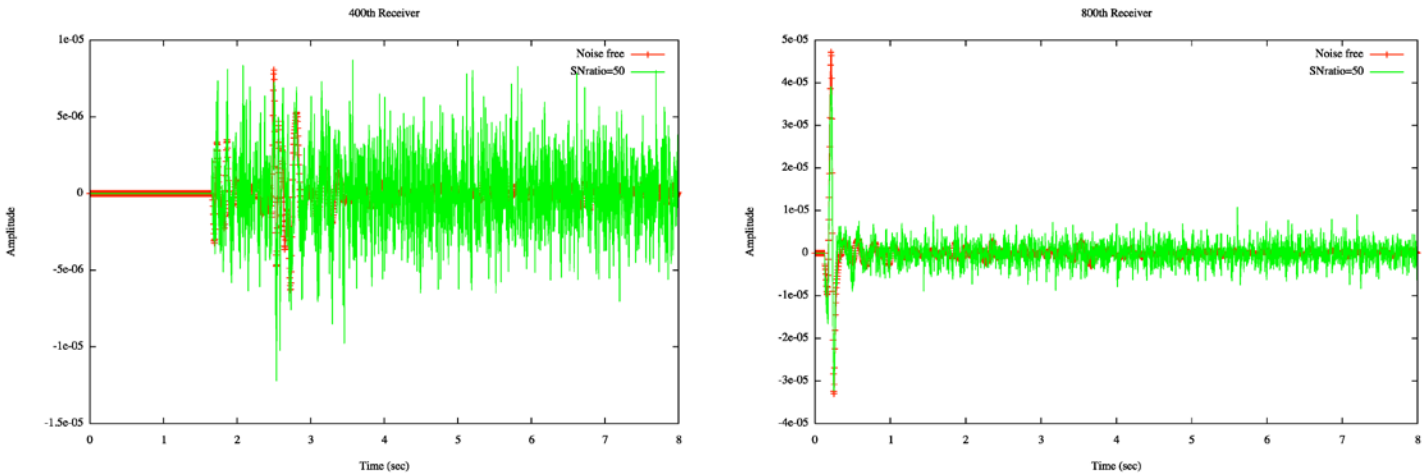

(a) (b)

Figure 53. The comparison of the traces between noise free shot gather and noise applied shot gather (SN ratio: 50) at the (a) 400th and (b) 800th receiver.

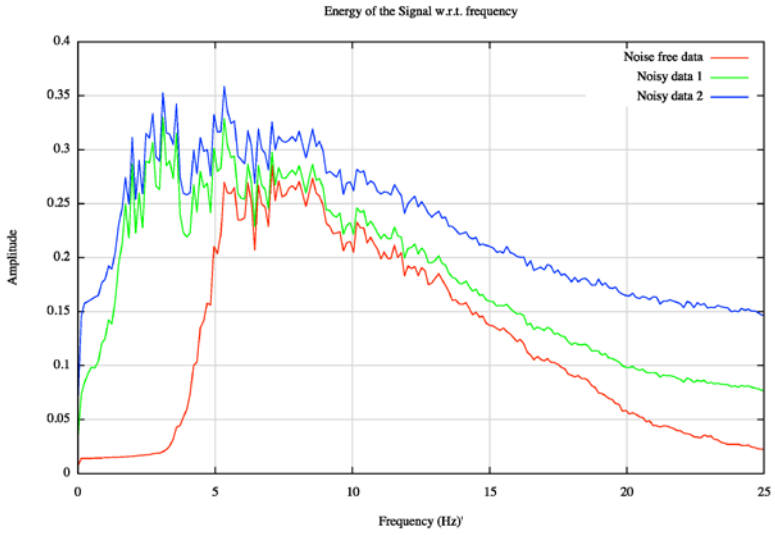

(a)

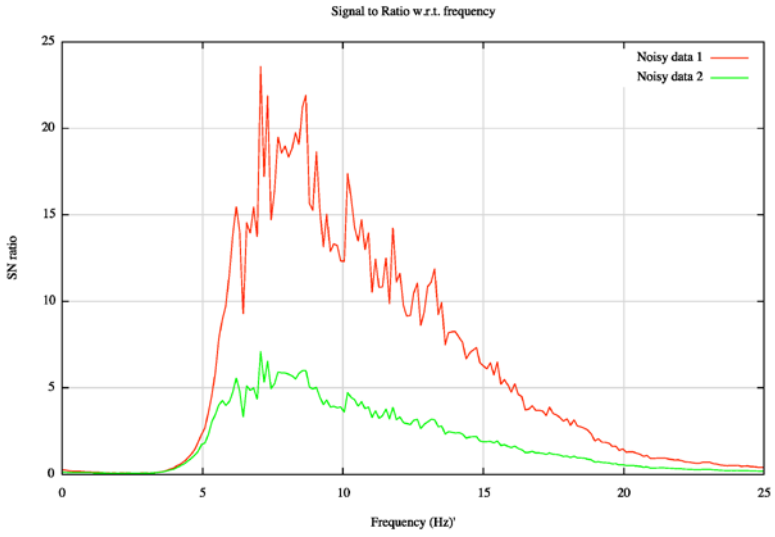

(b)

Figure 54. (a) The comparison of the energy of noise-free, noisy 1, and noisy 2 dataset shown in Figure 42, Figure 51, and Figure 51, with respect to the frequency. (b) SN ratios of noisy datasets with respect to the frequency.

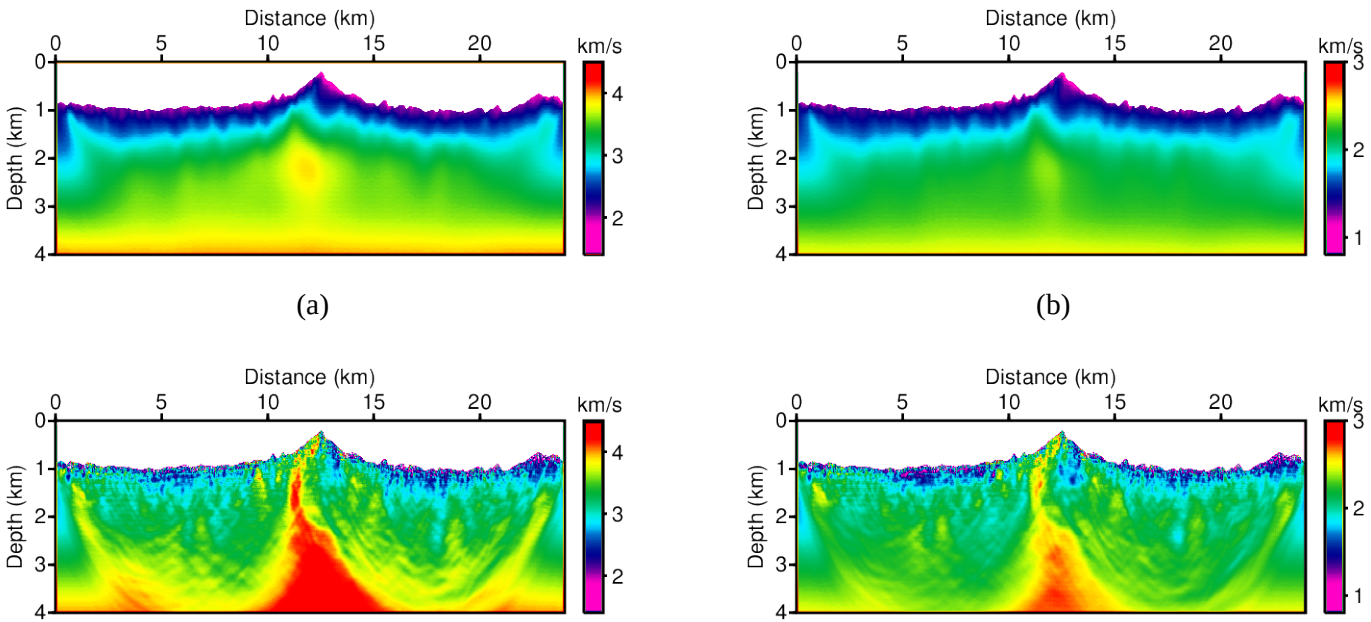

Figure 55. Inverted (a) P-wave and (b) S-wave velocity models obtained using Laplace-domain inversion with time domain IPATI dataset. Inverted (c) P-wave and (d) S-wave velocity models obtained using Laplace-Fourier-domain inversion with time domain IPATI dataset. The inversion results are obtained with the time domain dataset applied the 1st high-pass filter and the Gaussian white noise with intensity of SN ratio 100 as presented in Figure 51a.

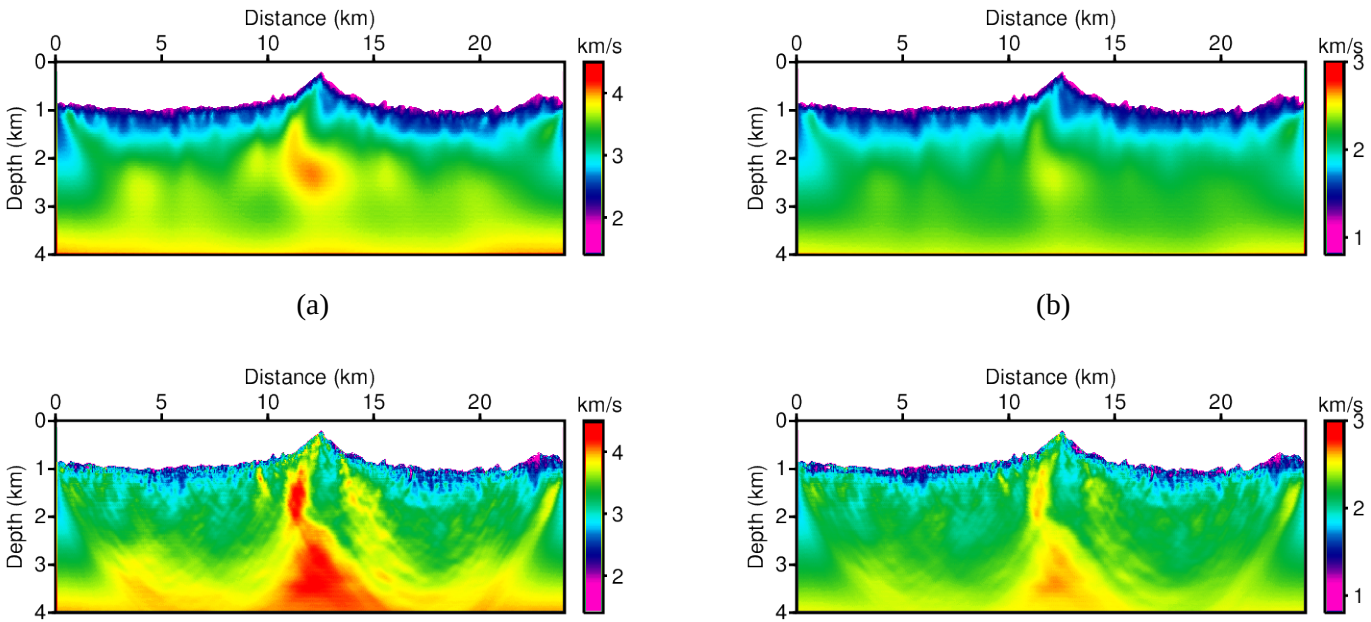

Figure 56. Inverted (a) P-wave and (b) S-wave velocity models obtained using Laplace-domain inversion with time domain IPATI dataset. Inverted (c) P-wave and (d) S-wave velocity models obtained using Laplace-Fourier-domain inversion with time domain IPATI dataset. The inversion results are obtained with the time domain dataset applied the 1st high-pass filter and the Gaussian white noise with intensity of SN ratio 50 as presented in Figure 51b.

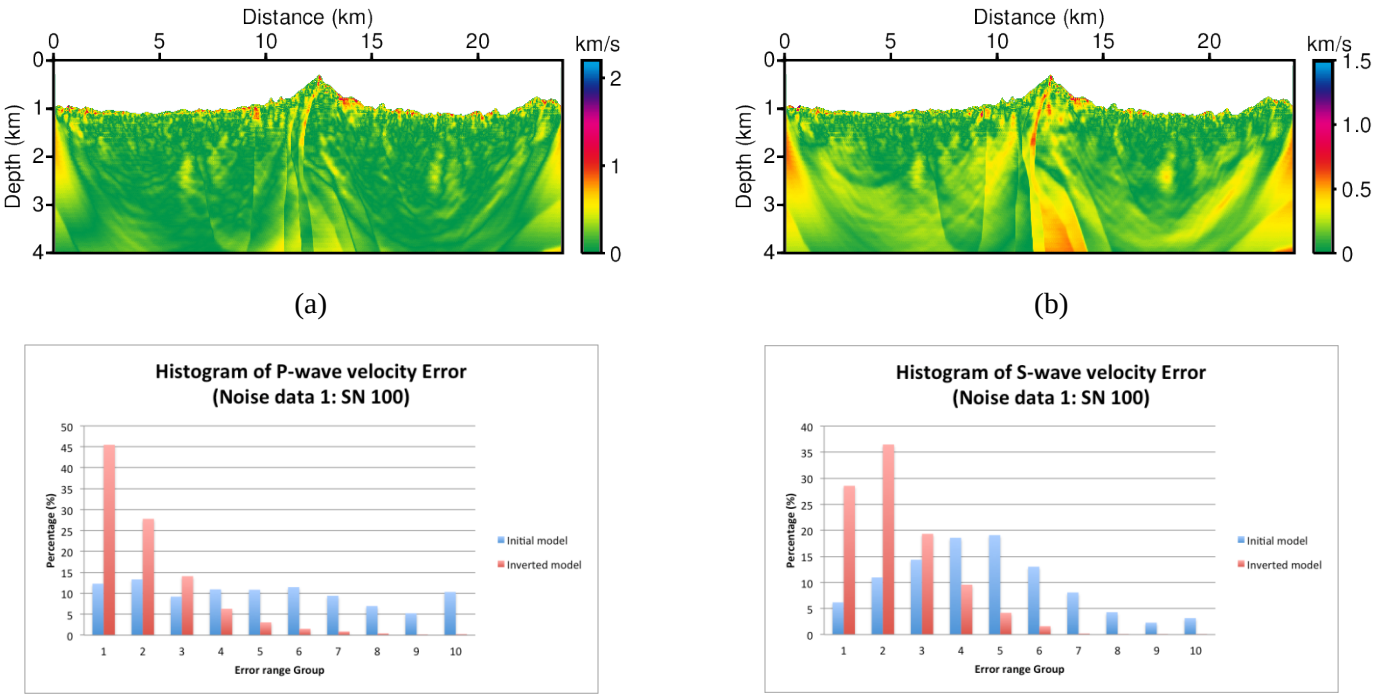

Figure 57. The residuals between true models and the inverted models with noise added dataset as shown in Figure 51a (SN ratio 100): (a) P-wave and (b) S-wave velocity models. Histogram of the magnitude of the residuals of inverted (c) P-wave and (d) S-wave velocity models.

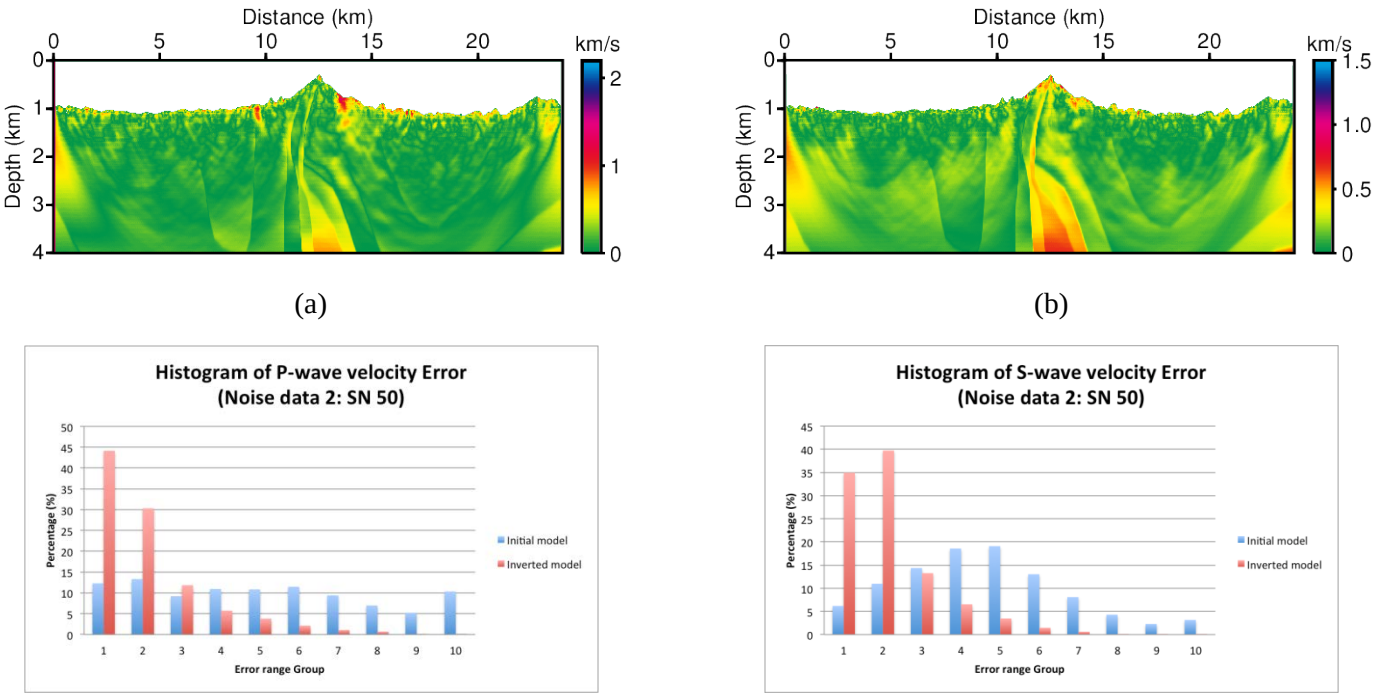

Figure 58. The residuals between true models and the inverted models with noise added dataset as shown in Figure 51b (SN ratio 50): (a) P-wave and (b) S-wave velocity models. Histogram of the magnitude of the residuals of inverted (c) P-wave and (d) S-wave velocity models.

The information of the residuals

	Range of P-wave residuals	Range of S-wave residuals	Average of P-wave residuals	Average of S-wave residuals
Initial model	0.000 ~ 2.143 km/s	0.000 ~ 1.460 km/s	0.47587389 km/s	0.41591409 km/s
Inverted model set 1	0.000 ~ 0.904 km/s	0.000 ~ 0.786 km/s	0.14256380 km/s	0.22438702 km/s
Inverted model set 2	0.000 ~ 1.962 km/s	0.000 ~ 1.330 km/s	0.15310143 km/s	0.17840558 km/s
Inverted model set 3	0.000 ~ 1.552 km/s	0.000 ~ 1.003 km/s	0.15749350 km/s	0.15841290 km/s

Table 11. The information of the velocity residuals computed with the true velocity models and initial models and inverted models. Inverted model set 1 denotes the inverted results with noise free dataset, Inverted model set 2 denotes the inverted results with the noise applied dataset 1 (SN ratio: 100), and Inverted model set 3 denotes the inverted results with the noise added dataset 2 (SN ratio: 50).

Distribution of the magnitude of the residuals

	Initial model		Inverted model set 1		Inverted model set 2		Inverted model set 3	
Group	P-wave	S-wave	P-wave	S-wave	P-wave	S-wave	P-wave	S-wave
1	12.30 %	6.179 %	**56.23 %**	**13.51 %**	**45.47 %**	**28.55 %**	**44.13 %**	**34.93 %**
2	13.32 %	10.97 %	**21.96 %**	**32.83 %**	**27.78 %**	**36.47 %**	**30.31 %**	**39.73 %**
3	9.208 %	14.36 %	8.214 %	**34.75 %**	**14.09 %**	**19.33 %**	**11.84 %**	**13.26 %**
4	10.94 %	18.57 %	5.073 %	9.415 %	6.315 %	9.575 %	5.737 %	6.532 %
5	10.85 %	19.08 %	3.314 %	4.834 %	3.063 %	4.180 %	3.800 %	3.468 %
6	11.47 %	13.02 %	2.021 %	2.630 %	1.539 %	1.613 %	2.112 %	1.458 %
7	9.405 %	8.081 %	1.818 %	1.163 %	0.891 %	0.201 %	1.087 %	0.605 %
8	6.959 %	4.293 %	0.691 %	0.868 %	0.414 %	0.042 %	0.687 %	0.015 %
9	5.228 %	2.287 %	0.710 %	-	0.179 %	0.023 %	0.127 %	0.007 %
10	10.32 %	3.158 %	0.002 %	-	0.250 %	0.024 %	0.169 %	0.005 %

Table 12. The distribution of the magnitude of the velocity residuals computed with the true velocity models and initial models and inverted models. Inverted model set 1 denotes the inverted results with noise free dataset, Inverted model set 2 denotes the inverted results with the noise applied dataset 1 (SN ratio: 100), and Inverted model set 3 denotes the inverted results with the noise added dataset 2 (SN ratio: 50).

3.2.3 Acoustic approach for an elastic dataset

The two different signals, especially at the later times can be made equal by applying a damped function with respect to time. Thus, the Laplace transform, the integral of the damped signal with respect to time, is able to ignore seismic signals to some degree. Ha et al., in 2010, applied the 2D acoustic Laplace-domain inversion algorithm to an elastic dataset with the expectation that the damping factor could reduce the differences between the wave propagation of the acoustic and elastic surface waves. Their approach recovered a reasonable velocity model for an elastic CCSS dataset (Zelt et al., 2005).

Their algorithm was applied to the 1st filtered synthetic dataset shown in Figure 39 to compare the inverted results obtaining using the elastic and acoustic approaches. For the inversion test, all inversion parameters and conditions were the same as those used for the elastic inversion, except hessian matrix. The acoustic inversion was performed with the acoustic pseudo-Hessian introduced by Ha et al., in 2012.

Figure 55 shows the inverted P-wave results obtained via Laplace- and Laplace-Fourier-domain inversion. The recovered velocity model by acoustic approach seems to agree well with the true P-wave velocity model in overall shape. Especially the Laplace-domain inverted result is not worse than elastic Laplace-domain inverted result.

However for the Laplace-Fourier-domain results, the elastic inverted P-wave velocity result presented in Figure 42c shows much more detailed subsurface structures than acoustic result shown in Figure 55b. From the residual in Figure 56a, we believe the surface wave disturbs to recover proper parameters in near surface region in the Laplace-Fourier domain. The detailed infor-

mation of residuals and its distribution of this test are presented in Table 11 and Table 12, respectively.

The results of this test demonstrate that although the acoustic approach can effectively compute the inverted velocity for land dataset, the elastic approach can yield superior results.

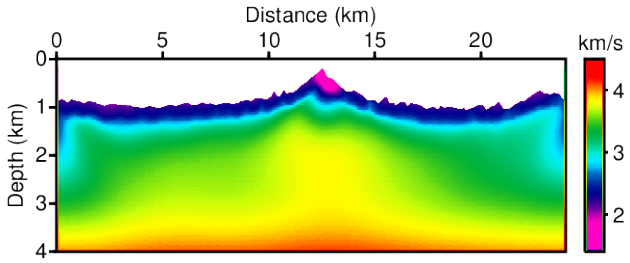

(a)

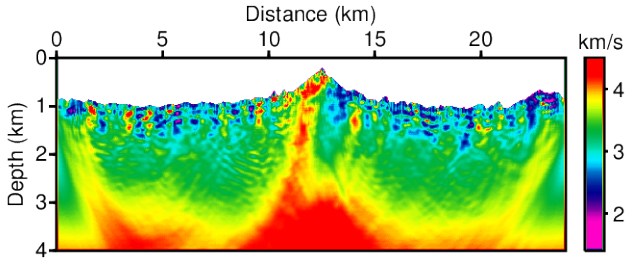

(b)

Figure 59. Inverted P-wave models via acoustic (a) Laplace-domain inversion and (b) Laplace-Fourier-domain inversion.

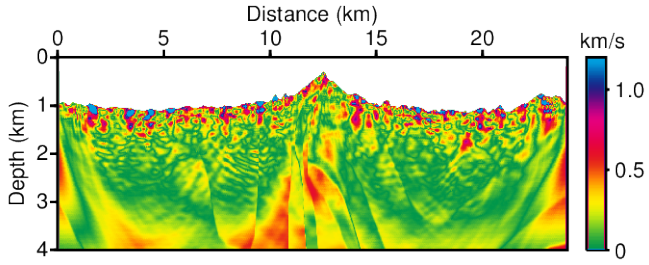

(a)

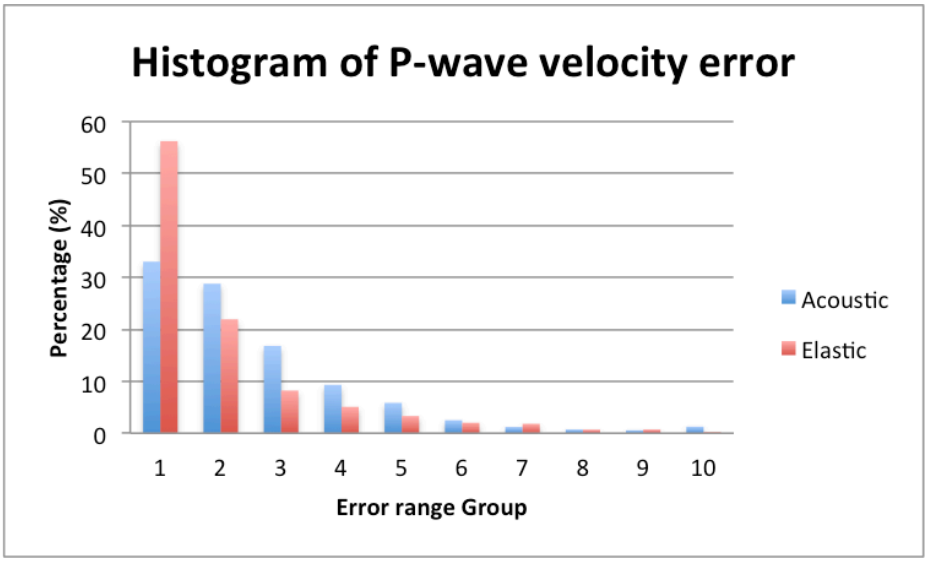

(b)

Figure 60. (a) The residuals between the true P-wave model and the inverted P-wave models via acoustic approach Laplace-Fourier-domain inversion shown in Figure 59b. (b) Histogram of the magnitude of the residuals of acoustic inverted and elastic inverted P-wave velocity models.

The information of the residuals (P-wave velocity)

	Range of P-wave residuals	Average of P-wave residuals
Initial model	0.000 ~ 2.143 km/s	0.47587389 km/s
Elastic inversion	0.000 ~ 0.904 km/s	0.14256380 km/s
Acoustic inversion	0.000 ~ 2.264 km/s	0.19696705 km/s

Table 13. The information of the P-wave velocity residuals computed with the true velocity model, initial model and inverted models with the elastic approach shown in Figure 45c and the acoustic approach shown in Figure 59b.

Distribution of the magnitude of the residuals (P-wave velocity)

Group	Initial model	Elastic inversion	Acoustic inversion
1	12.30 %	**56.23 %**	**33.02 %**
2	13.32 %	**21.96 %**	**28.77 %**
3	9.208 %	8.214 %	**16.82 %**
4	10.94 %	5.073 %	9.312 %
5	10.85 %	3.314 %	5.835 %
6	11.47 %	2.021 %	2.503 %
7	9.405 %	1.818 %	1.967 %
8	6.959 %	0.691 %	0.710 %
9	5.228 %	0.710 %	0.565 %
10	10.32 %	0.002 %	1.264 %

Table 14. The distribution of the magnitude of the P-wave velocity residuals computed with true P-wave velocity model and initial P-wave model and inverted models with the elastic and acoustic approaches.

Chapter 4. Conclusion

In this thesis, we introduced a 2D elastic Laplace-Fourier inversion algorithm on unstructured grids. The Laplace- and Laplace-Fourier-domain inversion methods have been studied with respect to their characteristics, limitations, and use for various media, such as acoustic, elastic, and acoustic-elastic coupled media, by many geophysicists (Shin et al., 2008; Shin el., 2009; Cha et al., 2010; Ha et al., 2010; Chung et al., 2010; Bae et al., 2010; Kim et al., 2013).

This study began with the simple extension from elastic Laplace-domain inversion to elastic Laplace-Fourier-domain inversion and the application of the unstructured grid. However, we encountered many problems, not those related to the choice of a structured or unstructured grid, but those originating from the complex-topography effect. For instance, for elastic Laplace-domain inversion with a flat surface it is possible to adopt the one-source assumption; thus, the source-estimation algorithm can be performed using a single source wavelet. However for an elastic inversion with complex topography, the source wavelets must be estimated independently for each shot because the different surface conditions encompassed by the topography lead to different source amplitudes and phases.

Moreover, irregular surface conditions make the regularized steepest-gradient direction more sensitive to damping factor in the flat surface case; thus, we were obliged to suggest a modified pseudo-Hessian matrix to address this issue. In this paper, it was derived using the difference in the definition of the pseudo-Hessian matrix based on the l_2 norm by Shin et al., 2001, and the

log norm by Ha et al., 2012.

In addition, the increased non-linearity in the signal caused by complex topography requires reasonable stopping criterion instead of the empirically determined number of iterations to guarantee accurate results. This type of multi-loop inversion is easy to yield an over- or underestimated velocity, depending on the number of iterations.

First, the stopping criterion based on the objective function was applied for the Laplace-Fourier-domain inversion. However, it was unable to obtain satisfactory results. Thus, the normalized stopping criterion was suggested based on studies of the characteristics of the logarithmic objective function (Shin et al, 2007; Bednar et al., 2007; Pyun et al., 2007). This stopping criterion was defined with the multi-objective assumption of real part amplitude error and imaginary part phase error, and it ensures the equal weighting of the influence of the two by assigning a normalized error to each. Numerical experiment successfully demonstrated the improvement in the results that was obtained using this approach. In this study, we imposed equal weighting for the phase and amplitude; however, we believe that an optimized weighting between the two exists that is a function of the frequency and Laplace damping constant and it will be studied in the future.

The developed algorithms are verified with synthetic and land dataset. For the time-domain synthetic test, 3 numerical tests was performed with different purposes, and the results demonstrated that the developed elastic Laplace-Fourier inversion algorithm is not entirely dependent to the low-frequency information, can recover an appropriate inversion result using a noisy dataset, and yields better results than the acoustic approach.

This research is a preliminary step in a promising line of investigation and

we plan to continuously improve this algorithm by applying it to many land datasets that represent many different conditions. In this study, we used only the vertical displacement as the observed but in the future, we wish to study elastic inversion using multi-component datasets and also for anisotropic media.

Appendix A. The 2D elastic wave simulation using interior penalty discontinuous Galerkin method in the time domain

The interior penalty discontinuous Galerkin finite element method (IPDG-FEM) is a type of FEM has been proven to yield accurate results using every type of mesh. This method relies on the exchange of numerical fluxes between adjacent elements. It is illustrated in Figure A.1. In contrast to classical FEMs, no continuity of a basis functions is imposed between elements, and therefore, the method supports discontinuities in the seismic wavefield between at the nodal points of two neighboring elements. Thus, this method does not suffer from spurious reflections, unlike classical FEMs, which generate unexpected reflection when applied to a changeable mesh.

Not only does the IPDG-FEM accommodate elements of various types and shapes, irregular non-matching grids, and even locally varying polynomial order, hence offering significant flexibility in mesh design, but it also produces block-diagonal mass matrices and therefore yields fully explicit, inherently parallel methods when coupled with explicit time stepping. The mass matrix that arises from a DG discretization is always block diagonal, with a block size equal to the number of degrees of freedom per element; hence, it can be computed at low computational cost without using the FEM lumping method (Marfurt, 1984).

The DG methods for the 2D elastic wave equation have been derived and applied by many geophysicists in recent years (Mercerat et al. 2006; Dumbser et al., 2006; Frey et al., 2008; Delcourte et al, 2009; Tago et al., 2012). Here, we derive the DG formulation from the 2^{nd}-order elastic equation, which dif-

fers from the 1st-order velocity-stress elastic equation that has previously been utilized.

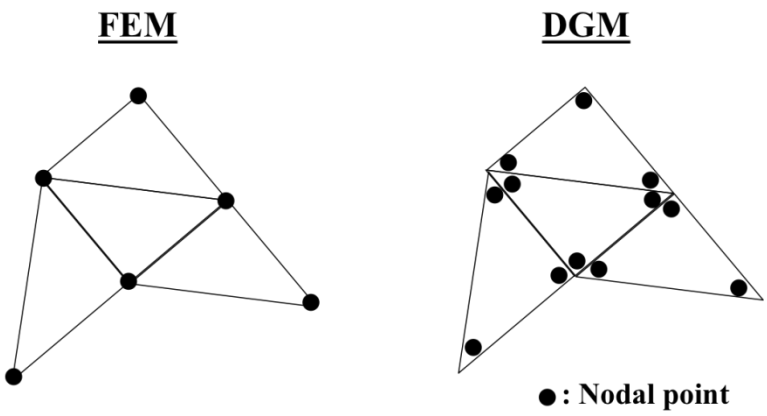

A 1. The comparison of the nodal point between FEM and DGM.

A.1 The notations

For a given domain Ω, we consider shape-irregular meshes Γ_h that partitions the domain Ω into disjointed triangular elements K, such that $\overline{\Omega} = \sum k$. $\overline{\Omega}$ is the domain for computation. k^- denotes neighboring elements of the element k^+. In addition, the following notation is used in this appendix.

- F_i represents the set of all interior edges, i.e., $F_i \coloneqq \partial K^+ \cap \partial K^-$;
- F_b represents the set of all boundary edges, i.e., $F_b \coloneqq \partial K^+ \cap \partial \overline{\Omega}$;
- F represents the set of all edges, i.e., $F \coloneqq F_i \cup F_b$;
- $\boldsymbol{n}^{\pm}$ denotes the unit normal vector of $K^{\pm}$;
- $[\![\ \ ]\!]$ is the jump function, i.e., $[\![\phi]\!] := \begin{cases} \phi^+\boldsymbol{n}^+ + \phi^-\boldsymbol{n}^- & f \in F_i \\ \phi\boldsymbol{n} & , f \in F_b \end{cases}$;
- $\{\{\ \ \}\}$ is the mean function, i.e., $\{\{\phi\}\} \coloneqq \begin{cases} (\phi^+ + \phi^-)/2 & f \in F_i \\ \phi & , f \in F_b \end{cases}$.

Where f denotes the edge at each element.

A.2 The IPDG formulation of the 2D elastic wave equation

The 2nd-order elastic wave equation in the time domain has already been presented in equations (2-2) to (2-6); however, for convenience in deriving the IPDG formulation from the beginning, we present it here again. Note that the notations used here are different from those used in the main article. The 2D elastic equation in the time domain can be expressed as

$$-\rho\frac{\partial^2}{\partial t^2}u = \frac{\partial}{\partial x}\sigma_{xx} + \frac{\partial}{\partial z}\sigma_{xz}, \tag{A.1}$$

$$-\rho\frac{\partial^2}{\partial t^2}v = \frac{\partial}{\partial x}\sigma_{zx} + \frac{\partial}{\partial z}\sigma_{zz}, \tag{A.2}$$

$$\sigma_{xx} = \lambda\Delta + 2\mu\varepsilon_{xx}, \tag{A.3}$$

$$\sigma_{zz} = \lambda\Delta + 2\mu\varepsilon_{zz},$$

$$\sigma_{xz} = \sigma_{zx} = \mu\varepsilon_{zx},$$

$$\Delta = \frac{\partial u}{\partial x} + \frac{\partial v}{\partial z}, \tag{A.4}$$

$$\varepsilon_{xx} = \frac{\partial u}{\partial x}, \tag{A.5}$$

$$\varepsilon_{zz} = \frac{\partial v}{\partial z},$$

$$\varepsilon_{zx}\frac{\partial v}{\partial x} + \frac{\partial u}{\partial z}.$$

Where u and v represent the horizontal displacement and vertical displacement, respectively. Equation (A.1) and (A.2) can be expressed using the Galerkin approximation as follows:

$$-\rho\frac{\partial^2}{\partial t^2}\int_{\bar{\Omega}}(u,\phi_x)d\bar{\Omega} = \int_{\bar{\Omega}}\left(\frac{\partial}{\partial x}\sigma_{xx},\phi_x\right)d\bar{\Omega} + \int_{\bar{\Omega}}\left(\frac{\partial}{\partial z}\sigma_{xz},\phi_x\right)d\bar{\Omega}, \tag{A.6}$$

$$-\rho\frac{\partial^2}{\partial t^2}\int_{\bar{\Omega}}(v,\phi_z)d\bar{\Omega} = \int_{\bar{\Omega}}\left(\frac{\partial}{\partial x}\sigma_{zx},\phi_z\right)d\bar{\Omega} + \int_{\bar{\Omega}}\left(\frac{\partial}{\partial z}\sigma_{zz},\phi_z\right)d\bar{\Omega}, \tag{A.7}$$

where (a,b) denotes the inner product of a and b. ϕ_x and ϕ_z are test functions for u and v, respectively.

The IPDG formulation for the horizontal displacement given by equation (A.6) will be presented in below, term by term. The 1st term on the right-hand side of it can be derived using Green's 1st identity and the jump and mean relations as follows:

$$\int_{\bar{\Omega}}\left(\frac{\partial}{\partial x}\sigma_{xx},\phi_x\right)d\bar{\Omega} \tag{A.8}$$

$$= \int_F(\sigma_{xx}\boldsymbol{n}_x,\phi_x)dF - \int_{\bar{\Omega}}\left(\sigma_{xx},\frac{\partial}{\partial x}\phi_x\right)d\bar{\Omega}$$

$$= \int_F\{\{\sigma_{xx}\}\}\cdot[\![\phi_x]\!] + [\![\sigma_{xx}]\!]\cdot\{\{\phi_x\}\}dF - \int_{\bar{\Omega}}\left(\sigma_{xx},\frac{\partial}{\partial x}\phi_x\right)d\bar{\Omega} + \gamma$$

(Because of $\sigma_{xx}\boldsymbol{n}_x$ is continuous; $[\![\sigma_{xx}]\!]$ is zero)

$$= \int_F\{\{\sigma_{xx}\}\}\cdot[\![\phi_x]\!]dF - \int_{\bar{\Omega}}\left(\sigma_{xx},\frac{\partial}{\partial x}\phi_x\right)d\bar{\Omega} + \gamma$$

$$= \int_F \frac{1}{2}(\sigma_{xx}{}^{+} + \sigma_{xx}{}^{-}) \cdot \left(\phi_x{}^{+}\boldsymbol{n}_x{}^{+} + \phi_x{}^{-}\boldsymbol{n}_x{}^{-}\right) dF - \int_{\bar{\Omega}} \left(\sigma_{xx}, \frac{\partial}{\partial x}\phi_x\right) d\bar{\Omega}$$

$$+\gamma.$$

Where, F is all edges. γ is the interior penalty constant and it will be defined later. The stress term in equation (A.8) can be replaced by the relationship expressed by equation (A.3). Then, equation (A.8) can be rewritten as follows,

$$\int_{\bar{\Omega}} \left(\frac{\partial}{\partial x}\sigma_{xx}, \phi_x\right) d\bar{\Omega} \tag{A.9}$$

$$= \int_F \frac{1}{2}\left(\lambda^{+}\Delta^{+} + 2\mu^{+}\frac{\partial u^{+}}{\partial x} + \lambda^{-}\Delta^{-} + 2\mu^{-}\frac{\partial u^{-}}{\partial x}\right) \cdot \left(\phi_x{}^{+}\boldsymbol{n}_x{}^{+} + \phi_x{}^{-}\boldsymbol{n}_x{}^{-}\right) dF$$

$$- \int_{\bar{\Omega}} \left(\lambda\Delta + 2\mu\frac{\partial u}{\partial x}, \frac{\partial}{\partial x}\phi_x\right) d\bar{\Omega} \; + \gamma$$

Similarly, the 2nd term on the right-hand side of equation (A.6) can be written as

$$\int_{\bar{\Omega}} \left(\frac{\partial}{\partial z}\sigma_{xz}, \phi_x\right) d\bar{\Omega} \tag{A.10}$$

$$= \int_F \frac{1}{2}\left(\mu^{+}\frac{\partial u^{+}}{\partial z} + \mu^{+}\frac{\partial v^{+}}{\partial x} + \mu^{-}\frac{\partial u^{-}}{\partial z} + \mu^{-}\frac{\partial v^{-}}{\partial x}\right) \cdot \left(\phi_x{}^{+}\boldsymbol{n}_z{}^{+} + \phi_x{}^{-}\boldsymbol{n}_z{}^{-}\right) dF$$

$$- \int_{\bar{\Omega}} \left(\mu\frac{\partial u}{\partial z} + \mu\frac{\partial v}{\partial x}, \frac{\partial}{\partial z}\phi_x\right) d\bar{\Omega} \; + \gamma$$

Thus, the horizontal displacement equation (A.6) can be transformed into equation (A.11), which does not contain the stress term, using equations (A.9) and (A.10).

$$-\rho\frac{\partial^2}{\partial t^2}\int_{\bar{\Omega}}(u,\phi_x)d\bar{\Omega} \tag{A.11}$$

$$=-\int_{\bar{\Omega}}\left(\lambda\Delta+2\mu\frac{\partial u}{\partial x},\frac{\partial}{\partial x}\phi_x\right)d\bar{\Omega}-\int_{\bar{\Omega}}\left(\mu\frac{\partial u}{\partial z}+\mu\frac{\partial v}{\partial x},\frac{\partial}{\partial z}\phi_x\right)d\bar{\Omega}$$

$$+\int_F\frac{1}{2}\left(\lambda^+\Delta^++2\mu^+\frac{\partial u^+}{\partial x}+\lambda^-\Delta^-+2\mu^-\frac{\partial u^-}{\partial x}\right)\cdot\left({\phi_x}^+\boldsymbol{n}_x{}^++{\phi_x}^-\boldsymbol{n}_x{}^-\right)dF$$

$$+\int_F\frac{1}{2}\left(\mu^+\frac{\partial u^+}{\partial z}+\mu^+\frac{\partial v^+}{\partial x}+\mu^-\frac{\partial u^-}{\partial z}+\mu^-\frac{\partial v^-}{\partial x}\right)\cdot\left({\phi_x}^+\boldsymbol{n}_z{}^++{\phi_x}^-\boldsymbol{n}_z{}^-\right)dF$$

$$+\gamma.$$

The vertical displacement equation can be rewritten as equation (A.12) using the same procedure.

$$-\rho\frac{\partial^2}{\partial t^2}\int_{\bar{\Omega}}(v,\phi_z)d\bar{\Omega} \tag{A.12}$$

$$=-\int_{\bar{\Omega}}\left(\lambda\Delta+2\mu\frac{\partial v}{\partial z},\frac{\partial}{\partial z}\phi_z\right)d\bar{\Omega}-\int_{\bar{\Omega}}\left(\mu\frac{\partial v}{\partial x}+\mu\frac{\partial u}{\partial z},\frac{\partial}{\partial x}\phi_z\right)d\bar{\Omega}$$

$$+\int_F\frac{1}{2}\left(\lambda^+\Delta^++2\mu^+\frac{\partial v^+}{\partial z}+\lambda^-\Delta^-+2\mu^-\frac{\partial v^-}{\partial z}\right)\cdot\left({\phi_z}^+\boldsymbol{n}_z{}^++{\phi_z}^-\boldsymbol{n}_z{}^-\right)dF$$

$$+\int_F\frac{1}{2}\left(\mu^+\frac{\partial v^+}{\partial x}+\mu^+\frac{\partial u^+}{\partial z}+\mu^-\frac{\partial v^-}{\partial x}+\mu^-\frac{\partial u^-}{\partial z}\right)\cdot\left({\phi_z}^+\boldsymbol{n}_x{}^++{\phi_z}^-\boldsymbol{n}_x{}^-\right)dF$$

$$+\gamma.$$

The 2nd order elastic wave equation can be expressed as a system of equations by considering the source term.

$$-\rho\frac{\partial^2}{\partial t^2}\mathbf{Ma}=\mathbf{Ka}+\mathbf{f}, \tag{A.13}$$

where **M** is the mass matrix; **a** is the displacement vector, which contains both horizontal and vertical components; **K** is the stiffness matrix; and **f** is the source vector.

$$\mathbf{M} = \begin{pmatrix} m_{11} & 0 \\ 0 & m_{22} \end{pmatrix}, \tag{A.14}$$

$$m_{11} = m_{22} = \sum_{K} \int_{k} \phi_I \phi_J d\,k, \tag{A.15}$$

$$\mathbf{a} = \begin{pmatrix} \boldsymbol{u} \\ \boldsymbol{v} \end{pmatrix}, \tag{A.16}$$

$$\mathbf{K} = \begin{pmatrix} k_{11} & k_{12} \\ k_{21} & k_{22} \end{pmatrix}. \tag{A.17}$$

The components of the stiffness matrix k_{11}, k_{12}, k_{21}, and k_{22} can be derived from the relations expressed in equations (A.11) and (A.12).

$$\begin{aligned} k_{11} = \sum_{K} \Bigg[& -\int_{k} (\lambda_k + 2\mu_k) \frac{\partial \phi_i}{\partial x} \frac{\partial \phi_j}{\partial x} dk - \int_{k} \mu_k \frac{\partial \phi_i}{\partial z} \frac{\partial \phi_j}{\partial z} dk \\ & + \sum_{F \in \partial k} \int_{f} \frac{1}{2} \left(\left(\lambda_k{}^{+} + 2\mu_k{}^{+}\right) \frac{\partial \phi_i{}^{+}}{\partial x} \phi_j{}^{+} \boldsymbol{n}_x{}^{+} + \left(\lambda_k{}^{-} + 2\mu_k{}^{-}\right) \frac{\partial \phi_i{}^{-}}{\partial x} \phi_j{}^{+} \boldsymbol{n}_x{}^{+} \right) df \\ & + \sum_{F \in \partial k} \int_{f} \frac{1}{2} \left(\mu_k{}^{+} \frac{\partial \phi_i{}^{+}}{\partial z} \phi_j{}^{+} \boldsymbol{n}_z{}^{+} + \mu_k{}^{-} \frac{\partial \phi_i{}^{-}}{\partial z} \phi_j{}^{+} \boldsymbol{n}_z{}^{+} \right) df \\ & + \sum_{F \in \partial k} \int_{f} \gamma_f \left(\phi_i{}^{+} \boldsymbol{n}^{+} \phi_j{}^{+} \boldsymbol{n}^{+} + \phi_i{}^{-} \boldsymbol{n}^{-} \phi_j{}^{+} \boldsymbol{n}^{+} \right) df \Bigg], \end{aligned} \tag{A.18}$$

(A.19)

$$k_{12} = \sum_K \left[-\int_k \lambda_k \frac{\partial \phi_i}{\partial z}\frac{\partial \phi_j}{\partial x} dk - \int_k \mu_k \frac{\partial \phi_i}{\partial x}\frac{\partial \phi_j}{\partial z} dk \right.$$

$$+ \sum_{F\in\partial k} \int_f \frac{1}{2}\left({\lambda_k}^+ \frac{\partial {\phi_i}^+}{\partial z} {\phi_j}^+ {\boldsymbol{n}_x}^+ + {\lambda_k}^- \frac{\partial {\phi_i}^-}{\partial z} {\phi_j}^+ {\boldsymbol{n}_x}^+ \right) df$$

$$\left. + \sum_{F\in\partial k} \int_f \frac{1}{2}\left({\mu_k}^+ \frac{\partial {\phi_i}^+}{\partial x} {\phi_j}^+ {\boldsymbol{n}_z}^+ + {\mu_k}^- \frac{\partial {\phi_i}^-}{\partial x} {\phi_j}^+ {\boldsymbol{n}_z}^+ \right) df, \right.$$

(A.20)

$$k_{21} = \sum_K \left[-\int_k \lambda_k \frac{\partial \phi_i}{\partial x}\frac{\partial \phi_j}{\partial z} dk - \int_k \mu_k \frac{\partial \phi_i}{\partial z}\frac{\partial \phi_j}{\partial x} dk \right.$$

$$+ \sum_{F\in\partial k} \int_f \frac{1}{2}\left({\lambda_k}^+ \frac{\partial {\phi_i}^+}{\partial x} {\phi_j}^+ {\boldsymbol{n}_z}^+ + {\lambda_k}^- \frac{\partial {\phi_i}^-}{\partial x} {\phi_j}^+ {\boldsymbol{n}_z}^+ \right) df$$

$$\left. + \sum_{F\in\partial k} \int_f \frac{1}{2}\left({\mu_k}^+ \frac{\partial {\phi_i}^+}{\partial z} {\phi_j}^+ {\boldsymbol{n}_x}^+ + {\mu_k}^- \frac{\partial {\phi_i}^-}{\partial z} {\phi_j}^+ {\boldsymbol{n}_x}^+ \right) df, \right.$$

(A.21)

$$k_{22} = \sum_K \left[-\int_k (\lambda_k + 2\mu_k) \frac{\partial \phi_i}{\partial z}\frac{\partial \phi_j}{\partial z} dk - \int_k \mu_k \frac{\partial \phi_i}{\partial x}\frac{\partial \phi_j}{\partial x} dk \right.$$

$$+ \sum_{F\in\partial k} \int_f \frac{1}{2}\left(\left({\lambda_k}^+ + 2{\mu_k}^+ \right) \frac{\partial {\phi_i}^+}{\partial z} {\phi_j}^+ {\boldsymbol{n}_z}^+ \right.$$

$$\left. \left. + \left({\lambda_k}^- + 2{\mu_k}^- \right) \frac{\partial {\phi_i}^-}{\partial z} {\phi_j}^+ {\boldsymbol{n}_z}^+ \right) df \right.$$

$$+ \sum_{F\in\partial k} \int_f \frac{1}{2}\left({\mu_k}^+ \frac{\partial {\phi_i}^+}{\partial x} {\phi_j}^+ {\boldsymbol{n}_x}^+ + {\mu_k}^- \frac{\partial {\phi_i}^-}{\partial x} {\phi_j}^+ {\boldsymbol{n}_x}^+ \right) df$$

$$+\sum_{F\in\partial k}\int_{f}\gamma_f\left(\phi_i{}^{+}\boldsymbol{n}^{+}\phi_j{}^{+}\boldsymbol{n}^{+}+\phi_i{}^{-}\boldsymbol{n}^{-}\phi_j{}^{+}\boldsymbol{n}^{+}\right)df\Bigg],$$

where the γ_f is the interior penalty constant for stabilization and it is defined on each edge of the element as (Baldassari, 2009)

$$\gamma_f = ac_{max}h_{min}, \tag{A.22}$$

$$a = \frac{1}{2}l(l+1), \tag{A.23}$$

$$c_{max} = \begin{cases} max(c_{k^+}, c_{k^-}) & f \in F_i \\ c_k & f \in F_b \end{cases}, \tag{A.24}$$

$$h_{min} = \begin{cases} min(h_{k^+}, h_{k^-}) & f \in F_i \\ h_k & f \in F_b \end{cases}, \tag{A.25}$$

Finally, the IPDG formulation of the 2D elastic wave equation can be presented as in equation (A.26) via the central FDM scheme for a 2nd-derivative displacement vector with respect to time.

$$\mathbf{a}^{i+1} = 2\mathbf{a}^{i} - \mathbf{a}^{i-1} - \mathbf{M}^{-1}\frac{(dt)^2}{\rho}\left(\mathbf{K}\mathbf{a}^{i} + \mathbf{f}\right), \tag{A.26}$$

where, i is the number of discrete time samples with the interval dt.

Figure A 2 presents the modeling results computed using the parameters shown in Figure 8, 9 and the time-domain IPDG scheme, and it shows the horizontal and vertical displacement after 1 sec.

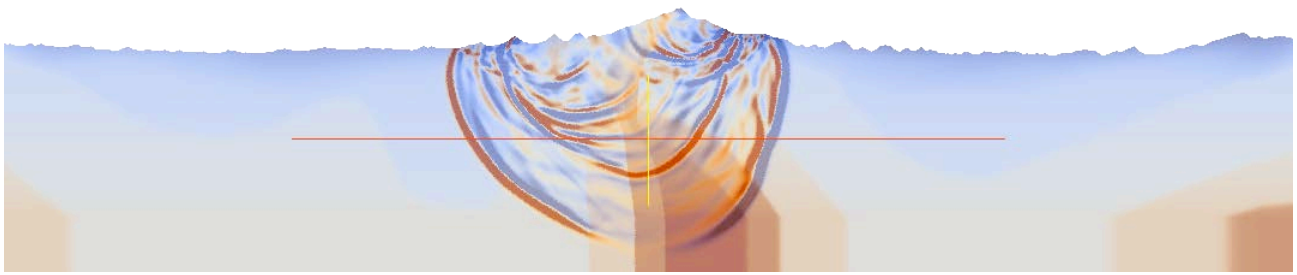

(a)

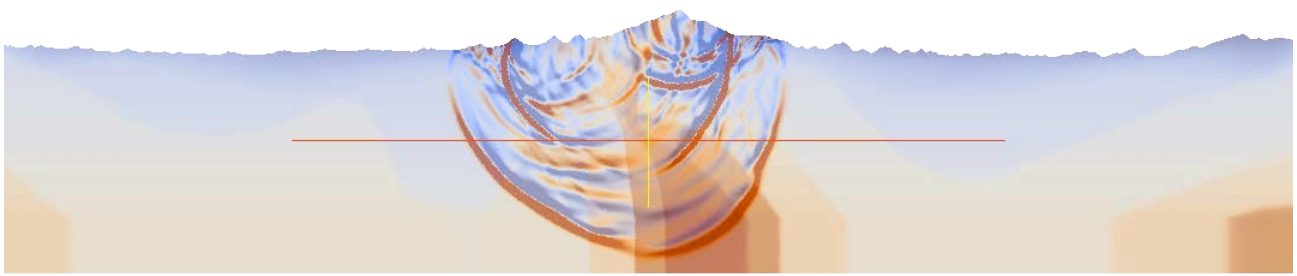

(b)

A 2. Snap shots after 1sec of the (a) horizontal and (b) vertical displacements obtained using IPDG method.

REFERENCES

Bae, Ho Seuk, Sukjoon Pyun, Wookeen Chung, Seung-Goo Kang, and Changsoo Shin. "Frequency-domain acoustic-elastic coupled waveform inversion using the Gauss-Newton conjugate gradient method." Geophysical Prospecting 60, no. 3 (2012): 413-432.

Baeten, Guido, Jan Willem de Maag, René-Edouard Plessix, Rini Klaassen, Tahira Qureshi, Maren Kleemeyer, Fons ten Kroode, and Zhang Rujie. "The use of low frequencies in a full-waveform inversion and impedance inversion land seismic case study." Geophysical Prospecting (2013).

Baldassari, Caroline. "Modélisation et simulation numérique pour la migration terrestre par équation d'ondes." PhD diss., Université de Pau et des Pays de l'Adour, 2009.

Bleibinhaus, Florian, and Stéphane Rondenay. "Effects of surface scattering in full-waveform inversion." Geophysics 74, no. 6 (2009): WCC69-WCC77.

Brenders, A. J., and R. G. Pratt. "Full waveform tomography for lithospheric imaging: results from a blind test in a realistic crustal model." Geophysical Journal International 168, no. 1 (2007): 133-151.

Brossier, Romain. "Imagerie sismique à deux dimensions des milieux visco-élastiques par inversion des formes d'ondes: développements méthodologiques et applications." PhD diss., Université de Nice Sophia-Antipolis, 2009.

Brossier, Romain. "Two-dimensional frequency-domain visco-elastic full waveform inversion: Parallel algorithms, optimization and performance." Computers & Geosciences 37, no. 4 (2011): 444-455.

Bunks, Carey, Fatimetou M. Saleck, S. Zaleski, and G. Chavent. "Multiscale seismic waveform inversion." Geophysics 60, no. 5 (1995): 1457-1473.

Cha, Young Ho, and Changsoo Shin. "Two-dimensional Laplace-domain waveform inversion using adaptive meshes: an experience of the 2004 BP velocity-analysis benchmark data set." Geophysical Journal International 182, no. 2 (2010): 865-879.

Chung, Wookeen, Changsoo Shin, and Sukjoon Pyun. "2D elastic waveform inversion in the Laplace domain." Bulletin of the Seismological Society of America 100, no. 6 (2010): 3239-3249.

Cohen, Gary. Higher-order numerical methods for transient wave equations. Springer, 2002.

Delcourte, Sarah, and Nathalie Glinsky. "ANALYSIS OF A DISCONTINUOUS GALERKIN METHOD FOR ELASTODYNAMIC EQUATIONS. APPLICATION TO 3D WAVE PROPAGATION." (2013).

Dumbser, Michael, and Martin Käser. "An arbitrary high-order discontinuous Galerkin method for elastic waves on unstructured meshes–II. The three-dimensional isotropic case." Geophysical Journal International 167, no. 1 (2006): 319-336.

Gélis, Céline, Jean Virieux, and Gilles Grandjean. "Two-dimensional elastic full waveform inversion using Born and Rytov formulations in the frequency domain." Geophysical Journal International 168, no. 2 (2007): 605-633.

Wansoo Ha, Wookeen Chung, and Changsoo Shin. “Pseudo-Hessian matrix for the logarithmic objective function in full wave inversion.”Journal of Seismic Exploration, vol.21, no.3, (2012) 201-214

Ha, Wansoo, Sukjoon Pyun, Jewoo Yoo, and Changsoo Shin. "Acoustic full waveform inversion of synthetic land and marine data in the Laplace domain." Geophysical Prospecting 58, no. 6 (2010): 1033-1048.

Jeong, Woodon, Ho-Yong Lee, and Dong-Joo Min. "Full waveform inversion strategy for density in the frequency domain." Geophysical Journal International 188.3 (2012): 1221-1242.

Kim, Youngseo, et al. "An algorithm for 3D acoustic time-Laplace-Fourier-domain hybrid full waveform inversion." Geophysics 78.4 (2013): R151-R166.

Konak, Abdullah, David W. Coit, and Alice E. Smith. "Multi-objective optimization using genetic algorithms: A tutorial." Reliability Engineering & System Safety 91.9 (2006): 992-1007.

Lailly, Patrick. "The seismic inverse problem as a sequence of before stack migrations." In Conference on inverse scattering: theory and application, pp.

206-220. Society for Industrial and Applied Mathematics, Philadelphia, PA, 1983.

Latimer, Rebecca Buxton, Rick Davidson, and Paul Van Riel. "An interpreter's guide to understanding and working with seismic-derived acoustic impedance data." The leading edge 19.3 (2000): 242-256.

Lee, Ho-Yong, June Mo Koo, Dong-Joo Min, Byung-Doo Kwon, and Hai Soo Yoo. "Frequency-domain elastic full waveform inversion for VTI media." Geophysical Journal International 183, no. 2 (2010): 884-904.

Lee, Shiann-Jong, Dimitri Komatitsch, Bor-Shouh Huang, and Jeroen Tromp. "Effects of topography on seismic-wave propagation: an example from Northern Taiwan." Bulletin of the Seismological Society of America 99, no. 1 (2009): 314-325.

Marfurt, Kurt J. "Accuracy of finite-difference and finite-element modeling of the scalar and elastic wave equations." Geophysics 49.5 (1984): 533-549.

Mercerat, E. D., J. P. Vilotte, and F. J. Sánchez-Sesma. "Triangular Spectral Element simulation of two-dimensional elastic wave propagation using unstructured triangular grids." Geophysical Journal International 166.2 (2006): 679-698.

Mora, Peter. "Nonlinear two-dimensional elastic inversion of multioffset seismic data." Geophysics 52.9 (1987): 1211-1228.

Operto, S., C. Ravaut, L. Improta, J. Virieux, A. Herrero, and P. Dell'Aversana. "Quantitative imaging of complex structures from dense wide-aperture seismic data by multiscale traveltime and waveform inversions: a case study." Geophysical Prospecting 52, no. 6 (2004): 625-651.

Plessix, René-Édouard, Guido Baeten, Jan Willem de Maag, Fons ten Kroode, and Zhang Rujie. "Full waveform inversion and distance separated simultaneous sweeping: a study with a land seismic data set." Geophysical Prospecting 60, no. 4 (2012): 733-747.

Pratt, Gerhard, and Changsoo Shin. "Gauss–Newton and full Newton methods in frequency–space seismic waveform inversion." Geophysical Journal International 133.2 (1998): 341-362.

Prechelt, Lutz. "Automatic early stopping using cross validation: quantifying the criteria." Neural Networks 11.4 (1998): 761-767.

Pyun, Sukjoon, Changsoo Shin, and J. B. Bednar. "Comparison of waveform inversion, part 3: amplitude approach." Geophysical prospecting 55.4 (2007): 477-485.

Recktenwald, Gerald. "Stopping Criteria for Iterative Solution Methods." (2012).

Romdhane, Anouar, Gilles Grandjean, Romain Brossier, Fayçal Rejiba, Stéphane Operto, and Jean Virieux. "Shallow-structure characterization by 2D elastic full-waveform inversion." Geophysics 76, no. 3 (2011): R81-R93.

Shewchuk, Jonathan Richard. "Delaunay refinement algorithms for triangular mesh generation." Computational geometry 22.1 (2002): 21-74.

Shin, Changsoo, Sukjoon Pyun, and J. Bednar. "Comparison of waveform inversion, part 1: conventional wavefield vs logarithmic wavefield." Geophysical Prospecting 55.4 (2007): 449-464.

Shin, Changsoo, Nam-Hyung Koo, Young Ho Cha, and Keun-Pil Park. "Sequentially ordered single-frequency 2-D acoustic waveform inversion in the Laplace–Fourier domain." Geophysical Journal International 181, no. 2 (2010): 935-950.

Shin, Changsoo, Seonghyung Jang, and Dong-Joo Min. "Improved amplitude preservation for prestack depth migration by inverse scattering theory." Geophysical prospecting 49.5 (2001): 592-606.

Shin, Changsoo, and Dong-Joo Min. "Waveform inversion using a logarithmic wavefield." Geophysics 71.3 (2006): R31-R42.

Shin, Changsoo, Sukjoon Pyun, and J. Bednar. "Comparison of waveform inversion, part 1: conventional wavefield vs logarithmic wavefield." Geophysical Prospecting 55.4 (2007): 449-464.

Shin, Changsoo, and Young Ho Cha. "Waveform inversion in the Laplace domain." Geophysical Journal International 173.3 (2008): 922-931.

Shin, Changsoo, and Wansoo Ha. "A comparison between the behavior of objective functions for waveform inversion in the frequency and Laplace domains." Geophysics 73.5 (2008): VE119-VE133.

Shin, Changsoo, and Young Ho Cha. "Waveform inversion in the Laplace—Fourier domain." Geophysical Journal International 177.3 (2009): 1067-1079.

Shipp, Richard M., and Satish C. Singh. "Two-dimensional full wavefield inversion of wide-aperture marine seismic streamer data." Geophysical Journal International 151.2 (2002): 325-344.

Stoughton, D., J. Stefani, and S. Michell. "2D elastic model for wavefield investigations of subsalt objectives, deep water Gulf of Mexico." 63rd EAGE Conference & Exhibition. 2001.

Tago, J., V. M. Cruz-Atienza, J. Virieux, V. Etienne, and F. J. Sánchez-Sesma. "A 3D hp-adaptive discontinuous Galerkin method for modeling earthquake dynamics." Journal of Geophysical Research: Solid Earth (1978–2012) 117, no. B9 (2012).

Tarantola, Albert. "Linearized inversion of seismic reflection data." Geophysical prospecting 32.6 (1984): 998-1015.

Tarantola, Albert. Inverse problem theory: Methods for data fitting and model parameter estimation. Elsevier Science, 2002.

Virieux, Jean, and Stéphane Operto. "An overview of full-waveform inversion

in exploration geophysics." Geophysics 74.6 (2009): WCC1-WCC26.

Zielinski, Karin, Dagmar Peters, and Rainer Laur. "Stopping criteria for single-objective optimization." Proceedings of the Third International Conference on Computational Intelligence, Robotics and Autonomous Systems. 2005.

Zielinski, Karin, and Rainer Laur. "Stopping criteria for a constrained single-objective particle swarm optimization algorithm." Informatica (Slovenia) 31.1 (2007): 51-59.

Zelt, C. A., et al. "Advancements in long-offset seismic imaging: A blind test of traveltime and waveform tomography." AGU Spring Meeting Abstracts. Vol. 1. 2005.

초 록

현재 탄성파 자료 획득분야에서의 놀라운 발전은 지금까지 완전 파형역산의 현장자료에 대한 적용을 어렵게 해온 저주파수 성분의 부재 문제를 해결할 수 있는 가능성을 보여준다. 그러나 아직까지 대부분의 현장 탄성파 자료에서 저주파수 성분을 기대하기는 어려운 상황이다. 따라서 저주파수의 부재 문제를 해결해 줄 수 있는 좋은 장파장 속도 모델을 구축 하는 것은 푸리에 영역에서의 파형역산을 통해 고해상도의 속도모델을 구축하거나 구조보정을 통한 지하영상 획득에 있어서 매우 중요한 의미를 갖는다.

본 논문에서는 라플라스-푸리에 영역에서 2차원 탄성 파동방정식을 이용하여 육상탐사에 적용 가능한 파형역산 기법을 개발하였다. 이 기술은 비정규 격자를 이용한 유한요소법에 기반하여 개발되었다. 비정규 격자를 적용함으로써 육상 탐사 자료가 획득된 지형을 정확하게 묘사하는 것이 가능해졌고, 이를 통해 불규칙한 지표면에 의해 발생되는 자료의 비선형성을 줄이는 효과를 기대 할 수 있다.

탄성 매질에서 적용할 수 있는 수정된 헤시안 매트릭스를 정의함으로써 라플라스-푸리에 완전 파형 역산의 결과가 지금까지 유사 헤시안을 적용할시에 함께 정의된 감쇄상 없이 이전의 방법에 비해 깊은 탐사심도와 정확성을 동시에 가질 수 있게 만들었다.

또한 로그 목적함수가 진폭 오차와 위상 오차를 자연적으로 분리해내는 특성에 착안하여 라플라스-푸리에 영역 완전파형 역산에서 잔차의 진폭정보와 위상정보를 균형 있게 이용할 수 있는

진폭 오차와 위상 오차를 정규화 시켜 이용하는 반복중단 알고리즘을 소개하였다. 이를 적용함으로 잘못된 역산 반복횟수 결정이나 과대적합에 의해 야기될 수 있는 부적절한 파형역산 결과 획득을 막고자 하였다.

본 논문을 통해 개발된 알고리즘의 실제 탐사자료에 대한 적용 가능성을 실험하기 위해 현장자료가 가질 수 있는 대표적인 문제점인 저주파수가 없는 경우와 잡음이 가해진 시간영역 인공합성 자료를 이용하여 수치실험을 수행하였다. 그 결과 저주파수 성분에 의존하지 않고 성공적으로 장파장 속도모델을 구축할 수 있었고, 잡음이 섞인 자료에 대해서도 만족할 만한 결과를 보여주었다.

주요어: 2차원 탄성 매질, 완전 파형 역산, 비정규 격자요소, 반복중단 알고리듬, 유사 헤시안, 라플라스-푸리에 영역

학 번: 2009-22977